

Plasma synthetic jet actuators for active flow control

Zong, Haohua

DOI

[10.4233/uuid:b2592fae-0a96-4aba-90a8-12c18e849a4c](https://doi.org/10.4233/uuid:b2592fae-0a96-4aba-90a8-12c18e849a4c)

Publication date

2018

Document Version

Final published version

Citation (APA)

Zong, H. (2018). *Plasma synthetic jet actuators for active flow control*. [Dissertation (TU Delft), Delft University of Technology]. <https://doi.org/10.4233/uuid:b2592fae-0a96-4aba-90a8-12c18e849a4c>

Important note

To cite this publication, please use the final published version (if applicable).
Please check the document version above.

Copyright

Other than for strictly personal use, it is not permitted to download, forward or distribute the text or part of it, without the consent of the author(s) and/or copyright holder(s), unless the work is under an open content license such as Creative Commons.

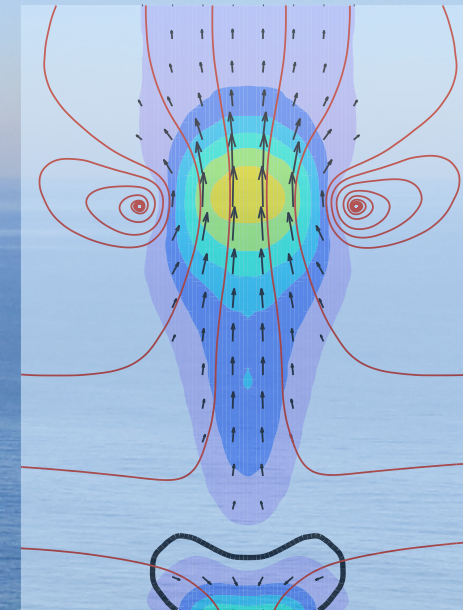
Takedown policy

Please contact us and provide details if you believe this document breaches copyrights.
We will remove access to the work immediately and investigate your claim.

Plasma Synthetic Jet Actuators for Active Flow Control

H. Zong

Plasma Synthetic Jet Actuators for Active Flow Control



Haohua Zong



ISBN 978-94-6186-954-8

PLASMA SYNTHETIC JET ACTUATORS FOR ACTIVE FLOW CONTROL

Propositions

accompanying the dissertation

PLASMA SYNTHETIC JET ACTUATORS FOR ACTIVE FLOW CONTROL

by

Haohua ZONG

1. If a surface dielectric barrier discharge actuator can be compared to a micro gas turbine engine (space-dependent cycle), the plasma synthetic jet actuator can refer to the piston engine (time-dependent cycle). (this thesis)
2. An ideal type of plasma for efficiently producing synthetic jets is the one that can pressurize the actuator cavity uniformly and instantly. (this thesis)
3. The limit working frequency of a plasma synthetic jet actuator is determined not only by the natural Helmholtz oscillation frequency of the cavity, but also the thermal cutoff frequency derived from the energy equilibrium during the actuation cycle. (this thesis)
4. When dealing with boundary layer separation control, the mild suction flow induced by the plasma synthetic jet actuator, although weaker, is as significant as the high-velocity jet flow. (this thesis)
5. The destiny of plasma synthetic jets in high-Reynolds-number flow control depends more on the efforts of electrical engineers rather than aerodynamic experts.
6. Although not all knowledge gaps are significant, they are used ubiquitously to justify the significance of all investigations.
7. To get a publication on the topic of plasma flow control, the simplest way would be to design an actuator and test its characteristics.
8. Connection, comparison, normalization and generalization are secrets for publishing articles in high-impact journals.
9. Happiness is a transient feeling sensitive to the positive changes of our lives. For most people, the sensitivity decays monotonically with the age since born.
10. Interests, capabilities and chances are sufficient conditions for success. They respectively determine how much time you wish to sacrifice, how efficient you can be and how lucky you are.

These propositions are regarded as opposable and defensible, and have been approved as such by the promotor prof. dr. F. Scarano.

Stellingen

behorende bij het proefschrift

PLASMA SYNTHETIC JET ACTUATORS FOR ACTIVE FLOW CONTROL

door

Haohua ZONG

1. Als een oppervlakte diëlektrische barrière ontlading actuator vergeleken kan worden met een micro gasturbine (ruimte-afhankelijke cyclus), dan kan een plasma synthetische jet actuator verwijzen naar een zuigermotor (tijdsafhankelijke cyclus). (dit proefschrift)
2. Een ideaal type plasma dat efficiënt synthetische jets kan produceren is een plasma dat instantaan en uniform de druk in de holte kan verhogen. (dit proefschrift)
3. De limiet van de werkfrequentie van een plasma synthetische jet actuator is niet alleen afhankelijk van de natuurlijke Helmholtz oscillatiefrequentie van de holte, maar is ook afhankelijk van de thermische afkap frequentie afgeleid van het energie-evenwicht tijdens de aandrijfcyclus. (dit proefschrift)
4. Wanneer het gaat om het beïnvloeden van grenslaagscheiding is de milde zuigstroom opgelegd door de plasma synthetische jet actuator, hoewel zwakker, net zo belangrijk als de krachtige jet tijdens de expansie fase. (dit proefschrift)
5. Het lot van plasma synthetische jet actuators in het regelen van hoge Reynolds stromen, is meer afhankelijk van de inspanningen van elektrotechnici dan van aerodynamici.
6. Hoewel niet alle kennislacunes significant zijn, worden ze alomtegenwoordig gebruikt om de significantie van alle onderzoeken te rechtvaardigen.
7. Om een publicatie op het gebied van plasmastroomregeling te bemachtigen is de eenvoudigste manier het ontwerpen van een actuator en het testen van diens karakteristieken.
8. De kunst van het verbinden, vergelijken, normaliseren en generaliseren is het geheim voor het publiceren van artikelen in toonaangevende tijdschriften.
9. Geluk is een kortstondig gevoel dat ontvankelijk is voor de positieve veranderingen in ons leven. Voor de meeste mensen vervalt de gevoeligheid monotoon met diens leeftijd.
10. Interesses, capaciteiten en kansen zijn voldoende om succes te bereiken. Ze bepalen de hoeveelheid tijd die je wenst op te offeren, hoe efficiënt je kunt zijn en hoeveel geluk je hebt.

Deze stellingen worden oponeerbaar en verdedigbaar geacht en zijn als zodanig goedgekeurd door de promotor prof. dr. F. Scarano.

PLASMA SYNTHETIC JET ACTUATORS FOR ACTIVE FLOW CONTROL

Dissertation

for the purpose of obtaining the degree of doctor
in Delft University of Technology,
by the authority of the Rector Magnificus prof. ir. T.H.J.J. van der Hagen,
Chair of the Board for Doctorates,
to be defended publicly on
Thursday 1 November 2018 at 10:00 am.

by

Haohua ZONG

Bachelor of Science in Flight Vehicle Propulsion Engineering,
Air Force Engineering University, Xi'an, China
born in Ruzhou, Henan Province, China.

Thus dissertation has been approved by the

promotor: Prof. dr. F. Scarano

copromotor: Dr. M. Kotsonis

Composition of the doctoral committee:

Rector Magnificus,	Chairman
Prof. dr. F. Scarano,	Delft University of Technology
Dr. M. Kotsonis,	Delft University of Technology

Independent members:

Prof. dr. L. L. M. Veldhuis,	Delft University of Technology
Prof. dr. L. N. Cattafesta III,	Florida State University, United States
Prof. dr. K. -S. Choi,	University of Nottingham, United Kingdom
Prof. dr. L. De Luca,	University of Naples Federico II, Italy
Dr. J. -P. Bonnet,	University of Poitiers, France

Reserved:

Prof. dr. S. Hickel,	Delft University of Technology
----------------------	--------------------------------



Keywords: plasma, synthetic jet, flow control

Front & Back: Representative flow topology of plasma synthetic jets superimposed on the panoramic view of Cabo da Roca (Portugal, taken by the author in 21 December 2017)

Copyright © 2018 by H. Zong

ISBN 978-94-6186-954-8

An electronic version of this dissertation is available at
<http://repository.tudelft.nl/>.

SUMMARY

In the last few decades, active flow control (AFC) technology has been developed to minimize the aerodynamic drag of transportation vehicles and maximize the propulsion efficiency of thermodynamic engines. The key of this technology is the actuators. Among all the actuators that have been proposed (i.e. fluidic, moving object, or plasma-based), plasma synthetic jet actuators (PSJAs) exhibit the unique capability of producing high-velocity pulsed jets at high-frequency, thus promising to be applied in high-Reynolds-number practical flows (e.g. aircraft wings, inlets, helicopter blades). The main objective of this thesis is to provide a deep understanding of the operation characteristics and flow control mechanisms of PSJAs, by virtue of advanced flow diagnostics and simplified theoretical analysis.

In the first part, the formation and evolution characteristics of plasma synthetic jets in quiescent air were treated, and several non-dimensional scaling laws linking electrical and geometrical parameters of the actuator with jet intensity metrics (e.g. velocity, density, duration) were derived. The peak jet exit velocity (U_p) is dominated by the non-dimensional energy deposition (ϵ) defined as the ratio of discharge energy to the initial enthalpy of cavity gas. For actuators with approximately unchanged electromechanical efficiency, U_p increases linearly with $\epsilon^{1/3}$. The mean jet exit density (ρ_e) is mainly affected by the energy equilibrium within the actuator cavity. At steady working stage of the repetitive operation, ρ_e declines monotonically with the square of dimensionless discharge frequency, and the declining rate drops with increasing convective heat transfer rate between the actuator cavity and the outer environment. Duration of the pulsed jet (T_{jet}) can be tuned by both discharge waveforms and geometrical parameters of the actuator. For instant energy deposition with a dimensionless discharge frequency much less than 1, T_{jet} can be approximated by the natural Helmholtz oscillation period of the actuator cavity. Orifice shape does not change the above-mentioned jet formation laws. Nevertheless, compared to circular jets, a much higher entrainment rate of the surrounding fluids is experienced by slot jets, leading to a lower jet penetration length.

The second part concerns the interaction between plasma synthetic jets and a cross-flow turbulent boundary layer. The jet issued initially in the wall-normal direction bends noticeably to the crossflow during subsequent evolution, resulting in a time-dependent jet trajectory. The penetration ability defined by the outer envelope of jet trajectories is governed by vortex ring dynamics. A downstream-tilting vortex ring with trailing jet column and an upstream-tilting vortex ring driven by Kutta-Joukowski lift are manifested at high and low jet-to-crossflow velocity ratio respectively, and the jet penetration length is maximized when the time-mean pitching angle of the ring approaches zero. Additionally, at high velocity ratio, a hanging vortex pair is created in the leeward side of jet body, which gradually evolves into a quasi-streamwise counter-rotating vortex pair (CVP) during jet bending. This CVP induces a weak downwash velocity beside its two legs, transporting high-momentum flow from the freestream to near-wall region thus

leading to a fuller boundary layer velocity profile favouring flow separation control. In the case of low velocity ratio, no CVP is created, nevertheless similar downwash effects are imposed by the two longitudinal edges of the front vortex ring.

In the last part, plasma synthetic jets are tested in two types of flows, namely airfoil leading-edge flow separation at a chord-based Reynolds number of $Re_c = 1.7 \times 10^5$ and shock wave/boundary layer interaction (SWBLI) control at Mach number 2. In the former case, the stall angle is postponed by 8 degrees, meanwhile the peak lift coefficient is increased by 21%. Distinct separation control mechanisms are exhibited depending on the angle of attack. At moderate stall angle, plasma actuation is able to shift the separation point downstream to mid-chord position, as a result of energizing the incoming boundary layer through mixing enhancement. At deep stall angle, the separation point remains near the leading edge, whereas the zero-velocity line is periodically swept towards the suction surface by the convective spanwise vortices induced by plasma synthetic jets, leading to a decrease of time-averaged separation area. For the SWBLI control case, the optimal discharge frequency for separation suppression is demonstrated to be $F^* = 0.02$. Compared to non-actuated condition, the sonic line in time-averaged velocity field retreats downstream by approximately half of the boundary layer thickness, meanwhile the separation area derived from flow reversal probability is reduced by 14%.

SAMENVATTING

In de laatste paar decennia zijn technieken van het actief beïnvloeden van luchtstromingen, beter bekend als Active Flow Control (AFC) technieken, ontwikkeld om de aerodynamische wrijving van transportvoertuigen te verminderen en de voortstuwings efficiëntie van thermodynamische motoren te maximaliseren. De sleutel tot het effectief beïnvloeden van stromingen zijn de actuatoren. Hoewel elk type actuator (dwz. fluïde, bewegend object of op plasma gebaseerd) zijn eigen voor- en nadelen heeft, hebben Plasma Synthetische Jet Actuatoren (PSJAs) de unieke capaciteit om gepulseerde jets op hoge snelheid (> 300 m/s) en hoge frequentie (> 5 kHz) te produceren. Dit type actuator is daarom veelbelovend in praktische applicaties met een hoog Reynoldsgetal (dwz. $O(10^6 - 10^7)$), zoals vliegtuigvleugels, inlaten en helikopterbladen. Het doel van dit proefschrift is het verstreken van een diep begrip van de werkingskarakteristieken en stroomregelmingsmechanismen van PSJAs op grond van geavanceerde stroom diagnostiek en vereenvoudigde theoretische modellen.

In het eerste deel van dit proefschrift zijn de formatie- en evolutiekarakteristieken van plasma synthetische jets in stille lucht behandeld en de verschillende schalingswetten, die de elektrische en geometrische parameters van de actuator koppelen aan de metingen van de jet intensiteit (bijv. Snelheid, dichtheid en duratie), afgeleid. De piek van de uittreed-snelheid van de jet (U_p) wordt gedomineerd door de niet-dimensionale energiedepositie (ϵ) die wordt gedefinieerd als de ratio tussen ontladingsenergie tot de initiële enthalpie van het holtegas. Voor actuatoren met een nagenoeg constante elektro-mechanische efficiëntie stijgt U_p lineair met $\epsilon^{1/3}$. De gemiddelde uittreed-dichtheid van de jet (ρ_e) wordt vooral beïnvloed door de energiebalans binnenin de actuator. Zodra de opererende actuator een stabiel werkingspunt heeft behaald daalt ρ_e monotoon met het kwadraat van de dimensieloze ontladingsfrequentie. De snelheid van deze daling is afhankelijk van de convectieve warmteoverdrachtssnelheid tussen de actuatorholte en de buitenomgeving. De looptijd van een gepulseerde jet (T_{jet}) kan worden afgestemd door zowel de ontladingsgolfvormen als door de geometrische parameters van de actuator. In het uiterlijke geval van een onmiddellijke energiedispositie met een dimensieloze ontladingsfrequentie van aanzienlijk minder dan 1, kan T_{jet} worden benaderd met de natuurlijke Helmholtz-oscillatieperiode van de actuatorholte. De vorm van de opening veranderd de bovengenoemde jetvormingswetten niet. Desalniettemin is aangetoond dat gleufvormige jets in staat zijn de lucht beter met zich mee te slepen dan een cirkelvormige jet, wat leidt tot een lagere penetratie lengte van de jet.

Het tweede deel van dit proefschrift betreft PSJAs geplaatst in een stroom, waarbij de interactie tussen de plasma synthetische jets en turbulente grenslagen werd onderzocht. De jet, die aanvankelijk in de muur-normale richting wordt afgegeven, buigt aanzienlijk tijdens de daaropvolgende evolutie, wat resulteert in een tijdafhankelijk traject van de jet. Het penetratievermogen, wat is gedefinieerd als de buitengrens van de jet, wordt bepaald door de werveling dynamica. Zo manifesteert zich een stroomaf-

waarts draaiende werveling gevolgd door een jet kolom wanneer de verhouding tussen de jet en hoofdstroom snelheden groot genoeg is en een werveling gedreven door de Kutta-Joukowski stijgkracht wanneer deze snelheidsverhouding laag is. De jet penetratiediepte is maximaal wanneer de tijdgemiddelde pitchhoek van de werveling de 0α nadert. Bovendien wordt bij een hoge snelheidsverhouding een hangend wervelpaar gevormd in de lijwaartse zijde van de jet, wat geleidelijk evolueert in een quasi-stroomsgeviert tegengesteld-roterend wervelpaar, ook bekend als een Counter-rotating Vortex Pair (CVP), tijdens het afbuigen van de jet. Dit tegengesteld-roterende wervelpaar veroorzaakt een zwakke neerstroming naast zijn twee benen. Dit zorgt dat de hoge-momentum stroom in de hoofdstroom wordt vervoerd naar de lage-momentum stroom nabij de muur, wat leidt tot een voller grenslaag profiel, wat beter bestandig is tegen het loslaten van de grenslaag. In het geval van een lage snelheidsverhouding tussen de jet en de hoofdstroom worden geen tegengesteld-roterende wervelingen gemaakt, al worden er vergelijkbare neerstrom effecten opgelegd door de twee longitudinale randen van de voorste werveling.

In het laatste deel van dit proefschrift worden plasma synthetische jets getest op twee types stromingen. Zo wordt er gekeken of een reeks PSJAs het loslaten van de stroom vanaf de voorzijde van een vleugel ($Re_c = 1.7 \times 10^5$) kan beïnvloeden maar ook hoe plasma synthetische jets de interactie tussen schokgolven en grenslagen kunnen beïnvloeden bij een Mach getal van 2. In het eerste geval, waarbij gekeken wordt of een PSJAs de loslating van de stroom tegen kan gaan, werd de kritieke invalshoek vertraagd met 8α , terwijl de maximale stijgkracht met 21% werd vergroot. Ook heeft dit experiment licht geworpen op de verscheidene mechanismen waarbij het loslaten van de stroom wordt tegen gegaan. Bij licht kritieke invalshoeken, kan plasma aandrijving, door middel van het bekrachtigen van de grenslaag door de verbeterde vermenging, het punt van loslating stroomafwaarts naar de middenkoordepositie duwen. Bij sterke kritieke invalshoeken blijft het scheidingspunt nabij de voorzijde, al wordt de nul-snelheidslijn naar de zuigkant van de vleugel getrokken. De oorzaak hiervan zijn de convectieve spanwijdte-wervelingen geïnduceerd door plasma synthetische jets, wat leidt tot een afname van de tijdgemiddelde scheidingsoppervlakte. In het geval van de schokgolf/grenslaag interactie, ook bekend als Shock Wave/Boundary Layer Interaction (SWBLI), experiment is gevonden dat een optimale ontladingsfrequentie van $F^* = 0.02$ kan leiden tot het effectief onderdrukken van het loslaten van de stroom. In vergelijking met de niet aangedreven conditie trekt de sonische lijn van het tijdgemiddelde snelheidsveld in het optimale geval stroomafwaarts terug met een lengte van ongeveer $0.5\delta_{99}$. Tegelijkertijd wordt het scheidingsoppervlak, afgeleid van de stroomomkeerwaarschijnlijkheid, verminderd met 14%.

NOMENCLATURE

LATIN LETTERS

A_b	Backflow area
A_e	Jet exit orifice area
A_r	Area of the recirculation region
A_s	Separation area
c	Airfoil chord length
c_f	Skin friction coefficient
c_p	Constant-pressure specific heat capacity
c_v	Constant-volume specific heat capacity
C_1	Capacitance of the energy-storing capacitor
C_d	Drag coefficient
C_l	Lift coefficient
C_μ	Blowing momentum coefficient
D	Exit orifice diameter
D_c	Jet duty cycle
D_v	Vortex ring diameter
E_c	Capacitor energy
E_{cm}	Cumulative jet mechanical energy
E_d	Discharge energy
E_{diss}	Heat dissipation caused by convection and radiation
E_{ex}	Heat exchange caused by the mass exchange
E_g	Internal energy of ideal gas
E_h	Localized gas heating energy
$E_{h,uniform}$	Equivalent uniform heating energy
E_m	Jet mechanical energy
E_{total}	Total electrical energy provided by the power supply
f^*	Dimensionless discharge/actuation frequency
f_d	Discharge frequency
f_h	Helmholtz natural resonance frequency
F_p	Time-averaged thrust
$\overline{G_e}$	Normalized grayscale of the exit jet in Schlieren images

h_c	Convective heat transfer coefficient
H	Boundary layer shape factor
i, j	Subscripts denoting the spatial coordinates (x, y, z)
i_d	Instantaneous discharge current
I_{cp}	Cumulative impulse
I_p	Jet impulse
I_p^*	Dimensionless jet impulse
k_{abs}	Absorptivity of the ceramic shell
k_{emi}	Emissivity of the cavity gas
k_{xy}	Turbulent kinetic energy in the xy-plane
k_τ	Normalized wall shear stress
L_e	Ejection length
L_I	Interaction length
L_p	Jet penetration length
L_s	Stroke length
L_s^*	Nondimensional stroke length/ stroke ratio
L_{sep}	Nondimensional separation length
L_{th}	Actuator throat length
M	Magnification ratio
M_{ce}	Cumulative mass flow
M_e	Mass of the expelled gas
M_e^*	Nondimensional expelled gas mass
Ma_e	Jet exit Mach number
Ma_p	Peak jet Mach number
Ma_∞	Freestream Mach number
n	Refractive index
N	Sample size
N_c	Cycle number
p_s	Flow reversal probability
P_0	Ambient pressure
P_d	Discharge power
Q_{ent}	Mass flow entrained by the jets
r	Radial coordinate; also jet velocity ratio
R	Gas constant
R_w	Electrical resistance of the hotwire
Re	Reynolds number
s_a	Spanwise actuator spacing
S_c	Cross-section area of the jet

S_{in}	Internal surface area of the cavity
S_k	Stokes number
S_r	Jet spreading rate
St	Strouhal number
t	Physical time/ jet phase
t^*	Dimensionless time units
T_0	Ambient temperature
T_{ca}	Spatially-averaged cavity temperature
T_{dis}	Duration of the arc discharge
T_d	Cycle period
T_h	Helmholtz natural oscillation period
T_{jet}	Duration of the primary jet stage
u	Instantaneous velocity
\tilde{u}	Periodical fluctuation velocity
u'	Random fluctuation velocity
u_d	Instantaneous discharge voltage
u_t	Instantaneous trigger voltage
u_τ	Friction velocity
$\overline{u_i u_j}$	Reynolds stress
\overline{U}	Time-averaged velocity
\overline{U}_c	Time-averaged jet centreline velocity
U_e	Spatially-averaged jet exit velocity
U_p	Peak jet exit velocity
U_s	Suction velocity
U_v	Propagation velocity of the front vortex ring
U_∞	Freestream velocity
V_1	Initial voltage of the energy-storing capacitor
V_{ca}	Cavity volume
V_p	Jet penetration rate
w_h	Full width at half maximum
W	Cycle work
x	Streamwise/axial coordinate
y	Wall-normal coordinate
z	Spanwise coordinate

GREEK LETTERS

α	Angle of attack
α_{ent}	Jet entrainment coefficient
γ	Gas specific heat ratio
Γ	Vortex ring circulation
δ^*	Boundary layer displacement thickness
δ_{99}	Boundary layer thickness
δ_U	Velocity measurement uncertainty
δ_ν	Viscous length scale
$\Delta\alpha$	Light deflection angle
ϵ	Non-dimensional energy deposition
ϵ_T	Temperature ratio
η_c	Real thermodynamic cycle efficiency
$\eta_{c,ideal}$	Ideal thermodynamic cycle efficiency
η_d	Discharge efficiency
η_h	Gas heating efficiency
$\eta_{h,uniform}$	Equivalent uniform heating efficiency
η_m	Electro-mechanical efficiency
η_p	Power saving ratio
η_t	Total efficiency
$\eta_{transfer}$	Transfer efficiency
θ	Boundary layer momentum thickness
κ	Von Karman constant
ν	Kinematic viscosity
ρ_0	Ambient density
ρ_{ca}	Spatially-averaged cavity gas density
ρ_e	Spatially-averaged jet exit density
σ	Stefan-Boltzmann constant
σ_U	Standard deviation of velocity
τ_f	Flow characteristic time
τ_p	Particle response time
τ_w	Wall shear stress
ϕ	Cross-correlation coefficient
ω	Vorticity

ABBREVIATIONS

AFC	Active Flow Control
CCD	Charge-Coupled Device
CVP	Counter-rotating Vortex Pair
DC	Direct Current
DNS	Direct Numeric Simulation
EMI	Electro-Magnetic Interference
FOV	Field Of View
FVR	Front Vortex Ring
FWHM	Full Width at Half Maximum
HFSB	Helium-Filled Soap Bubbles
HV	Hairpin Vortices
JICF	Jets In Cross Flow
K-H	Kelvin-Helmholtz
LES	Large Eddy Simulation
NACA	National Advisory Committee for Aeronautics
PIV	Particle Imaging Velocimetry
PSJ	Plasma Synthetic Jet
PSJA	Plasma Synthetic Jet Actuators
PSJICF	Plasma Synthetic Jets In Cross Flow
PTU	Programmable Timing Unit
RMS	Root Mean Square
SDBDA	Surface Dielectric Barrier Discharge Actuator
SJA	Synthetic Jet Actuator
SVR	Stretched Vortex Rings
SWBLI	Shock Wave/ Boundary Layer Interaction
TBL	Turbulent Boundary Layer
TDVR	Distorted Vortex Rings
TKE	Turbulent Kinetic Energy
ZNMF	Zero-Net Mass-Flux

CONTENTS

Summary	v
Samenvatting	vii
Nomenclature	ix
I Prologue	1
1 Introduction	3
1.1 Background	3
1.1.1 Active flow control	3
1.1.2 Steady jets, synthetic jets & plasma synthetic jets	4
1.2 Basics of plasma synthetic jet actuator	5
1.2.1 Actuator structure	5
1.2.2 Electrical circuitry	6
1.2.3 Working principles.	8
1.3 Characterization of PSJAs	9
1.3.1 Effect of electrical parameters	9
1.3.2 Effect of geometrical and atmospheric parameters.	11
1.3.3 Energy efficiency.	12
1.4 Flow control applications of PSJAs	14
1.5 Motivation and objectives of this research	17
1.6 Thesis layout	18
2 Equipment and Methodologies	19
2.1 Generation of plasma synthetic jets.	19
2.1.1 Actuator design	19
2.1.2 Electrical circuitry development	20
2.2 Wind tunnel facilities	22
2.3 Flow measurement techniques	22
2.3.1 Schlieren imaging	22
2.3.2 Hot-wire anemometer	23
2.3.3 Particle imaging velocimetry.	24
2.4 Data analysis methods	26
2.4.1 Jet intensity metrics extraction.	26
2.4.2 PIV measurement uncertainty quantification	29
2.4.3 Triple decomposition	31

II	Plasma Synthetic Jets in Quiescent Air	33
3	Formation, Evolution and Scalings	35
3.1	Introduction	35
3.2	Formation and evolution metrics of PSJs	36
3.2.1	Non-dimensional energy deposition and frequency	37
3.2.2	Stroke length and Reynolds number	38
3.3	Experimental setup and measurement system	38
3.3.1	Actuator and power supply	38
3.3.2	The PIV system and measurement scheme.	39
3.4	Phase-averaged results	40
3.4.1	Phase-averaged velocity fields	41
3.4.2	High-speed jet	43
3.4.3	Localized suction	52
3.4.4	Front vortex ring	53
3.5	Time-averaged results.	57
3.5.1	Time-averaged velocity fields	57
3.5.2	Centreline velocity and jet width	58
3.5.3	Jet entrainment	60
3.6	Conclusions.	62
4	Effect of Discharge Frequency	65
4.1	Introduction	65
4.2	Experimental setup	66
4.2.1	Actuator and power supply	66
4.2.2	PIV measurement scheme	66
4.3	Phase-averaged results at steady-state	67
4.3.1	Jet penetration length and exit velocity	67
4.3.2	Mean cavity density and cavity temperature	71
4.3.3	Expelled gas mass, impulse, and issued mechanical energy	72
4.4	Time-averaged characteristics at steady state	74
4.5	Transient-stage analysis.	77
4.6	Energy equilibrium analysis in one cycle	79
4.7	Conclusions.	82
5	Effect of Orifice Shape	83
5.1	Introduction	83
5.2	Equipments and measurement systems.	83
5.2.1	Actuator, power supply and discharge waveform.	83
5.2.2	Flow diagnosis systems	85
5.3	Schlieren results	88
5.3.1	Flow field evolution	88
5.3.2	Vortex ring propagation velocity	89
5.4	PIV results.	90
5.4.1	Phase-averaged velocity field	90
5.4.2	Penetration length and exit velocity	96
5.4.3	Pseudo time-averaged velocity fields.	98

5.5	Conclusions.	100
III	Plasma Synthetic Jets in Crossflow	101
6	Evolution and Scalings	103
6.1	Introduction	103
6.2	Experimental setup	104
6.2.1	Actuator and power supply	104
6.2.2	Wind tunnel and test section.	104
6.2.3	Hotwire anemometer and particle image velocimetry	105
6.3	PIV Data validation	107
6.3.1	PIV statistical convergence validation	107
6.3.2	Comparison of PIV with hotwire measurements	107
6.4	Phase-averaged flow organization	109
6.4.1	XY-plane	109
6.4.2	YZ-plane	114
6.5	Turbulent kinetic energy	119
6.5.1	XY-plane	119
6.5.2	YZ-plane	122
6.6	Conclusion	123
7	Effect of Velocity Ratio	125
7.1	Introduction	125
7.2	Experimental setup	126
7.2.1	Wind tunnel, actuator, and power supply	126
7.2.2	Measurement techniques and test scheme.	127
7.3	Baseline results	130
7.3.1	Symbol convention	130
7.3.2	Unactuated turbulent boundary layer	130
7.3.3	Plasma synthetic jets in quiescent flow.	131
7.4	Plasma synthetic jets in crossflow at $r = 1.6$	134
7.4.1	Symmetry plane	134
7.4.2	Spanwise planes	140
7.5	Effect of velocity ratio	145
7.5.1	Vortex ring evolution.	145
7.5.2	Pseudo-3D vortex structure, boundary layer shape factor and wall shear stress	147
7.6	Conceptual model	149
7.7	Conclusions.	152
IV	Flow Control Applications	153
8	Airfoil leading edge separation control	155
8.1	Introduction	155
8.2	Experimental setup	156
8.2.1	Wind tunnel, airfoil model and actuators	156
8.2.2	Discharge scheme and power supply system.	157

8.2.3	Baseline actuator characteristics	159
8.2.4	Measurement scheme	160
8.3	Balance measurement results	161
8.4	PIV results and analysis	163
8.4.1	Time-averaged velocity fields for baseline case	163
8.4.2	Leading edge separation control at $\alpha = 15.5^\circ$	164
8.4.3	Leading edge separation control at $\alpha = 22^\circ$	170
8.5	Concluding remarks	175
9	SWBLI Control at Mach Number 2: Preliminary Results	177
9.1	Introduction	177
9.2	Experimental setup	178
9.2.1	Test section, actuator and discharge circuitry	178
9.2.2	Schlieren and PIV system	180
9.3	Phase-averaged schlieren results	180
9.4	PIV results and discussions	182
9.5	Conclusions.	186
V	Epilogue	187
10	Conclusions and Outlook	189
10.1	Plasma synthetic jets in quiescent flow	189
10.2	Plasma synthetic jets in cross flow	190
10.3	Flow control.	191
10.4	Outlook	192
	References	194
	Scientific Contributions	209
	Acknowledgements	211
	Biography	213

I

PROLOGUE

1

INTRODUCTION

*Good tools are prerequisite to
the successful execution of any jobs!*

Analects of Confucius

1.1. BACKGROUND

1.1.1. ACTIVE FLOW CONTROL

IN 1904, Prandtl [1] made an epoch-breaking presentation in the Third International Congress of Mathematicians held in Heidelberg, Germany, titled ‘On Fluid Motion with Very Small Friction’. This short eight-page presentation dramatically changed the understanding of real fluid motion from two aspects, one for the proposal of boundary layer theory and the other for the pioneering attempt to delay the flow separation on a cylinder with boundary layer suction. Notwithstanding that the charming potential of flow control (drag reduction) was demonstrated a century ago, aircraft designers before the Second World War were simply sticking to the predestined lift and drag characteristics of airfoils without any intentions to tamper [2]. Due to the oil crisis in the 1970s and the unprecedented global warming since the 1950s, our society finally felt the urgency for conserving fossil fuels and reducing greenhouse gas emissions. Of all the economy sectors, transportation sectors including both road and aviation are responsible for 14% of the greenhouse gas emission and 57% of the fossil fuel consumption globally. Therefore, it was timely to shift the motto of aviation from ‘faster, higher and further’ to ‘cheaper, lighter and quieter’.

Under these circumstances, fundings were generously allocated to investigate the active flow control (AFC) technology in the last decade, which consequently gives the author a chance to earn a PhD degree out of this thesis. Technically, AFC relies on actuators

Part of this chapter is submitted for review as **Zong et al.**, *Plasma synthetic jet actuators for active flow control*, Actuators, (2018)

to generate controllable disturbances to favorably correct the overall flow behavior, including transition delay/advancement, separation elimination/promotion, drag reduction, lift augmentation, and jet noise mitigation [3]. These disturbances can be either brute forces that are capable of modifying the mean-flow structure, or small-amplitude forcing that leverages hydrodynamic instabilities of the target flow [4]. Depending on the working principles, the actuators employed to seed the disturbances are classified into three categories, fluidic actuators (i.e. jets, suction, synthetic jets), moving object/surface (i.e. vibrating flap, oscillating wire, morphing surface) and plasma-based actuators (i.e. corona discharge, dielectric barrier discharge, local arc filament). In the following section, several of the most popular fluidic actuators are discussed in detail.

1.1.2. STEADY JETS, SYNTHETIC JETS & PLASMA SYNTHETIC JETS

Each actuator has its limitations and merit, and thus should be selected wisely based on the application. For conventional fluidic actuators like steady/unsteady jets, the jet-to-mainflow momentum coefficient required for effective flow separation control typically ranges from $O(0.1\%)$ to $O(1\%)$, depending on the excitation strategy (brute-forcing modification or instability leverage) [5]. In 2015, a noteworthy flight test was conducted by Boeing and NASA, where 31 sweeping jet actuators were arranged in the vertical tail of an aircraft (ecoDemonstrator 757) to control the flow separation on a highly deflected rudder and a side force increase of 13% to 16% was reported [6, 7]. Notwithstanding the encouraging results, the air taken away from the Auxiliary Power Unit compressor was temporarily ignored and must be compensated for other purposes (e.g. cabin pressure, engine startup). Moreover, the equipments installed to condition the air (i.e. heat exchanger, pipe system et al.) bring additional weight and volume penalty for the whole aircraft. To minimize these penalties, synthetic jet actuators (SJAs), capable of imparting momentum/energy to fluid systems in a zero-net mass-flow (ZNMF) manner, were investigated to substitute steady/unsteady jets [8].

Morphologically, SJAs involve the use of an enclosed cavity and an exit orifice through which fluid is ejected and ingested alternately. Compression of the cavity relies either on mechanical volume modification (e.g. piezoelectric membrane, electromagnetic coil and piston) or on rapid thermalization (e.g. micro-combustion) [9]. Piezoelectric SJAs feature simple construction, high operation frequency ($O(1\text{ kHz})$) and relatively low peak jet velocity (typically less than 60 m/s) [10, 11]. By using a dual-disk configuration and operating at resonance frequency (700 Hz in their study), van Buren, Whalen & Amitay [12] demonstrated an improvement of the peak jet velocity to 210 m/s. Nevertheless, a fast deterioration of jet velocity is observed in off-resonance operation (less than 40 m/s after 1200 Hz), limiting the available frequency range. Piston-type SJAs can create compressible jets at supersonic exit velocity (approximately 600 m/s); however, the peak operation frequency is limited to 200 Hz as a result of the inherent mechanical design [11]. For combustion-type SJAs, notwithstanding the robustness and high jet velocity, the low working frequency on the order of $O(100\text{ Hz})$, limited by mixing and refilling of the reactants as well as the complex construction incorporating an internal ignitor and several pipes, poses significant challenges for implementation [13].

High-speed high-Reynolds-number flow control in flight conditions (e.g. separation control on wing flap, shock wave boundary layer interaction control in engine in-

let) demands actuators with sufficient bandwidth and control authority, while still being relatively robust and simple [4]. In 2003, Grossman, Cybyk & Vanwie [14] proposed to rapidly pressurize the actuator cavity with pulsed arc/spark discharges instead of micro-combustion, leading to a simple construction (one cavity plus two/three electrodes). Due to the inherent short time scale of gas discharge at atmospheric pressure ($O(10 \mu s)$) and easily tunable pulse energy, high-velocity ZNMF jets (300 m/s) can be produced reliably by this device at high frequency (>5 kHz) [15, 16], thus consisting the main interests of the current research.

Different terminologies including ‘sparkjet actuator’ [17–19], ‘pulsed-plasma jet actuator’ [15, 20], ‘plasma synthetic jet actuator’ [16, 21, 22] are used across the active flow control community to refer to the above-mentioned discharge-driven synthetic jet actuators. In this thesis, ‘plasma synthetic jet actuators’ (PSJAs) is preferred over the other terminologies for the following two reasons. Firstly, the gas discharge adopted in vast majority of the studies falls into the arc regime instead of the spark, as evidenced by the low sustain voltage ($O(100 V)$) and high discharge current ($O(10\text{--}100 A)$) [15, 18, 23–25]. Secondly, the terminology of ‘pulsed-plasma jet actuators’ does not indicate the ZNMF feature and can be easily confused with the plasma jets for medical and chemical purposes [26]. Additionally, distinctions should also be made between the thermodynamically driven plasma synthetic jets treated in this investigation and the wall-normal jets induced by the ring-type surface dielectric barrier discharge actuators (SDBDAs). The latter, also referred to as ‘plasma synthetic jets’ by some researchers [27, 28], are essentially steady impinging jets driven by the electrostatic force, without any alternations between the ejection and ingestion phases.

1.2. BASICS OF PLASMA SYNTHETIC JET ACTUATOR

This section involves the system required to generate plasma synthetic jets (PSJs). Geometrical constructions and working mechanisms of the actuators are introduced in Section 1.2.1. The diverse discharge circuitries employed to initiate gas discharge inside the actuator cavity are reviewed in Section 1.2.2.

1.2.1. ACTUATOR STRUCTURE

A gallery of plasma synthetic jet actuators is shown in Figure 1.1. Typically, the actuators consist of a ceramic shell and a cap (or nut), which can be assembled to form an enclosed cavity. The cavity is in cylindrical shape and its volume ranges from 20 mm^3 to 2000 mm^3 , depending on the discharge energy ($O(1\text{--}1000 \text{ mJ})$). The shell of the cavity is commonly made of ceramic (MACOR [31], Boron Nitride [22]) for insulation and heat-resistance purposes, while the cap/nut can be either ceramic or metallic pieces. On top of the cap/nut, one or several holes in a diameter of 0.5–4 mm are drilled and act as the jet exit orifice. From the bottom or side of the ceramic shell, several tungsten needles (one in [29], two in [15, 16, 25], three in [22, 30]) are inserted into the cavity, serving as anode, cathode and/or trigger electrode. The electrode gaps are on the order of 1 mm to allow gas breakdown at an applied voltage of $O(10 \text{ kV})$. The tip of the electrodes can be either sharpened to reduce the breakdown voltage, or rounded to opt for robustness (i.e. slow down erosion/oxidation).

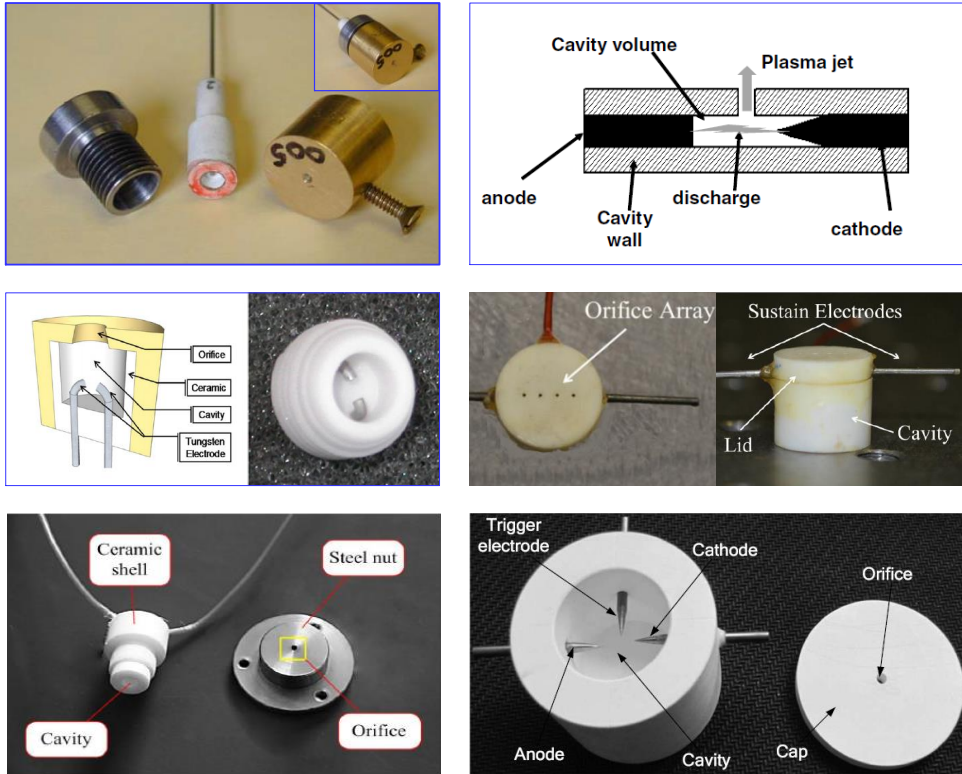


Figure 1.1: Gallery of plasma synthetic jet actuators. From left to right and top to bottom, these pictures are reproduced respectively from Cybyk et al. [29], Narayanaswamy et al. [15], Belinger et al. [25], Emerick et al. [30], Zong et al. [16], and Wang et al. [22].

1.2.2. ELECTRICAL CIRCUITRY

Depending on the electrode configuration (two or three electrodes) and the required discharge energy level, different discharge types including high-voltage nanosecond pulsed discharge [16, 35], capacitive discharge [29], inductive discharge [25] and pulsed DC discharge [36], can be employed to thermalize/pressurize the gas inside the actuator cavity. Two representative electrical circuitries to create capacitive and pulsed DC discharge are shown in Figure 1.2 (a) and (b). In the former case (capacitive discharge), a DC power supply (typical voltage: 300-3000 V) is used to charge an energy-storing capacitor C1, and the peak charging current is limited by a resistor R1 ($O(100-1000) \Omega$). As the DC power supply is only responsible for energy addition and its peak voltage is typically lower than the breakdown voltage of the electrode gap, an extra high-voltage pulsed power supply is required for trigger purposes. These high-voltage trigger pulses are applied on a trigger electrode located in between the anode and cathode, to ignite the gas gap with a weak spark. Once a complete discharge channel is initiated, the energy stored in the capacitor C1 is rapidly released into the electrode gap by arc heating. After the arc quenches, the capacitor is recharged by the DC power supply, awaiting the next trigger

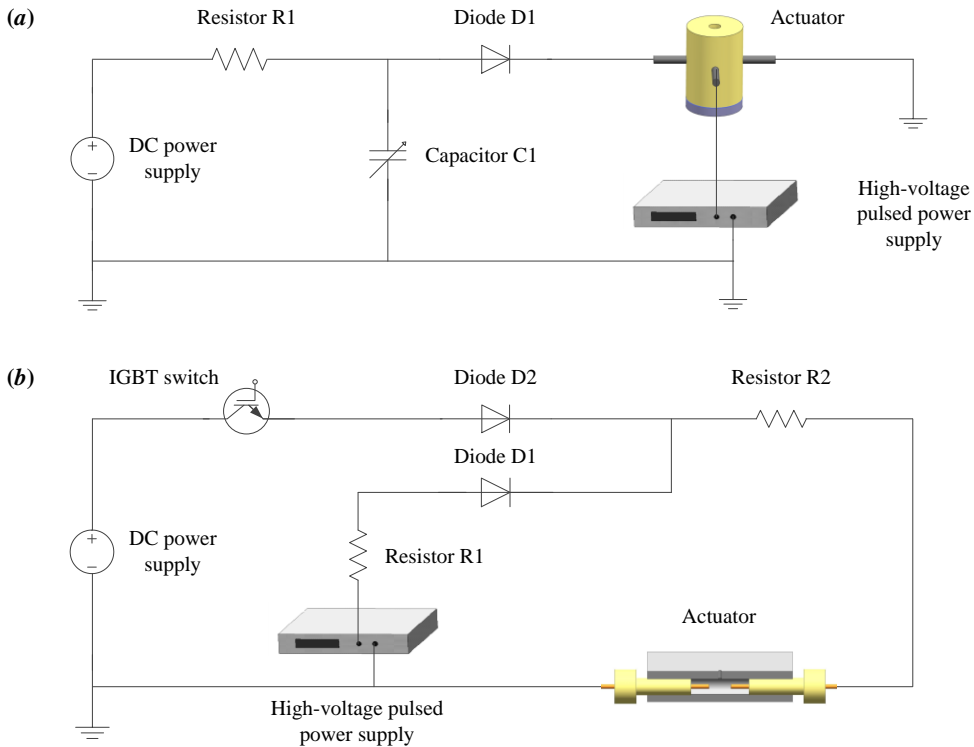


Figure 1.2: Representative electrical circuitries employed to produce pulsed arc. (a) Capacitive discharge for three-electrode PSJAs [32, 33]; (b) Pulsed DC discharge for two-electrode PSJAs [34].

pulse. A high-voltage diode D1 is added in between the low voltage charging circuit and the high-voltage power supply for isolation purposes (optional), leading to a single-peak current waveform. The discharge energy is determined by the initial voltage and the capacitance of C1, whilst the discharge frequency is tuned by the trigger frequency.

Multiple variants of the above discharge circuitry were proposed by Belinger et al. [25], Wang et al. [37] and Zong et al. [23]. In [25], the capacitor is charged by a high-voltage transformer, and the peak capacitor voltage is already sufficient to ignite the electrode gap. As thus, no additional high-voltage trigger power supply is required, leading to a simple structure. Nevertheless, the discharge energy is set by the breakdown voltage which can be easily affected by the electrode distance, electrode tip erosion, and cavity density/temperature. The inter-correlations between these factors pose significant challenges to interpret the trends obtained in parametric studies. In [37], the isolation diode D1 is removed to enable the periodic oscillation of discharge current in the circuit, leading to a high discharge efficiency. Zong et al. [23] replaced the high-voltage diode with a magnetic switch and integrated the trigger function to the anode, leading to a simplified sequential discharge circuitry for two-electrode actuators.

With regard to the pulsed DC discharge shown in Figure 1.2 (b), no energy-storing capacitor is needed, and the discharge current is modulated by a resistor R2. A high-

voltage switch is typically positioned between the actuator and power supply, tailoring the discharge waveform into repetitive pulses. In the case that DC voltage is insufficient for gas breakdown, an external high-voltage pulsed power supply can be introduced to assist the discharge ignition, similar as that in Figure 1.2 (a). Moreover, two high-voltage diodes are needed to isolate the low-voltage and the high-voltage circuits from each other for protection purposes (mandatory). For the case that DC voltage already exceeds the breakdown voltage of electrode gaps, the diodes as well as the high-voltage trigger circuit can be directly omitted [15, 38]. The discharge energy for pulsed DC discharge can be adjusted by either the switch-on time or the discharge current, whilst the discharge frequency is controlled by switch rate.

Compared to capacitive discharge and pulsed DC discharge, nanosecond discharge features a high gas heating efficiency ($> 60\%$) but low pulse energy ($O(1 \text{ mJ})$), limiting its capability to feed small cavity-volume actuators ($O(10 \text{ mm}^3)$). Inductive discharge is similar to pulsed DC discharge, in the sense that the discharge current in both cases is on the order of 1 A and the discharge duration can reach $O(0.1\text{--}1 \text{ ms})$, thus will not be detailed here [25, 34].

1.2.3. WORKING PRINCIPLES

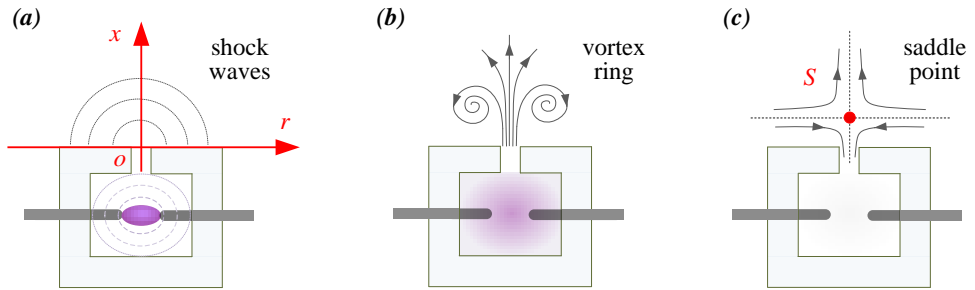


Figure 1.3: Working process in one cycle. (a) Energy deposition stage; (b) Jet stage; (c) Refresh stage. Reproduced from Zong & Kotsonis [39].

As shown in Figure 1.3, a complete working cycle of the actuator includes three stages, i.e. energy deposition stage, jet stage and refresh stage. During the energy deposition stage (Figure 1.3 a), a strong pulsed arc or spark is initiated between the electrodes by external circuitry, heating and pressurizing the cavity rapidly ($O(10 \mu\text{s})$). Since the arc heating is locally confined in the inter-electrode gap, the spatial distribution of temperature and pressure in the cavity is considerably nonuniform. As a result, several shock waves are produced, propagating outwards at supersonic speed [40]. During the jet stage (Figure 1.3 b), the high-temperature low-density gas is expelled through the exit throat at high velocity, driven by the pressure differential between the inner cavity and the ambient external flow. The jet shear layer separates at the orifice lip and rolls into a starting vortex ring. As cavity gases are ejected, the cavity pressure drops monotonically. Nevertheless, the jet stage will not terminate at the moment of zero differential pressure due to the inevitable inertia of the throat gas. A negative cavity pressure is developed at full

Table 1.1: Classification of literature based on the jet formation parameters investigated

Category	Parameters	Relevant literature
Electrical	Discharge energy, E_d	[18, 20, 22, 25, 32, 33, 41–45]
	Discharge frequency, f_d	[15, 16, 24, 30, 31, 45, 46]
	Discharge duration, T_{dis}	[25, 34]
Geometrical	Cavity volume, V_{ca}	[15, 34, 47–49]
	Exit diameter, D	[23, 47, 50]
	Throat length, L_{th}	[23]
	Electrode configuration	[23, 51, 52]
	Orifice shape	–
Atmospheric	Ambient pressure, P_0	[18, 24, 30, 53]
	Ambient temperature, T_0	–
	Humidity et al.	–

cessation of the throat flow, which provides the drive for refresh stage. During the refresh stage (Figure 1.3 *c*), ambient cold gas is ingested into the cavity, mixing with the residual high-temperature low-density gas therein. Considering the effects of the just emitted jet, a saddle flow pattern with the presence of both jet and suction flow can be observed [8].

1.3. CHARACTERIZATION OF PSJAS

Characterisation studies concern the influence of various parameters on the actuator performance in quiescent air. As the actuator is essentially an energy-conversion system which converts the electrical energy into jet mechanical energy, all the influencing parameters (termed as jet formation parameters) can be classified into three categories, i.e. electrical, geometrical and atmospheric. These three categories specify respectively the ‘input’, ‘structure’, and ‘working environment’ of an actuator system, thus constituting a complete representation of the parameter space. For each of the jet formation parameter, the relevant investigations are summarized in Table 1.1.

1.3.1. EFFECT OF ELECTRICAL PARAMETERS

Electrical parameters mainly include discharge energy (E_d), discharge frequency (f_d) and discharge duration (T_{dis}). Discharge energy is typically normalized by the internal energy of the cavity gas at initial state, resulting in a non-dimensional energy deposition [32, 54], $\epsilon = E_d / (c_v \rho_0 V_{ca} T_0)$, where c_v and T_0 denote the constant-pressure specific heat capacity and the ambient temperature, respectively.

The non-dimensional energy deposition (ϵ) plays a crucial role in tuning the intensity of pulsed jets. Specifically, the energy deposition process can be described as a constant-volume heating process. The peak pressure ratio reached inside the actuator cavity after arc heating is proportional to ϵ [17, 42], and further determines the time-varying exit velocity in the jet stage. As demonstrated by the experimental datasets gathered in Figure 1.4, the peak jet velocity (U_p) increases monotonically yet nonlinearly with the non-

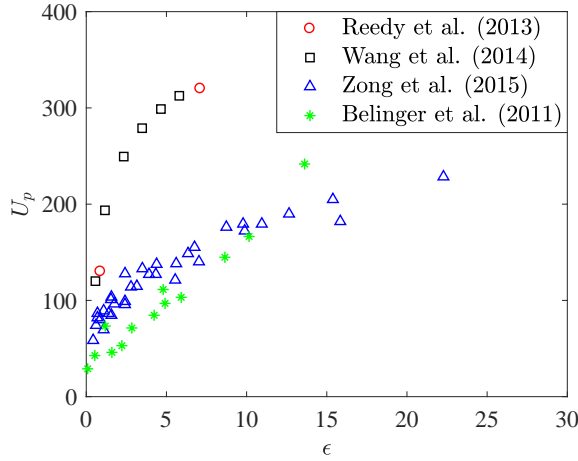


Figure 1.4: Variation of peak jet velocity (U_p) with non-dimensional energy deposition (ϵ).

dimensional energy deposition [16, 20, 22, 25]. This nonlinear relationship is crucial in extrapolating the peak jet velocity to unknown energy deposition level, yet remains unclear at present. In addition, with increasing energy deposition, the jet duration time (T_{jet}) initially increases and then saturates [25, 32]. The saturation at large energy deposition is ascribed to the limited gas mass inside the actuator cavity. Based on the above-mentioned trends of exit velocity and jet duration time, it is straightforward to derive that the expelled gas mass, jet impulse and jet mechanical energy also increase with the non-dimensional energy deposition, as has been demonstrated in [33, 34, 41, 54].

When the actuator is operated repetitively, a transient stage is exhibited in the initial tens of cycles, where the mean cavity temperature increases cycle by cycle due to heat accumulation and the exit velocity variation in one period is not repeatable [16, 46, 55]. The transient stage is followed by a steady stage featuring approximately unchanged mean cavity temperature/density and excellent repeatability of the exit velocity variation from cycle to cycle. The mean cavity temperature in the steady stage increases, whereas the mean cavity density as well as jet density decreases monotonically with increasing discharge frequency, as a result of the decrease of refresh time [16, 25, 55]. Discharge frequency (f_d) is typically normalized by the Helmholtz natural frequency of the actuator cavity (denoted as f_h) [46, 56], resulting in a non-dimensional working frequency ($f^* = f_d / f_h$). f_h is a function of both atmospheric parameters and actuator geometrical parameters. With increasing orifice diameter, f_h increases monotonically.

The significance of Helmholtz natural oscillation frequency can be interpreted by comparing the actuator to a spring-mass-damper system. Assuming the actuator cavity is initially at rest and a small pressure disturbance is abruptly imposed to the actuator cavity (e.g. rapid compression by piston). This disturbance leads to an uneven pressure across the actuator throat, which drives the fluid to escape from the actuator cavity (analogous to 'spring'). While the cavity gas is being ejected, the cavity pressure drops and the jet velocity decreases. Nevertheless, the ejection phase will not terminate at the

moment of zero cavity pressure due to the inertia of throat gas (analogous to ‘mass’). A negative cavity pressure is required to stop the ejection, which provides the driving force for the subsequent ingestion phase. The alternation between the ejection and ingestion phases will not cease until all the disturbance energy is damped out by viscous forces (analogous to ‘damper’).

Theoretically, at least one alternation between the ejection and ingestion phases is needed to reset the actuator, thus the Helmholtz natural frequency can be interpreted as the theoretical limit working frequency of PSJAs, beyond which the intensity of pulsed jets deteriorates considerably. Evidences of this conclusion can be found in [15, 16]. For the actuator used by Narayanaswamy et al. in [15], the Helmholtz natural frequency is estimated to be 10.7 kHz ($L_{th} \approx 2$ mm, exact value not provided). When this actuator is operated at a frequency (10 kHz) close to the Helmholtz natural frequency, considerable misfires were observed in one sequence as a result of the insufficient refresh time that breaks cycle-to-cycle repeatability [15]. In [16], the intensity of PSJs at increasing frequency was diagnosed by a total-pressure probe, and a ‘saturation frequency’ was observed, above which the time-averaged jet total pressure (equivalent to thrust) no longer increases with the discharge frequency. The ‘saturation’ frequencies of the two tested actuators (4 kHz for $D=1$ mm, 6 kHz for $D=1.5$ mm) agree well with the Helmholtz natural frequency computed theoretically (3.6 kHz and 5.4 kHz, see Equation 3.2 for the mathematical expression). Additionally, Zong et al. [16] concluded a linear relationship between the ‘saturation frequency’ and the exit orifice diameter, which is also consistent with the theoretical variation trend of the Helmholtz natural frequency.

As a comparison to the ubiquitous trend of decreasing jet density at increasing repetition rate, the variation of peak jet exit velocity with discharge frequency remains disputable. In [31], a pulsed DC power supply was adopted to feed the actuator, and the peak jet velocity determined from high-speed Schlieren imaging (89 m/s–97 m/s) changes marginally with the actuation frequency in the range of 100 Hz–1000 Hz. Sary et al. [55] performed a numerical simulation based on the actuator used by Belinger et al. in [25]. As a result, the peak exit velocity changes marginally at $f_d < 1$ kHz and drops significantly afterwards. These observations are roughly consistent, however contradicting the results predicated by the analytical model in [16] where the peak jet velocity increases monotonically with the discharge frequency.

The effect of discharge duration on intensity of pulsed jets are experimentally examined in [25, 34]. Compared to the case of capacitive discharge where the energy is deposited in less than 10 μ s, PSJs generated by inductive discharge (discharge duration: $O(100 \mu$ s)) exhibit a lower peak jet velocity but a longer jet duration time [25]. For pulsed DC discharge with fixed energy deposition, both the heating efficiency and the thermodynamic cycle efficiency decrease with increasing discharge duration [34].

1.3.2. EFFECT OF GEOMETRICAL AND ATMOSPHERIC PARAMETERS

Geometrical parameters mainly include cavity volume, exit diameter, throat length and electrode configuration. Effects of the first three parameters have actually been covered by the two dimensionless parameters defined earlier on (i.e. ϵ and f^*). When the cavity volume increases, the peak jet velocity drops as a result of the decreasing non-dimensional energy deposition, nevertheless the jet duration time increases due to an

increasing Helmholtz natural oscillation period [47, 48]. The overall efficiency of PSJAs decreases with increasing cavity volume, not only because the temperature ratio that can be reached after energy deposition is lowered, but also because the arc heating inside the actuator cavity becomes more localized which decreases the heating efficiency [34].

With increasing orifice diameter, the jet duration time decreases as a direct consequence of higher mass flow rate, whereas the peak jet velocity and the jet impulse remain approximately unchanged [23, 47]. Additionally, the theoretical limit working frequency of PSJAs increases linearly with orifice diameter, as a result of increasing Helmholtz natural frequency [16]. Variation of the throat length doesn't affect the peak jet velocity and the jet duration time of PSJAs in single-shot mode. Nevertheless, a longer throat length leads to a lower Helmholtz frequency and a fast deterioration of the jet intensity at high-frequency operation [23]. With increasing electrode distance and unchanged energy deposition, the arc heating region is enlarged and the overall efficiency of PSJAs is improved, leading to a higher peak jet velocity as well as a longer jet duration [23]. The ratio of the arc heating volume to the cavity volume is defined as the dimensionless heating volume, which quantifies the uniformity of arc heating. The electro-mechanical efficiency of PSJAs is demonstrated to increase significantly with the dimensionless heating volume [57]. This conclusion can somehow be validated from the results in [15] *a posteriori*. In their study, the dimensionless heating volume was kept unchanged. Two cases with different cavity volume (20 mm^3 and 40 mm^3) were tested with Schlieren imaging, and similar jet trajectories were obtained consequently.

Atmospheric parameters (e.g. pressure, temperature and humidity) define the environment in which the actuators are operating. Driven by the need of implementing flow control technology to flight vehicles cruising at high-altitudes, effects of the ambient pressure on the performance of PSJAs were investigated extensively. Under the condition that the discharge energy is fixed [30, 42, 53], the dimensionless energy deposition increases with decreasing ambient pressure/density. As such, an increasing trend of the peak jet velocity as well as the peak nozzle pressure ratio (equivalent to peak jet Mach number) is expected while the ambient pressure drops. In contrast, the discharge energy in [24] depends on the breakdown voltage of the inter-electrode gap and decreases monotonically with the decreasing ambient pressure. Consequently, the peak jet velocity changes marginally with the ambient pressure.

1.3.3. ENERGY EFFICIENCY

This section is dedicated to the energy efficiency of plasma synthetic jet actuators. Depending on the jet formation parameters, the overall efficiency of PSJAs, defined as the ratio of jet mechanical energy (output) to electrical energy (input), can vary from $O(0.01\%)$ to $O(1\%)$ [34, 37, 58]. Note that this efficiency does not represent the overall effectiveness of the active flow control system, which is typically quantified by the power saving ratio and can be much higher than 100% [59]. When the non-dimensional energy deposition ratio keeps constant, the peak jet velocity increase monotonically with the overall actuator efficiency [16, 42]. As such, for flow control purposes, the actuator geometry as well as the discharge circuitry shall be optimized to boost the intensity of pulsed jets.

The energy flow in the PSJA system is illustrated by Figure 1.5 (reproduced from [34]). As shown, the conversion from electrical energy to mechanical energy is not straightfor-

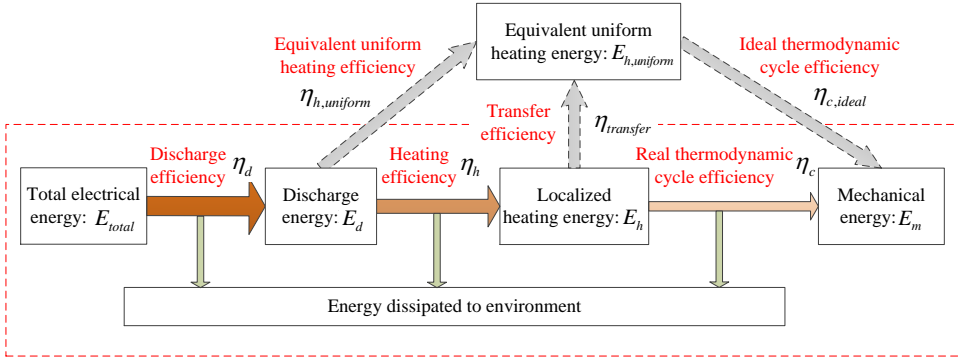


Figure 1.5: Energy flow in the plasma synthetic jet actuator system (reproduced from [34]). Note that the processes outside the red dash box as well as the pertinent efficiencies ($\eta_{h,uniform}$, $\eta_{transfer}$ and $\eta_{c,ideal}$) are not physical.

ward, consisting of three sequential sub-processes including gas discharge, arc heating and thermodynamic cycle process [15, 34, 43, 60]. Each of the sub-processes exhibits inevitable energy losses, corresponding to a sub-efficiency. The overall efficiency of the actuator system ($\eta_t = E_m/E_{total}$) is essentially the product of these three sub-efficiencies.

In the case of capacitive discharge, the total electrical energy refers to the capacitor energy prior to discharge ignition, i.e. $E_{total} = C_1 V_1^2/2$, where C_1 and V_1 denote the capacitance and the initial voltage of the energy-storing capacitor, respectively [24]. During the gas discharge, part of the electrical energy is converted into the arc discharge energy (E_d), while the rest are consumed by the parasitic resistance of connecting wires and capacitors [24, 43]. The discharge efficiency defined by $\eta_d = E_d/E_{total}$ is related to the ratio of the time-averaged arc resistance to the total parasitic resistance. As the arc resistance ($O(1 \Omega)$) is mainly determined by the arc length and the arc temperature (plasma conductivity), the discharge efficiency decreases with increasing discharge energy, whereas increases monotonically with the electrode distance [19, 43]. Typical values of η_d for capacitive discharge range from 33% to 90% [24, 33, 53]. In the case of pulsed DC discharge, a current-limiting resistor ($O(100-1000 \Omega)$) is usually placed in between the actuator and the DC power supply [38], leading to a much lower discharge efficiency (approximately 20 % in [15]; 10%–60% in [34]), compared to a well-designed capacitive discharge circuitry.

During the arc heating process, the ionized species drift energy from the local electrical fields and collide with neutral species. Several gas heating mechanisms are presented in this process, including ion joule heating, elastic collisions between electrons and heavy species, and vibration-to-translation relaxation of the excited heavy particles [15]. In [60], arc plasma at atmospheric condition is simulated with a magnetohydrodynamical model under the local-equilibrium assumption. Sheath loss is demonstrated to reach as high as half of the discharge energy, whereas radiation loss is typically less than 5 % of the discharge energy, resulting in a gas heating efficiency (η_d) of approximately 50% for capacitive discharge. Narayanaswamy et al. [15] analysed the non-equilibrium effects in low-pressure arc plasma (35 torr) and concluded that 90% of the electrical en-

ergy is locked into the vibrationally-excited heavy species (N_2 and O_2) due to the high reduced electric field ($E/N = 16$ Td), leading to a gas heating efficiency of only 10% for pulsed DC discharge. In contrast with capacitive discharge and pulsed DC discharge, the gas heating efficiency pertaining to nanosecond-pulsed discharge is much higher (60%–77%) and increases monotonically with the slope of the voltage rising-edge [35].

In the last stage of the energy flow chart, the gas heating energy (E_h) is converted into the mechanical energy of the pulsed jets (E_m) through a thermodynamic cycle process, resulting in a cycle efficiency (η_c). As the gas inside the actuator cavity is left in a non-equilibrium state after the non-uniform arc heating, direct computation of the cycle efficiency using the pressure-volume diagram is infeasible. To solve this issue, a non-physical process is introduced which converts the non-equilibrium state left by the localized arc heating to a equivalent equilibrium state thermalized after uniform gas heating energy ($E_{h,\text{uniform}}$), under the condition that both states will produce the same amount of mechanical energy [34]. The energy conversion factor (i.e. transfer efficiency, η_{transfer}) should be less than 1 to account for the losses corresponding to shock wave propagation and reflection. The ratio of jet mechanical energy to the equivalent uniform heating energy defines the ideal thermodynamic cycle efficiency, $\eta_{c,\text{ideal}} = E_m/E_{h,\text{uniform}}$. With the energy deposition stage and the jet stage modelled as a constant-volume heating process and an isentropic expansion process respectively, $\eta_{c,\text{ideal}}$ is derived to be a simple relation of the temperature ratio during constant-volume heating process (ϵ_T), as shown in Equation 1.1 [34], where γ denotes the gas specific heat ratio. Consequently, $\eta_{c,\text{ideal}}$ increases monotonically with the temperature ratio in energy deposition stage. For a typical range of $\epsilon_T < 5$ in the literature (i.e. peak jet temperature less than 1400 K, [15, 16, 25, 61]), $\eta_{c,\text{ideal}}$ is less than 20%.

$$\eta_{c,\text{ideal}} = 1 - \gamma \frac{\epsilon_T^{1/\gamma} - 1}{\epsilon_T - 1} \quad (1.1)$$

As opposed to the physical heating efficiency, the equivalent heating efficiency is much easier to access in experiments. Typically, one of the jet intensity metrics (e.g. jet impulse [33, 34], peak cavity pressure [18, 49]) is measured, and the heating energy required by the actuator to yield the same jet intensity metric under assumptions of constant-volume heating and thermodynamic equilibrium is estimated by an analytical model. This estimated heating energy is essentially the equivalent uniform heating energy, and the ratio of $E_{h,\text{uniform}}$ to E_d defines the equivalent uniform heating efficiency ($\eta_{h,\text{uniform}}$). As a result, $\eta_{h,\text{uniform}}$ ranges from 10% to 35% and decreases with increasing energy deposition and cavity volume [34]. The overall efficiency of PSJAs driven by pulsed DC discharge is $O(0.1\%)$ [34], which is not striking after multiplying the three sub-efficiencies together (η_d : 10%–60%; η_h : 4%–40%; η_c : <20%).

1.4. FLOW CONTROL APPLICATIONS OF PSJAS

Owing to the unique feature of producing high-velocity (>300 m/s) pulsed jets at high frequency (>5 kHz), applications of PSJAs can be found widely from moderate- to high-Reynolds-number flows including flow separation control in airfoils/ramps [62], jet noise control [21], and shock wave/boundary layer interaction control [63], as shown in Figure

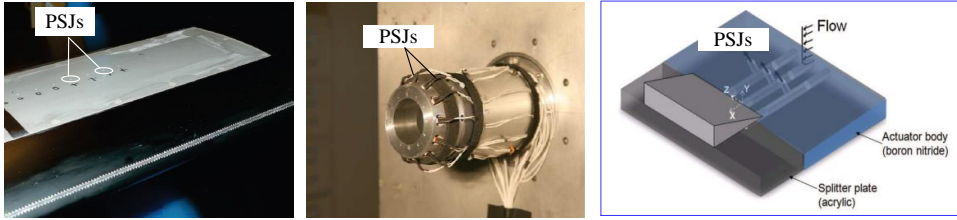


Figure 1.6: Applications of plasma synthetic jet actuators (left to right): airfoil flow separation control [62], jet noise control [64] and shock wave/boundary layer interaction control [65].

Table 1.2: Institutions involved in the application studies of plasma synthetic jet actuators. ONERA–The French Aerospace Lab; UNINA–The University of Naples Federico II; UT Austin–The University of Texas at Austin; AFEU–Air Force Engineering University; NUDT–National University of Defense Technology.

Category	Institutions	Representative literatures
Separation control at moderate-Reynolds number	ONERA; UNINA; Xiamen University	[62, 66, 67]
Jet noise control	ONERA	[21, 64, 68]
Shock wave/boundary layer interaction control	UT Austin; AFEU; NUDT	[63, 65, 69–75]

1.6. For each of these applications, the research groups involved as well as the representative publications are classified in Table 1.2.

In separation control cases, PSJs are typically issued upstream of the separation region, either in the wall-normal direction to create a quasi-streamwise counter-rotating vortex pair [76] or pitched and skewed with respect to the main flow to produce a single dominant streamwise vortex [21]. These vortices transport the high-momentum flow from the outer boundary layer to the near-wall region, resulting in a fuller boundary layer velocity profile and a reduction in boundary layer shape factor. In Caruana et al. [62], 5 actuators with 30° pitching angle and 60° skew angle are embedded in the plateau upstream of a decelerating ramp to eliminate the separated flow. At a freestream velocity of 37 m/s (ramp-height based Reynolds number: 6.2×10^4), the area of the separation region decreases significantly with the increasing actuation frequency at $f_d < 500$ Hz whereas remains unchanged afterwards. Additionally, Caruana et al. [62] used an array of 20 actuators to control the trailing-edge separation over an NACA-0015 airfoil model. The actuators are placed 32% chord length (denoted as c) away from the leading edge, and the same pitch and skew angle as that in the ramp experiment are used. With a freestream velocity of 40 m/s (chord-based Reynolds number: $Re_c = 1.2 \times 10^6$) and an angle of attack of 11.5° , the separation region initially occupying half of the chord shrinks when the actuation frequency increases, and a fully attached flow is obtained at $f_d > 250$ Hz. In [66], three PSJAs are employed to control the flow separation over an NACA 0021 wing model at $U_\infty = 20$ m/s and $Re_c = 3.4 \times 10^5$. Different actuation locations ($0.15c$ and

0.45c) and jet pitching angles (45° and 60°) are examined. As a result, PSJs issued at 15% chord length is able to postpone the stall angle by 2 degrees and increase the peak lift coefficient by 9%. The two jet pitching angles show similar control effects.

For the purposes of jet noise control, the actuators are generally embedded in the nozzle lip to seed disturbances in the jet shear layer. As a result of Kelvin-Helmholtz instability, these disturbances are expected to grow into large-scale structures and change the overall sound level emitted by jets [21]. In [64], 12 actuators are distributed evenly around the lip of a 50 mm diameter nozzle, and an exit Mach number of 0.6 is tested (exit-diameter based Reynolds number: 7×10^5). For an actuation Strouhal number close to 0.3, the jet noise is increased by 3-4 dB. A slight noise decrease of -0.3 dB is demonstrated when the neighbouring actuators are operated 180° out of phase. Chedevergne et al. [68] performed numerical simulation on the same jet flow tested by [64]. Only one actuator is modelled and a hybrid RANS-LES approach is adopted to save the computation resources. Based on their results, the pressure waves created by the arc discharge are responsible for the development of the large-scale structures observed in the jet mixing layer, whereas the pulsed jets play a secondary role.

Recent studies of PSJAs in supersonic flow show consistent interest in shock wave boundary layer interaction (SWBLI) control. The objectives of SWBLI control include two aspects: one to reduce the massive flow separation induced by the steep pressure rise, the other to shift/mitigate the low-frequency unsteadiness related to the separated flow [77]. The researchers from UT Austin are pioneers in SWBLI control with PSJAs. In [63, 65], an array of plasma jets pitched at 45° and skewed at 90° were positioned approximately 4 times of the boundary layer thickness (δ_{99}) upstream of the separation shock, to control the SWBLI induced by a ramp model in a Mach 3 crossflow. Results show that the separation shock executes a small initial downstream displacement of $\delta_{99}/4$ for a time period of 5–10 μs , followed by a large upstream displacement of about $1\delta_{99}$. When PSJs are pulsed at an interaction-length based Strouhal number of $St_L = 0.04$, the overall magnitude of the pressure fluctuations associated with the unsteady large-scale motion of the separated flow is decreased by 30%. As a follow-up and complement of the above-mentioned works, Greene et al. [70] performed a parametric study on the major factors that influence the mean separation length induced by a 20° ramp. Surface oil streak visualizations showed that PSJA is able to reduce the distance between the separation line and the compression corner by 40%. The optimum jet placement proves to be $1.5\delta_{99}$ upstream of the compression corner, beyond which the effect of the jets diminishes. The optimum jet configuration is a combination of low pitch angle and zero skew angle.

In [73], a row of five PSJAs arranged in the spanwise direction was used to control the SWBLI induced by a 30° ramp in a Mach 2 flow. The size of the separation zone was reduced during the interaction with the jet plume, meanwhile an upstream motion of both the separation and the reattachment shock was observed. The control effect improves while the discharge energy and the orifice diameter increase, which is consistent with that in [75]. In [71, 72], different configurations of the actuator array (i.e. spanwise, streamwise) were considered, and a longer modification of the shock wave system is demonstrated when actuators are arranged in the streamwise direction and triggered simultaneously. Yang et al. [78] numerically investigated the control mechanism of SWBLI and concluded that the jet plume acts as a virtual micro vortex generator, which pro-

notes the mixing within the turbulent boundary layer and enhances its ability to resist flow separation.

1.5. MOTIVATION AND OBJECTIVES OF THIS RESEARCH

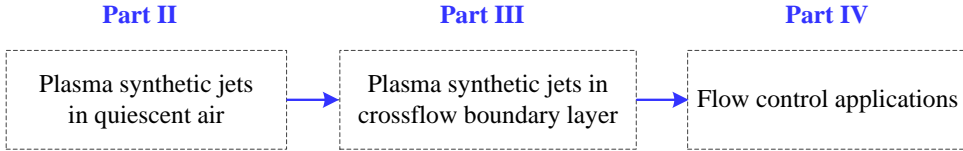


Figure 1.7: Research logic map

A three-step research logic map with increasing complexity is sketched in Figure 1.7. Pivoting around this logic map, the existing knowledge gaps can be detected. In Table 1.1, significant efforts from the plasma flow control community have been invested into the characterization of PSJAs. Notwithstanding the relatively clear trends of how electrical and geometrical parameters affect the jet intensity metrics, the non-dimensional scaling laws to generalize these trends to actuators with different geometries and diverse operating conditions remain to be unveiled. Taking Figure 1.4 as an example, the exit velocity has been demonstrated to increase nonlinearly with the energy deposition, whereas the exponent of this nonlinear relation remains disputable. Similar questions can be posted w.r.t the variation of jet density at increasing discharge frequency. As such, the first objective of this research is to determine ***‘the non-dimensional formation and evolution laws of plasma synthetic jets in quiescent air’***. Advanced flow measurement techniques including high-speed PIV and Schlieren imaging will be deployed to quantify the time evolution of jet-induced flow structures (e.g. vortex rings, shock waves), particularly their correlations with the electrical and geometrical parameters.

Flow control essentially requires plasma synthetic jets to interact with the flow that passes over the exit orifice, which is typically a turbulent boundary layer. For the interaction between conventional steady jets and boundary layer, a clear scenario is depicted in [76], where rich vortex structures including a horseshoe vortex, shear layer vortices, hanging vortices, and a counter rotating vortex pair are observed in the near-exit region and the far field. These vortices enhance the transportation and mixing process, thus potentially elevating the capability of boundary layer to withstand the adverse pressure gradient. As a comparison, significantly less information is available for the interaction between PSJs and boundary layer (only several PIV snapshots can be found in [21]). Due to the ZNMF feature of plasma synthetic jets, a phase-dependent vortex system different from the one created by steady jets in crossflow is expected. Therefore, ***‘the evolution and scaling of plasma synthetic jets in crossflow’*** is set as the second objective.

After the abovementioned studies, the control authority of PSJAs will be validated in two types of flows, i.e. airfoil leading-edge separation control at moderate Reynolds number and impinging shock wave/boundary layer interaction control at Mach number 2. Although similar cases have been treated in the literature (Table 1.2), the detailed

control mechanisms in these two specific scenarios are still missing and should be interpreted with advanced flow diagnostics techniques (i.e. high-speed PIV and Schlieren imaging). As such, the final objective of this study is directed to ***‘reveal the interaction mechanisms and identify the practical limitations of PSJA-based flow control.***

1.6. THESIS LAYOUT

- I Prologue** includes the first two chapters. In Chapter 1, the background of this research is introduced, and the achievements made in previous studies are reviewed. From the review, several knowledge gaps are identified and the research objectives are set. Chapter 2 describes the equipments, flow measurement techniques and data analysis methods.
- II Plasma synthetic jets in quiescent air** is the first step of our research logic map. In Chapter 3 and 4, formation and evolution of PSJs at increasing energy deposition and discharge frequency are investigated with high-speed PIV measurements, and the non-dimensional scaling laws are derived based on experimental evidences and simplified theoretical analysis. Chapter 5 focuses on the effect of orifice shape on jet evolution.
- III Plasma synthetic jets in crossflow** deals with the second objective of this research. In Chapter 6, a representative interaction case between PSJs and a crossflow turbulent boundary layer is analysed, from the perspectives of phase-averaged velocity field evolution, turbulent kinetic energy generation as well as boundary layer shape factor variation. In Chapter 7, the distinct vortex systems created by PSJs in crossflow at low and high velocity ratios are studied, and a preliminary regime map is established.
- IV Flow control practices** cover the efforts to apply PSJAs in two types of flows, i.e. airfoil leading edge separation control at $Re_c = 1.7 \times 10^5$ (Chapter 8), and impinging shock wave boundary layer interaction control at Mach number 2 (Chapter 9).
- V Epilogue** presents the conclusions in this research and the recommendations for future studies (Chapter 10).

2

EQUIPMENT AND METHODOLOGIES

2.1. GENERATION OF PLASMA SYNTHETIC JETS

2.1.1. ACTUATOR DESIGN

TWO versions of actuators (A1 and A2) are developed to cater for the research needs of Part II and Part III, as shown in Figure 2.1. Actuator A1 mainly consists of a cylindrical cavity and a metal lid. The cavity is made of glass ceramic (MACOR), with a diameter of 12 mm and height of 15 mm resulting in a cavity volume of 1696 mm^3 . Four uniformly spaced holes (diameter: 1.1 mm) are drilled in the circumferential direction, in a plane positioned 7.5 mm above the cavity bottom. Three of the holes accommodate tungsten needles, which are configured as anode, cathode and trigger electrode, respectively. The remaining hole is connected with a metal capillary tube (inner diameter: 0.4 mm), which delivers the particles necessary for PIV measurements into the actuator cavity. This intra-cavity seeding is devised to solve the issue of lack of particles in the jet core region reported by Ko et al. [61]. The metal lid can be combined together with the ceramic cavity through a step trough. A round (or slot) orifice is drilled in the lid centre, to accommodate the jet exit. Four needle holders with screw thread, and a nylon support base, are designed to enable accurate adjustment of the distance between electrodes, as shown in Figure 2.1 (c).

For purposes of convenient extension into an actuator array, A2 is constructed by a cubic ceramic shell (dimension: $15 \times 15 \times 15 \text{ mm}^3$) and a flat-plate cap (thickness: 3 mm). These two parts are also made of MACOR and can be assembled together through a step groove. A cylindrical cavity resides in the cubic ceramic shell. The diameter and height of this ceramic cavity are 10 mm and 12 mm, respectively, resulting in a cavity volume of 942 mm^3 . Three round holes (diameter: 1.1 mm) are drilled in the centres of the two side walls and the bottom surface, respectively. Two tungsten needles are inserted into the two side holes, serving as the anode and cathode, respectively. The remaining bottom hole is connected with a capillary tube (inner diameter: 0.4 mm) for intra-cavity seeding.

Part of this chapter is published as **H. Zong** & M. Kotsonis, *Electro-mechanical efficiency of plasma synthetic jet actuator driven by capacitive discharge*, Journal of Physics D: Applied Physics, **49**, 455201 (2016).

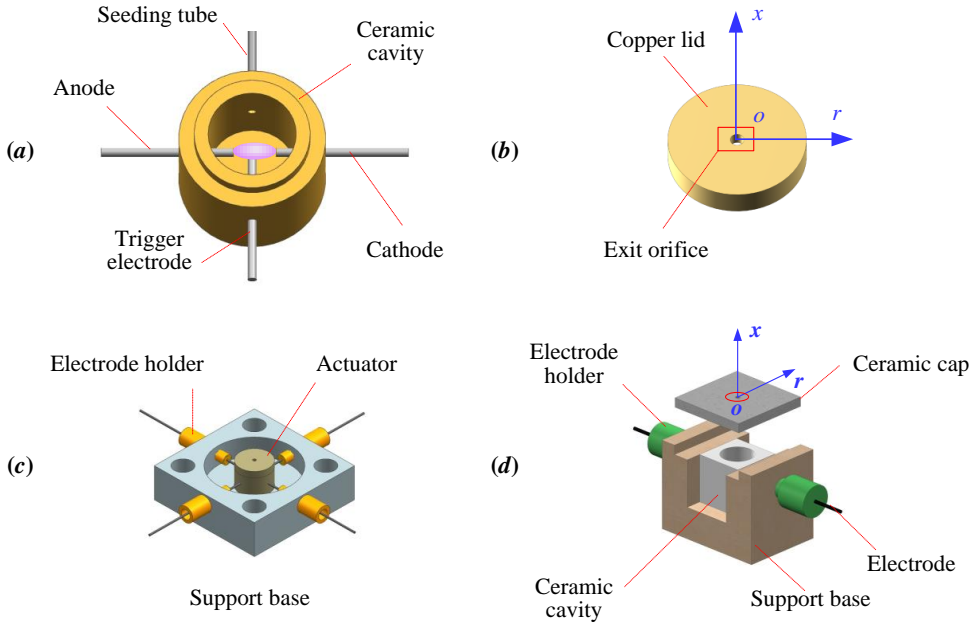


Figure 2.1: (a–c) Components of actuator version 1 (A1, in short); From left to right, they are respective ceramic cavity, copper cap and support base. (d) Assembly of actuator version 2 (A2, in short).

The distance between the anode and the cathode are fixed at 3 mm. On the ceramic cap, a round orifice (diameter: 1.5 mm) is created and serves as the jet exit. For both Actuator A1 and Actuator A2, a cylindrical coordinate system is established in the centre of the jet exit, with the r -axis and x -axis along the axial and radial directions, respectively.

2.1.2. ELECTRICAL CIRCUITRY DEVELOPMENT

A sequential discharge scheme (i.e. trigger discharge to capacitive discharge) is selected to execute the energy deposition in this study [50], largely attributed to the weak connection between capacitor energy and discharge frequency. Depending on whether a trigger electrode is configured in the actuator, two electrical circuitries (E1 and E2) are proposed, as shown in Figure 2.2. E1 is featured by the simple structure, as no external DC power supply is required and both the triggering and charging function are realized by a high-voltage amplifier. The working process of E1 is as follows. Initially, the high-voltage amplifier (Trek Model 20/20C, amplification ratio: 2000), is programmed to output a low-voltage pulse (typical amplitude: 2.5 kV) to charge capacitor C1 (withstand voltage: 5 kV, capacitance: 1 μ F). The charging current is limited by a resistor R1 (200 k Ω , 100 W) to not exceed the maximum allowable output current (20 mA) of the high-voltage amplifier. The width of the charge pulse ($O(1000$ ms)) is determined by the characteristic time of the charging circuit (i.e. the product of capacitance C1 and resistance R1). Immediately after the capacitor charging, a high-voltage trigger pulse (amplitude: 20 kV, pulse width: 100 μ s) is outputted to establish a voltage higher than the breakdown threshold

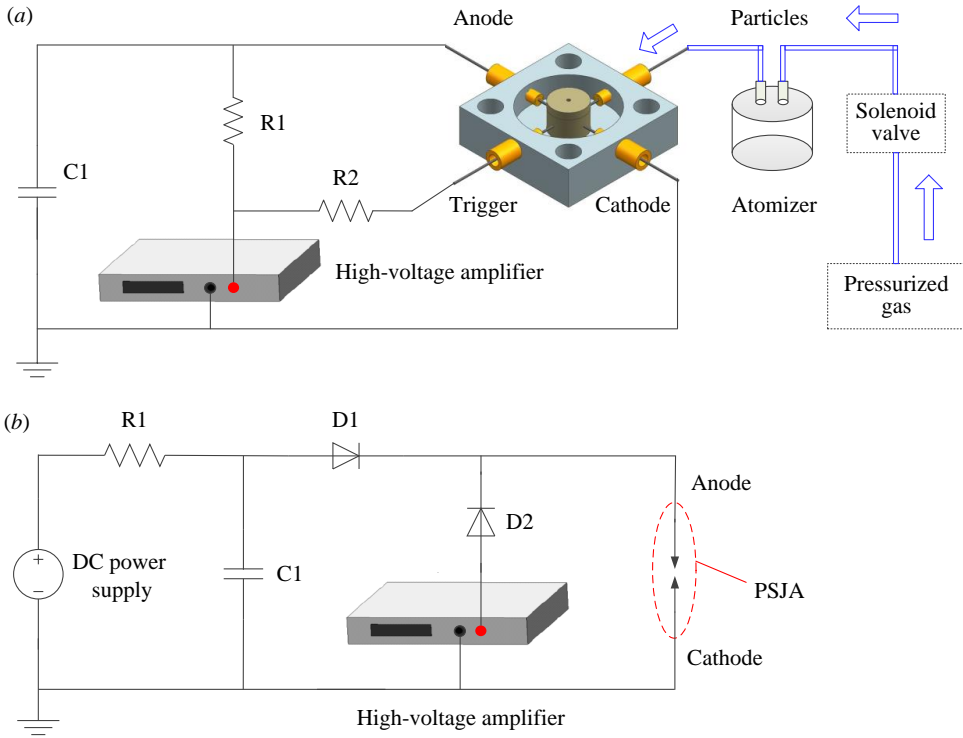


Figure 2.2: (a) Electrical circuitry version 1 (E1) for three-electrode actuator; (b) Electrical circuitry version 2 (E2) for two-electrode actuator;

of the inter-electrode gap, thus is able to ignite a spark. This spark serves as a virtual switch and enables the electrical energy stored in capacitor C1 to be released rapidly into the actuator cavity by virtue of arc heating. To prevent the arc current flowing back to the high-voltage amplifier, a protective resistor R2 (2 k Ω , 100 W) is added between the high-voltage amplifier and the trigger electrode.

Notwithstanding the simple structure, the peak frequency that can be achieved with circuitry E1 is limited to several hertz for capacitance of $O(1 \mu\text{F})$, largely due to the low charging current constraint of the high-voltage amplifier. Driven by the need of frequency investigation, circuitry E2 is developed. This circuitry is an upgraded version of the circuitry shown in Figure 1.2 (a), in the sense that trigger electrode and anode are effectively merged, reducing the number of electrodes into two. Compared to E1, a DC power supply (peak voltage 2.5 kV, power 2000 W) is added to provide the energy necessary for charging capacitor C1, and the resistance of current-limiting resistor R1 is reduced to 1 k Ω . As a result of the decrease of the characteristic timescale of charging circuit, it only takes several milliseconds to top up a capacitor of 1 μF , leading to a peak repetition rate of $O(100 \text{ Hz})$. For smaller capacitance (e.g. 0.1 μF), the peak repetition

rate can even reach several kilo hertz. Additionally, to isolate the low-voltage circuit from the high-voltage one in circuitry E2, two high-voltage diodes (D1 and D2, withstanding voltage: 20 kV) are added.

The working principle of circuitry E2 resembles that of E1. High-voltage low-energy trigger pulses are initially sent by the high-voltage amplifier for discharge ignition. After the discharge channel is ignited, the energy stored in capacitor C1 is rapidly evacuated and recharged by the DC power supply, awaiting the next trigger pulse. For both circuitries (E1 and E2), the discharge frequency is controlled by the trigger rate, while the intensity of arc discharge can be tuned conveniently by changing the capacitor voltage or capacitance.

2.2. WIND TUNNEL FACILITIES

Two wind tunnels from the Delft University of Technology (W-tunnel and ST-15) are involved in this research. The W-tunnel is a low-speed open-jet wind tunnel, featuring interchangeable contraction parts and test sections. With a typical square test section of 0.4 m×0.4 m, the maximum velocity is about 35 m/s and the minimum achievable turbulence level is approximately 0.5%. The ST-15 is a supersonic blow-down wind tunnel equipped with inflexible wall nozzles. Interchangeable sets of nozzles are used to obtain Mach numbers of either 1.5, 2, or 3 in a 15 cm×15 cm test section. High-pressure air is stored in a 300 m³ pressure vessel, leading to a total running time of about 18 minutes before recharging is required.

2.3. FLOW MEASUREMENT TECHNIQUES

Three measurement techniques including Schlieren imaging, hotwire anemometry and PIV are used for flow field diagnostics. Here, only a brief introduction of their working principles is provided. For more details, please refer to Settles et al. [79], Lomas et al. [80], and Raffel et al. [81].

2.3.1. SCHLIEREN IMAGING

Schlieren imaging has been so far the most widely used technique in PSJs-related studies. This technique is rooted in the variation of the refractive index (n) in a medium. For gases, the refractive index is linearly dependent on the gas density according to the Gladstone-Dale relation, i.e. $n = K\rho_0 + 1$, where ρ_0 is the gas density and K is the Gladstone-Dale constant. When a light ray passes through a variable refractive index field (e.g. compressible flows), it will bend towards the region with greater refractive index as governed by Snell's law, leading to a minor angular deflection from the original propagation direction (denoted as z -direction). The overall deflection angle of the ray ($\Delta\alpha$) after passing through a medium can be integrated from Equation 2.1, where x denotes a direction orthogonal to the ray propagation.

$$\Delta\alpha = \frac{1}{n} \int \frac{\partial n}{\partial x} \partial z \quad (2.1)$$

Schlieren imaging visualizes compressible flows by correlating the overall deflec-

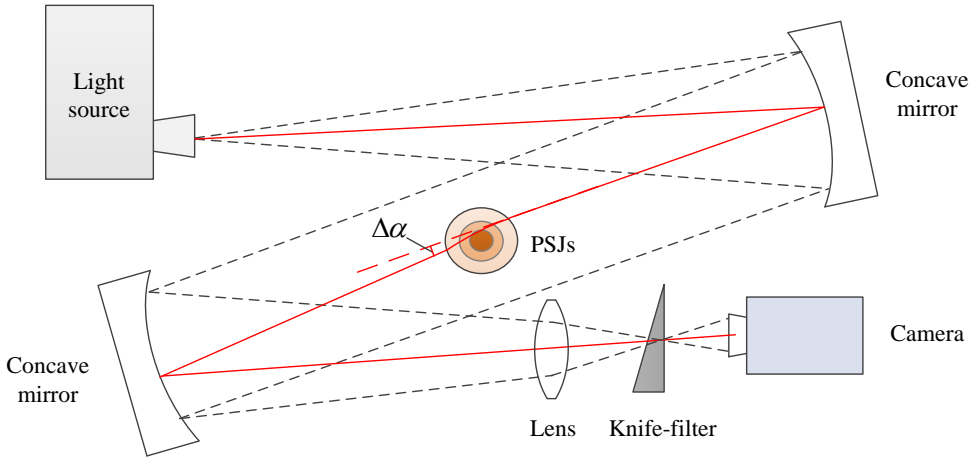


Figure 2.3: Z-type Schlieren imaging system. Reproduced from Zong & Kotsonis, [82]

tion angle ($\Delta\alpha$) with the brightness at different regions of the images. A typical Z-type Schlieren imaging system used in this study is shown in Figure 2.3, which mainly consists of a light source, two concave mirrors, a knife-filter and a high-speed digital camera. Light rays emitted from the continuous light source are first reflected by the two concave mirrors (diameter: 30 cm, focal length: 3 m), then converged by a 250 mm spherical lens, and finally projected onto the camera sensor directly. A knife edge is placed in the focal point to block part of the light spot. Depending on the local deflection direction and angle of light rays, the amount of photons received by different pixels the camera sensor varies. As a result, the density gradient of the flow is manifested by the brightness of the images. For a particular orientation of a linear knife edge, Schlieren imaging is only sensitive to the density gradient along the edge-normal direction. To obtain the sensitivity in all directions, circular knife edges can be adopted.

2.3.2. HOT-WIRE ANEMOMETER

Hot-wire anemometers (HWAs) use a thin wire that is electronically heated by a Wheatstone bridge, to measure the time-varying flow velocity. As fluids flow through the wire, heat is transferred away by cooling effect which has to be balanced by the Joule heating provided by the electrical circuit. Starting from the energy balance in steady stage and assuming that convective heat transfer plays a dominant role during the wire cooling, the King's law can be derived, as shown in Equation 2.2.

$$E_w^2 = (T_w - T_f)(A_0 + B_0 U^{C_0}) \quad (2.2)$$

where, E_w and U denote the wire voltage and the flow velocity, respectively. T_w and T_f represent the wire temperature and the flow temperature, respectively. A_0 , B_0 and C_0 are constants that have to be calibrated per probe.

The probe can be operated either in constant current or constant temperature mode. The latter is demonstrated to be much more popular than the former, largely due to the

high frequency response and the low risk of probe burnout. As the wire resistance is linearly correlated with the wire temperature ($R_w = R_0(1 + \alpha_0(T_w - T_0))$, α_0 and R_0 are the 'cold' resistance and the temperature coefficient respectively), constant temperature operation of the wire is typically realized by a Wheatstone bridge which continuously monitors the imbalance caused by wire resistance variation and a feedback circuitry which corrects the imbalance by adjusting the current flowing through the bridge. In constant temperature mode, the King's law shown in Equation 2.2 can be reformulated into a fourth-order polynomial, as $C_0 \approx 0.5$ in the forced heat convection regime. As such, the calibration of the wire probe is usually implemented by fitting a set of voltage-velocity data with a fourth-order polynomial.

To optimize the frequency response of an anemometer, the thermal inertia of the wire probe should be as small as possible. For the measurements in this study, a DANTEC probe (model number: P15) with a platinum-coated tungsten wire (diameter: $5 \mu\text{m}$, length: 1.25 mm) is selected, and operated in constant temperature mode by a TSI IFA-300 wheatstone bridge. The wire is supported by two prongs that are embedded in a ceramic cylinder. Based on the results of square-wave test, the cutoff frequency of the wire probe is estimated to be 20 kHz.

2.3.3. PARTICLE IMAGING VELOCIMETRY

TWO-COMPONENT PLANAR PIV

PIV is a non-intrusive whole-field velocity measurement technique that emerged in the past decades. A typical planar-PIV setup consists a laser, a digital camera, a particle generator, and a timing device for synchronization purpose. As shown in Figure 2.4, the external environment where actuators are submerged is seeded with small tracer particles (liquid droplets, smoke, $\text{TiO}_2/\text{Al}_2\text{O}_3$ powder, soap bubbles et al.). For high-jet-velocity cases where particles tend to escape from the vortex core region due to strong centrifugal forces, an intra-cavity seeding scheme is adopted to improve the spatial resolution [82]. As shown in Figure 2.2 (a), the thin capillary tube inserted inside of the actuator cavity is connected with a solenoid valve. The valve is activated shortly after jet termination to refill the actuator cavity with sufficient amount of particles, and disabled prior to discharge initiation in order not to interfere with the evolution of pulsed jets. The particles are illuminated by a thin laser sheet which is typically shaped from a circular laser beam using a combination of spherical and cylindrical lenses. The light scattered by these particles are collected by objectives and projected onto the digital camera sensor. In a very short time interval (Δt), the particle images are acquired twice, resulting in two frames. The motion of particles in Δt are analyzed by performing cross-correlation inside a small interrogation window of the two frames, as shown in Equation 2.3

$$\phi(m, n) = \frac{\sum \sum I(i, j) \cdot I'(i + m, j + n)}{\sqrt{\sum \sum I^2(i, j) \cdot \sum \sum I'^2(i, j)}} \quad (2.3)$$

where, I and I' represent the light intensity matrices of the two interrogation windows; ϕ is the cross-correlation coefficient.

In each of the cross-correlation map, the highest peak is fitted with a Gaussian function, and the most likely particle displacement (Δx) is determined within sub-pixel ac-

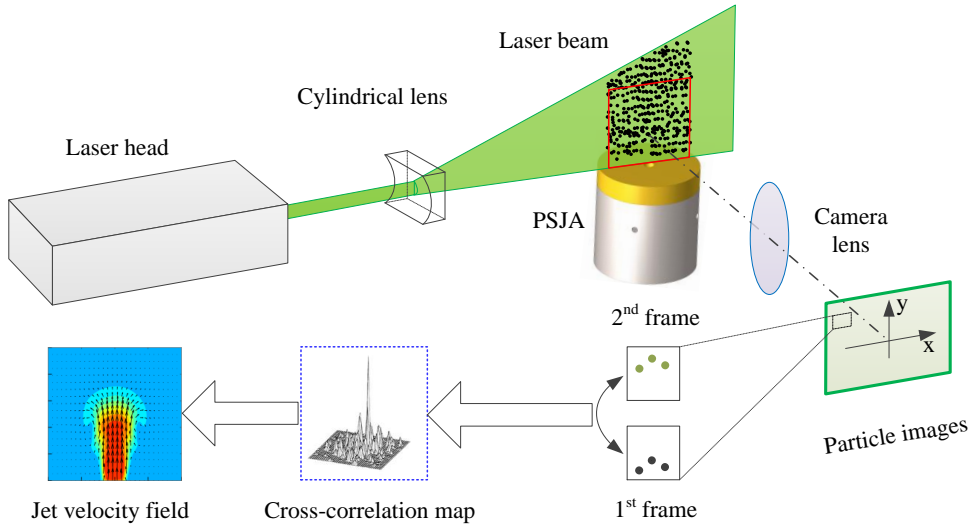


Figure 2.4: Representative PIV setup in jet characterization

curacy (0.1-0.2 pixel). Using the particle displacement, time separation, magnification ratio (M) and pixel pitch (d_τ), the particle velocity field can be computed, $U = \Delta x \cdot d_\tau / (M \cdot \Delta t)$. To what extent the particle velocity field can represent the authentic fluid velocity field (i.e. tracing fidelity) is quantified by the particle Stokes number (S_k) defined as the ratio of particle response time to flow characteristic time, τ_p / τ_f . Smaller and lighter the particle is, faster the particle can response to external velocity variation. In practice, $S_k < 0.1$ is preferred to limit the flow tracing errors to be less than 1%. Except for the mechanical properties of the tracer particles, the uncertainty in PIV measurements also depends on laser sheet thickness, particle displacement and so on. A dedicated measurement uncertainty analysis will be performed in Section 2.4.2.

In large-scale planar PIV measurements where the field of view (FOV) reaches the order of $O(1 \text{ m}^2)$ (or in 3D-PIV measurements where the measurement volume is $O(1000 \text{ cm}^3)$), special attentions should be paid to guarantee the selected particles can scatter sufficient light to be visible by the cameras. For particles with diameters larger than the laser wavelength, Mie's scattering theory can be applied, and the scattering intensity is linearly proportional to the square of particle diameter [83]. As a result, helium-filled soap bubbles (HFSB) with diameters of $O(0.1 \text{ mm})$ are widely chosen as tracing particles in large-scale PIV applications [84].

THREE-COMPONENT STEREO PIV

In planar-PIV measurements, since the particle motion is viewed from single perspective, the out-of-plane velocity component is always missing. For highly three-dimensional flows (e.g. jets in crossflow) where all the velocity components are interested, stereo PIV should be deployed. In this configuration, two non-collinear cameras are viewing the

same flow field from different perspectives, and two sets of velocity field can be computed. Using the geometrical relations between the object and image planes, the four measured vector components in the two sets of velocity field can be associated with the unknown three velocity components in Cartesian coordinate system. As this problem is overdetermined, the solution is typically determined by a least-square fitting procedure, and the residuals of this least-square fitting represent the measurement uncertainties of the three velocity components (range: 0.1-0.5 pixel).

The geometrical relations necessary for image mapping can be obtained from a two-step calibration procedure. In the first step (physical calibration), a twin-level calibration plate with precisely-painted dot patterns are imaged by the two cameras. The positions of these dots are detected, and the correlation between image and object plane is fitted with a second-order mapping function. After physical calibration, significant reconstruction residuals can still exist as a result of the manual alignment of the calibration plate with the laser sheet (view mismatch), thus need to be corrected by self-calibration (second step). In self calibration, raw particle images are recorded by the two cameras and dewarped to the laser-sheet plane according to the physical calibration functions. Subsequently, the dewarped images from the two cameras are cross-correlated to get a disparity vector field. This disparity vector field is used to correct the physical mapping functions, minimising the measurement uncertainty originated from calibration.

2.4. DATA ANALYSIS METHODS

Section 2.4.1 presents the metrics used to measure the intensity of plasma synthetic jets, e.g. jet velocity, jet duration, impulse, efficiency and so on. These metrics are either extracted from Schlieren images or from PIV measurements. Section 2.4.2 is dedicated to PIV measurement uncertainty analysis, where different sources of the uncertainty are identified and synthesized. Section 2.4.3 introduce the triple decomposition method.

2.4.1. JET INTENSITY METRICS EXTRACTION

Notwithstanding Schlieren imaging is a qualitative flow visualization technique, noticeable efforts have been made to extract quantitative information from a Schlieren image sequence [32]. As shown in Figure 2.5 (a), a vortex ring is expelled after discharge ignition. Based on the axial propagation distance in adjacent frames, the propagation velocity of the ring (U_v) can be computed, which is equivalent to the jet penetration rate as the ring is always located in the jet front. For the representative case shown in Figure 2.5 (b), U_v exhibits a sharp initial increase followed by a gradual decrease. Note that the peak value of U_v is only half of the peak jet exit velocity measured by PIV, as will be demonstrated in Chapter 3 and Chapter 5.

In addition to the ring propagation velocity, the jet duration can also be extracted. Specifically, an interrogation window (width: $1D$, height: $0.2D$, D is orifice diameter) is placed just above the jet exit orifice (Figure 2.5 (a)), and the variation of the spatially-averaged jet grayscale within the interrogation window (G_e) is monitored over a complete cycle. Normalizing G_e by its maximum observed value, the trend illustrated in Figure 2.5 (b) can be obtained, and the jet duration time is determined from a preset threshold of the normalized jet exit grayscale (\bar{G}_e). Typically, a good collapse with the

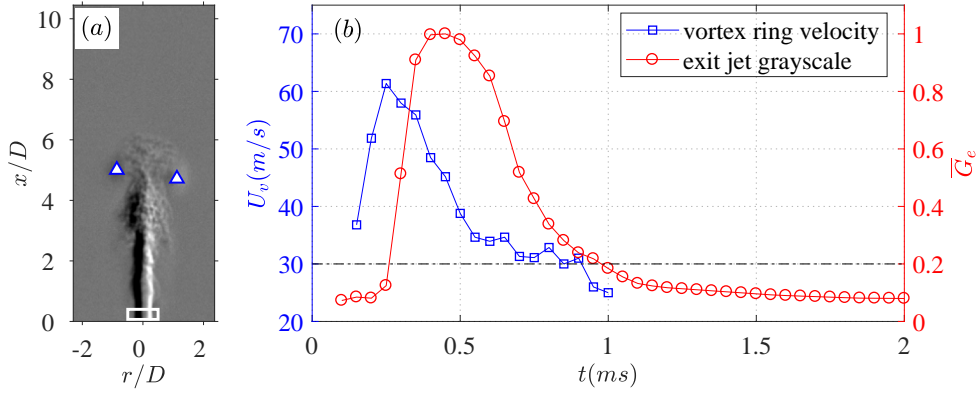


Figure 2.5: (a) Representative jet Schlieren image at a time delay of $t = 400 \mu\text{s}$ with respect to discharge ignition (reproduced from Zong & Kotsonis [82]). The centers of the vortex ring are pinpointed by triangles. The inter-rogation window used in jet duration time estimation is indicated by a white rectangle. (b) Time evolution of the front vortex ring velocity (U_v) and the normalized exit jet grayscale (\bar{G}_e).

results from other measurement techniques (i.e. PIV) can be obtained, by selecting a threshold value of $\bar{G}_e = 0.2 - 0.3$.

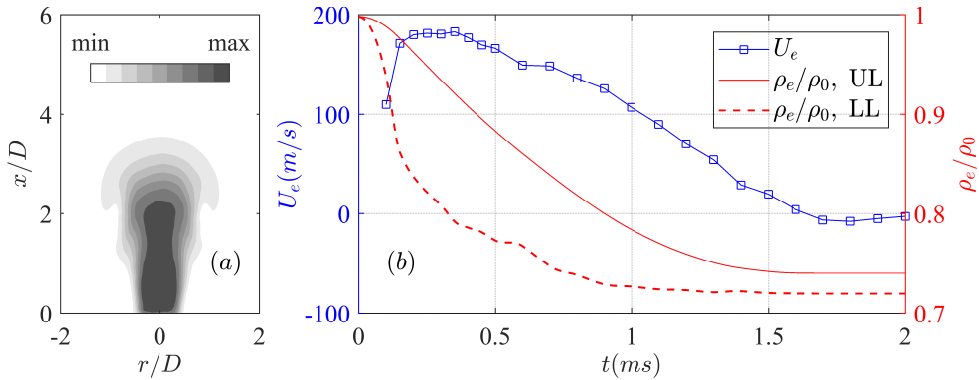


Figure 2.6: (a) Representative jet velocity field measured by phase-locked PIV at a time delay of $t = 150 \mu\text{s}$ with respect to discharge ignition (reproduced from Zong & Kotsonis [85]). Contours indicate the magnitude of in-plane velocity. (b) Time evolution of the mean jet exit velocity (U_e), and the upper and lower limits (in short, UL and LL) of the normalized jet exit density (ρ_e/ρ_0).

With PIV measurements, much more metrics of PSJs can be accessed. Figure 2.6 (a) shows a representative jet velocity field expelled from a circular orifice in single-shot mode (reproduced from the PIV results in Zong & Kotsonis [85]). Under the assumption of axisymmetric jet flow, the spatially-averaged jet exit velocity (U_e) can be estimated by integrating the exit velocity profile in the radial direction as shown in Equation 2.4,

$$U_e(t) = \frac{\int_0^{D/2} 2\pi r U_x(r, t|x=0) dr}{\pi D^2/4} \quad (2.4)$$

The temporal evolution of U_e is shown in Figure 2.6 (b), from which the peak jet exit velocity (U_p) and the duration of primary jet stage (T_{jet}) can be picked straightforwardly. In the following content, a simplified analytical model is derived to estimate the time-varying jet density based on the measured trend of U_e [85].

$$\begin{cases} \frac{d(\rho_{ca}(t)V_{ca})}{dt} = -\rho_e(t)U_e(t)A_e \\ \frac{\rho_{ca}(t)}{\rho_e(t)} = [1 + \frac{\gamma-1}{2}Ma_e^2(t)]^{1/(\gamma-1)} \\ Ma_e(t) = U_e(t)/\sqrt{\gamma RT_e(t)} \end{cases} \quad (2.5)$$

The governing equations of jet stage is shown in Equation 2.5, where $\rho_{ca}(t)$ denotes the time-varying spatially-averaged cavity density. A is the exit orifice area. $Ma_e(t)$ and $T_e(t)$ are the jet exit Mach number and the jet exit temperature. γ and R stand for the gas specific heat ratio and gas constant, respectively. In this equation set, the first formula is essentially the mass conservation law, while the second one is obtained under the assumption of isentropic expansion. Apart from $U_e(t)$, totally four unknown variables (ρ_{ca} , ρ_e , Ma_e and T_e) are introduced in the three formulas. Reformulating these formulas, the jet exit density can be expressed explicitly by the other variables as follows,

$$\begin{cases} \rho_e(t) = \rho_0/[f(t) \cdot \exp(\frac{A_e}{V_{ca}} \cdot \int_0^t \frac{U_e(t)}{f(t)} dt)] \\ f(t) = [1 + \frac{\gamma-1}{2}Ma_e^2(t)]^{1/(\gamma-1)} \end{cases} \quad (2.6)$$

Since the expelled gas is of high temperature, the relation $0 \leq Ma_e(t) \leq U_e(t)/\sqrt{\gamma RT_0}$ is always tenable. As such, the upper limit and lower limit of function $f(t)$ are determined as $f_{UL}(t) = [1 + (\gamma-1) \cdot U_e^2/(2\gamma RT_0)]^{1/(\gamma-1)}$ and $f_{LL} = 1$ respectively, and the variation of jet exit density should lie in the following interval.

$$\begin{cases} \rho_e(t) \geq \rho_0/[f_{UL}(t) \cdot \exp(\frac{A_e}{V_{ca}} \cdot \int_0^t U_e(t) dt)] \\ \rho_e(t) \leq \rho_0/\exp[\frac{A_e}{V_{ca}} \cdot \int_0^t \frac{U_e(t)}{f_{UL}(t)} dt] \end{cases} \quad (2.7)$$

Figure 2.6 (b) shows the upper and the lower limit of the time-varying jet exit density computed from Equation 2.7. Using the mean value of these two curves to approximate $\rho_e(t)$, a maximum error of less than 8% can be guaranteed. Additionally, based on the time-varying jet exit density and exit velocity, three crucial metrics pertaining to the single jet pulse including the expelled gas mass (M_e), impulse (I_p) and jet mechanical energy (E_m), are defined as follows.

$$\left\{ \begin{array}{l} M_e = \int_0^{T_{jet}} \rho_e(t) U_e(t) A_e \cdot dt \\ I_p = \int_0^{T_d} \rho_e(t) U_e(t) |U_e(t)| A_e \cdot dt \\ E_m = \int_0^{T_d} 0.5 \rho_e(t) U_e^2(t) |U_e(t)| A_e \cdot dt \end{array} \right. \quad (2.8)$$

T_d is the cycle period and can be replaced by T_{jet} in single shot mode. It is interesting to note that the three integrated terms in Equation 2.8 are the product of exit density and increasing exponents of exit velocity. As these metrics are dependent of the actuator geometry and input energy, another three non-dimensional parameters are proposed,

$$\left\{ \begin{array}{l} M_e^* = M_e / (\rho_0 V_{ca}) \\ I_p^* = I_p / \sqrt{2E_d \cdot \rho_0 V_{ca}} \\ \eta_m = E_m / E_d \end{array} \right. \quad (2.9)$$

$\rho_0 V_{ca}$ denotes the initial mass of cavity gas. E_d is the discharge energy integrated from discharge voltage and current, namely $E_d = \int u_d i_d dt$. η_m stands for the absolute electro-mechanical efficiency. The quantity $\sqrt{2E_d \cdot \rho_0 V_{ca}}$ is derived under the assumption that the entire discharge energy E_d is transformed into the kinetic energy of cavity gas (mass: $\rho_0 V_{ca}$, velocity: $\sqrt{2E_d / (\rho_0 V_{ca})}$). Obviously, the non-dimensional impulse I_p has an upper limit of 1 and a meaning of 'impulse efficiency'. For PSJAs driven by capacitive discharge, the order of magnitude for η_m and I_p is $O(0.1\%)$ and $O(1\%)$ respectively.

2.4.2. PIV MEASUREMENT UNCERTAINTY QUANTIFICATION

In this study, finite sample size, peak locking error, limited spatial resolution, finite laser sheet thickness, discharge timing uncertainty, and particle tracking lag are identified as the six main sources of PIV measurement uncertainty. Assuming that all the samples are uncorrelated and follow a normal distribution, the standard uncertainty of the phase-averaged velocity can be calculated as follows [86],

$$\delta_{U1} = \sigma_U / \sqrt{N} \quad (2.10)$$

where, σ_U and N denote the standard deviation of velocity and the sample size respectively. As a result, large measurement uncertainty resides in the region with high velocity fluctuation, namely the front vortex ring and the jet shear-layer. With increasing sample size, the first type of measurement uncertainty decreases.

The peak-locking error typically stems from the subpixel curve fitting in the cross correlation analysis and cannot be reduced using statistical averaging [87]. This error increases significantly when the particle image diameter is less than two pixels. For the investigated case (particle image diameter: 2-3 pixels), the peak-locking error has a periodic pattern with a typical amplitude of approximately 0.15 pixels [88]. Considering a maximum particle displacement of 10 pixels, the measurement uncertainty caused by peak-locking error (δ_{U2}) is 1.5% of the peak velocity.

The measurement error associated with the finite spatial resolution of PIV is modelled by Scarano [89]. As concluded, this error (δ_{U3}) is proportional to the second-order spatial derivative of the velocity field for a fixed interrogation window size, as shown in Equation 2.11.

$$\delta_{U3} = \frac{1}{24} \left(\frac{\partial^2 U}{\partial^2 x} l_x^2 + \frac{\partial^2 U}{\partial^2 y} l_y^2 \right) \quad (2.11)$$

where, l_x and l_y denote the window size in each direction (2D case). In practice, the actual velocity field is largely unavailable, and the second-order velocity derivatives can be evaluated either from other techniques (e.g. HWA), or from advanced PIV algorithms based on self-adaptive interrogation windows [89, 90].

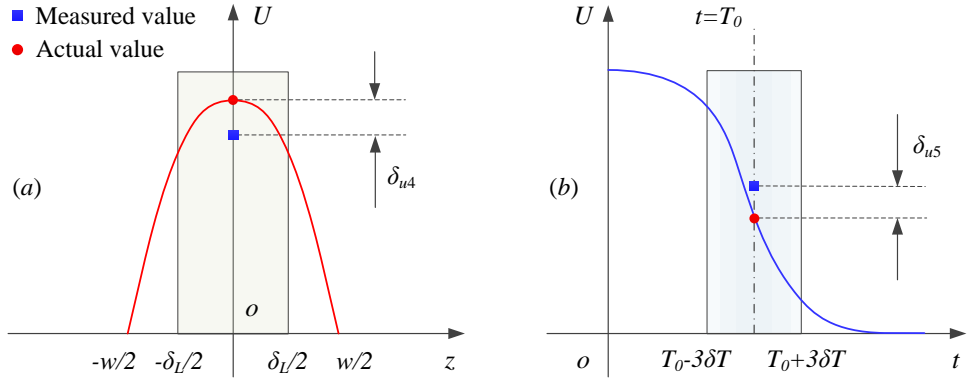


Figure 2.7: Velocity estimation errors caused by (a) thick laser sheet and (b) discharge timing uncertainty.

The finite laser sheet thickness (δL) imposes a similar spatial-averaging effect on the measured velocity field as the finite interrogation window. Considering a typical measurement of PJS emanating from circular orifices (Figure 2.4), the jet velocity distribution across the laser sheet is nonuniform and has a top-hat shape as illustrated in Figure 2.7 (a). Due to the projection from 3D volumetric flow to 2D planar vector field, the averaging effect is proportional to the laser sheet thickness as well as the second-order velocity derivatives in out-of-plane direction. Here, the worst case is considered, where the velocity distribution across the laser sheet is assumed to be parabolic. Based on this assumption, the measured velocity (U_m) and the corresponding estimation error (δ_{U4}) are deduced as follows,

$$\begin{cases} U_m = \int_{-\delta L/2}^{\delta L/2} U(z) dz = \int_{-\delta L/2}^{\delta L/2} U(0) \cdot \left(1 - \frac{4z^2}{D^2}\right) dz \\ \delta_{U4} = U_m - U(0) = -\frac{1}{3} \left(\frac{\delta L}{D}\right)^2 \cdot U(0) \end{cases} \quad (2.12)$$

where $U(0)$ is the actual velocity. z denotes the out-of-plane coordinate direction. As a result, the jet exit velocity tends to be underestimated, and the estimation error is posi-

tively proportional to the ratio of laser sheet thickness to orifice dimension. For a typical case of $D=2$ mm and $\delta_L=0.5$ mm, the relative measurement uncertainty caused by finite laser sheet thickness is 2%.

The fifth error is related to the discharge timing uncertainty (Figure 2.7 (b)). Specifically, due to internal impedance mismatch and non-ideal properties of the discharge power supply, the high-voltage trigger signal is not an ideal square wave and needs a short time to rise to the breakdown voltage. Since the breakdown voltage of spark discharge in the inter-electrode gap is not deterministic, the exact discharge timing fluctuates between pulses. This timing fluctuation is further propagated to the measurement uncertainty of the phase-averaged velocity [91]. The relationship between the standard deviation of the discharge timing (δ_T) and the produced measurement uncertainty (δ_{U5}) is derived in the following equation, where a local linear approximation is utilized.

$$\delta_{U5} = U(T_0 + \delta_T) - U(T_0) \approx \delta T \left. \frac{\partial U}{\partial t} \right|_{t=T_0} \quad (2.13)$$

Based on the results shown in [91], the standard deviation of δ_T is estimated as $3 \mu\text{s}$. Considering a typical jet acceleration time of $100 \mu\text{s}$ and a peak jet velocity of 200 m/s (Figure 2.6), the peak value of δ_{U5} is estimated to be 6 m/s .

The final error is caused by the particle tracking lag which is significant in the region featuring an abrupt velocity change (e.g. shock waves, sudden accelerations). Following Raffel et al. [81], the slip velocity of particles in these regions (δ_{U6}) can be estimated with the following relation,

$$\delta_{U6} = U_f - U = \tau_p \frac{\partial U}{\partial t} \quad (2.14)$$

where, U_f and U are fluid velocity and particle velocity respectively. τ_p is the particle response time determined by the fluid and particle properties, namely $\tau_p = d_p^2(\rho_p - \rho_f)/18\mu$, where d_p is the particle diameter; ρ_p and ρ_f are the particle and the fluid density respectively. μ denotes the fluid dynamic viscosity. For the liquid droplets (mineral oil, water-glycol) used in this study, τ_p is estimated to be $3.4 \mu\text{s}$ [91, 92], and the measurement uncertainty corresponding to particle tracking lag in accelerating jet is close to that originated from the discharge timing uncertainty.

The Euclidean sum of the above six measurement errors defines the total measurement uncertainty. However, it should be noted that each of the six errors is a function of the time delay (t) and the three spatial coordinates (x, y, z). An accurate estimation of this spatiotemporal total measurement error is far beyond the scope of this thesis. Thus, only the peak measurement uncertainty is provided in the subsequent chapters.

2.4.3. TRIPLE DECOMPOSITION

Reynolds & Hussain [93] proposed a triple decomposition of the instantaneous velocity (u), as shown in Equation 2.15, where \bar{U} , \tilde{u} and u' represent respectively the time-invariant contribution, the periodical fluctuation arising from repetitive actuation and the random fluctuation corresponding to turbulence. The summation of time-invariant and periodical-fluctuation parts yields the phase-averaged velocity (U). The integral of the phase-averaged velocity in one cycle period (T_d) defines the time-averaged velocity (\bar{U}). For phase-locked PIV measurements, this integral can be approximated by a

weighted summation relation as indicated in Equation 2.16, where Δt is the time step between adjacent phases.

$$u(x, y, z, t) = \bar{U}(x, y, z) + \tilde{u}(x, y, z, t) + u'(x, y, z, t) \quad (2.15)$$

$$\bar{U}(x, y, z) = \int_0^{T_d} U(x, y, z, t) \cdot dt \approx \frac{1}{T_d} \sum_{i=1}^N U_i(x, y, z, t) \cdot \Delta t_i \quad (2.16)$$

II

PLASMA SYNTHETIC JETS IN QUIESCENT AIR

3

FORMATION, EVOLUTION AND SCALINGS

3.1. INTRODUCTION

SINCE the proposal of PSJA by Grossman et al. in 2003 [14], considerable studies have been performed to characterize the formation and evolution processes of plasma synthetic jets in quiescent air [15, 21, 32, 33, 37]. These studies cover a wide range of parameter space (energy deposition: $O(1 \text{ mJ})$ – $O(10 \text{ J})$ per pulse, cavity volume: 20–2000 mm^3 , frequency: 1 Hz–10 kHz, discharge duration: $O(\text{ns})$ – $O(\text{ms})$), in an effort to better understand the underlying working mechanisms as well as to maximize potential flow control effects. However, the fast-expanding ($O(10 \mu\text{s})$) high-temperature jet ($O(1000 \text{ K})$), small-scale flow structures ($O(\text{mm})$) and strong electromagnetic interference (EMI) incurred by high-voltage ($O(\text{kV})$) high-current ($O(100 \text{ A})$) pulsed discharges pose significant challenges for flow measurement techniques such as dynamic pressure transducers, hotwire anemometry and time-resolved PIV [49, 61, 68, 94]. As a result, the non-dimensional formation and evolution laws of PSJs in repetitive working mode (e.g. centreline velocity decay, jet width, front vortex ring propagation) are largely unavailable in previous studies. Proper scaling laws for the formation and evolution of PSJAs are vital for a rigorous description of the pertinent working principles, as well as for optimized design of the actuator geometry and operation for flow control applications.

This chapter takes the first step towards tackling the abovementioned issue. A high-frequency phase-locked PIV system is employed to access both the phase-averaged and the time-averaged velocity fields of a PSJ in repetitive mode. Near-field ($0 < x < 7.5D$) and far-field measurements ($0 < x < 22.5D$) are carried out successively to enable both spatial resolution and spatial range. The effects of two crucial parameters, namely the non-dimensional energy deposition and the dimensionless working frequency, on the formation and evolution of the ensuing flow structures are examined in detail. Proper

Part of this chapter is published as H. Zong & M. Kotsonis, *Formation, evolution and scaling of plasma synthetic jets*, *Journal of Fluid Mechanics*, **837**, 147-181 (2018).

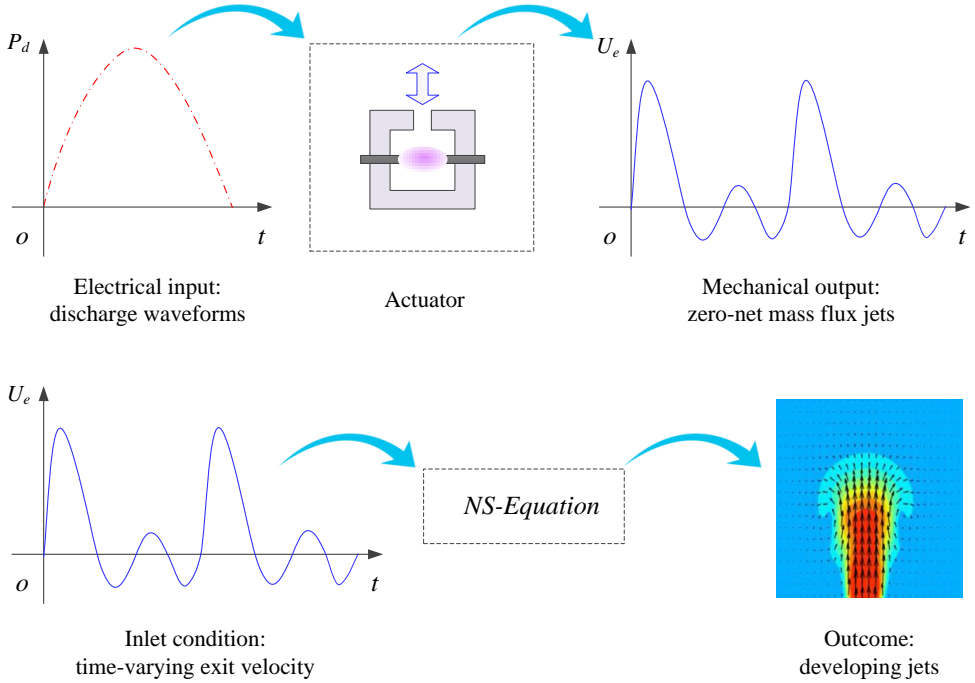


Figure 3.1: Sketch of formation (top row) and evolution (bottom row) process of plasma synthetic jets. $P_d(t)$ and $U_e(t)$ denote the discharge power and the time-varying exit velocity, respectively.

combination of the electrical and geometric parameter is used to scale these formation and evolution laws. Comparisons between PSJs and steady jets as well as conventional synthetic jets are executed throughout this work.

3.2. FORMATION AND EVOLUTION METRICS OF PSJS

As shown in the top row of Figure 3.1, formation of PSJs refers to the process that the total enthalpy of the cavity gas is suddenly elevated through arc discharge and further transformed into the mechanical energy of the expelled gas. The input of formation process is a time-varying discharge waveform determined by the coupling between the external discharge circuitry and arc plasma, while the outcome is zero-net mass flux jets. The goal of formation studies is to reveal the complex transfer function between inflow (electrical) and outflow (mechanical) parameters, which involves multiple disciplines including electrical engineering, gas discharge, plasma physics, and fluid dynamics. Evolution of PSJs mainly treats the process that a slug of low-density high-temperature fluids is abruptly released to the surroundings via an exit orifice and subsequently drawn back [8]. The bonds between formation and evolution process are the jet exit parameters (i.e. time-varying exit velocity, pressure and density). Once these parameters are set, the developing jets can be fully predicted by Navier-Stokes equations, as shown in the bottom row of Figure 3.1.

3.2.1. NON-DIMENSIONAL ENERGY DEPOSITION AND FREQUENCY

The pulsed arc energy and the frequency are commonly used to characterize the input discharge waveforms. For the capacitive discharge that is typically exploited to feed the actuator [25, 37], the pulsed arc energy can be simply represented by the capacitor energy (E_c). The ratio of this capacitor energy (E_c) to the internal energy of the cavity gas at initial state (E_g) gives the non-dimensional energy deposition (ϵ) as follows,

$$\epsilon = \frac{E_c}{E_g} = \frac{0.5 \cdot C_1 V_1^2}{c_v \rho_0 V_{ca} T_0} \quad (3.1)$$

where c_v is the constant-volume specific heat capacity; V_{ca} denotes the inner cavity volume of the PSJA and ρ_0 and T_0 are the atmospheric ambient density and temperature respectively; C_1 and V_1 represent the capacitance and initial voltage of the energy-storing capacitor responsible for powering the actuator.

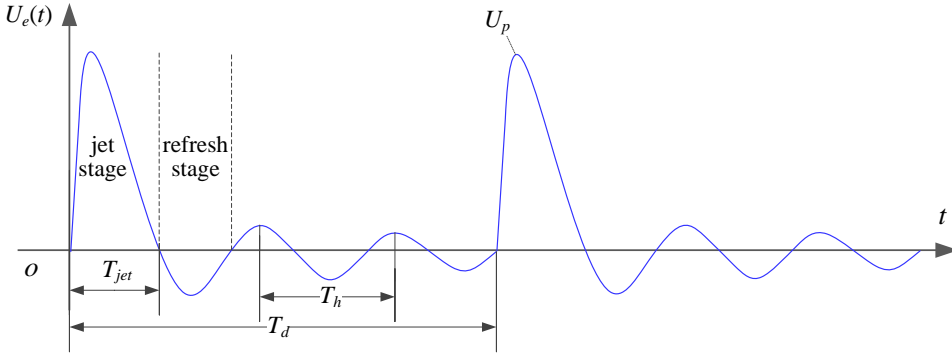


Figure 3.2: Conceptual temporal evolution of the exit velocity (U_e). Two actuation cycles are shown.

Based on the models in Zong et al. [16] and Chiatto & de Luca [46], a schematic exit velocity trace is shown in Figure 3.2. It should be noted that the energy deposition stage is not sketched due to its extremely short duration compared with the hydrodynamic time scales governing the jet evolution. After the primary jet stage, the actuator behaves like a Helmholtz resonator, where small-amplitude periodical oscillations of the exit velocity can be observed as a result of the inherent stiffness of the cavity air [56]. The frequency of alternation between jet and refresh stages ($f_h = 1/T_h$, namely the Helmholtz natural frequency) is related to both atmospheric parameters and geometrical parameters [95] as shown in Equation 3.2.

$$f_h = \frac{1}{2\pi} \sqrt{\frac{\gamma P_0}{\rho_0}} \sqrt{\frac{A_e}{V_{ca} L_{th}}} \quad (3.2)$$

Here, A_e is the area of the exit orifice; L_{th} , P_0 and γ represent the throat length, atmospheric pressure and specific heat ratio respectively. In the repetitive working mode, where multiple discharges are initiated in relatively close succession, the PSJA needs at

least one refresh stage for recovery. Hence, f_h can be interpreted as the maximum usable frequency of the PSJA, similar to the saturation frequency proposed by Zong et al. [16]. To describe how significant the frequency effect is, a dimensionless frequency (f^*) can be defined in Equation 3.3, where f_d , T_d and T_h denote the discharge frequency, discharge period and alternation period between jet and refresh stages ($1/f_h$) respectively,

$$f^* = \frac{f_d}{f_h} = \frac{T_h}{T_d} \quad (3.3)$$

In the case of $f^* \ll 1$, the cycle period (time between successive discharges) is long enough to reset the actuator to its original status. As a consequence, the jet intensity in repetitive working mode stays almost identical to that in single-shot operation. On the contrary, if f^* is comparable to or even larger than 1, the intensity of the pulsed jets is expected to deteriorate considerably [16, 46].

3.2.2. STROKE LENGTH AND REYNOLDS NUMBER

Several evaluation metrics including the peak jet velocity (U_p) and jet duration time (T_{jet}) can be directly extracted from the exit velocity curve shown in Figure 3.2. The ratio of jet duration time to cycle period (T_d) defines the jet duty cycle, $D_c = T_{jet}/T_d$. To normalize the formation and evolution characteristics, appropriate reference scales should be determined. In this study, the orifice diameter (D), cycle period (T_d) and peak jet velocity (U_p) are selected as the primary reference length, time and velocity scales respectively. The reference velocity is defined independently, instead of being derived from the length and time scales, largely due to the necessity of incorporating jet intensity information to collapse the evolution laws generated by PSJs with different energy level. Based on these reference scales, the non-dimensional stroke length (L_s^*) and the Reynolds number (Re_0) can be computed as follows [96],

$$\begin{cases} L_s^* = \frac{1}{\rho_0 D} \int_0^{T_{jet}} \rho_e(t) U_e(t) dt \\ Re_0 = \frac{U_p D}{\nu} \end{cases} \quad (3.4)$$

Here, ν is the kinematic viscosity at ambient conditions. Differently from the approach of Shuster & Smith [97], a correction for density changes is applied to the definition of L_s^* as PSJs of different densities are expected to behave differently in the axial penetration and radial spreading rate. In the current study, the influence of energy deposition and discharge frequency is examined. Keeping the energy deposition fixed and increasing the frequency, L_s^* and Re_0 hardly change, provided the frequency effect proposed by Zong et al. [16] is negligible. Conversely, with increasing discharge energy and unchanged frequency, both L_s^* and Re_0 will increase.

3.3. EXPERIMENTAL SETUP AND MEASUREMENT SYSTEM

3.3.1. ACTUATOR AND POWER SUPPLY

In this study, the actuator A1 shown in Figure 2.1 (a)-(c) is adopted and fed by the discharge circuitry E2 (see Figure 2.2 b). Since the trigger function has been integrated into

the anode in circuitry E2, no trigger electrode is configured by the actuator. The electrode gap between the anode and cathode is fixed at 3 mm. In the centre of the copper lid, a round orifice (diameter: 2 mm, throat length: 2 mm) is created, serving as the jet exit. A reference coordinate system is established in the centre of the jet exit, with r -axis and x -axis along the radial and axial directions respectively. Based on the geometrical dimensions of the actuator, the Helmholtz natural frequency (f_h) calculated by Equation 3.2 is 1.65 kHz, resulting in a theoretical jet-refresh alternation period (T_h) of 607 μ s. Additionally, the capacitance of C1 in circuitry E2 (Figure 2.2 *b*) is set as 1 μ F, and the voltage of the DC power supply is adjusted to get different energy deposition levels.

3.3.2. THE PIV SYSTEM AND MEASUREMENT SCHEME

A high-speed two-component planar PIV system was employed to measure the jet induced flow in the axisymmetric plane (xr -plane). The actuator was placed in an enclosed Plexiglas box ($1.5 \times 0.5 \times 0.5$ m³) and an atomizer (TSI, 9302) was used to seed dielectric mineral oil particles (Shell Ondina, average diameter: 1 μ m) into both the box and the actuator cavity. Prior to discharge ignition, the intra-cavity seeding was switched off by a mechanical valve to guarantee quiescent flow conditions. The PIV system consisted of a high-speed laser (Continuum Mesa PIV, 532-120-M, 30 mJ per pulse), a high-speed CCD camera (Photron, Fastcam SA-1) and a high-speed controller (LaVision, HSC). The laser beam emitted from the laser head was first shaped into a thin sheet by two spherical lenses and one cylindrical lens, and further conditioned by two knife edges. The final laser sheet (thickness: 0.5 mm) passing through the jet exit centre was kept strictly vertical, to eliminate the influence of buoyancy. The time delay between two subsequent laser pulses (dt) was adjusted dynamically to maintain a peak particle displacement of approximately 10 pixels.

A 200 mm macro lens (Nikon, Micro-Nikkor) attached to a 36 mm extension tube was mounted on the high-speed camera. By changing the object–camera distance, the jet flow was imaged in two sets of field of view (FOV), to achieve respectively highly resolved near-field structures and fully developed far-field characteristics. For the near-field measurement, the imaged FOV was 15×15 mm² ($7.5D \times 7.5D$), resulting in a magnification ratio of 1.37. For the far-field test, the imaged FOV was extended to 45×45 mm² ($22.5D \times 22.5D$), corresponding to a magnification ratio of 0.46. The digital resolution of the high-speed camera was 1024×1024 pixels². Raw images were recorded in double frame mode at a sampling rate corresponding to the discharge frequency (f_d). DaVis 8.3.1 was used to record and process the datasets. The final PIV interrogation window size and the overlapping ratio were 16×16 pixels² and 75% respectively, resulting in spatial resolutions of 0.059 mm/vector and 0.18 mm/vector in near-field and far-field tests respectively. The PIV system and the discharge system were synchronized by a digital delay/pulse generator (Stanford Research Systems, Model DG535) working in phase-locked mode. The camera recording frequency was identical to the discharge frequency for all of the tested cases (50 Hz, 100 Hz or 200 Hz). The time delay between discharge ignition and camera recording (denoted as t , namely the phase), was adjusted within an accuracy of less than 1 μ s. To retrieve the entire jet evolution pertaining to a single discharge event, approximately 60 phases were selected, at which PIV measurements were obtained. The selected phases ranged from the incipient emanation of shock waves, im-

mediately after discharge initiation ($t = 50 \mu\text{s}$), to the complete termination of one cycle (i.e. $t = T_d = 1/f_d$). The full resolution of the cycle enabled the synthesis of statistically converged time-averaged flow fields of the PSJ. The time step between adjacent phases increased gradually from $25 \mu\text{s}$ to $1000 \mu\text{s}$ depending on the peak jet velocity observed.

Table 3.1: The test parameters for each case.

Case No.	V_1 (kV)	E_c (J)	f_d (Hz)	ϵ	f_d/f_h
Case 1	1.25	0.78	100	1.8	0.06
Case 2	1.77	1.56	100	3.6	0.06
Case 3	2.50	3.12	100	7.2	0.06
Case 4	1.77	1.56	50	3.6	0.03
Case 5	1.77	1.56	200	3.6	0.12

For each resolved phase, three PIV sequences were recorded. Each sequence contained successively the snapshots of the first 100 pulses after the PSJA was activated. Due to the frequency effect postulated in Sary et al. [55] and Zong et al. [16], several of the initial pulses of each sequence (less than 20) were working in the transient stage signified by an unstable actuator performance, while the remaining pulses lay in the quasi-steady stage where the jet intensity remained almost unchanged from pulse to pulse. Based on this consideration, only the last 70 pulses of each sequence were used to execute the phase-averaging operation, resulting in 210 realizations in total for each phase. Five cases with varied capacitor energy and discharge frequency were investigated, as shown in Table 3.1. In cases 1–3, the discharge frequency is kept constant while the energy deposition increases monotonically by a factor of four ($1.8 \rightarrow 7.2$). For cases 4, 2 and 5, the dimensionless frequency increases from 0.03 to 0.12 while the energy deposition is kept constant. An overview of the tested cases and pertinent actuation parameters is shown in table 1. It should be noted that the maximum frequency tested here (200 Hz, case 5) is actually limited by the characteristic time of the charging circuit ($\tau_d = 1$ ms, product of R_1 and C_1). A time interval of at least $4.67\tau_d$ is necessary to fully recover the energy-storing capacitor (criterion: capacitor voltage reaches 99% of the DC voltage), leading to a maximum reliable working frequency of 214 Hz.

The finite sample size, PIV peak locking errors, finite laser sheet thickness, discharge timing uncertainty and tracer particle lag are recognized as the five main sources of phase-locked PIV measurement uncertainty. Following the methods in Section 2.4.2, the peak relative errors of the phase-averaged axial velocity (U_x) incurred by the aforementioned five sources are estimated to be 3.1%, 1.5%, 2.1%, 2.5% and 3.5% respectively. The Euclidean sum of these five errors gives the total measurement uncertainty, which is less than 5.9% of the peak jet velocity (U_p).

3.4. PHASE-AVERAGED RESULTS

In Section 3.4.1, the time evolution of the phase-averaged velocity fields is analysed, and the high-speed jet, localized suction and front vortex ring are identified as the three major flow structures pertaining to the jet evolution. From Section 3.4.1 to 3.4.4, these three

major flow structures are characterized sequentially, and intercase comparison of the non-dimensional formation and evolution laws is carried out to extract the effect of non-dimensional energy deposition and frequency.

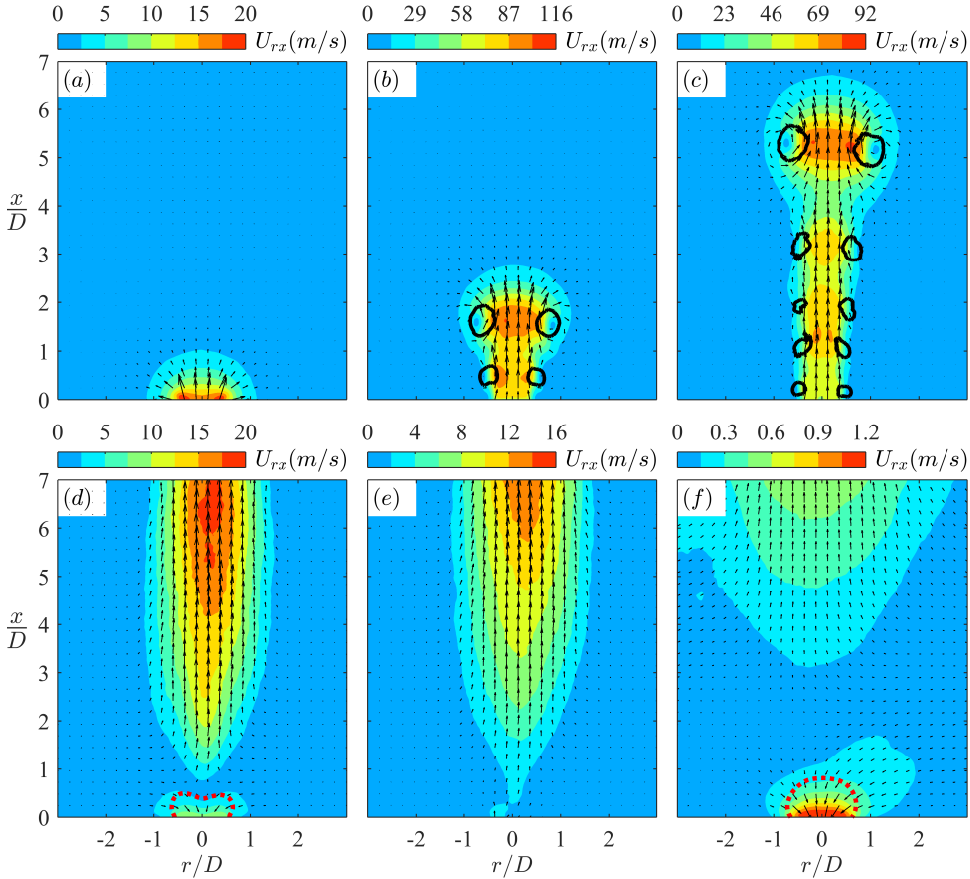


Figure 3.3: Phase-averaged velocity fields (small FOV) at increasing time delays for case 3 ($f_d = 100$ Hz): (a) $t = 50 \mu\text{s}$, $t/T_h = 0.08$; (b) $t = 150 \mu\text{s}$, $t/T_h = 0.25$; (c) $t = 300 \mu\text{s}$, $t/T_h = 0.49$; (d) $t = 700 \mu\text{s}$, $t/T_h = 1.15$; (e) $t = 900 \mu\text{s}$, $t/T_h = 1.48$; (f) $t = 9000 \mu\text{s}$, $t/T_h = 14.83$; The in-plane velocity is plotted as vectors and contours. The solid black lines in (b, c) indicate the vortices detected with the Q-criterion. The threshold values are selected as 10% of the maximum Q-values. The dashed red lines in (d) and (f) are contour lines of 50% of the peak suction velocity.

3.4.1. PHASE-AVERAGED VELOCITY FIELDS

Phase-averaged velocity fields at increasing time delays are shown in Figure 3.3 for case 3 and the small FOV. Here, U_{rx} denotes the Euclidean sum of the in-plane velocity components, $U_{rx} = (U_r^2 + U_x^2)^{1/2}$. At $t = 50 \mu\text{s}$, an incipient jet with relatively low exit velocity (< 20 m/s) is observed. The bow-shaped contour lines are footprints of the outward-propagating shock waves induced by the rapid arc discharge [82]. Subsequently, the jet

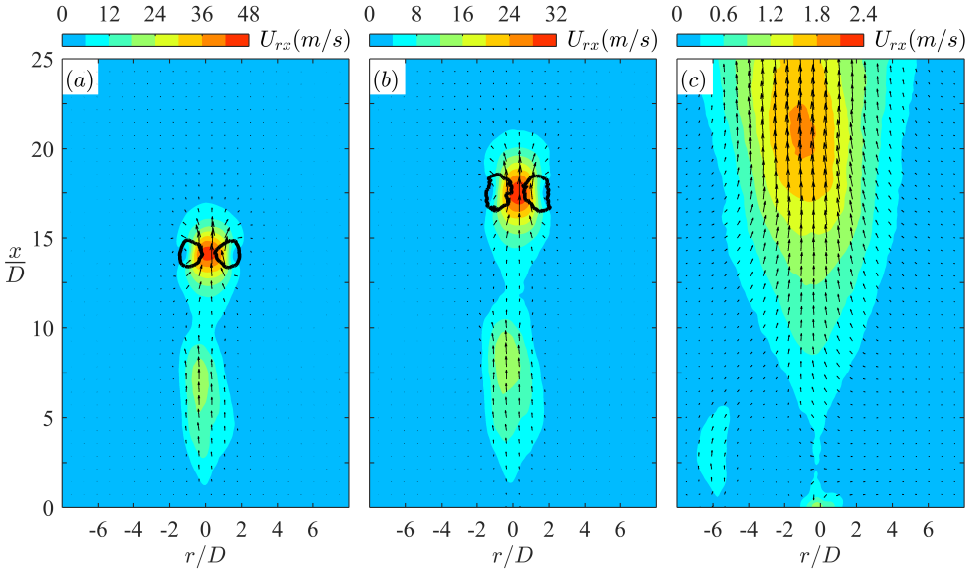


Figure 3.4: Phase-averaged velocity fields (large FOV) at increasing time delays for case 3 ($f_d = 100$ Hz). (a) $t = 700 \mu\text{s}$, $t/T_h = 1.15$; (b) $t = 900 \mu\text{s}$, $t/T_h = 1.48$; (c) $t = 9000 \mu\text{s}$, $t/T_h = 14.83$. The plotting methods are inherited from Figure 3.3.

forms and the circular shear layer rolls into a vortex ring, which always resides in the jet front during axial propagation. This front vortex ring (FVR) is essentially equivalent to the starting vortex ring in viscous pulsed jets [98]. Due to the self-induction effect, a velocity value as high as 116 m/s is registered at the centre of the FVR in Figure 3.3(b). The Reynolds number based on this velocity value and the orifice diameter (2 mm) is approximately 1.6×10^4 , indicating a fully turbulent regime for the front vortex ring. In addition, several shear-layer vortices along the body of the jet resulting from Kelvin–Helmholtz instability are prominent in Figure 3.3(b, c). The axial spacing of these vortices remains approximately constant at $1D$ during the propagation.

In Figure 3.3(d), the fluid near the exit orifice is ingested into the actuator cavity, indicating the presence of the refresh stage. The peak suction velocity is around 10 m/s, one order less than the corresponding peak jet velocity (Figure 3.3b). This feature differs significantly from the case of a piezoelectric synthetic jet actuator (SJA) where the velocity traces during the ejection and ingestion stages are roughly of the same order of magnitude [97]. At $t = 900 \mu\text{s}$, the suction phenomenon diminishes considerably, anticipating the emanation of a second jet stage. Multiple alternations between the jet and refresh stages are observed in one cycle, which differentiates the PSJA once again from the corresponding piezoelectric SJA, where only one alternation is observed per cycle. In Figure 3.3(f), it is striking to note that the suction flow persists until the launch of next cycle ($t = 9000 \mu\text{s}$).

Since the jet front in Figure 3.3(d–f) propagates out of the FOV, the velocity fields at these three phases are further illustrated in Figure 3.4 using the PIV measurements

within the larger FOV. The FVR can still be detected by the Q -criterion between $t = 700 \mu\text{s}$ and $t = 900 \mu\text{s}$, while other shear-layer vortices cease completely, possibly broken down during the propagation and filtered out by the phase-averaging operation [99]. Additionally, at these late stages of propagation, the FVR is pinched off from the jet body in figure 3.4(a, b), resulting in two separate high-velocity regions. This reconciles with schlieren observations pertaining to a case of comparable discharge energy in Zong et al. [32]. The ‘pinch-off’ is attributed to the rapidly declining jet exit velocity related to the short jet duration, which will be quantified later on in Section 3.4.2. The flow field at $t = 9000 \mu\text{s}$ is characterized by a diffused low-velocity region.

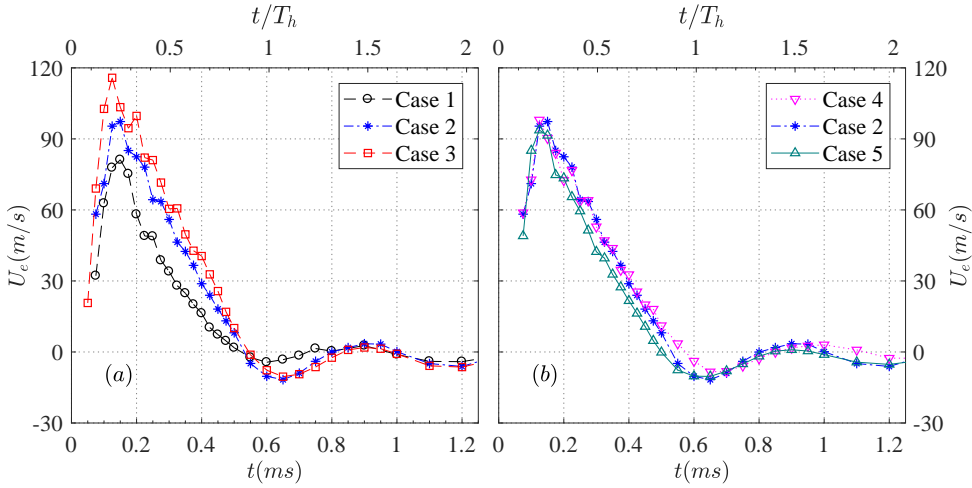


Figure 3.5: The time evolution of the jet exit velocity for $0 < t < 1.2$ ms: (a) influence of energy deposition and (b) influence of discharge frequency.

3.4.2. HIGH-SPEED JET

EXIT VELOCITY

To quantify the intensity of the pulsed jet, the exit velocity profiles at different time delays (namely $U_y(r, t|x = 0)$) are extracted from the phase-averaged flow fields. Subsequently, a spatially averaged exit velocity is estimated by integrating the exit velocity profile in the radial direction (see Equation 2.4). For the different tested cases, the temporal evolution of the spatially integrated exit velocity is shown in Figures 3.5 and 3.6. Overall, the qualitative trends between different curves are similar. Multiple jet and refresh stages are observed within one cycle. During the primary jet stage, the exit velocity initially shows a sharp increase and afterwards a slow linear drop. The peak value of the exit velocity (U_p) is reached between $t = 120 \mu\text{s}$ and $t = 150 \mu\text{s}$ for all cases. For constant repetition frequency (cases 1–3), U_p increases from 81 m/s to 116 m/s when the non-dimensional energy deposition ranges from 1.8 to 7.2 (Figure 3.5a). Additionally, the jet duration time remains approximately constant at $530 \mu\text{s}$. When the energy deposition is kept fixed at 2.61 and the dimensionless frequency is increased from 0.03 to 0.12 (cases 4, 2 and 5), the peak jet velocity remains approximately constant whereas the jet duration time drops

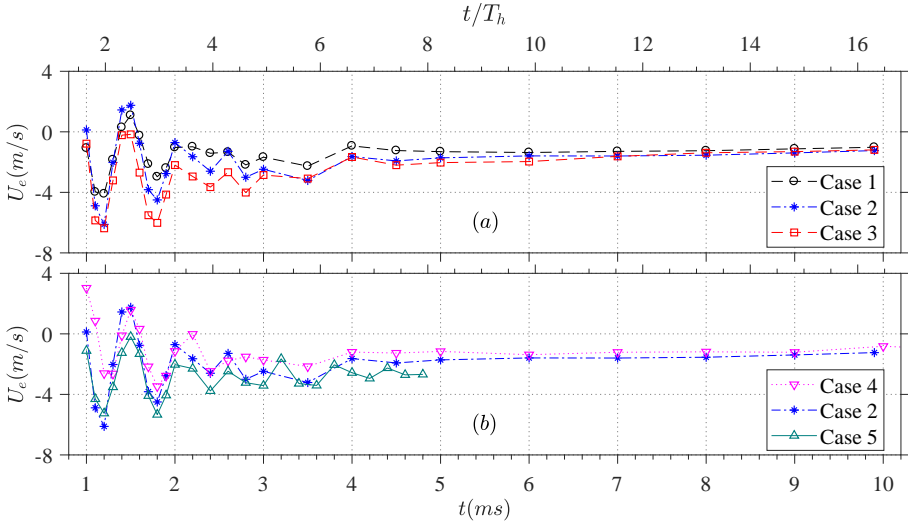


Figure 3.6: The time evolution of the jet exit velocity for $1 < t < 10$ ms: (a) influence of energy deposition and (b) influence of repetition rate.

slightly ($96 \text{ m/s} \rightarrow 85 \text{ m/s}$, $570 \mu\text{s}$ to $500 \mu\text{s}$). Based on these peak velocity values, the Reynolds number (Re_0) defined in Equation 3.4 can be computed as listed in Table 3.2. As a result, Re_0 ranges from 1.09×10^4 to 1.55×10^4 , indicating fully turbulent flow status for all of the tested cases. The peak jet velocity values obtained here are relatively lower than those reported in [15, 20], where U_p reaches more than 300 m/s . The distinction is mainly attributed to the different cavity volume (1696 mm^3 for the current study, in contrast to 23 mm^3 in [15] and 183 mm^3 in [20]).

The negative exit velocity observed after the primary jet stage signifies the onset of suction flow, pertinent to the refresh stage. With the exception of the low-energy case 1, the peak suction velocity for all of the tested cases is approximately 10 m/s . Multiple alternations between the jet and refresh stages are testified by the quasi-periodical oscillation of the exit velocity. The oscillation period is estimated to be approximately $600 \mu\text{s}$ and is largely insensitive to changes of f^* and ϵ . The corresponding oscillation frequency (1.67 kHz) agrees well with the predicted Helmholtz natural frequency ($f_h=1.65 \text{ kHz}$), indicating that the alternation between the jet and refresh stages is essentially an elastic process caused by the stiffness of the cavity gas. It should be noted that for a piezoelectric SJA, the ejection velocity tends to peak near f_h in the velocity–frequency spectrum [95]. However, operation to such high frequencies was beyond the capability of the discharge circuitry adopted in this study. The characteristics of PS-JAs at high discharge frequency (comparable to f_h) will be covered by Chapter 4.

During the later evolution of the exit velocity ($t > 1 \text{ ms}$), several distinctions should be made between the measured trace (Figure 3.6) and the theoretical traces predicted by Zong et al. [16] (Figure 11 in their paper). Small-amplitude periodic oscillations of the exit velocity after the primary jet stage are evident in these two traces. However, the oscillation in the measured trace is largely asymmetric, pivoting around a contin-

Table 3.2: Jet performance parameters pertaining to each case.

Case No.	U_p (m/s)	T_{jet} (μ s)	Re_0	L_e/D	L_s/D	ρ_e/ρ_0 (method 1)	ρ_e/ρ_0 (method 2)
Case 1	81.2	522	1.09×10^4	8.65	6.6	76.1 %	76.9-78.0 %
Case 2	97.3	531	1.31×10^4	12.5	9.3	74.3 %	75.6-77.1 %
Case 3	116	545	1.55×10^4	14.9	10.6	71.2 %	73.2-75.3 %
Case 4	98.0	574	1.32×10^4	12.6	10.4	82.7 %	84.0-85.6 %
Case 5	93.7	499	1.26×10^4	10.5	6.8	64.9 %	65.8-67.1 %

uously negative velocity. For all of the tested cases, the exit velocity after the third jet stage ($t > 1.6$ ms) never recovers back to positive values before the next pulse, indicating a longstanding refresh stage. The aforementioned phenomena are not predicted by the analytical model in [16] and can be traced to a cooling effect acting on the cavity. Specifically, the cavity temperature increases considerably during high-frequency and high-energy operation (1000 K in Sary et al. [55]; 500 K in Belinger et al. [25]). During the refresh stage, the high-temperature gas remaining in the actuator cavity will dissipate heat rapidly to the surrounding environment through heat convection and radiation. As a result of this constant-pressure heat dissipation, the residual gas experiences a reducing temperature and reducing specific volume, thus driving fresh air into the actuator cavity. This quasi-steady suction imposes a negative offset on the exit velocity trace, leading to an asymmetric oscillation as well as the longstanding refresh stage. On comparing the curves shown in Figure 3.6, it is evident that the averaged suction velocity increases with both the energy deposition and the working frequency.

EXIT DENSITY

Based on the time evolution of the jet exit velocity, the time-varying density of the exit fluid ($\rho_e(t)$) can be estimated with the analytical model shown in Section 2.4.1 [85]. Further, using the exit density and exit velocity, three crucial integral parameters including the expelled gas mass, jet impulse and jet mechanical energy can be derived to quantify the intensity of the pulsed jet. Nevertheless, the initial cavity density ρ_{ca0} has to be provided to initialize the model computation. Two methods are proposed here to estimate the initial cavity density, based on the principle of mass conservation in the actuator cavity, namely

$$\int_0^{T_d} \rho_e(t) U_e^+(t) A_e dt = \int_0^{T_d} \rho_0 U_e^-(t) A_e dt \quad (3.5)$$

where U_e^+ and U_e^- are the positive (ejection velocity) and negative (suction velocity) portions of U_e respectively, and ρ_0 and $\rho_e(t)$ represent the ambient (external) density and jet exit density respectively.

The first method relies on the assumptions of relatively low jet velocity ($Ma < 0.3$) and small expelled gas mass, which allow an approximation of the jet exit density with the initial cavity density as follows,

$$\left\{ \begin{array}{l} \rho_e(t) \approx \rho_{ca0} \\ \frac{\rho_{ca0}}{\rho_0} \approx \frac{\int_0^{T_0} U_e^-(t) dt}{\int_0^{T_0} U_e^+(t) dt} = \frac{L_s}{L_e} \end{array} \right. \quad (3.6)$$

The integrals of ejection velocity and suction velocity within one actuation cycle are denoted as L_e and L_s for simplification. It should be noted that L_s/D is essentially the non-dimensional stroke length, defined in Section 3.2.2. For the different tested cases, L_s and L_e , as well as the estimated initial cavity density during the steady working stage of repetitive operation (ρ_{ca0}), are listed in Table 3.2. As a result, L_s/D and L_e/D range from 6 to 15, increasing with energy deposition and decreasing with frequency.

The second method simulates the repetitive working process of the PSJA using a predictor–corrector approach based on Equations 3.7-3.11, which is more accurate, but complex, than the first method. During the jet stage, the upper and lower bounds of the exit density are approximated by Equations 3.7-3.9 proposed by Zong & Kotsonis [85]. This equation set is derived based on the governing equations during the jet stage, and subsonic throat flow is assumed. The term f_{UL} is introduced to simplify the expression and bears no physical meaning. During the refresh stage, the exit density is set as the ambient density Equation 3.10. Following the estimation of the exit density, the cavity density ($\rho_{ca}(t)$) is updated by Equation 3.11 based on mass conservation. Using these equations iteratively, the temporal evolution of the two bounds of $\rho_e(t)$ and $\rho_{ca}(t)$ in one cycle can be computed.

$$\rho_e(t) \geq \rho_{ca0} / [f_{UL}(t) \cdot \exp(\frac{A_e}{V_{ca}} \cdot \int_0^t U_e(t) dt)] \quad (3.7)$$

$$\rho_e(t) \leq \rho_{ca0} / \exp[\frac{A_e}{V_{ca}} \cdot \int_0^t \frac{U_e(t)}{f_{UL}(t)} dt] \quad (3.8)$$

$$f_{UL}(t) = [1 + \frac{\gamma - 1}{2\gamma RT_0} U_e^2(t)]^{1/(\gamma - 1)} \quad (3.9)$$

$$\rho_e(t) = \rho_0 \quad (3.10)$$

$$\rho_{ca}(t) = \rho_{ca0} - \int_0^t \rho_e(t) U_e(t) A_e dt / V_{ca} \quad (3.11)$$

To launch the simulation, the initial cavity density of the first cycle (ρ_{ca0}) is set as the ambient density (ρ_0). Since $L_s > L_e$, the quantity of ejected fluid is more than the quantity of fluid subsequently ingested. As a result, the gas in the cavity has not fully recovered to ambient conditions and the ultimate cavity density of the first cycle, $\rho_{ca}(T_d)$ ends up to be slightly lower than the ambient density. For the next cycle, ρ_{ca0} is initialized as $\rho_{ca}(T_d)$ and Equations 3.7-3.11 are solved iteratively again. The iterative simulation stops after a dynamic balance of cavity density is reached, namely $\rho_{ca}(T_d) = \rho_{ca0}$.

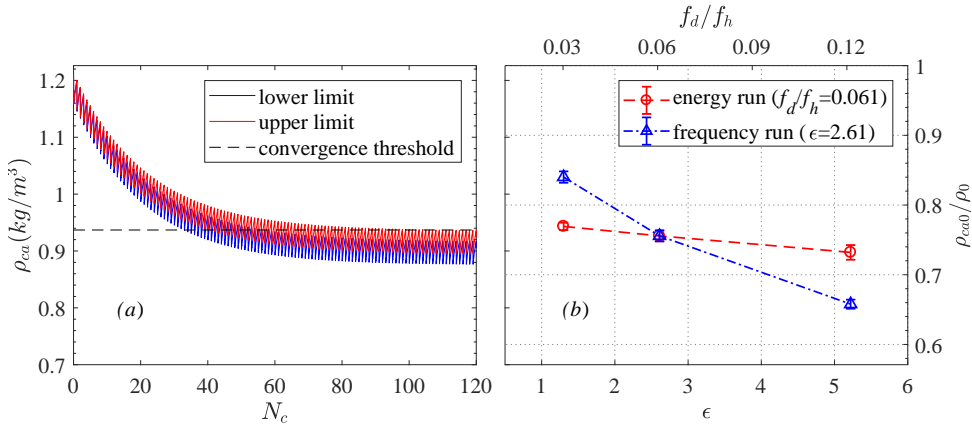


Figure 3.7: (a) Convergence of the two limits of cavity density within the first 120 iterations for case 2; N_c denotes the iteration number. (b) Converged steady-state cavity density for different cases.

Convergence traces of the two limits of ρ_{ca0} are shown in Figure 3.7(a). Approximately 109 iterations are needed to arrive at a converged cavity density (threshold: relative variation of ρ_{ca0} in adjacent iterations <0.0001). The bounding limits of ρ_{ca0} at steady working status (i.e. steady-state cavity density) are listed in table 2 and further illustrated in Figure 3.7(b). Overall, the steady-state cavity density values estimated by the two methods agree well with each other. The ratio of steady cavity density to ambient density drops with both non-dimensional energy deposition and frequency. The effect of frequency is more pronounced than that of energy deposition. For case 5, the steady cavity density remains only 71% of the ambient density. It should be noted that the range of f^* investigated in this paper is still limited to 0.12. For the cases of dimensionless frequency close to 1 as adopted by Narayanaswamy et al. in [15] and Zong et al. in [32], the cavity density is expected to be even lower.

Steady-stage variations of the cavity density are shown in Figure 3.8 for all of the tested cases. It should be noted that the initial cavity density values are subtracted to facilitate intercase comparison. The cavity density drops sharply in the primary jet stage and rises almost linearly in the longstanding refresh stage. The expelled gas mass increases with the energy deposition whereas it decreases with the actuation frequency. The rising rate of the cavity density during the refresh stage increases with both the energy deposition and the actuation frequency, which corroborates the observed variation of the mean suction velocity shown in Figure 3.6.

MASS FLOW, IMPULSE AND JET MECHANICAL ENERGY

The combination of the estimated exit density and the directly measured exit velocity gives access to the cumulative mass flow (M_{ce}), cumulative impulse (I_{cp}) and cumulative jet mechanical energy (E_{cm}), defined as follows:

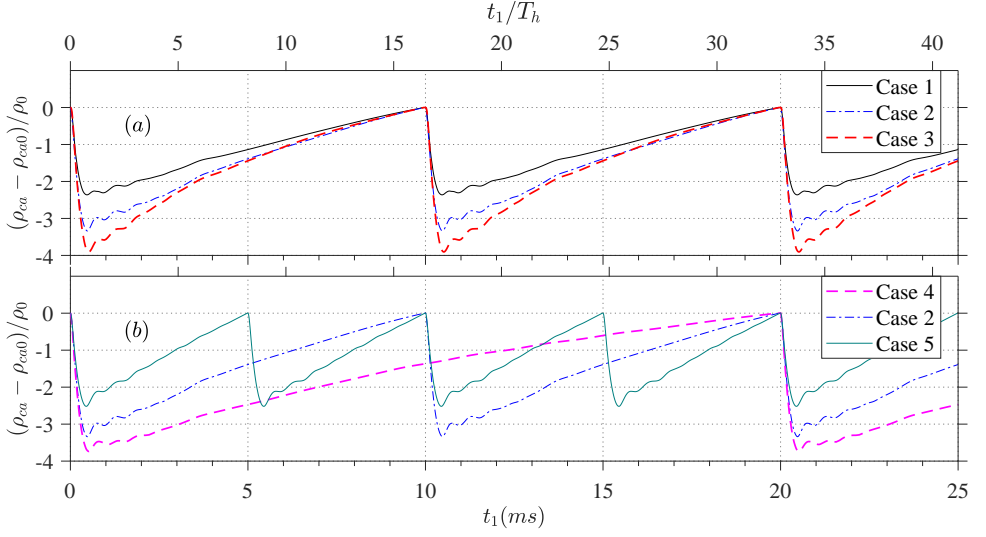


Figure 3.8: Steady-stage variation of the relative cavity density, $(\rho_{ca} - \rho_{ca0})/\rho_0$: (a) effect of energy deposition and (b) effect of actuation frequency.

$$\left\{ \begin{array}{l} M_{ce}(t_0) = \int_0^{t_0} \rho_e(t) U_e(t) A_e dt \\ I_{cp}(t_0) = \int_0^{t_0} \rho_e(t) U_e(t) |U_e(t)| A_e dt \\ E_{cm}(t_0) = \int_0^{t_0} 0.5 \rho_e(t) U_e^2(t) |U_e(t)| A_e dt \end{array} \right. \quad (3.12)$$

Prior to further analysis, it is necessary here to distinguish the above three time-dependent parameters with the three integral parameters defined in Equation 2.8 (Section 2.4.1). The two sets are associated as follows:

$$\left\{ \begin{array}{l} M_e = M_{ce}(T_{jet}) \\ I_p = I_{cp}(T_d) \\ E_m = E_{cm}(T_d) \end{array} \right. \quad (3.13)$$

Using these three integral parameters (M_e , I_p and E_m) to normalize the three cumulative parameters (M_{ce} , I_{cp} and E_{cm}), three non-dimensional parameters (\bar{M}_{ce} , \bar{I}_{cp} and \bar{E}_{cm}) can be obtained. For case 2, the variation of \bar{M}_{ce} , \bar{I}_{cp} and \bar{E}_{cm} (symbolized as \bar{X}_{ci}) computed with the phase-averaged exit velocity and exit density within one actuation cycle is shown in Figure 3.9.

Although multiple jet stages are present in one cycle, the contributions of later jet stages to the three cumulative parameters are negligible. As expected, the net mass flux in one full period is zero. Based on the time division between the jet and refresh stages,

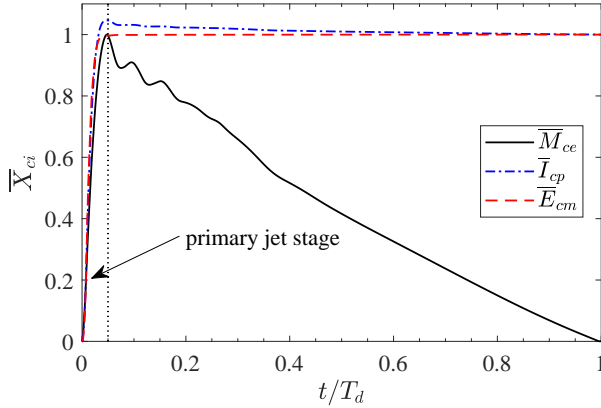


Figure 3.9: Variation of the three cumulative parameters (symbolized as \bar{X}_{ci}) within one actuation cycle at quasi-steady working status for case 2.

Table 3.3: Integral parameters pertaining to PSJs.

Case No.	$M_e/\rho_0 V_{ca}$ (%)	I_p ($\mu\text{N}\cdot\text{s}$)	I_p^* ($\times 0.1\%$)	F_p (mN)	E_m (μJ)	η_t ($\times 0.01\%$)
Case 1	2.33-2.40	2.52-2.61	1.40-1.45	0.25-0.26	82-85	1.05-1.09
Case 2	3.27-3.41	4.35-4.57	1.71-1.79	0.44-0.46	172-181	1.10-1.15
Case 3	3.79-4.02	5.88-6.29	1.63-1.74	0.59-0.63	269-288	0.86-0.92
Case 4	3.66-3.81	4.79-5.01	1.88-1.96	0.24-0.25	179-188	1.14-1.20
Case 5	2.47-2.57	3.09-3.24	1.21-1.27	0.62-0.65	121-126	0.77-0.81

the mean mass flow rate during the jet stage is estimated to be 19 times higher than the corresponding mass flow rate during the suction stage. This unique feature (rapid ejection + slow ingestion) enables the production of net impulse, which is the essential enabler for flight control [54]. The cumulative impulse peaks at the end of the primary jet stage. During the later evolution, a small portion (e.g. 5.1% for case 2) of the previously produced impulse is counteracted by the inevitable suction flow. If the overall impulse is computed from $I_{cp}(T_{jet})$, the net impulse produced by the PSJA will be slightly over-estimated [85]. Additionally, the overwhelming majority of mechanical energy (99.6 %) is produced during the primary jet stage. As such, the mechanical energy brought upon by suction flow can be neglected.

The estimated expelled gas mass ($M_e/\rho_0 V_{ca}$), net impulse (I_p) and issued mechanical energy (E_m) are listed in table 3.3 for all tested cases. A 4 times increase of energy deposition results in 1.6, 2.4 and 3.3 times increases in expelled gas mass, jet impulse and jet mechanical energy respectively. This is largely expected. A simplified theoretical analysis is performed to support the interpretation of these trends. Assuming that the non-dimensional expelled gas mass is relatively small (less than 4% in the current study), the jet exit density (ρ_e) can be approximated by the steady cavity density (ρ_{ca0}),

leading to a simplified expression for M_e as follows:

$$M_e \approx \rho_{ca0} \int_0^{T_{jet}} U_e(t) A_e dt \quad (3.14)$$

Further, if the temporal evolution of the exit velocity during the primary jet stage is self-similar (as evident in Figure 3.5), $U_e(t)$ can be written universally as $U_e(t) = U_p \cdot f(t/T_{jet})$, where f is the normalized exit velocity evolution. By substituting this relation into Equation 3.14, Equation 3.15 can be obtained. A similar analysis can also be performed on the expelled gas mass and jet impulse. The respective results are shown in Equations 3.16 and 3.17.

$$M_e \approx \rho_{ca0} T_{jet} U_p A_e \int_0^1 f(s) ds \quad (3.15)$$

$$I_p \approx \rho_{ca0} T_{jet} U_p^2 A_e \int_0^1 f^2(s) ds \quad (3.16)$$

$$E_m \approx 0.5 \rho_{ca0} T_{jet} U_p^3 A_e \int_0^1 f^3(s) ds \quad (3.17)$$

For the cases pertaining to the present study as well as the cases in Zong & Kotsonis [85], the integral of increasing exponents of $f(s)$ is largely invariant (relative deviation <5 %). Thus, the exit velocity temporal evolution shape plays a negligible role in Equations 3.15-3.17. For a fixed cavity geometry, the three integral parameters are positively proportional to the steady cavity density, jet duration time and increasing exponents of peak jet velocity.

By combining Equation 3.17 with Equation 3.1, the relation between the peak jet velocity and the energy deposition can be derived,

$$\epsilon \approx A_0 \frac{\rho_{ca0} T_{jet} U_p^3}{\eta_t} \quad (3.18)$$

where A_0 is a constant depending on the actuator geometry and total efficiency.

For cases 1–3, T_{jet} remains almost constant and ρ_{ca0} changes by less than 7%. Assuming small variations in the total efficiency (0.009–0.011 %, see Table 3.3), the peak jet velocity will increase with the cubic root of the energy deposition as follows:

$$U_p \propto \epsilon^{1/3} \quad (3.19)$$

While subject to several approximations, the simplified model proposed in Equation 3.19 reconciles favourably with the observed trends. A 4 times increase of energy deposition will bring a theoretical increase of 1.6 times in U_p , which roughly agrees with the experimental observation (81 m/s \rightarrow 116 m/s, 1.4 times). On propagating the energy deposition increment (1.6 times) to the pertinent performance parameters, the predicted growths of M_e , I_p and E_m are 1.6, 2.5 and 4 times respectively, which are consistent with

experimental data (1.7, 2.4 and 3.3 times respectively). The peak estimation error is approximately 20 % and can be attributed to the constant efficiency assumption. A significant outcome of the above analysis is the confirmation that significant improvement of jet intensity with energy deposition is mainly contributed by the peak jet velocity.

In contrast to energy deposition, a 4 times increase of actuation frequency leads to drops of 33%, 36% and 33% respectively for M_e , I_p and E_m . The reductions for the three integral parameters are almost identical since the peak jet velocity is effectively the same in cases 4, 2 and 5 (see Table 3.2). As indicated by Equations 3.15-3.17, the performance decay with increasing frequency is mainly related to the reduced cavity density (22%) and the shortened jet duration time (13%). Of these two factors, the reduced cavity density plays a dominant role.

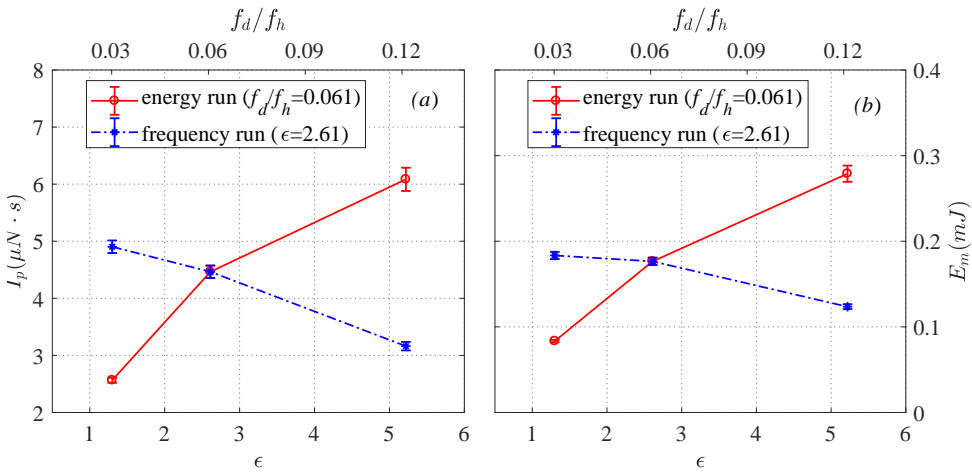


Figure 3.10: Variation of (a) net impulse and (b) issued mechanical energy with non-dimensional energy deposition (ϵ) and frequency (f^*).

Finally, the variation of I_p and E_m with non-dimensional energy deposition and frequency is shown in Figure 3.10. For the tested cases, I_p changes between 2–6 mN-s. The product of I_p and the discharge frequency f_d gives the time-averaged net thrust produced by the PSJA (denoted as F_p). As listed in Table 3.3, F_p is of the order of 0.1 mN and positively proportional to both the energy deposition and the frequency. The issued mechanical energy E_m is of the order of 0.1 mJ and the peak value observed is 0.246 mJ. The net impulse I_p and issued mechanical energy E_m can be further normalized to deduce another two dimensionless parameters, I_p^* and η_t respectively (see Section 2.4.1 for their definition). As listed in Table 3.3, both I_p^* and η_t reduce with the actuation frequency. However, no obvious trends are found in the energy deposition run. The distinction is caused by the different definitions. Specifically, the efficiency considered here incorporates not only the electro-mechanical efficiency but also the discharge efficiency, which drops with increasing capacitor voltage [34, 43].

3.4.3. LOCALIZED SUCTION

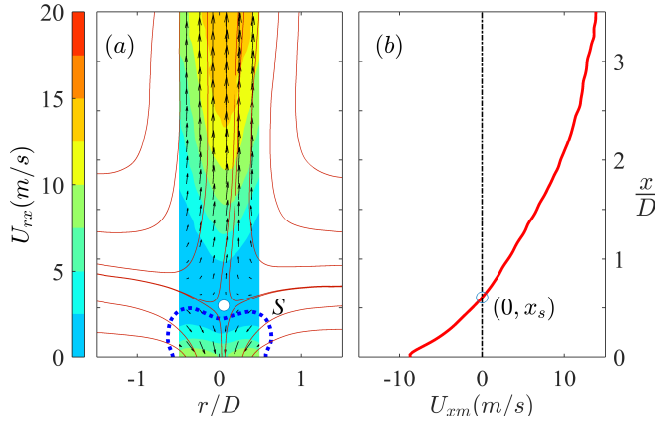


Figure 3.11: Extraction of the suction affected length. (a) The near-exit flow pattern at $t = 700 \mu\text{s}$ for case 3. The contour levels and vectors are based on the phase-averaged velocity; the red lines denote streamlines; the dashed blue line denotes the contour line of 50% of the peak suction velocity. (b) Axial variation of U_x , spatially averaged along the r direction in the range $-0.5 < x/D < 0.5$ (denoted as U_{xm}). The white points indicate the saddle points.

In the following discussion, the suction effect during the refresh stage is further analysed. The flow-field topology in the vicinity of the jet exit is shown in Figure 3.11 for case 3. The data correspond to the phase-averaged PIV measurements at $t = 700 \mu\text{s}$. As a result of the concurrent jet expulsion from the completed jet stage and the ongoing suction from the refresh stage, a saddle point is observed at approximately $x/D = 0.5$, separating the suction flow from the residual jet flow. The x -coordinate of this saddle point gives a first-order approximation of the axial range that is affected by the suction flow (defined as the suction affected length x_s). To facilitate a more accurate computation of x_s , the phase-averaged velocity field in the range $-0.5 < x/D < 0.5$ is extracted and the spatially averaged jet velocity along the radial (r) direction (defined as U_{xm}) is computed as shown in Figure 3.11(b). The suction affected length can be approximated by the intersection of U_{xm} with zero.

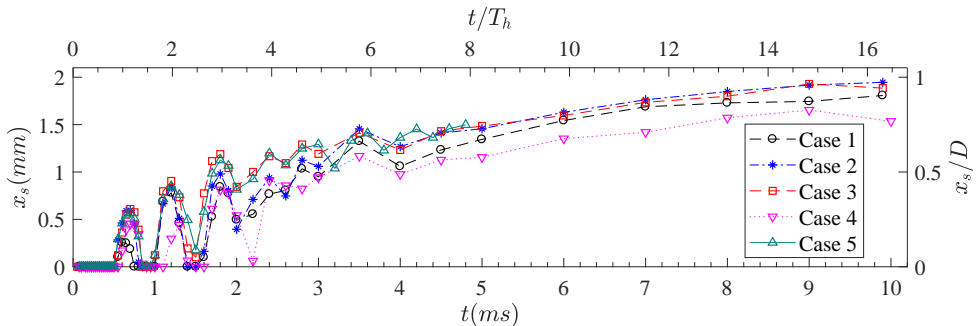


Figure 3.12: The temporal evolution of x_s for all tested cases.

The temporal evolution of the suction affected length (x_s) is shown in Figure 3.12 for all of the tested cases. By definition, a zero value for x_s corresponds to the jet stages. Between $t = 0$ and $t = 2$ ms, the suction affected length experiences considerable oscillations as a consequence of the multiple alternations between the jet and refresh stages. The oscillation period is close to the Helmholtz oscillation period (T_h). Notwithstanding the oscillation, the jet affected length for all of the tested cases increases slowly with time. Similarly to the time-averaged suction velocity, the jet affected length is positively proportional to both the energy deposition and the working frequency. For all of the tested cases, the peak value of x_s lies between $0.8D$ and $1D$, which is significantly smaller than that of piezoelectric synthetic jets [8]. According to the vortex ring propagation distance shown in Figure 3.4, the jet affected length is determined to be $20D$, approximately 20 times the suction affected length. To summarize, the suction flow induced by a PSJA exhibits three unique features, namely a relatively low suction velocity ($O(10$ m/s)), a localized affected region (up to $x = 1D$) and a rather long duration (to compensate the low suction velocity to maintain mass flow conservation).

3.4.4. FRONT VORTEX RING

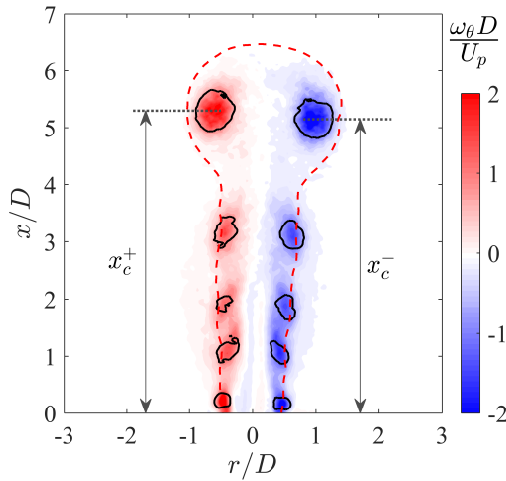


Figure 3.13: Representative vorticity field at $t = 300 \mu\text{s}$ for case 3. The solid black lines indicate the vortices detected by the Q -criterion, using a threshold value of 5% of the maximum Q -value; the red dashed line is the constant velocity contour line of $U_{rx}=20$ m/s; the x -coordinates of the two centres of the positive and negative vortices are denoted as x_c^+ and x_c^- respectively.

A representative vorticity field at $t = 300 \mu\text{s}$ is shown in Figure 3.13. As the velocity gradient in the jet shear layer scales with the ratio of the peak jet velocity (U_p) to the orifice diameter (D), the dimensionless vorticity can be defined as $\omega_\theta U_p / D$, similar to the definition of Gharib, Rambod & Shariff in [100]. The profile of the jet body is indicated by the red dashed line. The Q -criterion is used to detect the vortices, using a threshold value of 5% of the maximum Q -value. The propagation distance (x_c), diameter (D_v) and circulation (Γ) of the FVR are computed, following the procedure proposed by Zong & Kotsonis [40]. Here, x_c is given by the mean x -coordinate of the FVR, namely $(x_c^+ + x_c^-)/2$.

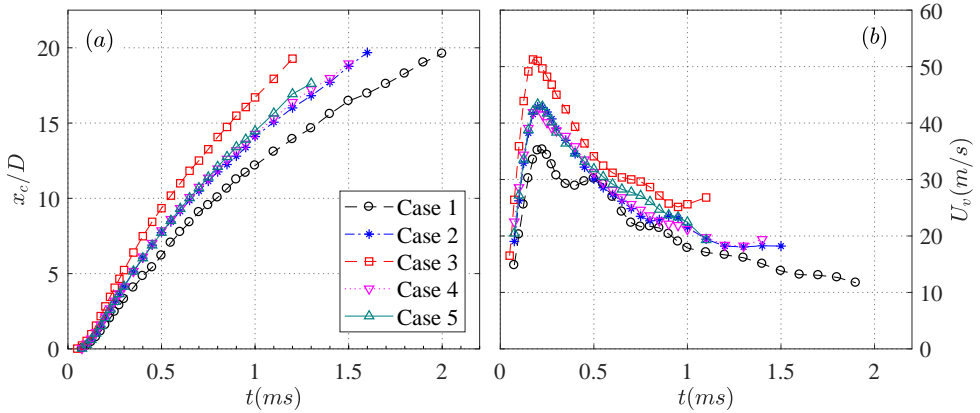


Figure 3.14: (a) Propagation distance and (b) propagation velocity of the FVR.

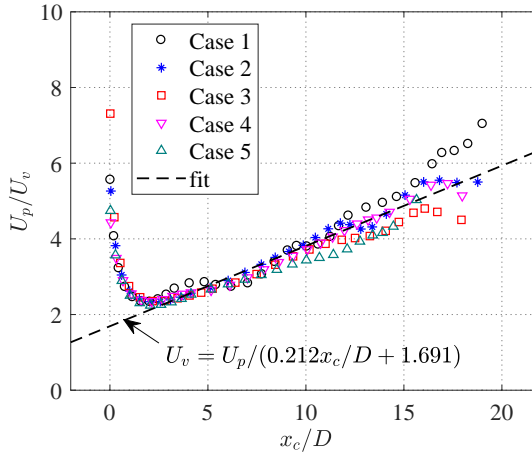


Figure 3.15: Normalized FVR propagation velocity with propagation distance.

The temporal evolution of x_c within one cycle is shown in Figure 3.14(a) for the tested cases. It is interesting to note that the trajectories of x_c are effectively independent of the actuation frequency. In contrast, the FVR lifts considerably faster with increasing energy deposition. The first-order temporal derivative of x_c gives the propagation velocity of the FVR (U_v), as shown in Figure 3.14(b). The propagation velocity U_v increases sharply during the primary jet stage, while it decreases mildly during later stages. The peak FVR propagation velocity is reached at approximately $t = 200 \mu\text{s}$, increasing from 35 m/s to 51 m/s with the energy deposition (cases 1–3) and remaining unchanged with the actuation frequency. The increase of U_v is related to the accelerated expulsion of cavity gas (see Figure 3.5), which continuously injects high-momentum flow into the vortex ring centre. The decay of U_v is ascribed to the decrease of momentum input, as well as the

entrainment of low-energy fluids by the FVR itself. The dependence of U_v on ϵ and f_d bears significant similarity to that of the peak jet velocity (Figure 3.5), motivating the utilization of U_p to normalize U_v .

The ratio of the peak jet velocity to the FVR velocity (U_p/U_v) is plotted against x_c in Figure 3.15 for all cases. As a result, all of the data points collapse onto the same curve. Two distinct regimes can be identified. In the vicinity of the exit ($x_c/D < 2$), the curve drops rapidly. However, once the FVR propagates further, the ratio is approximately linear. A linear regression model is used to fit the data after $x_c/D > 2$, resulting in a mean relative error of less than 6%. The minimum value of U_p/U_v reached at $x_c/D = 2$ is approximately 2.3. At this location, the peak propagation velocity of the FVR is roughly half of the peak jet velocity.

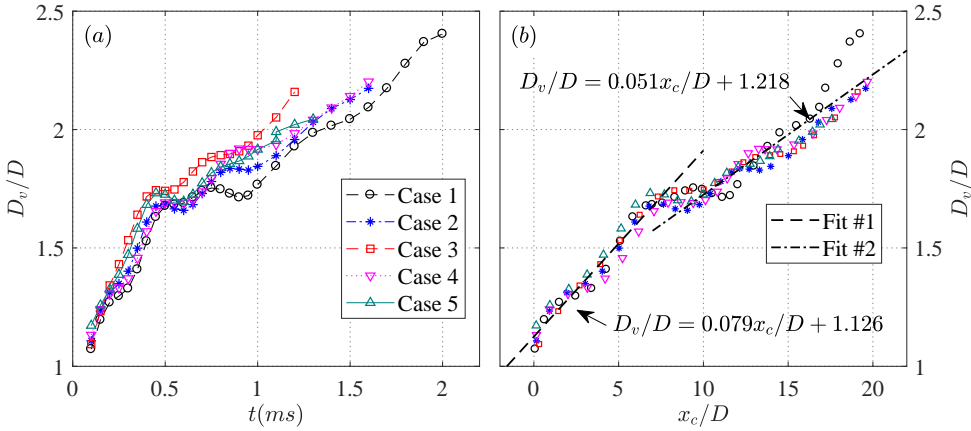


Figure 3.16: (a) The time evolution of the normalized vortex ring diameter. (b) The normalized vortex ring diameter versus the propagation distance.

Zong & Kotsonis [82] observed the high-velocity region in the vortex ring centre and further demonstrated that the acceleration of the jet exit velocity acts like an impulse, promoting the formation of vortex rings. As such, the peak velocity in the vortex ring centre (denoted as U_{cen} ; it should be noted that this is different from the propagation velocity) should be close to the peak jet velocity (U_p). Assuming that a constant spatial velocity gradient (uniform vorticity) is exhibited in the vortex core region, U_v should lie in between the vortex ring centre velocity (U_{cen}) and the outer periphery velocity (U_{out}). Since U_{out} is a negligible negative value for incipient jets, as shown in Figure 3.3(b), $U_v \approx U_p/2$. This relation was also confirmed by Zong & Kotsonis in [101] and can assist schlieren analysis to some extent. Specifically, the jet velocity obtained from schlieren imaging is typically based on the motion track of either the warm jet plume or the front vortex ring [22, 50]. This method severely underestimates the actual peak jet velocity by a factor of up to 2, further confirming the above identified behaviour.

The spacing between the two vortex centres along the radial direction shown in Figure 3.13 defines the vortex ring diameter (D_v). The time evolution of D_v/D is shown in Figure 3.16(a). Apart from several small-scale oscillations, the vortex ring diameter in-

increases steadily during propagation within one cycle. For each curve, a kink point can be observed between $t = 0.4$ ms and $t = 0.5$ ms, where the rising rate of D_v (namely the slope) declines considerably. This variation can be ascribed to the different entrainment rate of the FVR. Specifically, the high-speed jet body beneath the FVR acts as an ‘injector’. When the jet velocity is higher than U_v , the high-momentum fluid can be fed into the FVR rapidly, leading to a fast expansion of the vortex ring diameter. However, once the jet velocity drops below U_v , no external momentum input will be experienced by the FVR. As a result of this reduced entrainment rate, the expansion rate of the FVR is reduced. The time evolution of D_v shown here differs considerably from that in traditional synthetic jets, where the initial increase is followed by a slow decrease [97]. Inter-case comparison indicates that the rising rate of D_v increases with ϵ whereas it remains largely unchanged with f^* .

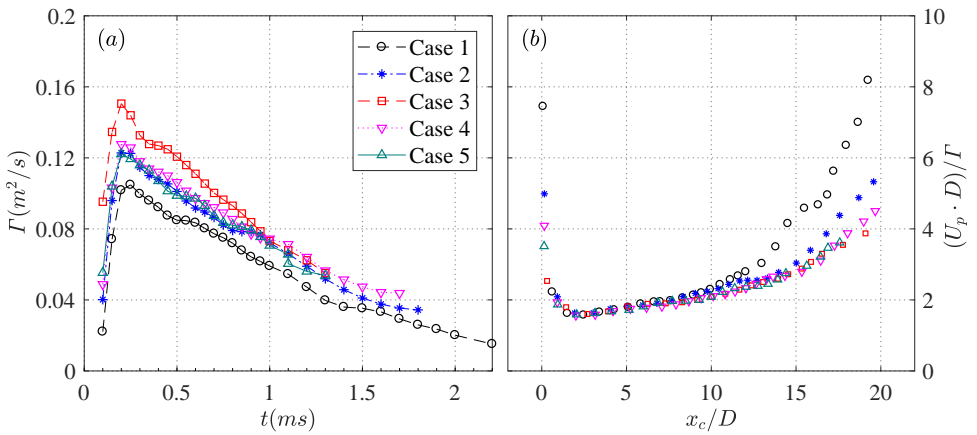


Figure 3.17: (a) The variation of the vortex ring circulation with time. (b) The variation of the normalized vortex ring circulation with the non-dimensional propagation distance.

In Figure 3.16(b), an evident collapse is obtained when D_v/D is plotted against the propagation distance. This is largely expected since the low-velocity vortex ring has a longer time to build up in size before reaching the same propagation distance, which compensates its slow expansion rate. The kink point observed in Figure 3.16(a) collapses at approximately $x_c/D = 8$, corresponding to a non-dimensional vortex ring diameter of 1.7. It should be noted that in [82], the kink point was not observed in the range of $x_c/D < 12$. The distinction can be ascribed to the different jet duration time (1.1 ms in [82], as opposed to 0.5 ms in the present study). Considering the two identified regimes ($x_c/D < 7$ and $x_c/D > 9$), two linear equations can be fitted, as shown in Figure 3.16(b). The slopes of these two fitting lines differ by a factor of 1.5, further confirming that different dynamics of the FVR growth are in play, depending on the status of the high-speed jet ‘injector’ lying beneath.

Figure 3.17(a) shows the time evolution of the vortex ring circulation. Within one cycle, the circulation goes up sharply during the primary jet stage $t < 0.2$ ms, while diminishing slowly at later times, ostensibly in a linear way. The peak circulation attained

at approximately $t = 0.2$ ms is unaffected by the actuation frequency and increases with the energy deposition, resembling the behaviour of the peak propagation velocity. This is largely expected. Based on vortex dynamics, the vortex ring propagation velocity is positively proportional to the ratio of the circulation to the diameter, Γ/D_v [102]. The vortex ring diameter at $t = 0.2$ ms is approximately constant for all of the tested cases (Figure 3.17a). As a consequence, the variation of the peak circulation with ϵ and f_d follows the peak propagation velocity closely.

As the circulation is expected to increase with the vorticity (in turn scaling with U_p/D) and the square of the vortex ring diameter (D^2), it is instructive to normalize the circulation by $U_p D$ [100, 103]. As shown in Figure 3.17(b), the ensemble of tested cases shows an excellent agreement in the range $x_c/D < 10$, but diverges afterwards. The peak value of Γ residing at approximately $x_c/D = 2$ is approximately $0.62U_p D$ for all cases. Assuming that the diameter of the vortex core region (D) and the vorticity (U_p/D) are uniformly distributed in the vortex core region, a peak circulation of $(\pi D^2/4) \times (U_p/D) = 0.79U_p D$ can be computed, which is a rather good estimation of the experimental value.

In the study of Gharib et al. [100], the maximum circulation of FVRs is attained universally at a ‘formation number’ of 3.6–4.5. The definition of ‘formation number’ is essentially the integral of the time-varying exit velocity. For the incipient jet of the present study, the exit velocity is roughly double the vortex ring propagation velocity (Figures 3.5 and 3.15). Thus, a ‘formation number’ of 3.6–4.5 corresponds to a non-dimensional propagation distance of 1.8–2.3, which agrees excellently with the present data (approximately $x/D = 2$; see Figure 3.17b). Similar results were also reported by Chang & Vakili in [104], where the vortex ring was not fully formed until $x = 3D$.

3.5. TIME-AVERAGED RESULTS

The PSJ is widely characterized in phase-averaged flow fields [20, 82]. Nevertheless, significantly fewer studies have focused on the time-averaged flow fields of the PSJ. The time-averaging metrics including the centreline velocity decay, the jet spreading rate and the jet entrainment rate are crucial to evaluate the mean mixing and penetration ability of the PSJ, and need to be extracted and compared with both steady jets and piezoelectric SJAs. The following discussion applies these principles to the tested cases.

3.5.1. TIME-AVERAGED VELOCITY FIELDS

The time-averaged velocity field for each case (denoted as $\overline{U}(x, y, z)$) can be computed by summing up the phase-averaged velocity fields $U(x, y, z, t)$, as has been shown in Equation 2.16 (Section 2.4.3). As the time-averaged velocity is expected to increase with both the stroke length and the repetition rate, a non-dimensional velocity can be defined as $\overline{U}_x/(L_s f_d)$. For the five different tested cases, the time-averaged velocity fields are shown in Figure 3.18. As is evident, the time-averaged flow organization of the PSJ has considerable similarity to that of steady jets and conventional (mechanically operated) synthetic jets [105, 106]. During the axial propagation, the jet expands as a result of entrainment. In contrast to steady jets, no potential core region is observed. The high-velocity region produced by the PSJ lies approximately in the range $2D < x < 10D$, instead of just above the exit. The peak values of the time-averaged velocity are approximately 1.2–1.6

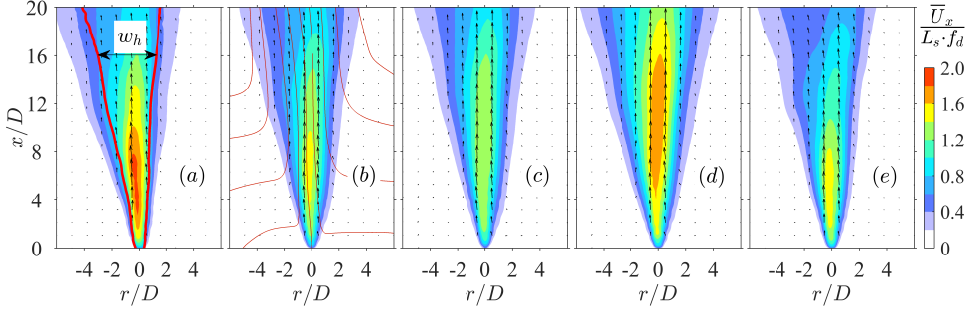


Figure 3.18: Time-averaged flow fields for cases 1–5 (a–e). The velocity vector field is indicated by arrows; the normalized axial velocity $\bar{U}_x/(L_s f_d)$ is displayed as coloured contours; the red lines in (a) pertain to the left and right bounds of the jet, determined by 50% of the peak jet velocity at each axial position; the thin red lines in (b) denote streamlines.

times of $L_s f_d$. The jet flow for all cases is not symmetric, leaning slightly to one side. This asymmetry was also observed by Zong & Kotsonis [82] and can be attributed to the non-uniform arc heating within the cavity. Specifically, due to the high electric field experienced locally, the near-cathode region produces more heat than other regions in the electrode gap, leading to higher gas pressure [107, 108]. Affected by this asymmetric pressure distribution, the jet is issued from the exit orifice at a small inclination. The angle is estimated to be approximately 2° and is largely inconsequential to the outcomes of the present study.

Several velocity profiles at increasing axial distance from the jet exit are extracted and shown in Figure 3.19(a) for case 2. Traces of suction flow (negative velocity) can only be observed at $x/D = 1$. The asymmetry in velocity profiles is imperceptible for locations below $x/D = 5$, but significantly pronounced after $x/D = 10$. Based on these velocity profiles, the peak velocity (\bar{U}_c) and the full width at which the jet velocity falls to 50% of the centreline velocity (w_h) can be computed. For the sake of consistency with previous literature, \bar{U}_c will be termed as the centreline velocity hereafter although it does not always occur in the nominal centre of the jet. A detailed definition of w_h is sketched in Figure 3.18(a). When \bar{U}_c and w_h are used to normalize the velocity profiles, a fairly universal collapse is obtained between $x/D = 2$ and $x/D = 20$, as shown in Figure 3.19(b). The normalized velocity profile agrees well with the profile from steady turbulent jets [105], and thus can be approximated by $\bar{U}_x/\bar{U}_c = 1/(1 + B_0(r - r_0)^2/w_h^2)^2$, where B_0 is a constant [109]. Nevertheless, it must be stressed that the similarity in velocity profiles does not indicate that the time-averaged flow of the PSJ is momentum-preserving, since the FVR dissipates a considerable proportion of kinetic energy during its axial propagation.

3.5.2. CENTRELINE VELOCITY AND JET WIDTH

The axial variation of \bar{U}_c in linear coordinates is shown in Figure 3.20(a). As expected, the centreline jet velocity is positively proportional to both the actuation frequency and the capacitor energy. Departing from the typical behaviour of incompressible ZNMF jets, the time-averaged velocity at the jet exit ($x/D = 0$) is non-zero [10, 106]. For the tested cases, \bar{U}_c ranges from 0.5 m/s to 6 m/s, which is one order of magnitude less

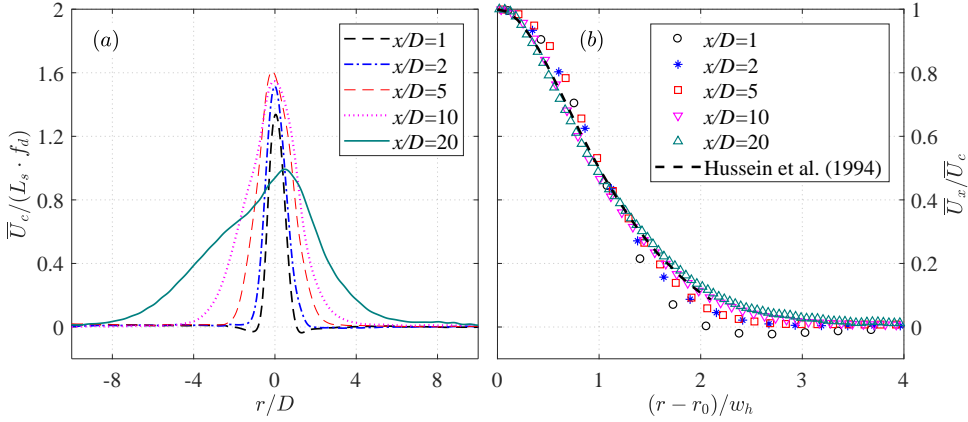


Figure 3.19: (a) Normalized time-averaged jet velocity profiles at different axial positions for case 2. (b) Comparison of normalized velocity profiles between the PSJ of the present study and steady jets (Hussein et al. 1994, [105]). Here, r_0 represents the radial coordinate of the velocity peak.

than U_p due to the low jet duty cycle (D_c , 0.01–0.1 for all of the tested cases). In linear coordinates, all cases show an initial sharp increase in the region of $x/D < 2$ and an ultimate slow decrease in the region of $x/D > 15$. The shape of these curves remains largely invariant with increasing energy (cases 1–3) but differs with frequency (cases 4, 2 and 5). Specifically, for case 4 ($f_d=50$ Hz), a plateau is observed between $x/D=2$ and $x/D=15$, where \bar{U}_c exceeds 80% of its maximum. The peak value of U_c is reached at $x/D=9$. As a result of increasing frequency ($f_d=200$ Hz, case 4), the plateau shrinks to $2 < x/D < 8$ and the peak position of U_c moves close to the exit ($x/D=2$).

The non-dimensional centreline velocity is normalized by $L_s f_d$ and plotted in semilogarithmic coordinates in Figure 3.20(b). As a result, two linear regimes can be identified on each curve, following results from piezoelectric synthetic jets [10]. The first linear regime ($x < 2D$) is related to the weakened influence of suction flow and collapses reasonably for the different investigated cases. The second linear regime corresponds to the fast momentum dissipation in the far field ($x/D > 15$) attributed to the detachment of vortex rings from the high-speed jet body as a result of relatively short jet duration (see Section 3.4.2). The second linear segment collapses for varying capacitor energy. However, at increasing frequency, a rapid decay of the centreline velocity is exhibited. The peak values of $\bar{U}_c / (L_s f_d)$ are 1.6 and 1.5 for cases 1 and 4 respectively (relatively weak suction) and 1.2 for the rest of the cases.

Figure 3.21(a) shows the axial variation of the jet width (w_h) in linear coordinates. As is evident, the jet width increases linearly and remains independent of the actuation frequency and capacitor energy. This monotonic variation is similar to that observed in turbulent jets, but differs from the respective width evolution in piezoelectric synthetic jets, since no local minimum is observed [97, 105]. A linear regression model is used to fit the data sets in Figure 3.21(a). Half of the slope of this linear equation defines the mean jet spreading rate of the PSJ (approximately 0.13), which is higher than the

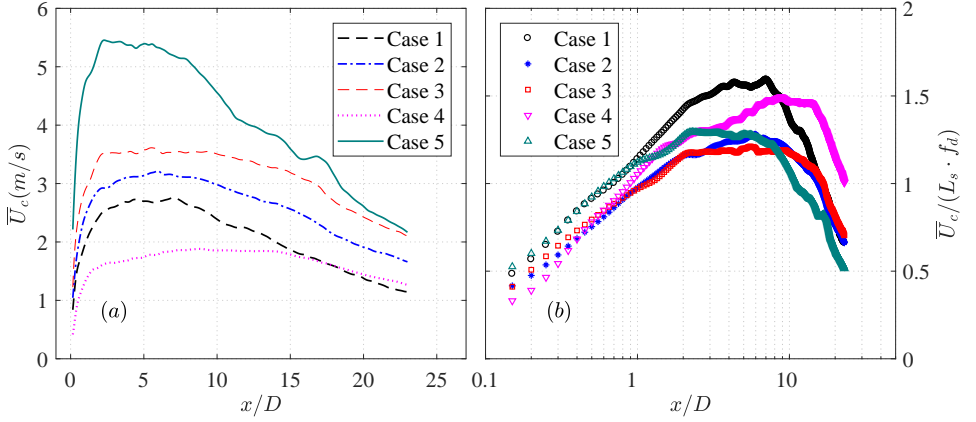


Figure 3.20: The decay of the normalized centreline velocity with the axial distance in (a) linear coordinates and (b) semilogarithmic coordinates.

values for steady turbulent jets (0.09–0.11) but lower than the values for piezoelectric synthetic jets (0.13–0.195) [97, 105]. This relatively high jet spreading rate indicates a high entrainment rate of surrounding fluid, which will be quantified in the following subsection. A zoomed-in view of the near-exit variation is further provided in Figure 3.21(b) in semilogarithmic coordinates. A kink point is observed at $x/D = 2$, prior to which the jet width shows a steady increase.

3.5.3. JET ENTRAINMENT

For incompressible flow, the mass flow entrained by jets (denoted as Q_{ent}) can be computed by the integral of the mass flow rate along the radial direction [105] as follows:

$$\begin{aligned}
 Q_{ent}(x) &= \int_0^{+\infty} \rho_0 \bar{U}_x(r, x) \cdot 2\pi r dr \\
 &\approx \bar{U}_c(x) w_h(x)^2 \int_0^{+\infty} \rho_0 g(\xi) \cdot 2\pi \xi d\xi
 \end{aligned} \tag{3.20}$$

where ξ equals r/w_h and $g(\xi)$ denotes the normalized velocity profile. Considering a self-similar velocity profile where g depends only on ξ , Q_{ent} is proportional to the product of the jet centreline velocity and the square of the jet width. In the case of a PSJ, the expelled gas is of somewhat lower density than ambient (Figure 3.7). However, Equation 3.20 can still give an acceptable estimation of the jet-entrained mass flow, since the expelled gas mass ($f_d M_e$) is one order of magnitude less than Q_{ent} after $x > 2D$, as will be shown in Figure 3.22(b).

The axial variation of the jet-entrained mass flow is shown in Figure 3.22(a). For all cases, a linear variation is exhibited. The entrained mass flow Q_{ent} increases with both the actuation frequency and the capacitor energy. The actuation frequency has a larger effect than the energy deposition. The variation of Q_{ent} with f_d and ϵ resembles that

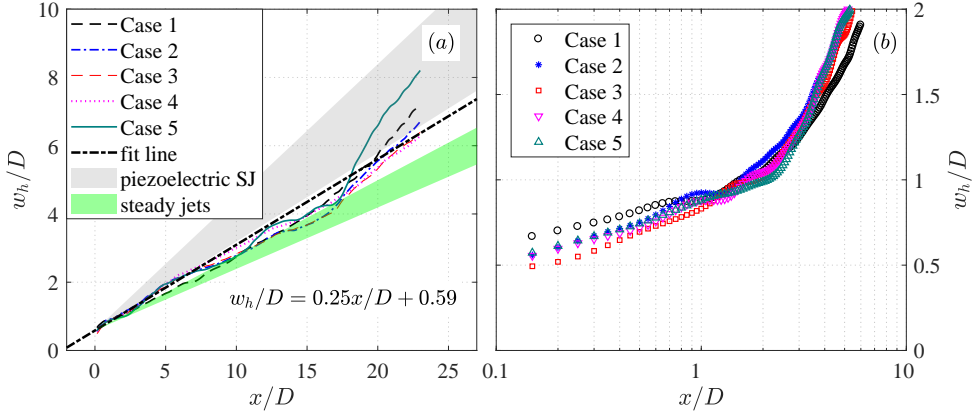


Figure 3.21: The evolution of the jet width with the axial distance in (a) linear coordinates and (b) semilogarithmic coordinates. The fitting law is indicated in (a).

of the centreline velocity, as expected, since the jet width and the normalized velocity profile change slightly for all of the tested cases. In Figure 3.22(b), Q_{ent} is normalized with the expelled gas mass ($f_d M_e$). Cases 2, 3 and 5 show a good agreement. For case 1 and case 4 (weak suction), the slope of these curves is steeper, indicating essentially a high entrainment rate.

The entrainment coefficient for round turbulent jets defined by Morton, Taylor & Turner in [110] and Hussein et al. in [105] can be reformulated as follows,

$$\alpha_{ent} = \frac{d \left(2 \int_0^{+\infty} \bar{U}_x r dr \right) / dx}{L_{ref} \bar{U}_{ref}} \quad (3.21)$$

Here, L_{ref} and U_{ref} are the equivalent top-hat length and velocity determined from the following two Equations.

$$\begin{cases} \rho_0 \bar{U}_{ref} L_{ref}^2 = f_d M_e \\ \rho_0 \bar{U}_{ref}^2 L_{ref}^2 = f_d I_p \end{cases} \quad (3.22)$$

Based on Equations 3.21-3.22, the relationship between the slope in Figure 3.22(b) (denoted as k) and the entrainment coefficient can be derived by

$$\begin{aligned} k &= d \left(\frac{Q_{ent}}{f_d M_e} \right) / d \left(\frac{x}{D} \right) \\ &= \frac{\pi D}{M_e} \sqrt{\frac{I_p \rho_0}{f_d}} \alpha_{ent} \end{aligned} \quad (3.23)$$

As a result, the entrainment coefficient ranges from 0.19 to 0.26 for the tested cases, twice as high as the values (0.08–0.1) reported in [105] for steady jets. This observation

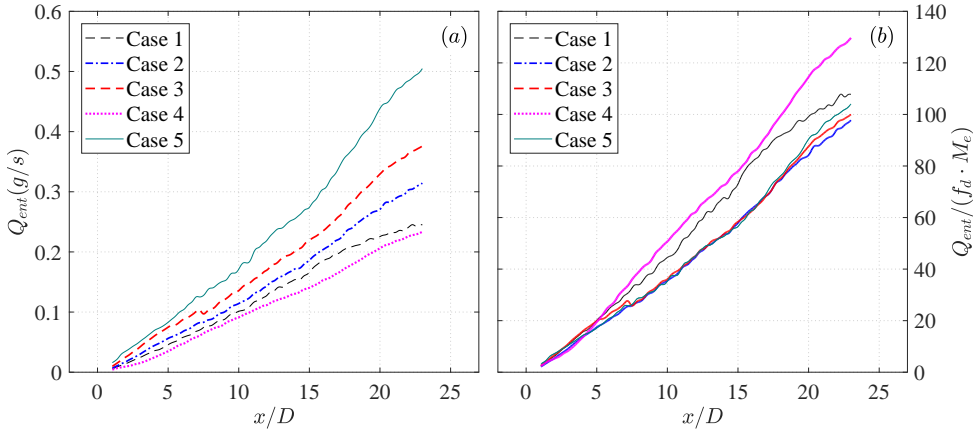


Figure 3.22: The variation of the entrained mass flow in the axial direction: (a) absolute values and (b) normalized values.

together with the jet spreading rate demonstrates that the entrainment ability of the PSJ is considerably higher than that of steady turbulent jets, which makes the PSJA a promising tool in mixing-enhancement applications (e.g. engine combustion chambers; [111]).

3.6. CONCLUSIONS

A high-speed jet, localized weak suction and an FVR are the three prominent features in the phase-averaged flow fields of the PSJ. With fixed f^* and increasing ϵ , the peak jet velocity (U_p) increases monotonically, whereas the jet duration time (T_d) extends moderately. When ϵ remains unchanged and f^* is increased, the peak jet velocity remains approximately constant and the jet duration time drops steadily. The theoretical model developed reveals that the expelled gas mass, impulse and jet mechanical energy are proportional to the jet duration time, cavity density and increasing powers of the peak jet velocity. When the total efficiency, jet duration time and cavity density remain unchanged, U_p increases with $\epsilon^{1/3}$.

The increasing jet intensity with ϵ is mainly contributed by the increasing peak jet velocity, while the decreasing jet intensity with f^* is attributed to both the reduced cavity density (primary factor, 22 %) and the reduced jet duration (secondary factor, 13 %). The time-averaged thrust produced by the PSJA ($O(1 \text{ mN})$) is positively proportional to both ϵ and f^* . The total energy efficiency ($O(0.01 \text{ %})$) reduces with increasing frequency. The velocity of the FVR (U_v) initially shows a sharp increase and subsequently a moderate decay. The peak propagation velocity reached at $x = 2D$ is approximately $0.43 U_p$. For the tested cases, the diameter of the FVR (D_v) increases monotonically in one cycle and collapses well when plotted against the dimensionless propagation distance. The peak circulation is also attained at $x = 2D$ and remains $0.62 U_p / D$ for different cases.

The time-averaged velocity fields of the PSJ resemble those of steady jets, but without the presence of a potential core region. The jet centreline velocity first increases and then

decays with the axial coordinate. The peak value observed in the range $2 < x/D < 9$ is approximately 1.2–1.6 times of $L_s f_d$. The decay rate of the jet centreline velocity increases with the frequency whereas it remains unchanged at different energy deposition levels. The mean jet spreading rate (0.13) for all of the tested cases is higher than the values for steady jets (0.1) but lower than the values for piezoelectric synthetic jets (0.13–0.195). The entrainment coefficient of the PSJ ranges from 0.19 to 0.26, which is twice as high as the values for steady jets (0.08–0.1), indicating a fast mixing rate.

4

EFFECT OF DISCHARGE FREQUENCY

4.1. INTRODUCTION

IN flow control applications, working frequency of the PSJA is directly related to the Strouhal number, thus serving as one of the most important actuation parameters. To the authors' knowledge, majority of the studies on the frequency characteristics of the PSJA are based on schlieren imaging and pressure measurements [16, 25, 46], which largely limits our current understanding of the repetitive working mechanism. Direct comparison has shown that the peak jet velocity determined by tracking the propagating features (jet front, front vortex ring) in schlieren images is only half of the peak exit velocity measured by Particle Imaging Velocimetry (PIV) [39, 101]. Similarly, the velocity estimated from the total pressure measurements based on incompressible flow relations also severely underestimates the real jet exit velocity, as the jet density can be far below of the ambient density even in the single-shot operation mode [58, 85].

Consequently, the systematic influence of the actuation frequency on crucial performance parameters of the PSJ such as peak jet velocity, jet duration time, and jet spreading rate are largely unclear. This also applies for the transient working mechanism during repetitive operation (namely, the start-up process). The present chapter provides an effort to fill this gap. A high-speed phase-locked planar PIV system is deployed to measure the jet-induced velocity fields in the axisymmetric plane in a wide range of actuation frequencies (50 Hz-1429 Hz). A detailed description of the experimental setup is provided in Section 4.2. The effect of frequency on performance characteristics of the PSJA is investigated using both phase-averaging and time-averaging in Section 4.3 and 4.4. The transient working mechanism is revealed in Section 4.5 and 4.6 with the support of both experimental data and theoretical energy equilibrium analysis.

Part of this chapter is published as **H. Zong** & M. Kotsonis, *Experimental investigation on frequency characteristics of plasma synthetic jets*, Physics of Fluids, **29**, 115107 (2018).

4.2. EXPERIMENTAL SETUP

4.2.1. ACTUATOR AND POWER SUPPLY

For the purposes of this investigation, the same circuitry as that used in Chapter 3 (circuitry E2, Figure 2.2*b*) is adopted, nevertheless configured with a low-capacitance capacitor ($C_1 = 0.1 \mu\text{F}$) to enable fast recharging. Based on the characteristic timescale of the charging circuit ($\tau_d = C_1 R_1 = 0.15 \text{ ms}$), the maximum discharge frequency for reliable and repeatable actuator operation (criterion: capacitor voltage reaches 99% of the DC voltage) is estimated to be $1/4.67\tau_d = 1429 \text{ Hz}$. As the capacitance is only $1/10^{\text{th}}$ of that in Chapter 3, the pulse energy delivered by circuitry E1 decreases significantly, which necessitates the usage of a small-cavity-volume actuator (i.e. actuator A2, see Figure 2.1*d*) to yield appreciable peak jet velocity. Based on the actuator geometric parameters provided in Section 2.1 ($D = 1.5 \text{ mm}$, $L_{th} = 3 \text{ mm}$, $V_{ca} = 942 \text{ mm}^3$), the Helmholtz natural frequency of actuator A2 is determined to be 1353 Hz (see Equation 3.2). Additionally, a cylindrical coordinate system is established in the jet exit center, with the r -axis and x -axis along the axial and radial directions, respectively.

4.2.2. PIV MEASUREMENT SCHEME

The high-speed phase-locked PIV system adopted in Chapter 3 is inherited to measure the ensuing jet-induced velocity fields in the axisymmetric plane, which mainly consists of a high-speed laser (Continuum Mesa PIV, 532-120-M), a high-speed camera (Photron, Fastcam SA-1, resolution: $1024 \times 1024 \text{ pixels}^2$), and a programmable timing unit (PTU) (LaVision, HSC). To ensure quiescent flow conditions, the actuator is placed in a closed plexiglass box. Dielectric mineral oil particles are delivered into both the actuator cavity and the plexiglass box through an atomizer (TSI, 9302). Prior to discharge ignition, the intra-cavity seeding is switched off to avoid possible interferences on the jet flow. The laser beam is shaped into a thin sheet (thickness: approximately 0.6 mm) by two spherical lenses and one cylindrical lens. The laser sheet is kept strictly vertical, passing through the xr -plane. A 200 mm macro lens (Nikon, Micro-Nikkor) and an extension tube (36 mm) are mounted on the high-speed camera to image a field of view of $12 \text{ mm} \times 12 \text{ mm}$ ($8D \times 8D$), achieving a magnification factor of 1.7 . Davis 8.3.1 is used to process the recorded data set. The final interrogation window size and overlapping ratio used in PIV cross correlation are $24\% \times 24\%$, and 75% , respectively, leading to a final spatial resolution of 0.07 mm/vector .

Raw images are recorded in the double frame mode, synchronized with the discharge ignition. The time delay between discharge ignition and image recording (t , namely, the phase) is adjusted by a digital delay/pulse generator (Stanford Research Systems, DG535) in high accuracy ($< 1 \mu\text{s}$). Six cases with increasing discharge frequency (50 Hz – 1429 Hz) and constant energy deposition ($C_1 = 0.1 \mu\text{F}$, $V_1 = 2.0 \text{ kV}$) are tested, as listed in Table 4.1. Based on the definitions in Equations 3.1 and 3.3, the non-dimensional energy deposition (ϵ) is computed to be 0.84 , while the dimensionless frequency (f^*) ranges from 0.037 to 1.056 . For each case, approximately 30 – 70 phases are selected to execute the PIV measurement. Time steps between adjacent phases range from $25 \mu\text{s}$ to 1 ms , depending on the peak flow velocity. For each phase, one long sequence containing 200 successive pulses is recorded.

Table 4.1: Discharge parameters for all cases

Cases	f_d (Hz)	T_d (ms)	f^*	ϵ
Case 1	50	20	0.037	0.84
Case 2	100	10	0.074	0.84
Case 3	200	5	0.148	0.84
Case 4	500	2	0.370	0.84
Case 5	1000	1	0.739	0.84
Case 6	1429	0.7	1.056	0.84

As noticed by Sary et al. in [55] and Zong et al. in [16], the first several pulses (less than 20) after the PSJA starts up lie in the transient working stage with unstable performance, while the later pulses lie in the steady working stage. Specifically, in the transient working stage, the cavity density and cavity temperature exhibit a stair-stepping variation and the peak jet velocity varies from cycle to cycle. In contrast, the steady working stage features a periodical variation of the exit velocity, cavity density, and cavity temperature. The transient stage during repetitive operation is inevitable and will transition to the steady state once two specific conditions are met. First, the mass ejected through the exit orifice in one cycle should be counteracted by that ingested into the cavity (satisfying cavity mass conservation). Second, the cycle work done by the PSJA should be balanced by the net heat exchange between the environment and the actuator during one period (satisfying energy conservation). Out of this consideration, only the last 100 measured snapshots of each sequence are adopted to get statistically averaged steady-state performance of the PSJA. Preliminary convergence study has verified that this sampling size (100) is enough to get statistically converged mean flow fields. Additionally, case 6 is selected to reveal the transient working mechanism due to the most significant frequency effect. For each phase of this case, 20 short sequences incorporating the snapshots of the first 50 pulses are recorded. The uncertainty in phase-locked PIV measurements has been discussed in detail in 2.4.2. Following a similar procedure, the total measurement uncertainty is computed to be less than 5% of the peak jet velocity.

4.3. PHASE-AVERAGED RESULTS AT STEADY-STATE

4.3.1. JET PENETRATION LENGTH AND EXIT VELOCITY

Phase-averaged velocity fields for the lowest frequency case (case 1, $f^*=0.037$) and the highest frequency case (case 6, $f^*=1.056$) are shown in Figure 4.1. In the case of $f^*=0.037$, a bow-shape velocity structure, in the vicinity of the jet exit, is formed at $t = 50 \mu\text{s}$. Such a structure is the result of multiple shock waves, spatially smoothed by the phase averaging procedure [82]. These shock waves are caused by the rapid heating of the pulsed arc and can be used to trigger the instability in the shear layers of high-subsonic jets [68]. Pulsed jets with a peak velocity of up to 70 m/s are released after these shock waves, creating a hammer-shaped jet body. In this upstanding jet body, several discrete high-velocity cores can be observed in Figure 4.1(b, c), as a result of the self-induction effect of shear-layer vortex rings [102]. The axial spacing between these high-velocity cores grows

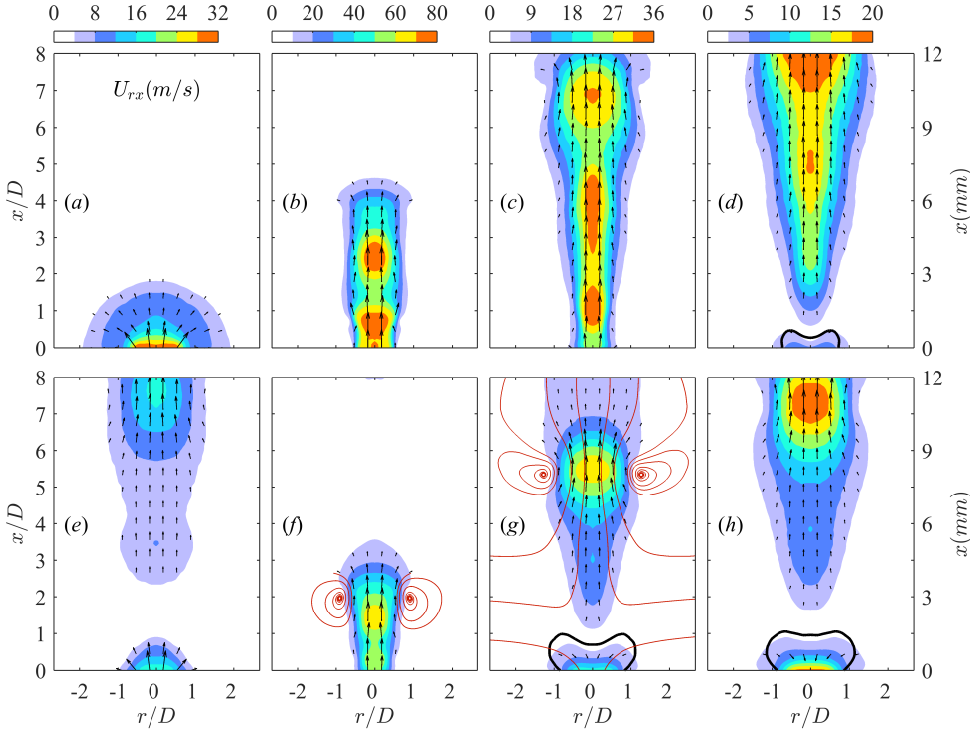


Figure 4.1: Time evolution of phase-averaged velocity fields at $f^*=0.037$ (Case 1) and $f^*=1.056$ (Case 6). (a) $t = 50\mu\text{s}$, $f^*=0.037$; (b) $t = 250\mu\text{s}$, $f^*=0.037$; (c) $t = 500\mu\text{s}$, $f^*=0.037$; (d) $t = 700\mu\text{s}$, $f^*=0.037$; (e) $t = 50\mu\text{s}$, $f^*=1.056$; (f) $t = 250\mu\text{s}$, $f^*=1.056$; (g) $t = 500\mu\text{s}$, $f^*=1.056$; (h) $t = 700\mu\text{s}$, $f^*=1.056$. The magnitude and direction of U_{rx} are indicated by contours and arrows, respectively. Solid black lines are velocity contour lines of $U_{rx}=-1$ m/s.

approximately from $2D$ at $t = 250\mu\text{s}$ to $3D$ at $t = 500\mu\text{s}$. After the jet stage ceases, fresh ambient air near the exit orifice ($1 < r/D < 1$, $x/D < 1$) is ingested into the actuator cavity at low velocity, mixing with the high-temperature low-density residual cavity gas.

In comparison to the low-frequency operation, the bowshape shock waves in case 6 are limited to the near-exit region at $t = 50\mu\text{s}$ and flooded by the residual jet flow of previous pulses. A relatively weak pulsed jet with 60 m/s peak velocity is issued at $t = 250\mu\text{s}$, followed by an early yet strong suction flow emerging at approximately $t = 500\mu\text{s}$. Only one high-velocity core can be observed in Figure 4.1(f, g), indicating a reduced amount of other shear-layer vortices. The peak suction velocity exhibited at $t = 700\mu\text{s}$ (15 m/s) is three times higher than the respective higher than the respective peak suction velocity for low-frequency operation (case 1, $f^*=0.037$).

The two major modifications resulting from high frequency operation are weakened jet and intensified suction. The jet penetration length and exit velocity will be exploited to quantify these modifications. For all tested cases, the velocity contours at $t = 250\mu\text{s}$ are shown in Figure 4.2. As a result, both peak jet velocity and jet penetration differ slightly at $f^*=0.739$ and drop significantly afterwards. The jet penetration length (L_p)

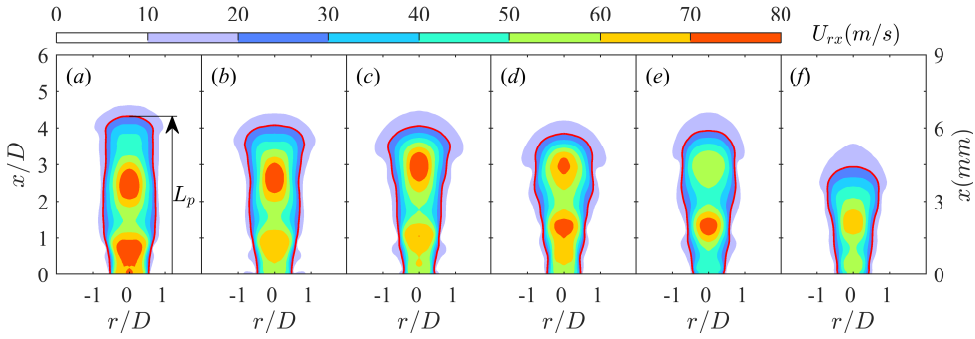


Figure 4.2: Phase-averaged velocity contours at $t = 250 \mu\text{s}$ for increasing frequency. (a) $f^* = 0.037$; (b) $f^* = 0.074$; (c) $f^* = 0.148$; (d) $f^* = 0.370$; (e) $f^* = 0.739$; (f) $f^* = 1.056$; Red lines are velocity contour lines of $U_{rx} = 20 \text{ m/s}$

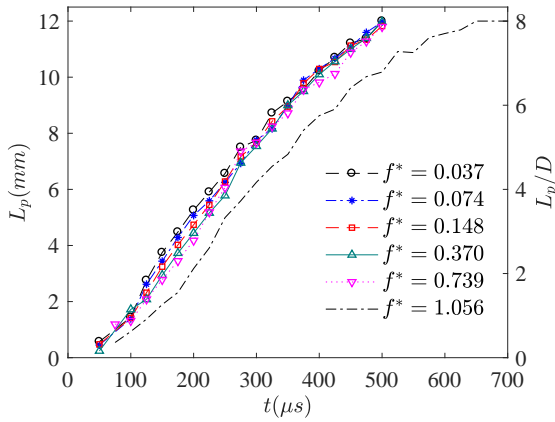


Figure 4.3: Time evolution of jet penetration length for increasing frequency.

is defined arbitrarily as the farthest propagation position of the 20 m/s velocity contour line [101], as sketched in Figure 4.2(a). The evolution of L_p with time for increasing frequency is shown in Figure 4.3. As evidenced, a steady increase of L_p is exhibited and the general trend agrees well with that shown in the work of Zong and Kotsonis [101]. For $f^* = 0.739$, all the curves collapse well except for the interval of $100 \mu\text{s} < t < 300 \mu\text{s}$ where L_p drops monotonically with increasing frequency. Nevertheless, these discrepancies are alleviated in later evolution. When f^* increases from 0.739 to 1.056, a sharp drop of L_p (on average, $1D$) is experienced. This abrupt drop is also evidenced in Figure 4.2 and mainly related to the enhanced suction flow, which will be quantified later on.

Phase-averaged velocity contours at $t = 500 \mu\text{s}$ for increasing frequency are shown in Figure 4.4. The sequence exemplifies how the jet and suction flows alternate. Initially, the air at the exit periphery is ingested into the throat, while the air near the exit core region is still being ejected. As the jet flow diminishes, the suction flow expands inwards, gradually occupying the entire exit. Finally, a saddle flow pattern takes shape where the

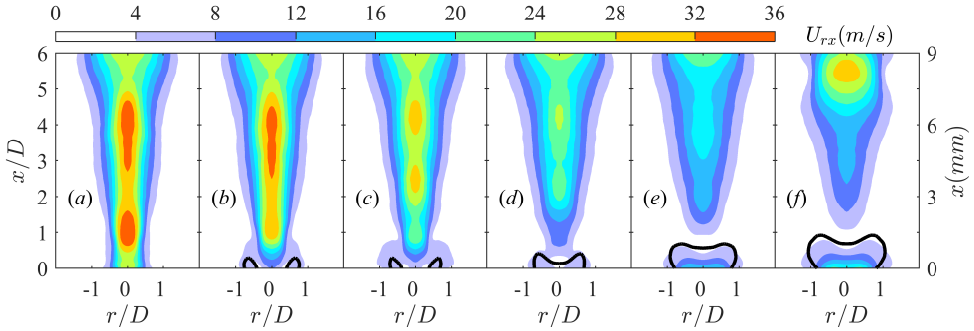


Figure 4.4: Phase-averaged velocity contours at $t = 500 \mu\text{s}$ for increasing frequency. (a) $f^* = 0.037$; (b) $f^* = 0.074$; (c) $f^* = 0.148$; (d) $f^* = 0.370$; (e) $f^* = 0.739$; (f) $f^* = 1.056$; Solid black lines indicate contour lines of $U_x = -1 \text{ m/s}$.

4

jet and suction flows reside in the near-field and far-field, respectively, divided approximately by $x/D = 1$ (see Figure 4.1.g). The exit velocity profiles (only axial component, i.e. U_x) are further extracted from Figure 4.4(a–f) and shown in Figure 4.5(a). These curves exhibit consistently bell shapes, and suction velocity profiles are significantly fuller than jet velocity profiles. Assuming that the jet-induced flow is axisymmetric, the spatially averaged exit velocity (U_e) can be computed from Equation 2.4 in Section 2.4.1.

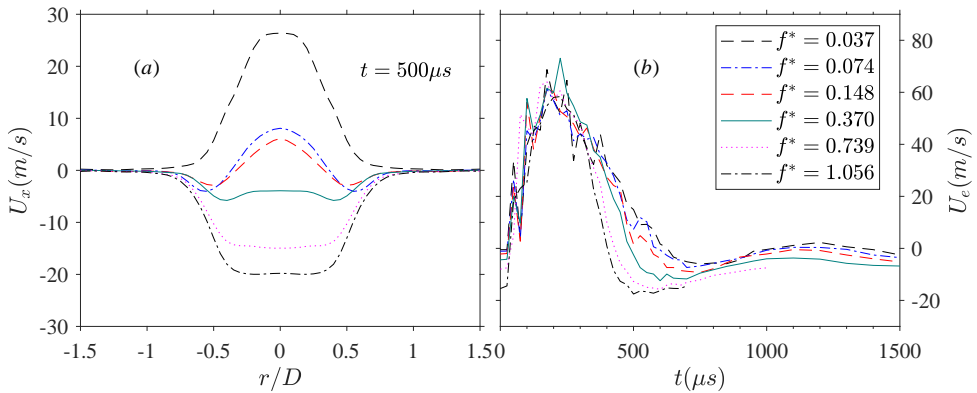


Figure 4.5: (a) Comparison of jet exit velocity profiles at $t = 500 \mu\text{s}$; (b) Time evolution of area-averaged exit velocity for different cases.

The time evolution of U_e for all the tested cases is shown in Figure 4.5(b). Positive and negative signs of U_e indicate the jet and refresh stages, respectively. In the primary jet stage, U_e shows initially a sharp increase, then small-amplitude oscillations around its peak value, and finally a slow linear drop. Peak values of U_e (denoted as U_p) are reached between $t = 200 \mu\text{s}$ and $t = 300 \mu\text{s}$, ranging between 58 m/s and 73 m/s for the different frequency cases. Additionally, based on the sign change of U_e , the jet duration time (T_{jet}) can be estimated. With increasing frequency, T_{jet} drops monotonically from 627 μs to 402 μs , whereas the peak suction velocity (denoted as U_s) experiences a triple increase

Table 4.2: Peak velocity, jet duration time and mean cavity density

f^*	$U_p(m/s)$	$U_s(m/s)$	$T_{jet}(\mu s)$	L_e/D	L_s/D	ρ_{ca1}/ρ_0	ρ_{ca2}/ρ_0
0.037	68.8	-6.0	627	12.8	12.5	97.7%	97.8%
0.074	61.3	-7.3	588	12.0	10.4	87.0%	87.0%
0.148	61.6	-9.2	563	11.6	8.8	75.6%	75.4%
0.370	73.1	-12.4	488	12.1	6.2	51.7%	51.6%
0.739	64.1	-15.7	430	10.8	4.4	40.9%	41.1%
1.056	58.4	-17.6	402	9.3	3.2	34.9%	34.2%

from 6 m/s to 18 m/s. For all the tested cases, peak jet and suction velocity and jet duration time are listed in Table 4.2. In the case of $f^*=0.037$, a weak second jet stage (peak velocity: 2.3 m/s) appears between $t=1100-1300 \mu s$. By contrast, for cases of $f^* \geq 0.074$ never restores back to positive values after $t = T_{jet}$, indicating the absence of multiple alternations between jet and refresh stages at high-frequency repetitive operation [39, 82].

At $f^* = 1.056$, it is striking to notice that the initial exit velocity at $t \leq 25 \mu s$ is a negative value (15 m/s) much higher than other cases (less than 7 m/s). This indicates that the jets in case 6 ($f^* = 1.056$) ensue while there is still a strong refresh stage (suction) from the previous pulse. This adverse suction flow obstructs the axial propagation of pulsed jets, leading to a reduction of the penetration length as shown in Figure 4.3.

4.3.2. MEAN CAVITY DENSITY AND CAVITY TEMPERATURE

Since the time evolution of the exit velocity in a complete cycle is resolved, the mean cavity density during the quasi-steady working state (ρ_{ca}) can be estimated using the law of mass flow conservation. Two approaches proposed in Chapter 3 can be used to calculate this [39]. The first method assumes that the expelled gas mass in one cycle is relatively small compared to the initial cavity gas mass (less than 5%). Based on this assumption, the normalized mean cavity density (ρ_{ca}/ρ_0) can be approximated by the ratio of the suction length (L_s) to ejection length (L_e) as shown in Equation 3.6.

The second method employs a reduced analytical model to simulate the repetitive working process of the PSJA and seeks for an optimal initial cavity density satisfying the law of mass flow conservation. With this method, the temporal evolution of both cavity density and exit density can be computed. For all the tested cases, the mean cavity density computed with the aforementioned two methods (distinguished by subscripts, ρ_{ca1}/ρ_0 and ρ_{ca2}/ρ_0) and non-dimensional ejection/ suction lengths are listed in Table 4.2. The two methods give comparable results with maximum relative deviation of less than 0.7%. The peak values of L_e/D and L_s/D are very close, being 12.8 and 12.5, respectively. With increasing frequency, both L_e/D and L_s/D decline monotonically. However, the declining rate of the suction length is significantly less than the rate of the ejection length, leading to a reduced mean cavity density.

Since the peak jet velocity for all cases is less than 80 m/s, the absolute cavity pressure (p_{ca}) is expected to vary between 101 kPa and 105 kPa (Bernoulli principle, $p_{ca} \approx P_0 + \rho_0 U_e^2/2$). Taking a mean cavity pressure (p_{ca}) of 103 kPa, the mean cavity temperature

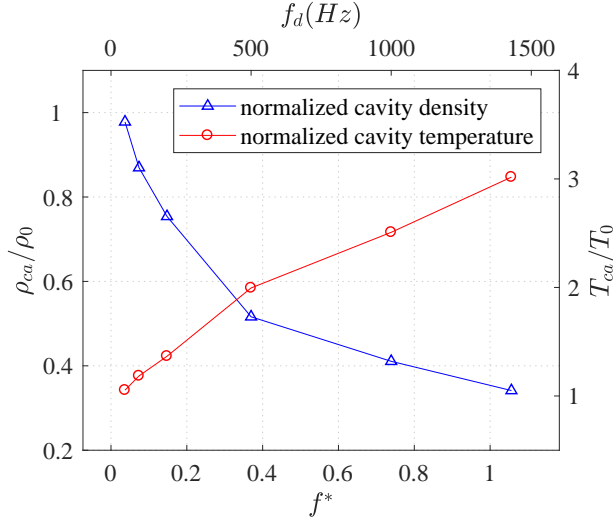


Figure 4.6: Normalized mean cavity density and temperature at steady working stage.

in the steady working stage (T_{ca}) can be estimated by the ideal gas law, $T_{ca} = p_{ca}/\rho_{ca}R$, where R is the gas constant. The variation of T_{ca} and ρ_{ca} (method 2) with f^* is shown in Figure 4.6. Below $f^*=0.037$, the mean cavity density at the steady working stage is above 97% of the ambient density, indicating negligible frequency effects. As the frequency increases, the normalized cavity density drops sharply between $0.037 \leq f^* \leq 0.370$ and slows down afterwards. At $f^*=1.056$, the mean cavity density remains only 1/3 of the ambient density, which corresponds to a mean cavity gas temperature of 860 K. The high-temperature low-density feature of the cavity gas is mainly caused by the continuous heat accumulation in the transient working stage [16], which will be elucidated later on in Section 4.5.

4.3.3. EXPELLED GAS MASS, IMPULSE, AND ISSUED MECHANICAL ENERGY

The combination of time-varying exit velocity and exit density (not shown) enables the evaluation of the cumulative expelled gas mass (M_{ce}), impulse (I_{cp}), and issued mechanical energy (E_{cm}) as shown in Equation 3.12. These three cumulative parameters can further be normalized by the total expelled gas mass (M_e), total impulse (I_e), and total issued mechanical energy (E_m) defined in Equation 2.8, leading to another three non-dimensional quantities, i.e. \bar{M}_{ce} , \bar{I}_{cp} and \bar{E}_{cm} (see Equation 3.13).

For all the tested cases, the evolution in time of these three non-dimensional quantities (generalized as \bar{X}_{ci}) in one cycle is shown in Figure 4.7 in order to identify the respective contribution of the jet and refresh stages. Observing the slope of the curve in Figure 4.7(a), the averaged mass flow rate in the primary jet stage is demonstrated to be significantly higher than that in the refresh stage at $f^*=0.037$ due to a small jet duty cycle (defined as T_{jet}/T_d , $D_c \approx 0.03$). As the dimensionless frequency increases, D_c increases rapidly and exceeds 0.5 at $f^*=1.056$, indicating that the averaged mass flow

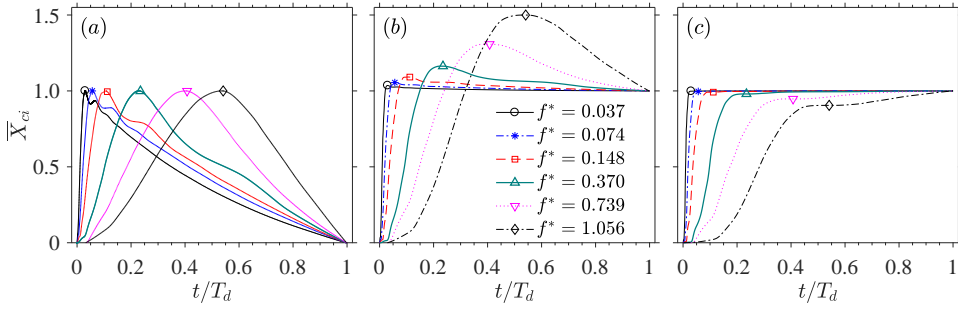


Figure 4.7: Time evolution of \bar{X}_{ci} in one cycle for all the tested cases; (a) \bar{M}_{ce} ; (b) \bar{I}_{cp} ; (c) \bar{E}_{cm} ; The symbol on each curve is located at $t = T_{jet}$, separating primary jet stage from refresh stage.

rate in the refresh stage has overtaken that in the jet stage. In Figure 4.7(b), the refresh stage contributes negatively to the total jet impulse yielded in one cycle. At $f^* < 0.148$, the proportion of this negative contribution is negligible (less than 10%). As the frequency increases, this negative effect grows. In the cases of $f^* = 1.056$, 33% of the jet impulse produced in the primary jet stage is counteracted by the suction flow. \bar{E}_{cm} bears a monotonic increase throughout one cycle. The contribution of the refresh stages to the total issued mechanical energy grows with increasing frequency, reaching 9.5% at $f^* = 1.056$.

M_e and I_p can further be normalized by the initial mass of cavity gas ($\rho_0 V_{ca}$) and the maximum convertible impulse $\sqrt{2E_c \cdot (\rho_0 V_{ca})}$ [54, 85], resulting in non-dimensional expelled gas mass (M_e^*) and non-dimensional impulse (I_p^*). Additionally, the ratio of E_m to E_c defines the total efficiency of the actuator (η_t). For all the tested cases, these parameters are listed in Table 4.3. The peak value of M_e^* is only 4.1%, indicating a relative small variation of cavity density in one cycle. The non-dimensional impulse and the total efficiency are on the order of 0.1% and 0.01% respectively, which are consistent with that reported in the previous chapter. The variations of M_e^* , I_p^* and η_t at increasing frequency are further shown in Figure 4.8. Similar to the trend of mean cavity density observed in Figure 4.6. M_e^* , I_p^* and η_t decrease monotonically with increasing frequency. The declining rate of M_e^* and I_p^* agrees well at $f^* < 0.370$ however differs slightly afterwards, which can be attributed to the enhanced negative contribution of the suction flow to the jet

Table 4.3: Integral parameters pertaining to PSJ at steady working stage

f^*	M_e^*	$I_p^* (\mu N \cdot s)$	I_p^*	$F_p (mN)$	$E_m (\mu J)$	$\eta_t (\%)$
0.037	4.14%	1.65	0.27	0.082	41.2	0.0206
0.074	3.50%	1.34	0.22	0.134	32.8	0.0164
0.148	2.95%	1.15	0.18	0.229	30.4	0.0152
0.370	2.09%	0.86	0.14	0.428	27.5	0.0137
0.739	1.47%	0.54	0.09	0.544	19.8	0.0099
1.056	1.05%	0.31	0.05	0.441	12.6	0.0063

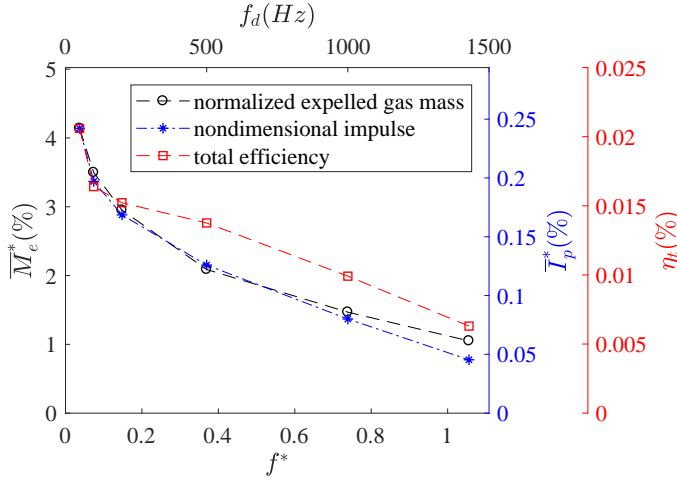


Figure 4.8: Effect of frequency on the non-dimensional expelled gas mass (M_e^*), non-dimensional impulse (I_p^*) and total efficiency (η_t).

impulse. For η_t , a relatively slow drop is experienced at $f^* > 0.148$. Compared to Case 1 ($f^* = 0.037$) where sufficient time is provided for recovery, the high-frequency operation at $f^* = 1.056$ demonstrates 3.9, 5.3 and 3.3 times reduction in M_e^* , I_p^* and η_t respectively. The product of the discharge frequency and impulse gives the time-averaged thrust produced by the PSJA (F_p). F_p first increases and then drops with f^* , reaching a peak value of 0.544 mN at $f^* = 0.739$. This observation is consistent with the total pressure measurement results in the work of Zong et al. [16].

Under the assumption of small expelled gas mass (valid in this paper, $< 5\%$) and self-similar exit velocity evolution (i.e. the normalized function of $U_e(t/T_{jet})/U_p$ is identical for all the tested cases), the total expelled gas mass, impulse and jet mechanical energy produced in the primary jet stage are demonstrated to scale with the mean cavity density, jet duration time and increasing orders of peak jet velocity (refer to Equations 3.15-3.17). When f^* is increased from 0.037 to 1.056, the peak jet velocity changes slightly whereas the mean cavity density and jet duration time are reduced by 2.8 times and 1.6 times respectively. These two factors together account for a theoretical drop of 4.4 times in M_e^* , I_p^* and η_t , which is comparable to the measured values (3.9, 5.3 and 3.3 times). The remaining discrepancy can be ascribed to the influence of suction flow and the assumption of self-similar exit velocity evolution. Overall, the reduced cavity density and shortened jet duration play a dominant role in the performance decline of the PSJA at high frequency operation.

4.4. TIME-AVERAGED CHARACTERISTICS AT STEADY STATE

Based on phase-averaged velocity fields in one period ($U(r, x, t)$), the time-averaged velocity field of the plasma synthetic jet ($\bar{U}(r, x)$) can be constructed using Equation 2.16. For all the tested cases, contours of time-averaged axial velocity (\bar{U}_x) are shown in Figure

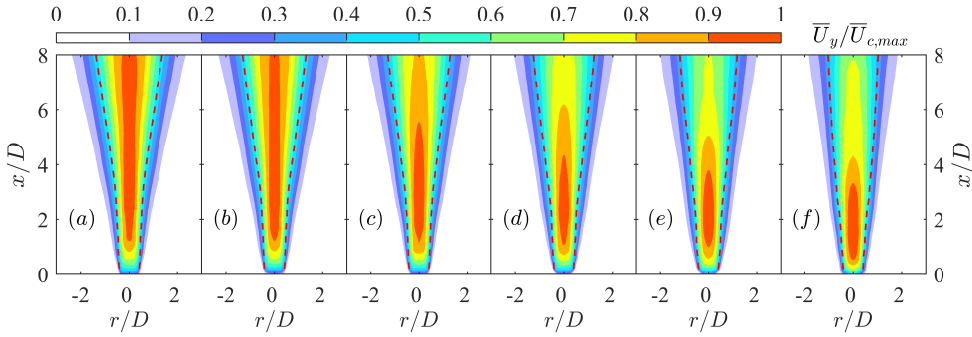


Figure 4.9: Contours of time-averaged axial velocity for increasing frequency. (a) $f^*=0.037$; (b) $f^*=0.074$; (c) $f^*=0.148$; (d) $f^*=0.370$; (e) $f^*=0.739$; (f) $f^*=1.056$; The red dash lines superimposed on contours are jet boundaries determined by 50% of the jet centreline velocity.

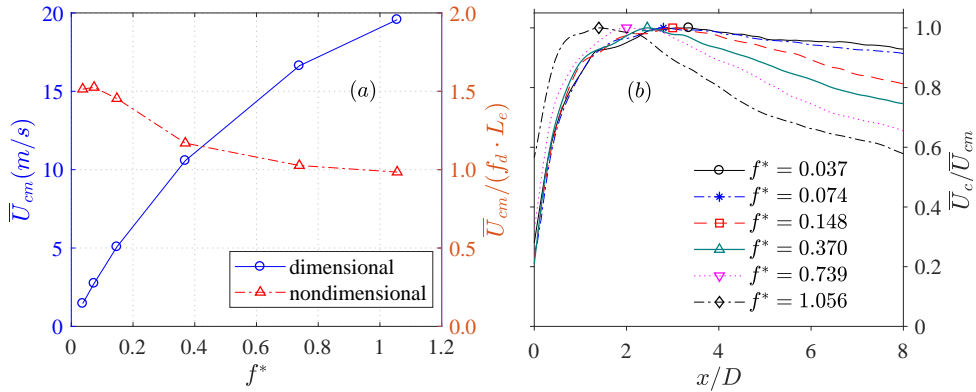


Figure 4.10: (a) Effect of frequency on peak jet centreline velocity; (b) Axial decay of jet centreline velocity.

4.9. The peak centreline velocity (\bar{U}_{cm}) is used to normalize \bar{U}_x , resulting in a normalized range of 0 to 1. The mean flow of the PSJ is similar to that of steady jets where an expanding jet plume is observed, entraining surrounding fluids during its propagation. No potential core region can be observed and a high-velocity region (defined as $\bar{U}_x/\bar{U}_{cm} > 0.9$) residing approximately $1D$ away from the jet exit is evident. The axial extent of this high-velocity region shrinks from $7D$ to $2D$ when f^* increases from 0.037 to 1.056. The two red dash lines on each contour correspond to the jet boundaries where \bar{U}_x drops to 50% of the jet centreline velocity. The distance between these two dash lines gives the jet width (w_h), which is also known as the full width at half maximum [109].

The variation of the peak centreline velocity (\bar{U}_{cm}) with dimensionless frequency is shown in Figure 4.10 (a). As expected, \bar{U}_{cm} increases monotonically with frequency, ranging from 1.5 m/s to 20 m/s. The product of the discharge frequency and ejection length is used to normalize \bar{U}_{cm} , resulting in a non-dimensional peak centreline velocity. For all the tested cases, $\bar{U}_{cm}/(f_d \cdot L_e)$ remains at around 1.5 for low-frequency operation

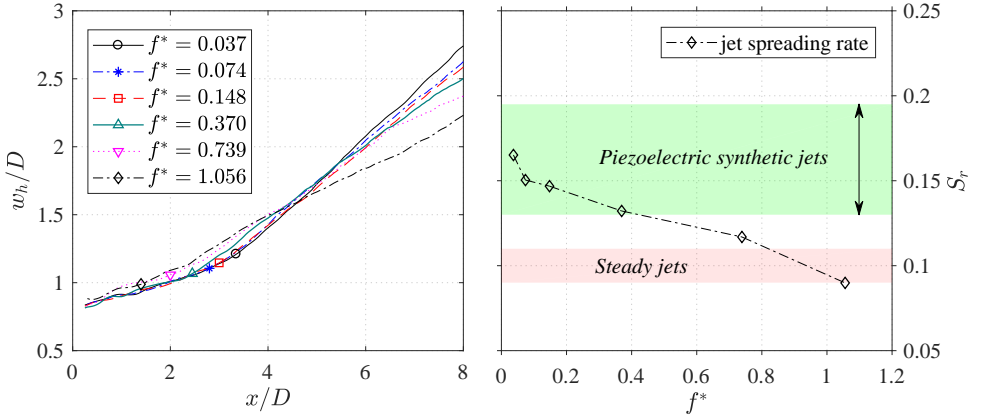


Figure 4.11: (a) Axial variation of normalized jet width; (b) Jet spreading rate against dimensionless frequency

($f^* < 0.148$) and reduces slowly to 1.0 at high frequency ($f^* > 0.739$). This is consistent with the observation in the previous chapter, where the non-dimensional peak centreline velocity varies between 1.2-1.6. Figure 4.10 (b) shows the axial variation of the jet centreline velocity. \bar{U}_c/\bar{U}_{cm} exhibits a non-monotonic change with axial distance. As frequency increases, the peak point moves close to the exit ($x = 4D \rightarrow x = 2D$), and the decay rate of \bar{U}_c/\bar{U}_{cm} increases which can be ascribed to the decreasing jet momentum.

The axial evolution of the jet width is shown in Figure 4.11 (a). A steady increase of w_h is experienced. The symbol of each curve denotes the position of the peak jet centreline velocity. These symbols mark notable discontinuities in the slope of the evolution curve, separating each curve into two linear segments. The jet spreading rate (denoted as S_r) determined by the slope of the second segment is shown in Figure 4.11 (b) (i.e. $S_r = 0.5 \cdot d(w_h)/dx$). As a result, the jet spreading rates of the PSJs (0.09-0.17; [105] and [109]) and the piezoelectric synthetic jets (0.13-0.195, [97]). With increasing actuation frequency, S_r decreases monotonically.

The high jet spreading rate at low-frequency cases ($f^* \leq 0.148$) can be ascribed to the front vortex ring (FVR). Specifically, the FVR induced by PSJs is comparable to the sequential vortex rings produced by piezoelectric synthetic jets of comparable power. Both types of jets produce vortex rings, which are considerably larger than the shear layer vortices residing in steady jets [82]. These large-scale vortex rings entrain rapidly the ambient fluids into the jet core region meanwhile distribute the jet fluids outwards, leading to a fast expansion of the vortex ring size as well as the jet width. Additionally, the entrainment waves created by intermittent termination of the jets further contribute to the high jet spreading rate [112]. At high frequency cases ($f^* \geq 0.739$), those effects are still active; however, the expelled gas mass in one cycle (M_e) declines. This declining expelled gas mass contributes negatively to the total entrained gas mass in one cycle and leads to a decreasing jet spreading rate with increasing frequency. The correlation between M_e and the entrained mass flow is verified as follows.

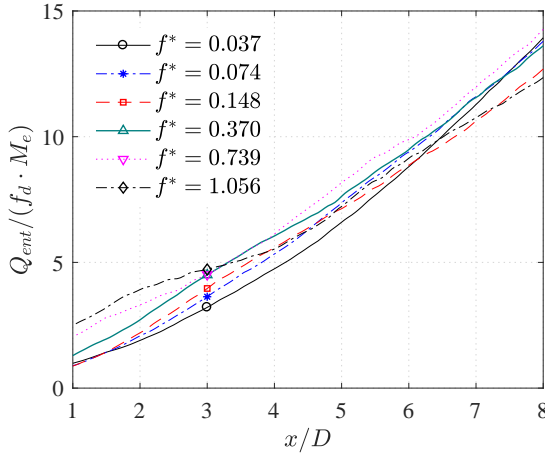


Figure 4.12: Axial variation of the entrained mass flow for all the tested cases.

In the previous chapter (Section 3.5.3), the entrained mass flow (Q_{ent}) of PSJs is defined in time-averaged velocity fields, and a close relationship between the jet entrainment and the jet spreading is demonstrated using simplified theoretical analysis. Specifically, Q_{ent} is proportional to both the peak jet centreline velocity (\overline{U}_{cm}) and the square of the jet width w_h , provided that the jet velocity profiles at different axial positions are self-similar (not necessarily momentum preserving). Following the same definition, the entrained mass flow at different axial positions for all the tested cases is computed and shown in Figure 4.12. As a result, Q_{ent} increases approximately linearly with the axial coordinate and collapse reasonably when scaled by $f_d M_e$. As $f_d M_e$ represents the total expelled gas mass per second (excluding suction), the positive correlation between the entrained mass flow and the expelled gas mass per pulse (M_e) is evident and expected.

4.5. TRANSIENT-STAGE ANALYSIS

Analysis of the quasi-steady state reveals that under high frequency operation, the intensity of the pulsed jet can deteriorate significantly compared to that obtained in the single-shot mode. Several important parameters are responsible for this deterioration including the reduced cavity density, reduced jet duration, and enhanced suction flow. In order to elucidate the origin of these dependencies, an analysis of the transient stages of operation, ensuing during the initial few actuation cycles, is performed in this section.

At $f^*=1.056$, the evolution of the phase-averaged exit velocity pertaining to the first 30 pulses is shown in Figure 4.13. To be noted that the ‘phase’ here (denoted as t_1) refers to the time elapsed after the first pulse is ignited, which is different from that used in Section 4.3 ($0 \leq t \leq T_d$). For each cycle, the peak jet and suction velocity, as well as the jet duration time are shown in Figure. 4.14. It is striking to notice that no refresh stage is present in the first cycle. Additionally, the peak jet velocity of the first cycle (70.4 m/s) is close to the steady-state value at $f^*=0.037$ (68.8 m/s) since in both cases the mean cavity density is approximately at the levels of ambient density. During the transient working

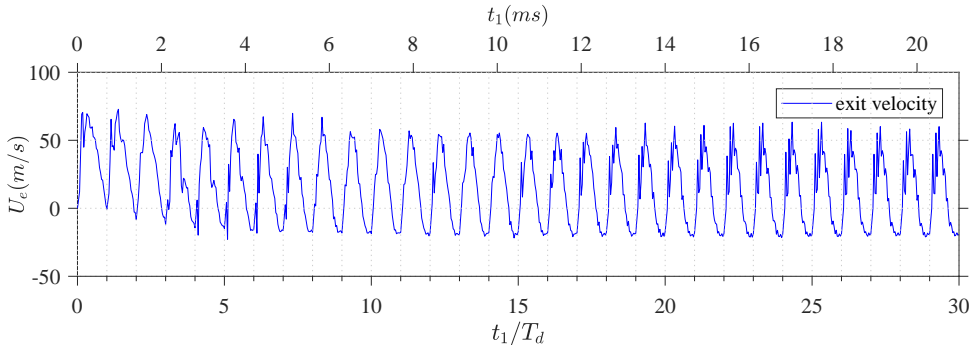


Figure 4.13: Time evolution of the exit velocity pertaining to the first 30 pulses at $f^*=1.056$.

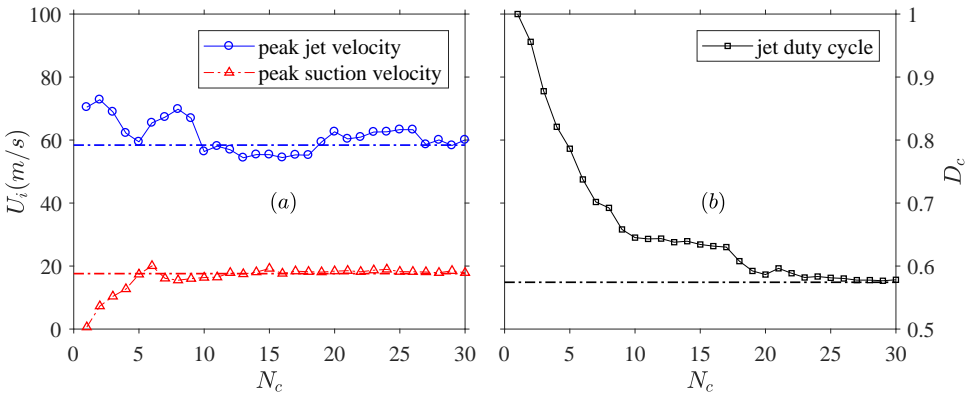


Figure 4.14: Evolution of jet performance parameters with cycle number (N_c) in transient stage at $f^*=1.056$. (a) Peak jet and suction velocity; (b) Jet duty cycle. The steady-state values of these performance parameters are indicated by dot-dash lines.

process, the peak suction velocity shows a steady increases at $N_c \leq 7$ and remains approximately constant at 18 m/s afterwards. For the jet duty cycle (D_c), a sharp drop from 1 to 0.65 is experienced during the first 10 cycles and the steady-state value (0.57) is not approached until $N_c \geq 20$. The increasing suction velocity and reducing jet duty cycle demonstrate an intensifying suction flow. The peak jet velocity appears unstable in the first 10 pulses as is evident in Figure. 4.14 (a). After $N_c \geq 10$, a mild fluctuation around the steady-state value (oscillation amplitude: less than 3 m/s) is exhibited. Based on the variations of these three parameters, it is concluded that the exit velocity takes approximately 20 cycles to stabilize, which is consistent with the analytical model results in the work of Zong et al. [16] and the simulation results in the work of Sary et al. [55].

Based on the exit velocity profile shown in Figure 4.13, the temporal variation of the cavity density in the transient stage can be computed using the model proposed by Zong & Kotsonis [39]. Following the same assumption made in Section 4.3 (mean cavity pressure: 103 kPa), the mean cavity temperature as a function of the elapsed cycles can be es-

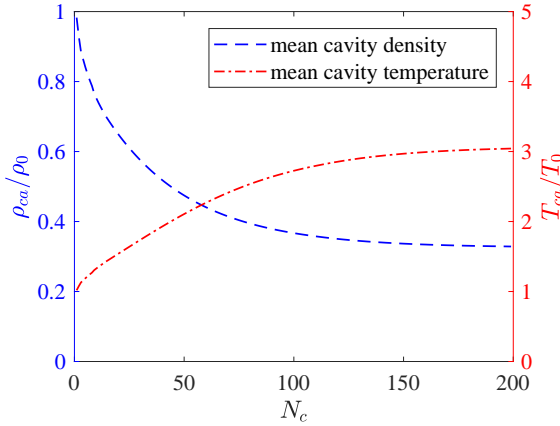


Figure 4.15: Variation of mean cavity density and temperature during transient stage at $f^* = 1.056$

timated. Figure 4.15 shows the variation of ρ_{ca} and T_{ca} pertaining to the first 200 pulses. Although the exit velocity already exhibits periodic variation after 20 cycles (Figure 4.13), the mean cavity density and temperature are not stabilised until $N_c = 129$ (convergence criterion: relative variation $< 5\%$). The slow convergence rate can be attributed to the low value of expelled gas mass ($< 5\%$) which limits the mass exchange rate between the actuator cavity and the outer environment.

The mean cavity temperature shows a steady increase with the cycle number (N_c), due to the continuous heat accumulation in the cavity during the transient stage. This increasing cavity temperature further affects the variation of the jet duration time. Anderson & Knight [54] indicated that the dimensionless jet duration time (T_{jet}^*) depends solely on the non-dimensional energy deposition (ϵ), regardless of the flow status in the actuator throat (sonic or subsonic).

$$T_{jet}^* = \frac{T_{jet} A_e \sqrt{\gamma R T_{ca}}}{V_{ca}} = g(\epsilon) \quad (4.1)$$

Therefore, with constant energy deposition and increasing mean cavity temperature as is the case for the transient stage, the jet duration time will decrease which is consistent with the observation in Figure 4.14(b).

4.6. ENERGY EQUILIBRIUM ANALYSIS IN ONE CYCLE

Once the PSJA reaches the quasi-steady working stage, the mean cavity temperature will remain constant and energy conservation should be satisfied in one working cycle. Starting from the energy conservation law, a relationship between the steady cavity temperature and the working frequency can be established. In a thermodynamic framework, the actuator cavity can be considered as an open system, exchanging both energy and mass with the surrounding environment. The first law of thermodynamics for the considered

open system is written as follows:

$$E_h - E_{ex} - E_{diss} = W \quad (4.2)$$

E_h is the gas heating energy, which is much smaller than the capacitor energy (E_c) due to inevitable energy losses on wire parasitic resistance and in gas ionization processes (see Figure 1.5, $E_h = E_c \eta_d \eta_h$); E_{diss} represents the heat dissipation term caused by convection and radiation. E_{ex} is the heat exchange brought by the mass exchange between the actuator and external environment since the air issued and ingested are of different temperatures. W stands for the cycle work. Under the assumption that the energy deposition stage, jet stage, and refresh stage are the constant-volume heating process, isentropic expansion process, and constant pressure cooling process, respectively, the cycle work and the heat exchange term can be estimated by the following equations, where ϵ_h denotes the ratio of heating energy to the initial internal energy of the cavity gas, E_h/E_g [23, 34]:

$$W = E_g [(1 + \epsilon_h) - (1 + \epsilon_h)^{1/\gamma}] \quad (4.3)$$

$$E_{ex} = c_v \Delta m (T_{ca} - T_0) = E_g [1 - (1 + \epsilon_h)^{-1/\gamma}] (1 - \frac{T_0}{T_{ca}}) \quad (4.4)$$

Under the condition of small ϵ_h (less than 0.5), Equations 4.3-4.4 can be further simplified using first-order approximation,

$$W \approx (1 - \frac{1}{\gamma}) \epsilon_h E_g \quad (4.5)$$

$$E_{ex} \approx \frac{1}{\gamma} (1 - \frac{T_0}{T_{ca}}) \epsilon_h E_g \quad (4.6)$$

Since the the heat capacity of the ceramic cavity shell is far beyond that of the cavity gas (approximately 10^4 times), a negligible temperature increase will be experienced by the ceramic shell during short-time operation (4 K for less than 200 pulses). Thus, the heat dissipation term can be written as follows:

$$E_{diss} = \frac{1}{f_d} h_c S_{in} (T_{ca} - T_0) + \frac{1}{f_d} k_{emi} k_{abs} \sigma S_{in} (T_{ca}^4 - T_0^4) \quad (4.7)$$

where h_c is the convective heat transfer coefficient (typical value for PSJA: $100 \text{ W}/[\text{K} \cdot \text{m}^2]$, [16]). S_{in} represents the area of the cavity internal surface. σ is the Stefan-Boltzmann constant. k_{emi} and k_{abs} stand for the emissivity of the cavity gas and the absorptivity of the ceramic shell respectively. k_{emi} depends on the chemical composition of the gas (CO_2 , H_2O et al.) and is estimated to be less than 0.01 for the tested cases (modeled as humid air due to seeding, reference pressure: 1 atm; reference length: 0.01 m) [113]. In the range of $300 \text{ K} < T_{ca} < 900 \text{ K}$, the ratio of radiative heat term to convective heat term in Equation 4.7 is computed to be less than 0.03, indicating negligible radiative heat transfer between the ceramic shell and the cavity gas. Substituting Equations 4.5-4.7 to Equation 4.2, the relationship between the mean cavity temperature/ density and discharge frequency can be derived as shown in the following equation.

$$\begin{cases} \frac{\rho_{ca}}{\rho_0} = \frac{T_0}{T_{ca}} = \frac{2}{1 + \sqrt{1 + 4(2 - \sqrt{2})f_d/f_c}} \\ f_c = \frac{(2 - \sqrt{2})h_c\gamma S_{in}T_0}{E_h} \end{cases} \quad (4.8)$$

As a result, the mean cavity density is inversely proportional to the square root of f_d/f_c . f_c is termed as a thermal cut-off frequency, quantifying the ratio of convective heat transfer rate to heat addition rate. The coefficient is chosen as $2 - \sqrt{2}$ such that ρ_{ca}/ρ_0 is reduced to 0.707 (3 dB) when $f_d/f_c = 1$. With an unchanged heating energy, f_c is positively proportional to the convective heat transfer coefficient and the area of cavity internal surface. By contrast, when h_c and S_{in} remain constant, f_c reduces with increasing heating energy.

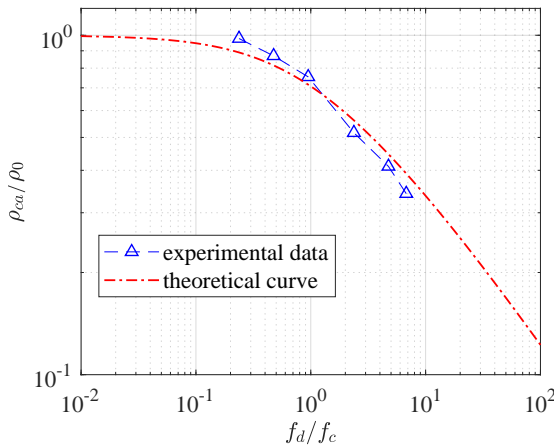


Figure 4.16: Comparison between theoretical and experimental cavity density at increasing frequency

Using Equation 4.8 to fit the experimental data shown in Figure 4.6, a good agreement is obtained as shown in Figure 4.16. The fitting value of f_c is 210 Hz. Below $0.1f_c$, the cavity density is close to ambient density and the frequency effect can be neglected. Beyond f_c , a significant drop of cavity density is exhibited which is detrimental to the repetitive performance of the PSJA. To obtain a higher value of f_c , the actuator cavity should be properly designed to accelerate the heat exchange between the cavity shell and the cavity gas. For example, slender cavities with large height-to-diameter ratio are recommended to increase the area of internal surface at a fixed cavity volume; Sharp corners in the actuator cavity should be avoided to improve the recirculation of internal flow, thus to increase the overall convective heat transfer coefficient. Additionally, for the same actuator geometry, large energy deposition will result in a fast decay of cavity density with increasing frequency. This fast declining cavity density can be further propagated into the three integral parameters (expelled gas mass, jet impulse, and jet

mechanical energy). Thus, to maintain a relatively high repetitive performance of the PSJA, the input energy should also be limited.

Revisiting Figure 4.6, the trend of increasing cavity temperature with increasing frequency can be interpreted from the perspective of energy equilibrium. Specifically as the frequency goes up, the energy deposited in the cavity increases linearly. According to the second law of thermodynamics (Equation 4.2), the difference between the energy deposited and the cycle work done to the external environment must be dissipated to a heat sink (namely, the surrounding air). The heat dissipation rate is related to both the heat transfer coefficients and the temperature difference between the cavity gas and the ambient air ($T_{ca} - T_0$, Equation 4.7). Consequently, for constant heat transfer coefficients, the mean cavity temperature at the steady state (T_{ca}) has to increase with the actuation frequency to meet the energy equilibrium in the actuator cavity

4.7. CONCLUSIONS

In this chapter, the influence of the dimensionless frequency on performance characteristics of a two-electrode PSJA was investigated in a wide range from $f^*=0.037$ to $f^*=1.056$, by virtue of a high-speed planar PIV system. Several conclusions can be drawn from the experimental analysis.

As frequency increases, the jet duration time drops monotonically, whilst the peak suction velocity goes up. The mean suction rate in one cycle increases with actuation frequency and becomes comparable with the mean ejection rate at $f^* \geq 0.739$. The three integral parameters (M_e , I_p , and E_m) decreases monotonically with increasing frequency, which is mainly attributed to the reduced cavity density. In one cycle, the impulse produced by the jet expulsion is partially counteracted by the inevitable suction flow. The proportion that is canceled is initially less than 10% and grows to 33% at $f^* = 1.056$. In the time-averaged flow field, the jet centreline velocity (\bar{U}_c) changes non-monotonically with the axial coordinate (x -coordinate). The peak centreline velocity normalized by $f_d L_e$ remains at around 1.5 for low-frequency operation ($f^* < 0.148$) and drops slowly to 1.0 afterwards. Peak values of \bar{U}_c are reached between $1 < x/D < 4$, and the decay rate of \bar{U}_c increases with the frequency. The jet spreading rate of the PSJ is much higher than comparable steady jets, decreasing with increasing frequency.

During the transient working stage of the PSJA at $f^* = 1.056$, the exit velocity trace elapses 20 cycles to stabilize. In comparison to the relatively fast convergence of the exit velocity, approximately 130 cycles are needed for the mean cavity density/ temperature to reach steady values, which is caused by the small expelled gas mass (approximately 5% of the initial cavity mass). Based on the energy equilibrium analysis of the cavity gas in one cycle, the mean cavity density decreases monotonically with the square root of the discharge frequency, and the declining rate is governed by a thermal cut-off frequency (f_c , 210 Hz for the current study). f_c is directly proportional to the convective heat transfer coefficient between the actuator shell and cavity gas, as well as the area of the cavity internal surface. A high value of f_c corresponds to a slow decay of the mean cavity density at high-frequency operation.

5

EFFECT OF ORIFICE SHAPE

5.1. INTRODUCTION

AMONG all the geometrical parameter pertaining to a synthetic jet actuator, exit orifice plays a dominant role in determining the dynamics of the developing jets in quiescent condition. For non-plasma-based jets, the effect of orifice shape has been investigated extensively [8, 114, 115]. Results show that a noncircular exit jet has a much higher entrainment rate than a circular jet with the same exit area. Additionally, some complex phenomena including azimuthal distortion, break-up and axis switching are present in the self-induced motion of vortex rings issued from slot orifices [116]. This distinction in mixing and vortex evolutions can significantly change a given outer flow, such as the velocity profiles of boundary layer and its ability to resist an adverse gradient flow [70, 76]. Hence, the influence of orifice shape on flow field of PSJA needs to be identified towards improving control authority.

In the present study, two actuator configurations with different exit orifice shapes (circular orifice and slot orifice) but same exit area are characterised with high-speed Schlieren imaging and phase-locked PIV systems. The morphological differences of the evolving plasma synthetic jets caused by the distinct orifice shape are analysed from the perspective of both phase- and time-averaging. Several prominent flow phenomena including the propagating shock waves, vortex rings, asymmetry jets and axes-switching are focused, and their generation/evolution mechanisms are revealed.

5.2. EQUIPMENTS AND MEASUREMENT SYSTEMS

5.2.1. ACTUATOR, POWER SUPPLY AND DISCHARGE WAVEFORM

To concentrate on the influence of orifice shape and avoid any side effects brought by the high-frequency operation (e.g. reducing jet density, see Chapter 4), the actuator used in

Parts of this chapter are published as **H. Zong** & M. Kotsonis, *Characterisation of plasma synthetic jet actuators in quiescent flow*, Journal of Physics D: Applied Physics, **49**, 335202 (2016); **H. Zong** & M. Kotsonis, *Effect of slotted exit orifice on performance of plasma synthetic jet actuator*, Experiments in Fluids, **58**, 17 (2017).

this study (A1, see Figure 2.1 (a-c)) is working in single-shot mode (i.e. rather low repetition rate, 0.5 Hz), powered by discharge circuitry E1 (see Figure 2.2). All the three electrodes are configured, and the distance from tips of anode, cathode and trigger electrode to the actuator axis is fixed as 1, 2 and 0.5 mm, respectively. Two metallic lids with different orifice shapes but same exit area are machined, as shown in Figure 5.1. The first lid features a conventional circular exit orifice with a diameter of $D = 3$ mm. The second lid carries a rounded slot orifice, with a length of $l = 7.3$ mm and width of $w = 1$ mm resulting in an aspect ratio (AR: length/width) of 7.3. The throat length for the two orifices is 2 mm. Notwithstanding the distinct dimensions of the two exit orifices, the spatial coordinates throughout this study are normalized uniformly by D .

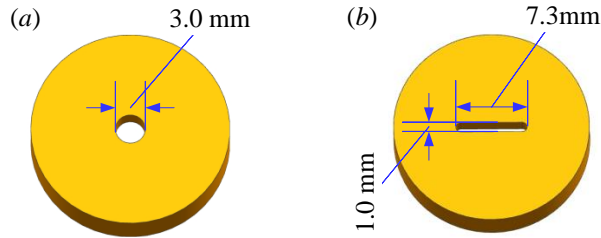


Figure 5.1: (a) Circular orifice; (b) Slot orifice.

For all the tests performed in this chapter, an energy-storing capacitor of $C_1 = 1 \mu\text{F}$ is used and its initial voltage is charged to $V_1 = 2.5$ kV, resulting in a fixed non-dimensional energy deposition of $\epsilon = 5.2$. Electrical measurements are performed towards quantifying the discharge behaviour. The trigger voltage (u_t), discharge voltage (u_d) and discharge current (i_d) are measured by a high-voltage probe (LeCroy, PPE20kV) and a current monitor (Pearson, Model 325), and recorded by a digital oscilloscope (Tektronix, TDS 3054 C) at 25 MHz sampling rate. The measurement stations for u_t , u_d and i_d are at the trigger electrode, anode, and the cable between cathode and ground, respectively (see Figure 2.2). Based on the discharge voltage and current, the instantaneous discharge power can be computed as $P_d = u_d \cdot i_d$.

Typical waveforms for all the discharge parameters are shown in Figure 5.2. The breakdown instant is set as the origin of time axes. Prior to the breakdown of electrode gap, u_t increases almost linearly with time and peaks at about 7 kV. During discharge ignition, the capacitor voltage drops sharply from 2.5 kV to approximately 0.1 kV. This sharp drop is caused by the change of load characteristics in the discharge channel. Prior to breakdown, the discharge channel can be treated as an infinite resistor and all the capacitor voltage is applied on the gap. During discharge ignition, a spark (arc) is formed and the resistance of discharge channel drops significantly from $+\infty$ to $O(0.1 \Omega)$ [99]. Note that the discharge capacitor is not an ideal capacitor. Its parasitic resistance and inductance can be comparable to or even larger than the wire inductance and the arc resistance. Thus, a considerable portion of the initial voltage (2.5 kV) is burdened by the parasitic resistance and inductance of the discharge capacitor. As a result, the voltage drop at the arc, namely the measured discharge voltage after discharge ignition, is very small ($O(0.1 \text{ kV})$).

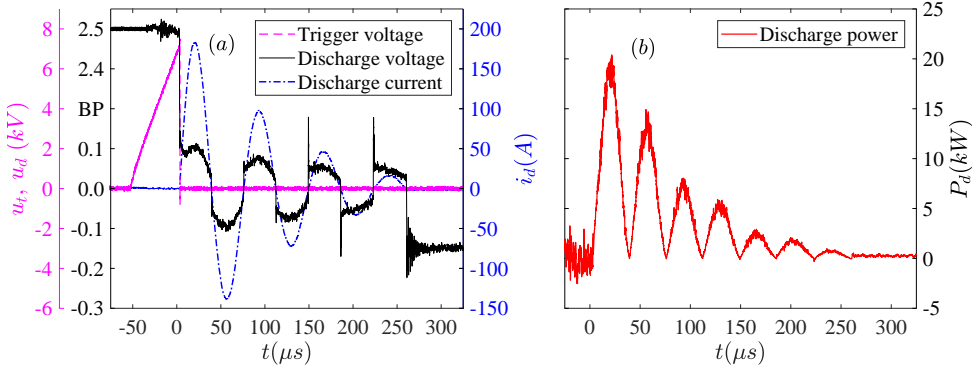


Figure 5.2: Discharge waveforms. (a) Trigger voltage (u_t), discharge voltage (u_d) and discharge current (i_d); note that the vertical axis for applied voltage has a break point (BP) and the scale jumps from 0.2 kV to 2.3 kV. (b) Instantaneous discharge power (P_d).

After discharge initialisation, the capacitor voltage experiences a quasi-periodical oscillation with a period of about $75 \mu\text{s}$. During the oscillation, the voltage oscillation amplitude gradually decreases. Based on the measured voltage and current signals, the duration of the arc discharge is estimated to be $260 \mu\text{s}$. The variation of the discharge current is similar to the arc voltage, and the observed peak discharge current is 183 A. The periodical oscillation behaviour of discharge waveforms indicates that the discharge circuit behaves similarly to a RLC circuit [43]. Regarding the instantaneous discharge power, 7 pulses with decreasing amplitudes are observed. The power pulse period is estimated to be $38 \mu\text{s}$, half of the oscillation period of the discharge voltage. Moreover, the peak discharge power reaches 20 kW and no negative values are observed. By integrating the instantaneous discharge power, the total discharge energy pertaining to one pulse (E_d) is estimated to be 1056 mJ, resulting in a discharge efficiency of $\eta_d = E_d/E_c = 34\%$, which is close to that of a comparable three-electrode PSJA reported in [117] ($\eta_d = 33\%$).

5.2.2. FLOW DIAGNOSIS SYSTEMS

High-speed Schlieren imaging and phase-locked Particle Image Velocimetry (PIV) are exploited to visualise the induced flow field of the PSJA. A typical Z-type Schlieren system, consisting of a light source, two concave mirrors, and a high-speed camera (PCO Dimax S4, 12 bit, 4MPix), is constructed on a self-balancing optical table. A continuous light source (Euromex Illuminator, EK-1) in conjunction with an adjustable circular iris provides illumination to the Schlieren arrangement. The light beam radiated from the point light source is first reflected by two concave mirrors (diameter: 30 cm, focal length: 3 m), subsequently converged by a convex lens (focal length of 200 mm) and finally projected directly on the camera sensor. Between the camera sensor and the convex lens, a knife edge is placed in vertical orientation, facilitating visualisation of density gradients in the direction parallel to the exit plane. 12-bit Schlieren images are recorded at $1.28\text{-}\mu\text{s}$ exposure time and 20 kHz acquisition frequency. The resolution and scaling factor of the images are $240 \times 500 \text{ pixels}^2$ and 0.0926 mm/pixel , respectively. After the acquisition, Schlieren images are post-processed, using techniques of background subtraction and

intensity range normalisation, in order to improve the contrast ratio [32]. For each case, 20 repetitions of single-pulse actuation are recorded to obtain the statistically averaged jet front positions.

The planar, two-component PIV system consists of a dual-head Nd: YAG laser (Quantel, CFR PIV-200, 200 mJ/pulse) and a LaVision camera (Imager Pro LX, resolution: 3248×4872 pixels). The laser beam is conditioned using a set of optics and knives into a sheet of approximately 0.6 mm thickness, illuminating the area in the vicinity of the actuator exit orifice. A field of view of $34 \times 51 \text{ mm}^2$ is imaged with a Nikon Micro-Nikkor 200 mm macro lens. The actuator is placed in a close Plexiglas box to ensure quiescent flow conditions. Both the box and the cavity are seeded with dielectric oil-based particles (Shell Ondina, mean diameter: $1 \mu\text{m}$), generated by an atomizer (TSI, 9302). The seeding provided to the actuator cavity is controlled by a solenoid valve (FESTO, MHJ10), and kept switched off before the discharge, in order to eliminate the interference on the developing flow field. Davis 8.3 software is used to record and process the particle images. For vector processing, an interrogation window of 32×32 pixels and an overlap ratio of 75% is adopted resulting in a final vector spacing of 12 vectors /mm.

5

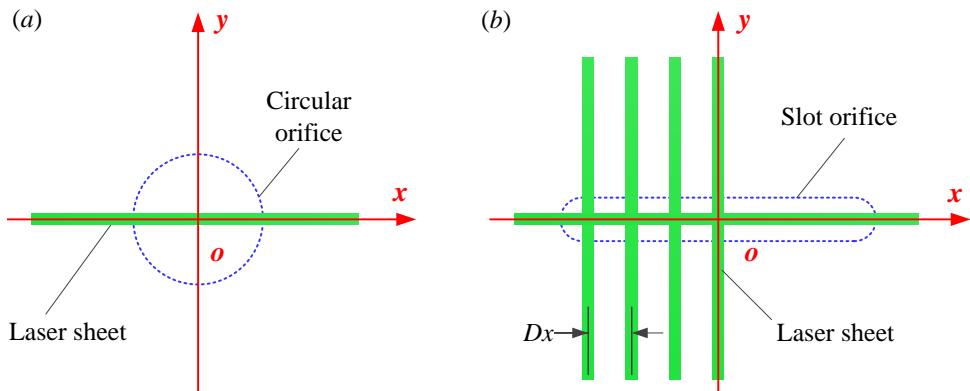


Figure 5.3: PIV measurement planes: (a) circular orifice; (b) slot orifice.

The deterministic time delay between discharge ignition and PIV recording (t) ranges from $100 \mu\text{s}$ to $2000 \mu\text{s}$ in order to track the evolution of the developing flow field. The time step between two subsequent phases is chosen to be $50 \mu\text{s}$ or $100 \mu\text{s}$ to facilitate the direct comparison with Schlieren results. For each phase, 200 PIV image pairs are recorded to obtain phase-averaged velocity fields. For the circular orifice, only the symmetry plane is chosen as the measurement plane. However, in the case of slot orifice, a total of 5 planes are measured, as shown in Figure 5.3. One of the measurement planes is the coordinate plane xz ($y=0 \text{ mm}$). The remaining four planes are aligned in the yz plane, starting from $x=0 \text{ mm}$ and ending at $x=3 \text{ mm}$, with a step of 1 mm.

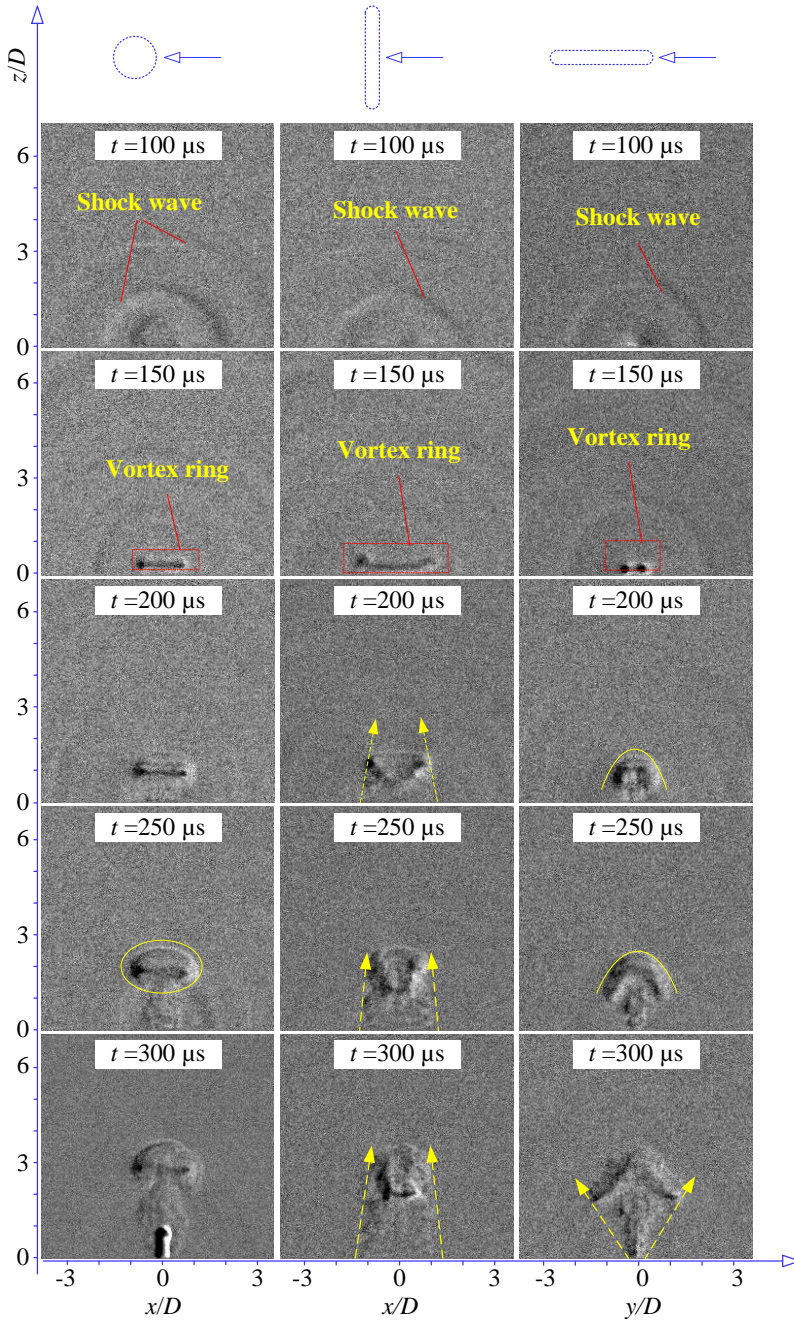


Figure 5.4: Instantaneous Schlieren images between $t=100 \mu\text{s}$ and $t=350 \mu\text{s}$. Orifice shape and view direction are indicated on the top line.

5.3. SCHLIEREN RESULTS

5.3.1. FLOW FIELD EVOLUTION

Instantaneous Schlieren images between $t=100 \mu\text{s}$ and $t=3000 \mu\text{s}$ are shown in Figures 5.4-5.5. At $t=100 \mu\text{s}$, several shock waves are formed due to the rapid pressure rise in the actuator cavity caused by the capacitive arc discharge. In the case of slot orifice, the observed shock wave is in a bow shape in the xz plane, slightly different from the half-circle shock waves pertaining to round orifice. A clearly identified starting vortex ring is observed at $t=150 \mu\text{s}$. Combining the two Schlieren views in xz plane and yz plane, it becomes evident that the starting vortex ring of the slotted actuator exhibits an elongated shape. This is largely expected, since vorticity distribution of the starting vortex ring is conditioned by the shear layer detached from the lip of exit orifice. Additionally, some weak shock waves, possibly caused by shock wave reflection in the cavity, can still be seen at $t=150 \mu\text{s}$. For the circular orifice, the front vortex ring gradually grows in size, and finally evolves into a semi-spherical vortex, due to rigorous entrainment of the surrounding fluids. However, for slot orifice, quite different scenarios are observed in the two measured planes. The jet body in the xz plane shrinks during the propagation, and distance of the developing vortex pair reduces. In the yz plane, the jet body quickly expands and assumes a mushroom shape at $t=250 \mu\text{s}$. Overall, the projections in xz and yz planes suggest a rapid deformation of the starting vortex for the case of the slot orifice. This deformation becomes negligible after $t=700 \mu\text{s}$, where the slot jet assumes almost the same width in both x direction and y direction, indicating that the narrow jet body is gradually evolving into a cylindrical shape [118].

In addition to the topological evolution of the jet, another two interesting phenomena are perceived in the Schlieren visualization. The first one is related to the time variation of jet grayscale. As the grayscale in Schlieren images reflects the integral of the density gradient along the view direction (see 2.3.1), a bright/dark region suggests a large density variation. Regardless of orifice shape, between $t=400 \mu\text{s}$ and $t=700 \mu\text{s}$, a distinctive jet is expelled from the cavity, illustrating that the exiting fluid density changes significantly during this period. The initially issued jet typically is supposed to be of high density close to the ambient value (cold gas), while the low-density jet (hot gas) always comes out at a later time. After $t=700 \mu\text{s}$, the jet body becomes less distinctive again, meaning that exit density increases in later jet stage. This agrees well with the simulation results in [58], where the jet exit density in one period first drops sharply, then sustains a relatively low value, and finally recovers. The source of the sudden change of jet exit density and temperature lies in the non-uniform heating nature of arc discharge. Specifically, during the energy deposition stage, most of the thermal energy is released locally in the inter-electrode region, which is only a small portion of the cavity volume located approximately 7.5 mm lower than the exit orifice. This region is dominated by high pressure, high temperature and low density fluid. Pressurization of the remaining region mainly relies on the fast propagation and reflection of arc-induced shock waves. Therefore, the initial issued jet ($t=300 \mu\text{s}$) is comprised of relatively cool air near the exit orifice characterized by high density, whereas the later issued jet ($300 \mu\text{s} < t < 700 \mu\text{s}$) is the low-density air directly heated by arc discharge.

The second interesting feature is the asymmetry of the jet. As shown in Figure 5.5, the front vortex ring is severed from the jet body after $t=500 \mu\text{s}$, and gradually leans to

the right side during its propagation. This feature has no relationship with statistical convergence, and still exists when the instantaneous images are phase-averaged over 20 samples. Detailed interpretations will be provided in Section 5.4.1.

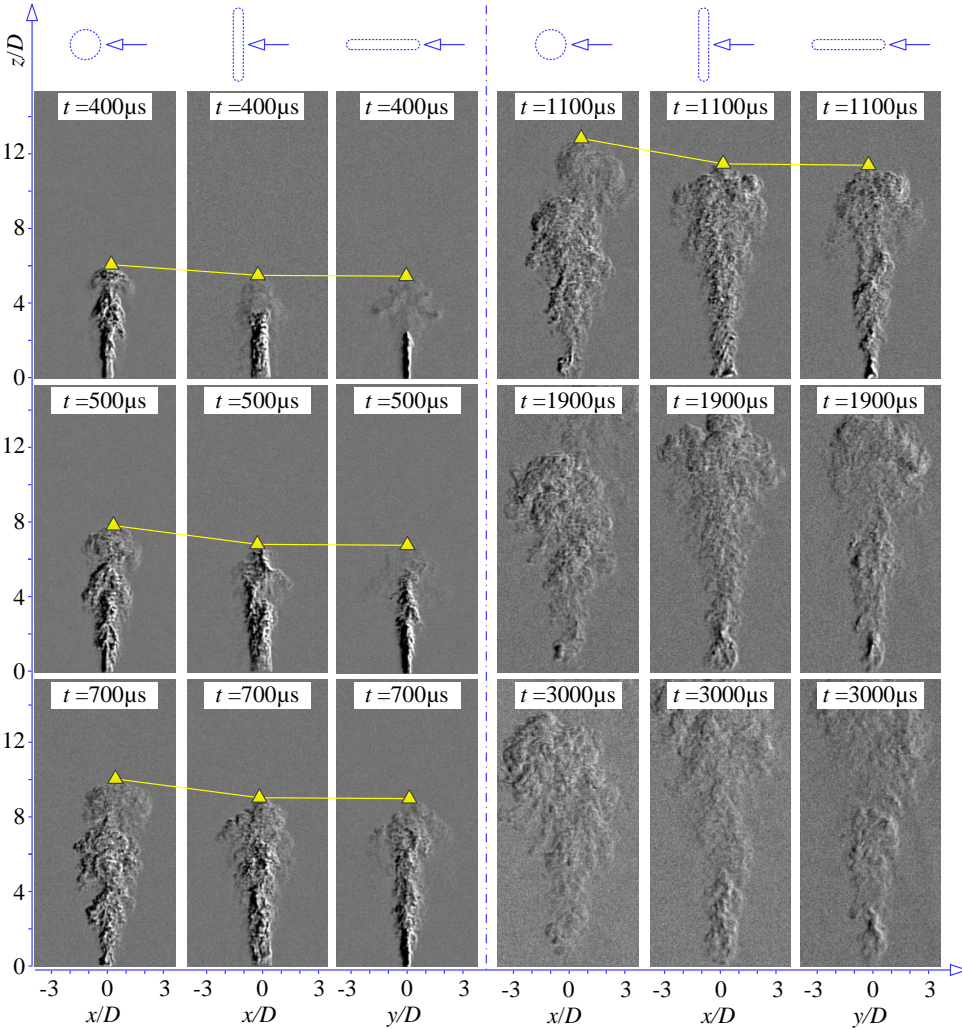


Figure 5.5: Instantaneous Schlieren images between $t=400 \mu\text{s}$ and $t=3000 \mu\text{s}$. Orifice shape and view direction are presented on the top line. The positions of jet front are indicated by yellow triangles.

5.3.2. VORTEX RING PROPAGATION VELOCITY

In Figure 5.5, the jet front positions are indicated by yellow triangles. It is clear that the slot jet propagates significantly slower than the round jet. This is attributed to viscous drag. More specifically, it is noted that although the exit area between the round and slot

orifice is identical, the perimeter of slot orifice is significantly larger than the perimeter of circular orifice. As such, the contact area between the high-speed core of the jet and the surrounding quiescent fluid is larger for the slot jet, which results in a higher viscous drag and lower propagation speed. Through accurate detection of the position and trajectory of the jet front, the temporal evolution of the jet front velocity (denoted as U_v , close to vortex ring velocity) can be estimated. Statistically averaged jet front velocity over 20 pulse repetitions are shown in Figure 5.6. The camera sensor detection error is approximately 2 pixels, while the variation of jet front position from shot to shot is typically 3 pixels. Based on these error bounds and the corresponding frame interval ($50 \mu\text{s}$), the uncertainty in velocity calculation can be determined, as indicated by error bars in Figure 5.6. Note that the performance parameters pertaining to the slot orifice shown in Figure 5.6 are the average of the two values obtained from the two view directions.

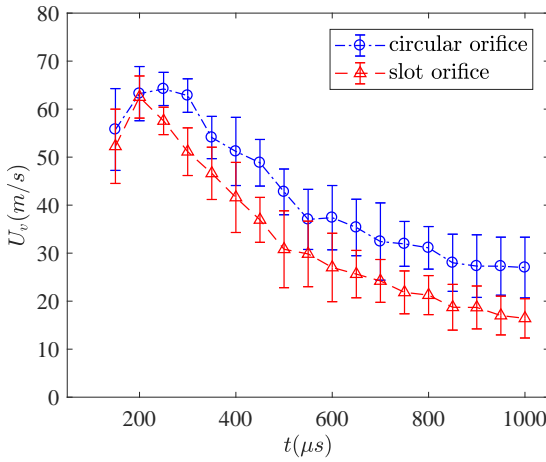


Figure 5.6: Temporal evolution of the jet front velocity (U_v) for the two tested actuators

5.4. PIV RESULTS

5.4.1. PHASE-AVERAGED VELOCITY FIELD

For both slot and circular orifices, time evolution of the phase-averaged velocity fields in symmetry planes between $t=100 \mu\text{s}$ and $t=200 \mu\text{s}$ are shown in Figure 5.7. Here, the two-dimensional Euclidean sum of the measured velocity components is denoted as $U_{xz} = (U_x^2 + U_z^2)^{1/2}$ and $U_{yz} = (U_y^2 + U_z^2)^{1/2}$ in the xz and yz plane respectively, where U_x , U_y and U_z are the components of velocity in the three coordinate directions.

At $t=100 \mu\text{s}$, a starting jet is issued out of the actuator cavity for both cases, and the jet velocity pertaining to the slot orifice (40 m/s) is much higher than that of the circular-orifice actuator (20 m/s). No spherical structures corresponding to the shock waves can be observed at this time delay, which seems to contradict with the Schlieren results shown in Figure 5.4 and can be attributed to the discharge timing uncertainty. Specifically, the breakdown voltage for a fixed electrode gap is not deterministic and fluctuates inevitably from pulse to pulse. This uncertainty in discharge voltage is fur-

ther propagated to the discharge timing (fluctuation level: $O(1 \mu\text{s})$), leading to a dispersion of the shock wave location in a wide band (5 mm). Consequently, the shock waves are smoothed out by statistical averaging and becomes undetectable in phase-averaged velocity fields.

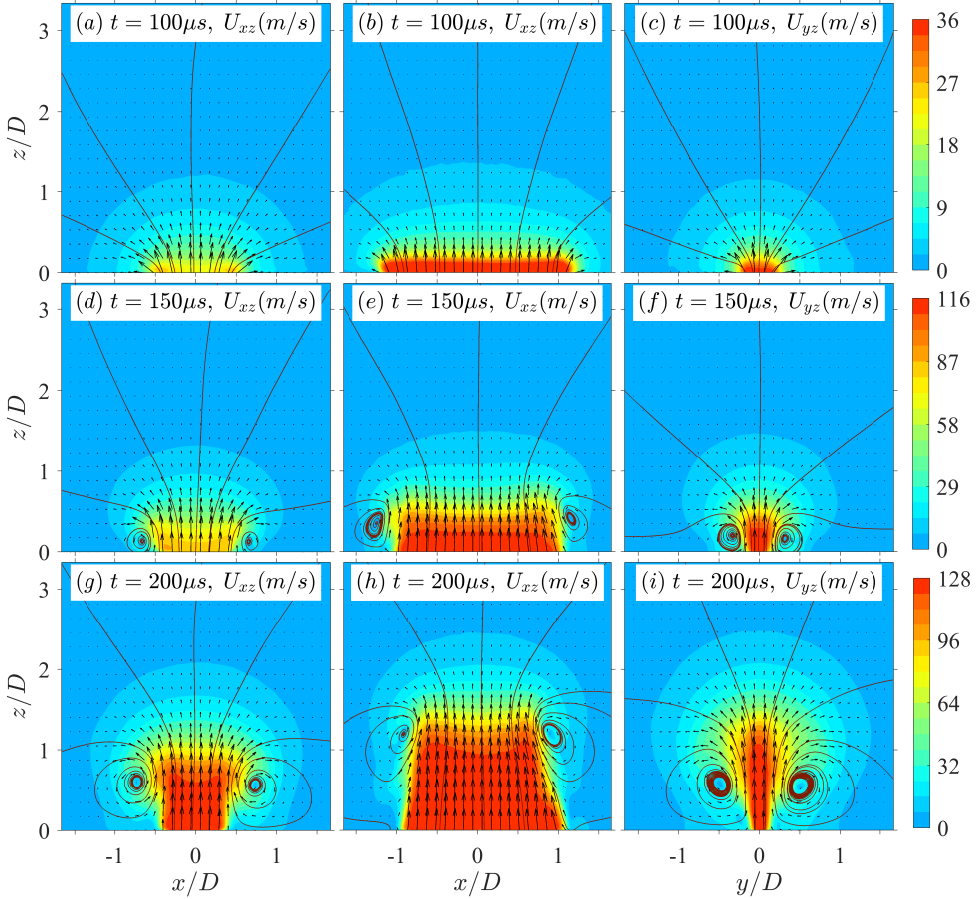


Figure 5.7: Phase-lock-averaged velocity field between $t=100 \mu\text{s}$ and $t=200 \mu\text{s}$. From left to right, the orifice shape and measurement plane pertaining to each row are consistent with that in Figure 5.4. Magnitude and direction of the in-plane velocity are displayed as contours and arrows, respectively. The solid red lines superimposed on the contours are streamlines.

In the case of circular orifice, a vortex ring is formed near the exit at $t=150 \mu\text{s}$, which is associated with the rolling of a shear layer. As the jet continues ($t=200 \mu\text{s}$), the vortex ring grows in size due to entrainment of the surrounding fluids. The vortex ring is characterized by the high velocities in the centre and low speed at the vortex core, which agrees well with the features of Hill's spherical vortex. For the slot orifice actuator, the vorticity in the shear layer rolls into an elongated vortex ring at $t=150 \mu\text{s}$. During the axial propagation ($t=200 \mu\text{s}$), the major axis of the elongated vortex ring (in the x direc-

tion) shrinks while the minor axis (in the y direction) extends. This signifies the onset of axes-switching phenomenon, which agrees well with the observations pertaining to steady slot-orifice jets [116, 118].

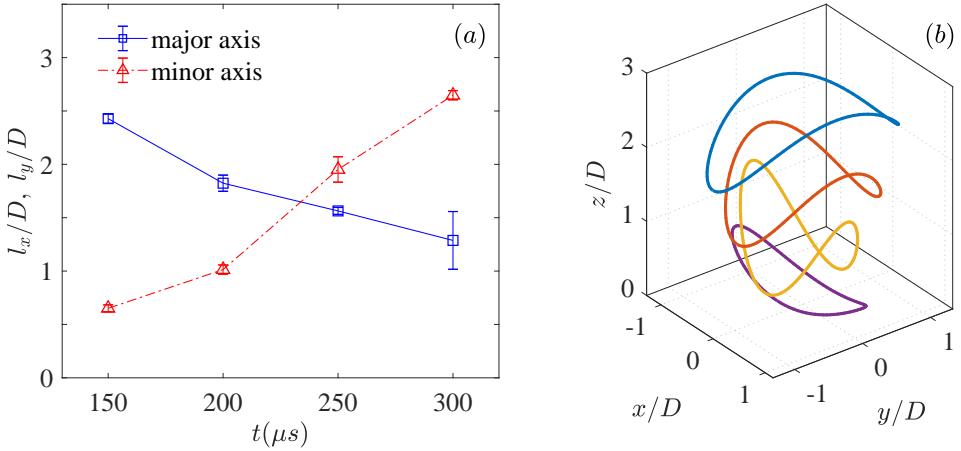


Figure 5.8: Elongated vortex ring issued from the slot orifice. (a) Variation of the major (l_x) and minor (l_y) axis. (b) Shape transformation during the axial propagation.

Under the assumption that projection of the front vortex ring on the xy -plane is an ellipse, a schematic diagram of the vortex ring transformation can be obtained based on the vortex core coordinates extracted from velocity fields. This is shown in Figure 5.8. During the propagation of the starting vortex ring, the length of the minor axis (l_y) gradually increases, and finally exceeds the length of the major axis (l_x) at approximately $t=250 \mu s$. This axes-switching behaviour agrees well with the simulation results in [119], and the fast entrainment rate along the y -direction is conjectured to be the principle cause of such axis-switching phenomenon. In addition, the shape of the vortex ring becomes severely warped at the later stages of propagation ($t>150 \mu s$). Warping is directly related to the disparate propagation velocity of different parts of the vortex ring. The motion of the front vortex ring is governed by both the momentum input of the high-speed core jet and the viscous drag caused by the shear and entrainment between the jet core and surrounding quiescent fluid. When the vortex ring is initially expelled, it is governed by an almost constant propagation velocity along its perimeter. However, the long edge (along the major axis) of the core jet experiences higher viscous drag than the short edge (along the minor axis) due to larger contact area with the quiescent fluid. As a result, the strong shear and the high entrainment rate along the y direction restrict the propagation velocity of the long edge of the front vortex ring, leading to the observed warping.

The phase-averaged velocity fields between $t=300 \mu s$ and $t=500 \mu s$ are shown in Figure 5.9. In Figure 5.9 (c, f, i), the high-speed jet seems to vacillate to the left and right, during the downstream propagation. This is possibly caused by the Kelvin–Helmholtz instability. In order to verify this phenomenon, the velocity field at $t = 400 \mu s$ is post-processed as follows. First, a threshold value of 70 m/s is selected to extract the high-

speed jet body from the background (Figure 5.10 *a*). Subsequently, the angle of each velocity vector is calculated and averaged along the y -direction. Variation of the averaged jet angle (denoted as θ) is shown in Figure 5.10 (*b*).

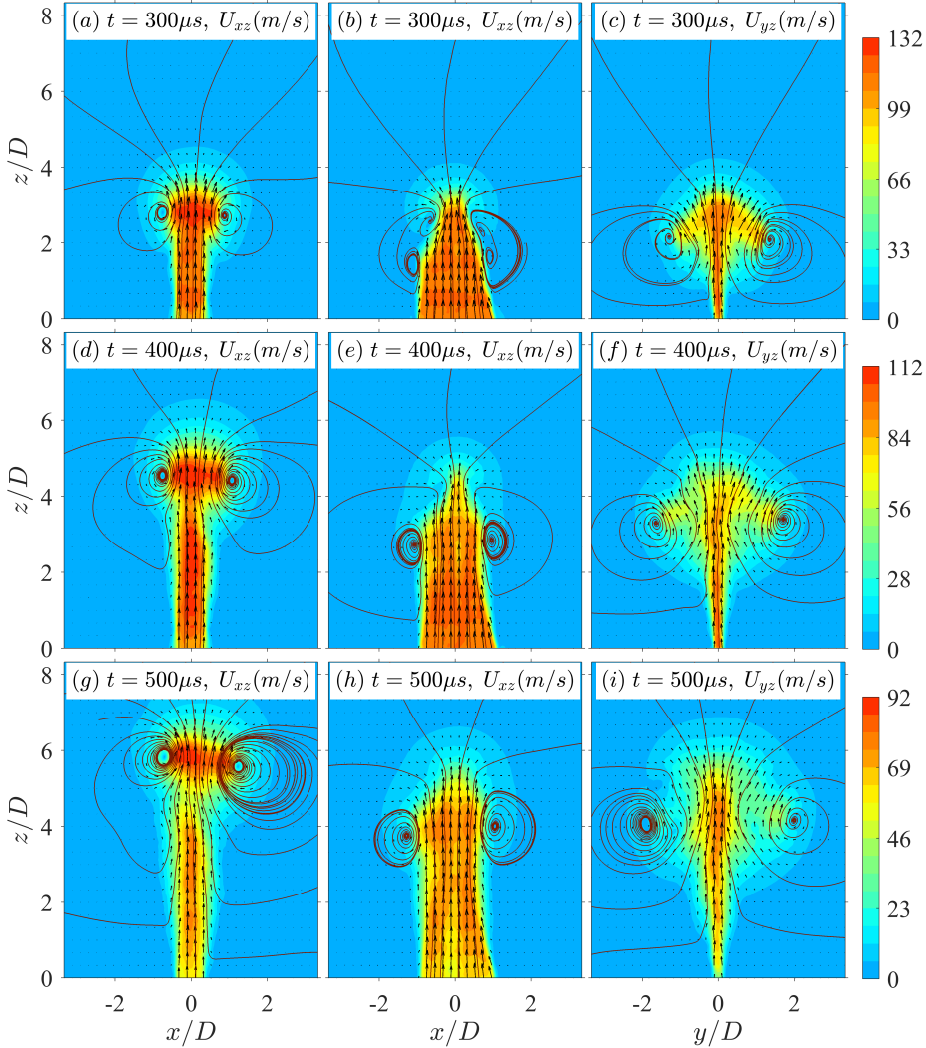


Figure 5.9: Phase-lock-averaged velocity field between $t=300 \mu\text{s}$ and $t=500 \mu\text{s}$. The plotting methods are identical to that in Figure 5.7.

When the jet propagates away from the exit orifice, the jet angle oscillates periodically, with a growing amplitude. This agrees well with the basic features of K-H instability, where the initial small disturbance is amplified in an exponential way [120]. The issued slot jet is essentially a thin shear layer, which provides the environment for

growth of K-H type instability. Yet, the identification of the origin of instability is less straightforward. In Figure 5.10, the evident periodic variation of the jet angle, even after phase-averaged operation, suggests a strong periodicity of the initial disturbance. Based on the mean jet velocity at $t=400 \mu\text{s}$ (approximately 70 m/s) and the averaged wavelength in Figure 5.10 (b) (2.6 mm), the disturbance period is estimated to be $37 \mu\text{s}$, which is close to the period of discharge power (Figure 5.2), indicating that the initial disturbance frequency and phase is locked to the discharge itself. As stated in Section 5.2.1, P_d oscillates periodically with a decreasing amplitude. Due to the asymmetric electrode configuration, the oscillating discharge energy imposes a periodic disturbances to the initial jet exit angle, thus exciting the K-H instability and amplified as a wavy jet.

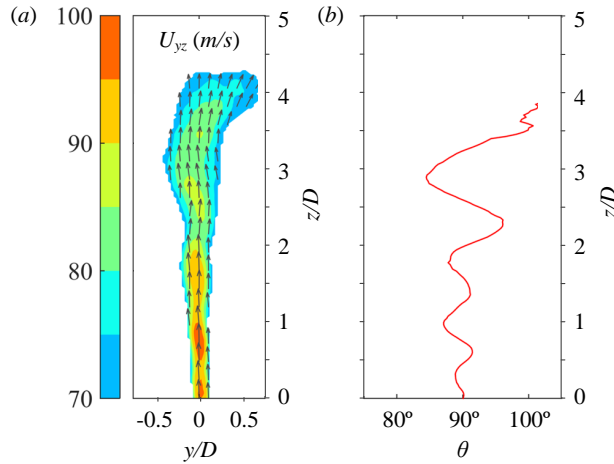


Figure 5.10: (a) The jet body at $t = 400 \mu\text{s}$ extracted from a criterion of $U_{yz} > 70 \text{ m/s}$. Magnitude and direction of the in-plane velocity are displayed as contours and arrows, respectively. (b) Axial variation of the jet angle (vertical direction is defined as 90 degrees).

Figure 5.11 presents the phase-averaged velocity fields between $t=600 \mu\text{s}$ and $t=1000 \mu\text{s}$. From $t=400 \mu\text{s}$ to $t=600 \mu\text{s}$, the exit velocity drops sharply from 120 m/s to about 40 m/s. The profile of the slot jet attains the form of a tadpole with its head surrounded by the front vortex ring (Figure 5.11 b–c). No observable jet is issued at $t=800 \mu\text{s}$ and a weak suction flow emerges afterwards (not shown). However, this such flow is rather short-lived, as a second jet pops out at $t=1000 \mu\text{s}$ although with a very small velocity ($< 10 \text{ m/s}$). In the case of slot orifice, the extents of the front vortex ring as well as the slot jet body show little difference in xz - and yz -plane, signifying that the initial quasi 2D-jet has evolved into an axisymmetric jet, which is consistent with the results from Schlieren imaging (see Figure 5.5). As a comparison, the jet expelled from circular orifice exhibits strong asymmetry in Figure 5.11 (a, d, g). The jet core slightly leans to the negative x -direction, whereas the front vortex ring tilts to the opposite direction.

The formation of this asymmetry phenomenon is an unstable process with positive feedback, as sketched in Figure 5.12. Two factors can trigger the amplification, including the asymmetric vorticity distribution (stage a) and the non-coaxis between the front vortex ring (FVR) and its trailing jet (stage b and stage c).

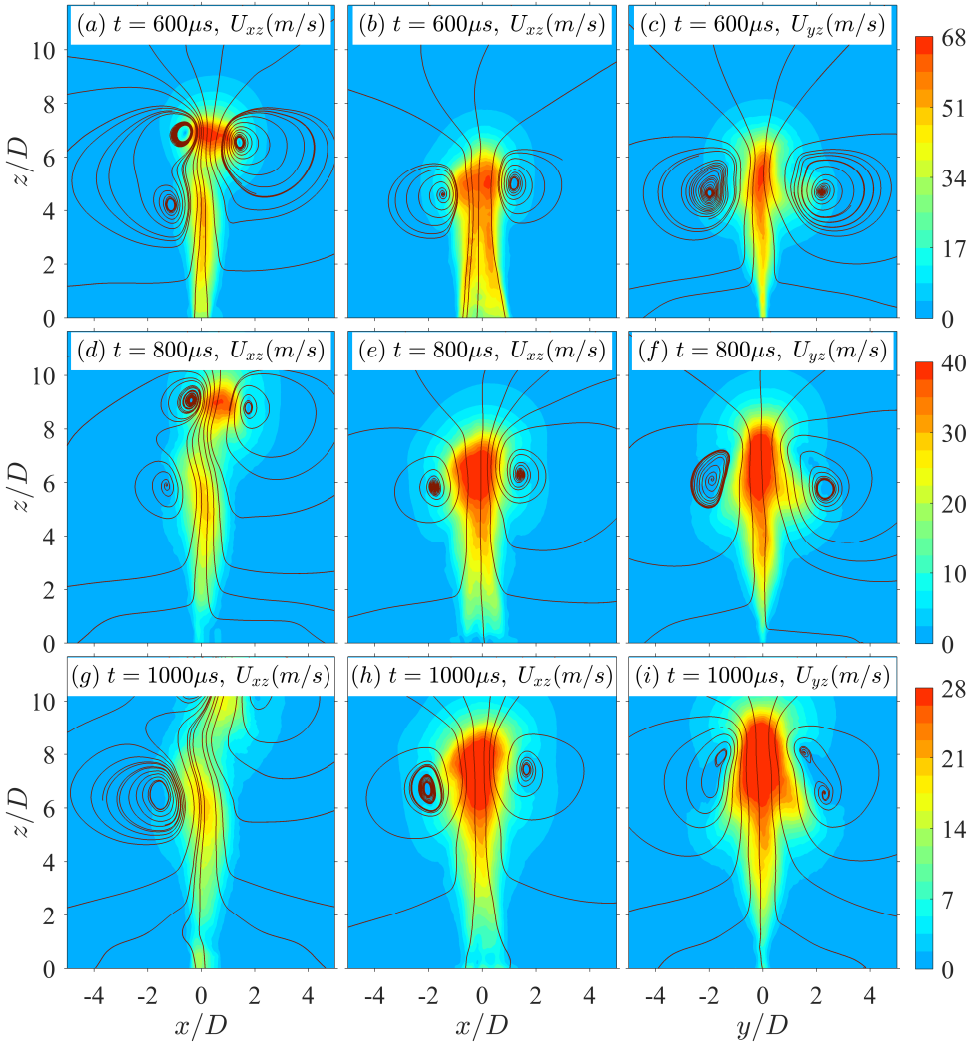


Figure 5.11: Phase-lock-averaged velocity field between $t=600 \mu\text{s}$ and $t=1000 \mu\text{s}$. The plotting methods are identical to that in Figure 5.7.

Let's first consider stage (a), where a small difference is exhibited w.r.t the vorticity distribution between the two sides of the vortex pair. Since the velocity induced by the vortex pair has a non-zero horizontal component, the initial vertical jet leans to the left side during propagation (stage b). This results in one side of the vortex pair receiving more momentum input than the opposite side. Thus the left side overtakes the right side and the vortex pair tilts slightly (stage c). The tilting of vortex pair further imposes a higher horizontal velocity on the trailing jet, which in turn increases the jet skew angle and amplifies the asymmetry (stage b-c). Consequently, the vortex pair and trailing

jet are disconnected, leaning to the opposite direction during later propagation, as evidenced by Figure 5.11.

For the investigated case of circular orifice, the asymmetry phenomenon is actually triggered by the slightly skewed jet at exit orifice. Specifically, the gap between the trigger electrode and cathode (2 mm), is larger than that between the trigger electrode and anode (1 mm). During the energy deposition stage, the arc heating region is not symmetric, so neither is the pressure distribution in the cavity. As a result of the nonuniform pressure distribution in throat inlet as well as the short throat length (2 mm), the jet is ejected with a small skew angle, which triggers the asymmetry amplification illustrated in Figure 5.12. It should be noted that the asymmetry electrode configuration does not always lead to an asymmetry jet. With decreasing orifice diameter, the ‘rectification effect’ of the throat (analogous to the honeycomb rectifiers in wind tunnels) enhances and the jet skew angle decreases. As such, the asymmetry in jet is less evident in the case of large value of L_{th}/D (i.e. small orifice diameter) [82].

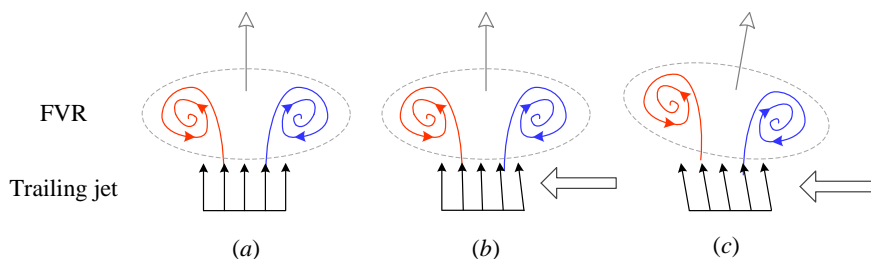


Figure 5.12: (a – c) Three stages of the asymmetry amplification. The front vortex ring (FVR) is sketched as streamlines. The high-speed trailing jet is indicated by arrows.

5.4.2. PENETRATION LENGTH AND EXIT VELOCITY

The previous analysis has shown apparent morphological differences between the two tested cases regarding the evolution of the jet core and the front vortex ring. It is thus instructive to evaluate whether the jet penetration length is also affected by the shape of the exit orifice. It must be noted here that the choice for an independent measure of the penetration length in quiescent conditions is not straightforward due to the absence of reference velocity. As such, a velocity contour line of 10 m/s is arbitrarily chosen as the jet edge. The y -coordinate of the upmost point of the 10 m/s contour line is defined as the penetration length (L_p). A preliminary sensitivity test shows that when the velocity contour line changes from 10 to 5 m/s, mean variation of the calculated penetration length is less than 2 mm. Figure 5.13 shows the time variation of the penetration length (L_p) as well as the derived penetration rate (defined as $V_p = dL_p/dt$). Note that the values pertaining to the slot orifice shown below in Figures 5.13-5.14 are the average of the two values obtained from the two symmetry planes.

Shortly after discharge ignition, the developing jet propagates away from the exit orifice and L_p increases monotonically. Prior to $t=250 \mu\text{s}$, the penetration rate for the circular orifice is slightly lower than that for the slot orifice. The peak value for V_p is (60 m/s) close to the peak jet front velocity identified with Schlieren imaging (Figure 5.6), which is

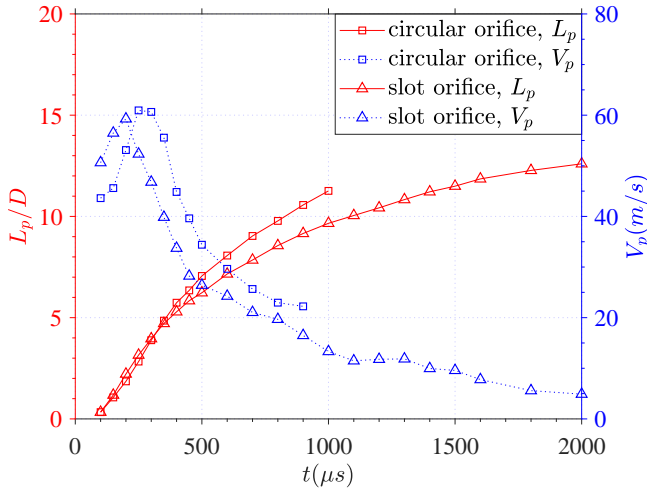


Figure 5.13: Variation of the penetration length (L_p) and penetration rate (V_p) with orifice shape.

expected from the non-dimensional analysis in Chapter 3. Between $t=250 \mu s$ and $t=900 \mu s$, the jet emanated from the circular orifice penetrates faster than that from the slot orifice, consistent with the basic trend shown in Figure 5.6. This difference in penetration rate can be once again attributed to the jet entrainment/spreading rate, which will be quantified in the next section. Owing to a constant exit area, the slot orifice case has a larger contact surface with the surrounding air, compared to the circular orifice case. This leads to a high entrainment rate of low-energy fluids and finally the slow penetration rate of the slot jet. The peak penetration length for both cases exceeds $10D$.

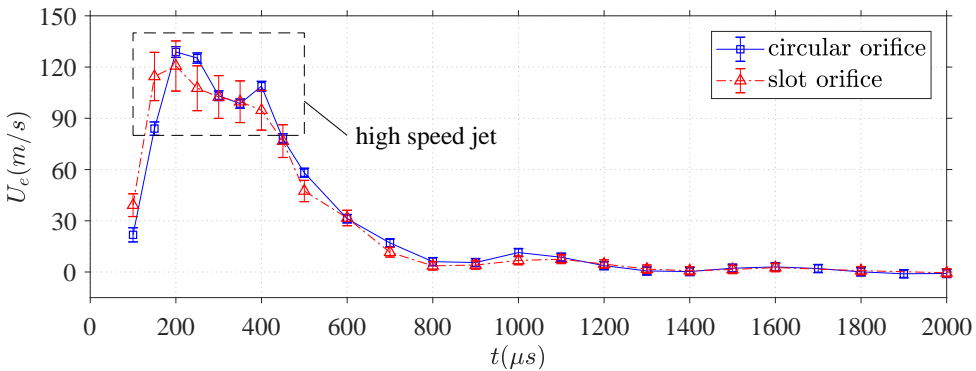


Figure 5.14: Time evolution of the spatially-averaged exit velocity (U_e) for the two tested orifice shapes.

Apart from L_p , another metric to measure the intensity of issued jet is the spatially-averaged exit velocity (U_e). For circular jet, U_e is well defined by Equation 2.4, whereas for slot jet, a simple arithmetic mean is used to compute the spatially averaged exit ve-

locity. Figure 5.14 shows the time evolution of U_e in the two investigated cases. Prior to $t=200 \mu\text{s}$, an acceleration stage is present, and the exit velocity increases rapidly from about 30 m/s to the peak value. Occurrence of the jet acceleration stage is related to the inertia of the throat gas [82]. Between $t=200 \mu\text{s}$ and $t=400 \mu\text{s}$, the exit velocity reaches a plateau, sustained at a relatively high level (100-130 m/s). The high-velocity plateau, absent from the results in previous Chapters (e.g. Figure 3.5), can be ascribed to the long discharge duration ($\sim 200 \mu\text{s}$, in contrast with less than $50 \mu\text{s}$ in Chapter 3). After $t=400 \mu\text{s}$, the exit velocity shows a linear decrease, and the first minimum value is reached at $t=800 \mu\text{s}$. Note that this minimum value is still a positive value, suggesting that the jet is still continuing at this time. After that, the jet velocity increases again, reaching a second maximum and a second minimum. It is evident that the emitting jet intensity presents an oscillatory amplitude variation. The oscillation period of the exit velocity is about $600 \mu\text{s}$, coinciding with the helmholtz natural oscillation period ($607 \mu\text{s}$) as expected. The refresh stage emerges at about $t=1900 \mu\text{s}$, indicated by a small negative exit velocity (fluid entering the actuator). Overall, the two velocity curves in Figure 5.14 collapse well, indicating that the orifice shape have no influence on the formation process of PSJs.

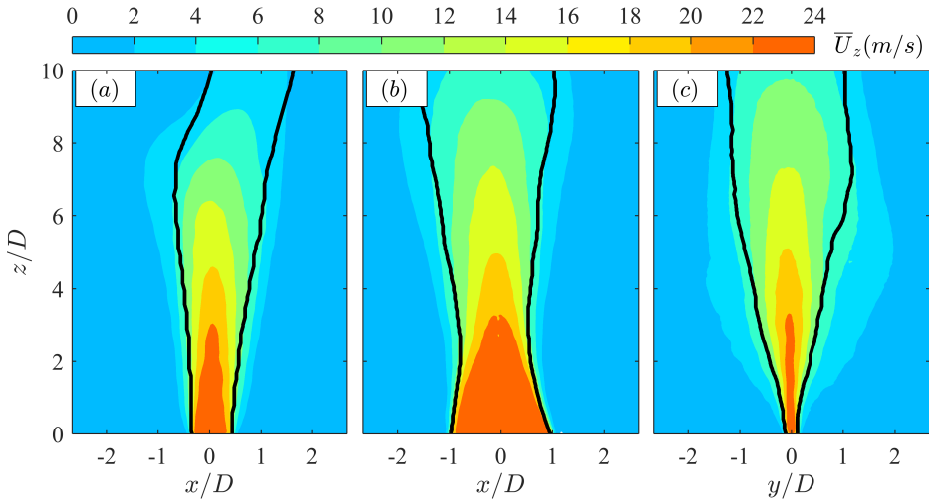


Figure 5.15: Time evolution of the spatially-averaged exit velocity (U_e) for the two tested orifice shapes.

5.4.3. PSEUDO TIME-AVERAGED VELOCITY FIELDS

Based on the above analysis, jet entrainment rate plays a dominant role in the axes-switching phenomenon and the formation of different penetration lengths. For steady jets, the entrainment rate can be quantified by the spreading jet profile in time-averaged flow field [115]. The boundary of the jet is typically defined from a fixed fraction of the centreline jet velocity. Extending this approach to the current study, the time-averaged velocity fields of PSJs ($\bar{U}_i(x, y, z)$, $i = x, y, z$) in the primary jet stage (i.e. $t \leq 1.9 \text{ ms}$) can be reconstructed using Equation 2.16. These time-averaged velocity fields are ‘pseudo’ with respect to those presented in Chapters 3 and 4 (e.g. Figures 3.18 and 4.9), since the

averaging operation is implemented in part of a cycle, instead of a complete cycle which requires repetitive operation of the actuators.

Focusing on the axial component of velocity, only $\overline{U}_z(x, y, z)$ is computed. Contours of \overline{U}_z are displayed in Figure 5.15 as function of the two orifice shapes. The jet boundaries indicated by dash-dot lines are determined by 50% of the peak axial velocity at different z positions. For the jet emitted from circular orifice, the time-averaged flow field is similar to that of the steady jets, where a quasi-linear spreading of the jet profile is observed [105]. In the case of slot orifice, the jet profile in xz -plane first contracts and then expands. In contrast, the jet profile in yz -plane expands monotonically. To quantitatively compare the influence of the orifice shape, the peak jet velocity values at different z -coordinates denoted as \overline{U}_{cz} are extracted, as shown in Figure 5.16 (a). Maximum values of \overline{U}_{cz} for the two tested cases are almost the same, approximately 27 m/s. However, the decay rate of \overline{U}_{cz} for circular orifice is moderately higher than the slot orifice, which is related to the fast propagation of jet body shown in Figure 5.13.

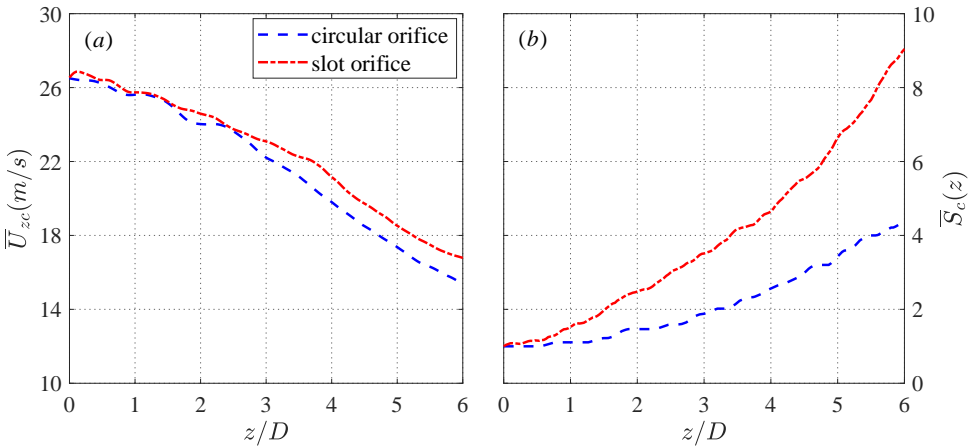


Figure 5.16: Time evolution of the spatially-averaged exit velocity (U_e) and the normalized cross-section area (\overline{S}_c) for the two tested orifice shapes.

The cross-sectional area of the jet body $S_c(z)$ is chosen to characterise the jet spreading rate. To compute $S_c(z)$, width of the jet body at different z coordinates is first calculated based on the extracted jet boundaries, as illustrated in Figure 5.15. For the circular orifice, $S_c(z)$ is defined as the square of the jet width in the xz -measurement plane, $w_x^2(z)$. Whereas for the slot orifice, $S_c(z)$ is approximated by the product of the two jet width values determined in both symmetry planes, $w_x \cdot w_y$. Subsequently, $S_c(z)$ is normalised by the cross-sectional area of the jet at the exit orifice $S_c(0)$, resulting in a non-dimensional cross-sectional area $\overline{S}_c(z)$. Variation of $\overline{S}_c(z)$ is presented in Figure 5.16 (b). As evidenced, the non-dimensional cross-sectional area for the slot orifice expands almost twice as faster as that for the circular orifice. This ratio is close to the perimeter ratio of slot orifice to circular orifice (1.7), testifying the association between jet entrainment rate and exit orifice perimeter.

5.5. CONCLUSIONS

The evolution characteristics of PSJs issued from two different orifice shapes (circular and slot) but the same exit area are investigated with high-speed Schlieren imaging system and phase-locked PIV system. The shapes of the front vortex rings (FVRs) are consistent with the shapes of the respective exit orifices, since the FVR is rolled from the jet shear layer. In the case of slot orifice, the elongated vortex ring gradually opens up, and its two ends become severely warped during the propagation. This transformation results from the difference in entrainment rate and propagation velocity. The quasi-2D slot jet produces a shear layer in the flow field, which allows the periodical disturbance on the jet exit angle being amplified as a wavy jet. In the case of circular orifice ($D = 3$ mm), a distinct asymmetric flow field is presented, where the front vortex ring and the high speed jet lean in opposite directions during their propagation. Development of the asymmetric flow field is essentially an unstable process with positive feedback. Misalignment between the vortex ring and the jet, caused by the asymmetric electrode configuration, triggers the amplification of asymmetry.

In pseudo-time averaged velocity fields, the entrainment rate of the surrounding low-energy fluids pertaining to slot jet is almost twice as that for the circular jet, thus resulting in a faster decay of penetration rate. For the two tested cases, the exit velocity in one period initially shows a rapid increase, then maintains at a relatively high level (100–130 m/s) for approximately 200 μ s determined by the discharge duration, and finally drops with some small-scale oscillations. The oscillation amplitude is less than 10 m/s, and the oscillation period agrees well with the Helmholtz natural period. With the deposited energy and exit area kept constant, orifice shapes have little influence on the variation of jet exit velocity.

III

PLASMA SYNTHETIC JETS IN CROSSFLOW

6

EVOLUTION AND SCALINGS

6.1. INTRODUCTION

As a unique actuator capable of producing high-velocity jets at high frequency, plasma synthetic jet actuators have been tested extensively in airfoil separation control, jet noise control, shock wave boundary layer interaction control and so on [62, 64, 65]. Typically, the actuators are flush-mounted in the wall, and high-speed jets are released from skewed and inclined orifices to impinge the crossflow. Although positive results have been reported in these flow control attempts, the flow scenario of plasma synthetic jets (PSJs) in a crossflow turbulent boundary layer (TBL), is still unclear. In conventional synthetic jets in a crossflow, Buren et al. [12, 121] observed a recirculation region downstream of the orifice and a streamwise vortex pair in the far-field. For the interaction between PSJs and turbulent boundary layers, identifying the similar dominant flow structures at different phases of the interaction and further investigating the pertinent spatiotemporal scales are essential not only to reveal the underlying physics but also to optimize the actuation parameters.

Towards tackling the above-mentioned issue, this chapter investigates a nominal case of the interaction between a wall-normal PSJ and a subsonic TBL in a single-shot mode. Phase-locked PIV measurements in multiple planes are deployed to capture the evolution of three-dimensional flow structures at different phases. In Section 6.2, the utilized experimental facilities including the actuator, hotwire anemometer, and PIV systems are introduced. Subsequently, PIV data validation is performed (Section 6.3). From Section 6.4 to Section 6.5, the phase-averaged flow organisation and the turbulent kinetic energy distribution are presented successively.

Part of this chapter is published as **H. Zong** & M. Kotsonis, *Interaction between plasma synthetic jet and subsonic turbulent boundary layer*, *Physics of Fluids*, **29**, 045104 (2017).

6.2. EXPERIMENTAL SETUP

6.2.1. ACTUATOR AND POWER SUPPLY

A three-electrode PSJA is adopted in this study, mainly composed of a ceramic cavity and a metal cap. The ceramic cavity is identical to that used in Chapter 5 (see Figure 2.1 *a*), whereas the cap of this actuator, which accommodates the exit orifice, is fabricated as a metal disk flush-mounted with the bottom wall of the wind tunnel test section, as will be shown in Section 6.2.2. The electrical circuitry E1 as shown in Figure 2.2 (*a*) is employed to operate the actuator in single-shot mode (0.5 Hz), and the capacitance and voltage of the energy-storing capacitor are set as $C_1 = 0.5 \mu\text{F}$ and $V_1 = 2.0 \text{ kV}$ respectively, resulting in a fixed energy deposition ration of $\epsilon = 2.6$. This energy level is selected to obtain a typical peak jet-to-crossflow velocity ratio of approximately 4.

6.2.2. WIND TUNNEL AND TEST SECTION

The experiments are carried out in the W-tunnel of Delft University of Technology. The W-tunnel is an open-return tunnel, with interchangeable contraction parts and test sections. A square test section of $0.5 \times 0.5 \text{ m}^2$ dimension and 3 m length is installed for the purpose of this study, resulting in a maximum velocity of 25 m/s and a turbulence level of about 0.5%. As shown in Figure 6.1, the test section is smoothly connected with the contraction part and fabricated using Plexiglas to facilitate the optical measurements. In this study, the freestream velocity is kept constant at $U_\infty = 20 \text{ m/s}$. The atmospheric pressure and temperature are measured to be $P_0 = 101 \text{ kPa}$ and $T_0 = 288 \text{ K}$, respectively.

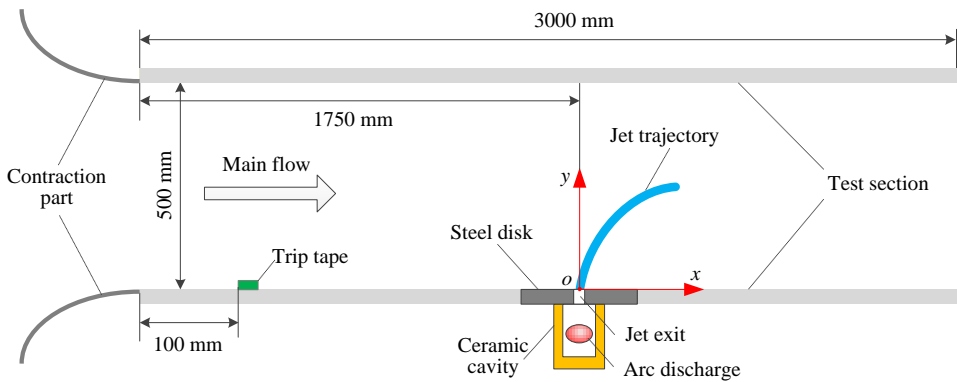


Figure 6.1: Schematic diagram of the test section.

The boundary layer developing naturally on the bottom wall of the contraction part is tripped by a zigzag tape located at 0.1 m downstream of the leading edge of the test section. A steel disk (diameter: 0.11 m) is flush-mounted in the bottom plate. The ceramic cavity shown in Figure 2.1 (*a*) is assembled in the steel disk via a step groove. In the centre of the steel disk, a round orifice (diameter: 2 mm) is drilled, serving as the jet exit. The distance from the jet exit centre to the leading edge of the test section is 1.75 m. A coordinate system is established in reference to the jet exit centre, with x , y , and z axes along the streamwise, wall-normal, and spanwise directions, respectively.

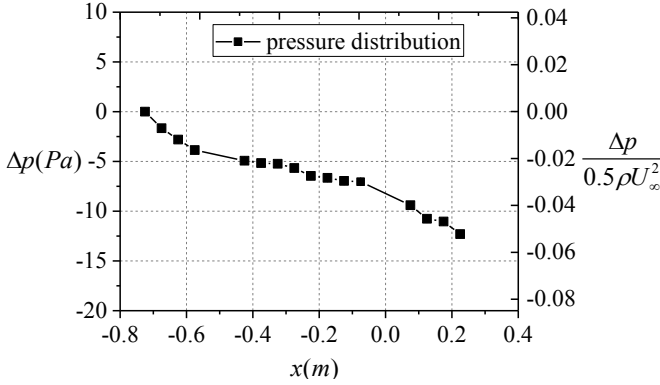


Figure 6.2: Schematic diagram of the test section.

The bottom wall of the test section is furnished with 16 pressure taps (diameter: 0.4 mm) located between $x=0.75$ m and $x=0.25$ m to acquire the pressure distribution. Additionally, a pitot-static tube is mounted at $x=0.15$ m to obtain the dynamic pressure of the uninterrupted freestream flow ($0.5\rho_0 U_\infty^2$). The pressure signals are scanned by a mechanical pressure scanning valve. A high-accuracy pressure transducer (Mensor, Model 2101), together with LabVIEW software, realizes the transformation and the recording of pressure signals. The recording length and the acquisition frequency are set as 5 s and 10 Hz, respectively. For the conditions of the current study ($U_\infty=20$ m/s), the measured pressure distribution on the bottom wall (denoted by Δp) is shown in Figure 6.2. The ratio of Δp to $0.5\rho_0 U_\infty^2$ defines the pressure coefficient. Due to the growth of the boundary layer, the effective flow area drops consistently along the streamwise direction. This results in a mildly increasing freestream velocity and a decreasing wall pressure. The peak value of the pressure coefficient is approximately -0.05. The PIV measurements are performed between 0.02 m $< x < 0.1$ m. In this interval, the pressure coefficient changes less than 1%. Thus, the turbulent boundary layer (TBL) investigated in this paper can be roughly treated as a zero-pressure-gradient TBL.

6.2.3. HOTWIRE ANEMOMETER AND PARTICLE IMAGE VELOCIMETRY

Hotwire measurements are performed in the baseline nonactuated case, in order to reference and validate the PIV data. A single-wire boundary layer probe (Dantec Dynamics, P15), operated by a TSI IFA-300 constant temperature bridge working in a constant-temperature mode, is utilized to obtain the boundary layer velocity profile at $x=50$ mm in the xy -plane ($z=0$ mm). The wire calibration is performed in situ in a velocity range of 0-25 m/s, and the calibration curve is fitted by a fourth order polynomial, with a maximum relative error less than 0.6%. In addition, atmospheric pressure and temperature corrections are applied to the calibration. In the y -direction, 60 measurement stations are selected to fully restore the boundary layer velocity profile. An automated traversing system with an accuracy of 2.5 μm is adopted to realize the probe motion in the y -direction. During the recording, the sampling frequency and the recording time are fixed as 50 kHz and 5 s, respectively, ensuring full statistical convergence.

The adopted PIV system is mainly composed of a single head Nd:YAG laser (Quantel

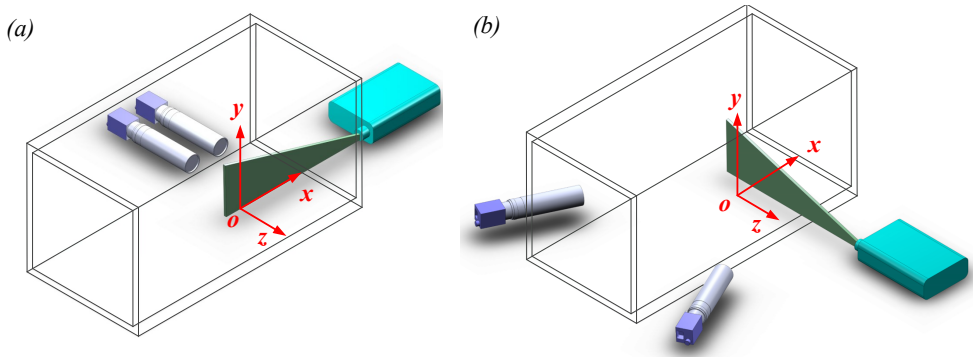


Figure 6.3: PIV measurement setup. (a) 2C-planar in the xy plane and (b) 3C-stereo in the yz plane.

Table 6.1: Overview of PIV measurement parameters.

Measurement plane	Location	FOV (mm ²)	Spatial resolution	M
xy -plane	$z/D = 0$	41×118	9.8 vectors/mm	0.54
yz -plane	$x/D = 2.5, 5, 10, 15, 20$	71×73	5.7 vectors/mm	0.30

EverGreen, peak pulse energy: 200 mJ), two LaVision digital CCD cameras (Imager Pro LX, resolution: 3248×4872 pixels, pixel pitch: $7.4 \times 7.4 \mu\text{m}$), and a programmable timing unit (PTU-v9). Depending on the measurement plane, a 3-component (3C) stereo PIV measurement or 2-component (2C) planar PIV measurement with two side-by-side cameras is performed, as shown in Figure 6.3. By virtue of one cylindrical and two spherical lenses, the laser beam emitted from the laser head is finally shaped into a thin sheet (thickness: 0.6 mm for planar PIV and 1 mm for stereo PIV). Each camera is equipped with a 200 mm macro lens (Nikon, Micro-Nikkor). The optical aperture of the lenses (namely f -stop) is fixed to 8 and 11, respectively, during planar and stereo PIV measurements to guarantee that all the illuminated particles are in focus. The particle image diameter is approximately 2-3 pixels. The laser and the two cameras are fixed on a two-axis traversing bed (accuracy: $2.5 \mu\text{m}$), facilitating the change of measurement planes in the x -direction and z -direction. In total, 6 measurement planes are selected to restore the 3D flow field, as listed in Table 6.1.

Regarding the flow seeding, two schemes are adopted. The primary system provides seeding by a SAFEX fog generator located in the settling chamber of the wind tunnel, using a working fluid of water-glycol mixture, producing particles of approximately $1 \mu\text{m}$ mean diameter. A separate, secondary seeding scheme as adopted in previous chapters is inherited (see Figure 2.2 a), to overcome the problem of low seeding density in the jet core [61]. Through the secondary system, the actuator cavity is seeded with dielectric mineral oil particles (Shell Ondina) of $1.5 \mu\text{m}$ mean diameter, generated by an atomizer (TSI 9302). To minimise possible interference with the developing jet, the intracavity seeding is switched off prior to trigger discharge by a fast-response solenoid valve (FESTO, MHJ10), synchronised to the PIV acquisition.

To capture the spatio-temporal evolution of the PSJ in the turbulent crossflow, all associated systems including the discharge, seeding, and PIV are synchronized, working in a phase-locked mode. The synchronization is implemented by the LabVIEW software. For each measurement plane, several time delays between the discharge initiation and the PIV acquisition (denoted as t) are selected to execute the measurement. For each time delay (phase), 500 image pairs are recorded. In Section III A, a simple convergence study is performed to demonstrate statistical convergence of the phase-averaged measurements. LaVision Davis 8.3 software is used to record and process the image pairs. The interrogation window used in the final pass has a size of 32×32 pixels² and an overlapping ratio of 75%. Detailed values of the field of view (FOV), spatial resolution, and magnification factor pertaining to each measurement plane are available in Table 6.1.

6.3. PIV DATA VALIDATION

Prior to further analysis, it is necessary to make a symbol convention for this chapter. The phase-averaged velocity is denoted by U_i , where the subscript i can be either of the three coordinate components (x, y, z). $\overline{u_i u_j}$ is the Reynolds stress. k stands for the turbulent kinetic energy. δ_v , u_τ , and y^+ represent the viscous length scale, friction velocity, and wall unit, respectively. D is the orifice diameter. δ_{99} is the boundary layer thickness determined by 99% of the freestream velocity. Other symbols will be introduced in their first occurrence.

6.3.1. PIV STATISTICAL CONVERGENCE VALIDATION

A PIV convergence study is performed in the xy measurement plane ($z=0$ mm) for the non-actuated case. 1000 vector fields are recorded. The statistic quantities analysed include the ensemble-averaged velocity and Reynolds stresses. At $x = 0$ mm, four monitor points are placed at different y coordinates ($y=1$ mm, 5 mm, 10 mm, and 20 mm), denoted as P1-P4, respectively. As the ensemble-averaged velocity is relatively faster to converge compared with the Reynolds stresses, only the variation of $\overline{u_x u_x}$ and $\overline{u_x u_y}$ with the sample number (N) is considered here. Regardless of the monitor location, $\overline{u_x u_x}$ and $\overline{u_x u_y}$ largely converge for $N > 400$ (less than 6% for $\overline{u_x u_x}$, not shown). Thus, an ensemble size of 500 is chosen in this study as a compromise between the measurement time and the statistical convergence.

6.3.2. COMPARISON OF PIV WITH HOTWIRE MEASUREMENTS

The hotwire probe used is a single-sensor probe, thus the measured velocity (U_{xy}) is actually the Euclidean sum of the streamwise and wall-normal velocities, $U_{xy} = (U_x^2 + U_y^2)^{1/2}$. Based on the measured velocity profiles, δ_{99} is determined to be 34.5 mm. The variations of U_{xy} at $x/D = 25$ and $z/D = 0$ determined by both PIV and hotwire measurements are shown in Figure 6.4 (a) for comparison.

The two velocity curves agree well in the outer layer ($y/\delta_{99} > 0.03$). However at $y/\delta_{99} < 0.03$, the velocity measured by the hotwire is slightly lower than that by PIV. This discrepancy can be attributed to the finite spatial resolution in the PIV measurement, which is largely affected by the interrogation window size in the final pass (approximately 0.5 mm in this study). The interrogation window behaves essentially as a spatial

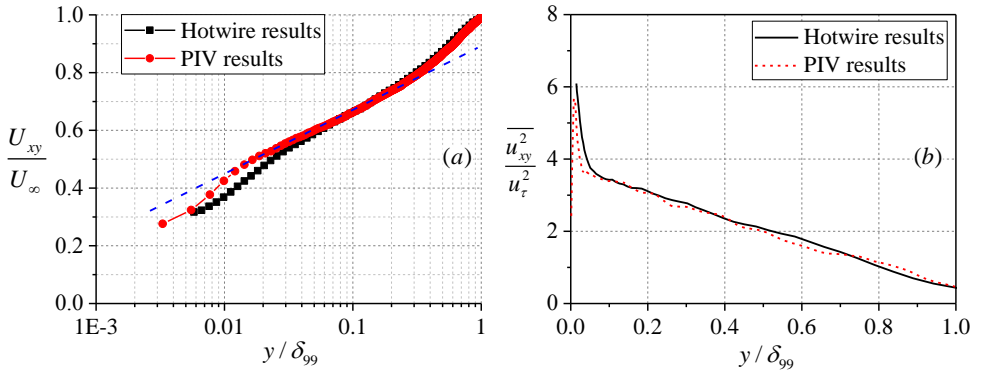


Figure 6.4: Comparison between hotwire results and PIV results at $x=50$ mm and $z=0$ mm. (a) Normalized boundary layer velocity profile (U_{xy}/U_∞); the blue dashed line is used to determine the wall friction velocity. (b) Reynolds shear stress normalized by u_τ^2

low pass filter, and the velocity determined by the cross correlation operation is in fact the spatially averaged velocity in the interrogation window [89]. In the outer layer, this spatial-averaging effect is not so significant since the velocity changes smoothly. However in the near-wall region, the measured velocity profile can be slightly distorted due to the large spatial velocity gradient. In the case of the zero-pressure-gradient boundary layer, the profile of u_{xy} is a convex function of the y -coordinate. Thus, the spatially averaged value should be larger than the actual value. This is confirmed by the positively biased PIV results shown in Figure 6.4 (a).

At $0.03 < y/\delta_{99} < 0.3$, PIV and hotwire data collapse on the same straight line. This region corresponds to the log layer [122], in which the velocity profile can be accurately described by the following equation,

$$\frac{U_{xy}}{u_\tau} = \frac{1}{\kappa} \ln \frac{y}{\delta_v} + b \quad (6.1)$$

where κ is the Von Karman constant (0.41). Theoretically, the slope of the blue dashed line shown in Figure 6.4 (a) is u_τ/κ . By comparing this theoretical slope with the fitted value, u_τ is determined to be 0.79 m/s for the present study and measurement location. The corresponding viscous length scale and time scale are 0.019 mm and 0.024 ms, respectively. Choosing δ_{99} as the reference length scale, the Reynolds numbers based on U_∞ and u_τ are 44 400 and 2060, respectively. The position of the measurement point closest to the wall is 6 and 10.5 in wall coordinates (inner scale) for PIV and hot wire, respectively. In addition, the variation of $\overline{u_{xy}^2}$ (root-mean-square value of the in-plane velocity fluctuation magnitude u_{xy}) is shown in Figure 6.4 (b) as a function of the outer scale. The two curves show a considerable agreement. A discrepancy exists in the hotwire results not capturing the drop of $\overline{u_{xy}^2}$ in the viscous wall region. The basic changing trend of $\overline{u_{xy}^2}$ reported here is similar to that obtained in the channel flow [123].

6.4. PHASE-AVERAGED FLOW ORGANIZATION

6.4.1. XY-PLANE

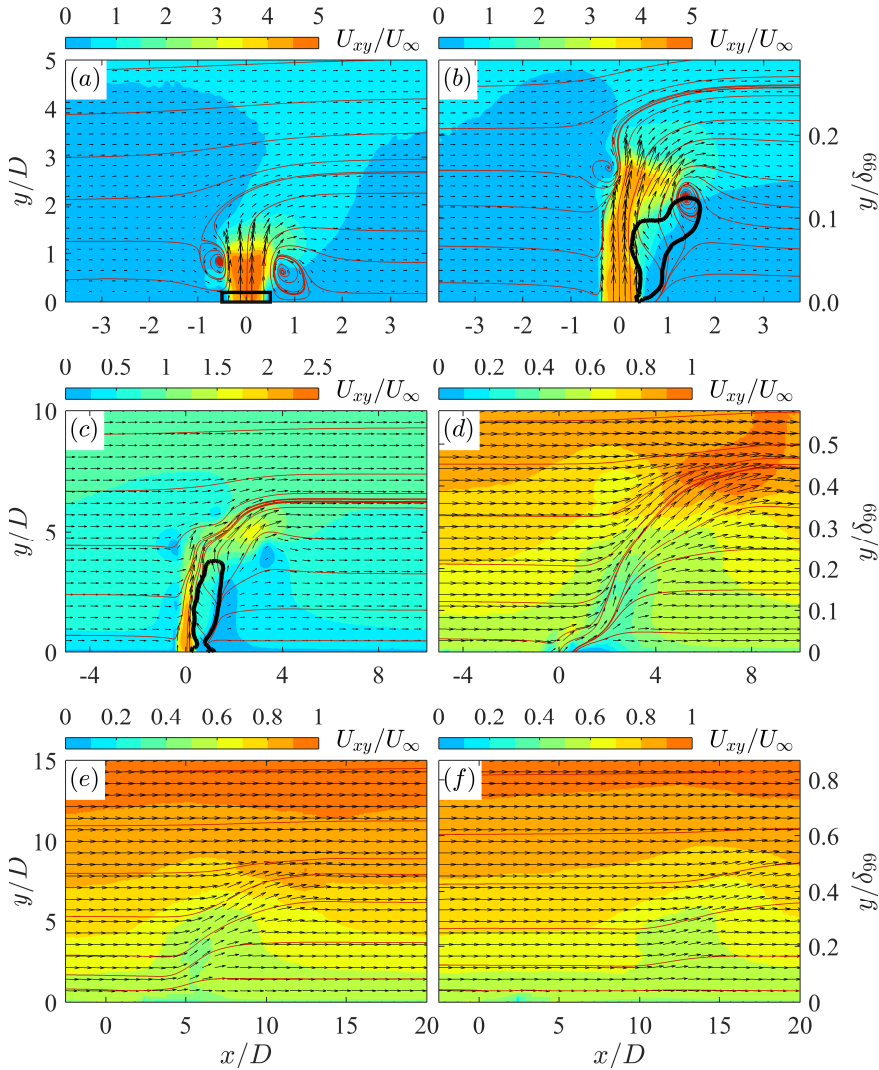


Figure 6.5: Phase-averaged velocity fields in the xy plane ($z=0$ mm). (a) $t^*=2$ ($t=200 \mu\text{s}$), (b) $t^*=3$ ($t=400 \mu\text{s}$), (c) $t^*=5$ ($t=500 \mu\text{s}$), (d) $t^*=10$ ($t=1000 \mu\text{s}$), (e) $t^*=15$ ($t=1500 \mu\text{s}$), and (f) $t^*=25$ ($t=2500 \mu\text{s}$). Note that both the spatial scales and colour map ranges are changing. The red lines superimposed on contour are phase-averaged streamlines. The recirculation regions at $t^*=3$ and $t^*=5$ (defined by $U_x < 0$) are indicated by solid black lines. The interrogation window used to obtain the jet exit velocity is illustrated in (a) by a solid black rectangle.

Phase-averaged flow fields in the xy plane ($z=0$ mm) are shown in Figure 6.5. U_∞ and D are used to normalize the time delay, resulting in a non-dimensional convective time

scale $t^* = tU_\infty/D$. At $t^* = 2$ ($t=200 \mu\text{s}$), a nominally wall-normal high-speed jet is expelled abruptly from the actuator, with a peak velocity of $4.6U_\infty$ (92 m/s). As a result of this abrupt eruption, a distinctive starting vortex ring (also termed as a front vortex ring) is shed from the orifice opening, experiencing an upward propagation [98]. A small portion of the fluid in the crossflow is entrained towards the upstanding jet by the front vortex ring, while the majority of the freestream flow bulk bypasses the high-speed jet as a solid protrusion. Despite the presence of the external flow, the incipient flow topology after discharge shares much similarity with that in the quiescent condition (see Figure 5.7). At increasing time delays from the discharge initiation, the jet body gradually bends to the crossflow ($3 < t^* < 10$). Following the bending jet trajectory, an inclined propagation of the front vortex ring is experienced. The bending jet can be attracted to the pressure difference between the windward side and the leeward side of the jet body, as well as the horizontal acceleration imposed by the crossflow [76].

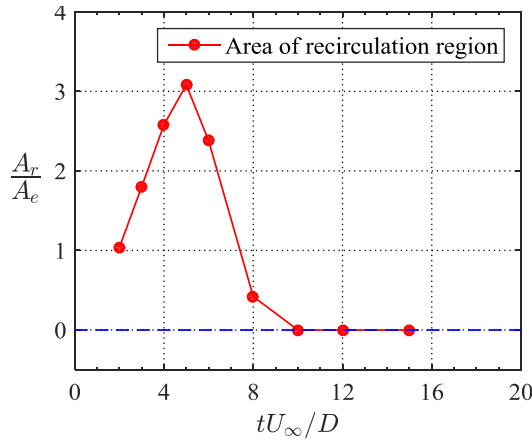


Figure 6.6: Normalized recirculation region (A_r/A_e) as a function of the non-dimensional time (tU_∞/D).

In addition to the bending jet trajectory, a prominent flow phenomenon in the xy plane is the formation of the recirculation region (defined by $U_x \leq 0$) residing in the leeward side of the jet body, as indicated by the solid black lines in Figures 6.5(b–c). Similar to the separation region formed behind bluff bodies [124], the recirculation region in the studied JICF is also accompanied by the production of unsteady vorticity, in the form of the so-called hanging vortices [125]. The streamwise extent of the recirculation region is around $1D$, consistent with the observation in steady jets in the crossflow [126]. At $t^* = 5$ ($t=500 \mu\text{s}$), no clear vortex rings can be identified from the velocity fields, nevertheless the curved streamlines at the jet front indicate the residual concentration of vorticity. Additionally, the peak jet exit velocity drops significantly to $2.4U_\infty$ (48 m/s) at $t^* = 5$ ($t=500 \mu\text{s}$). From $t^* = 10$ ($t=1000 \mu\text{s}$) on, the jet effectively terminates and the velocity fields in Figures 6.5 (d–f) show similar patterns. The issued jet body is severed from the orifice and experiences a quasi-drifting motion along the streamwise direction. During this drifting motion, momentum of the jet flow is gradually dissipated as a result of the mixing with the turbulent crossflow.

The area of the recirculation region (A_r) is computed, as shown in Figure 6.6. After each actuation pulse, the recirculation region increases in size prior to $t^* = 5$ ($t=500 \mu\text{s}$), shrinks afterwards, and disappears completely after $t^* = 10$ ($t=1000 \mu\text{s}$). The peak value of A_r is just over three times of the exit orifice area ($A_e = \pi D^2/4$). This agrees qualitatively with the results reported in steady jets in the crossflow, where a non-dimensional area of 2 is observed for a mean velocity ratio of 3 [126]. The increase of A_r in Figure 6.6 is ascribed to the continuing penetration of the high-speed jet body, while the decrease is directly related to the drop of the jet exit velocity since the blocking effect diminishes considerably. With a velocity ratio as low as 0.17, no clear jet body and recirculation region can be observed and a train of hairpin vortices will emanate consecutively from the exit orifice [127].

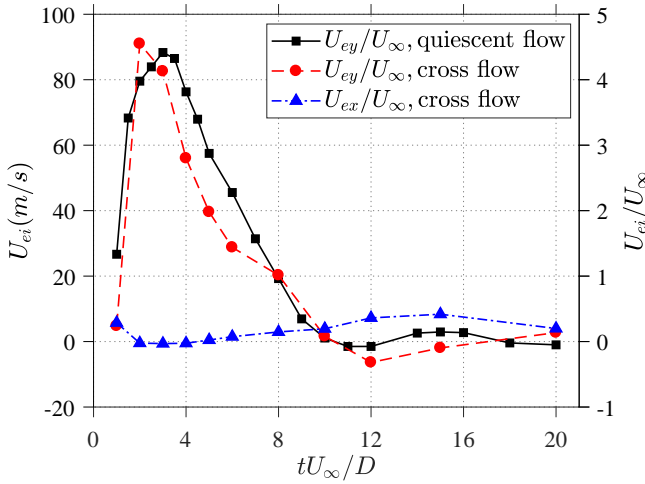


Figure 6.7: Exit velocity variation with the non-dimensional time in both quiescent and cross flow conditions.

The temporal evolution of the phase-averaged jet exit velocity can be monitored using an interrogation window located just above the jet exit (see Section 2.4.1), as indicated in Figure 6.5 (a) by a solid black rectangle. The two components of the spatially-averaged jet exit velocity in the x and y directions are denoted as U_{ex} and U_{ey} , respectively. The time variation of U_{ex} and U_{ey} in the investigated case is plotted in Figure 6.7, meanwhile the experimental data of U_{ey} in quiescent condition for an identical actuator are also plotted for comparison (excerpted from Zong and Kotsonis [85]).

After each actuation pulse, U_{ey} initially shows a sharp increase and then a slow decrease. In both cases, the peak values of U_{ey} are around $4.5U_\infty$ (90 m/s). After $t^* = 10$, a small negative exit velocity is evident, indicating the start of the refresh stage of the actuator. The peak suction velocity in the refresh stage is approximately $-0.3U_\infty$ (-6 m/s), considerably lower than the peak jet velocity. This feature promotes the conclusion that as a typical synthetic jet actuator, PSJA has an inherent zero-net mass flux whereas nonzero net momentum flux. As a result, a quasi-steady impulse (net impulse) will be produced by PSJAs working in the repetitive mode, with promising extensions towards flight control [54]. Based on the sign change of U_{ey} , the non-dimensional jet duration

time (denoted as $T_{jet}U_\infty/D$) is determined to be 10 ($T_{jet}=1000\ \mu\text{s}$) in both crossflow and quiescent conditions. Overall, the two curves of U_{ey} agree well, although some disparities exist between $t^*=3$ and $t^*=8$. This agreement is largely expected, as suggested by the analytical model proposed by Zong et al. in [16] where only significant changes in external atmospheric parameters (ambient pressure, temperature, and density) can alter the exit velocity variation of the PSJA. Additionally, a non-zero lateral component of the jet exit velocity is exhibited in the crossflow. U_{ex} varies inversely with U_{ey} , with a peak value of $0.5U_\infty$ (10 m/s).

In order to quantify the penetration ability of the PSJA, the jet trajectories at different time delays are evaluated. For steady jets in the crossflow, the jet trajectory can be defined as the positions of local velocity maxima, local vorticity maxima, or as the ensemble-averaged streamline originating from the jet exit centre [76]. For the PSJ in the crossflow, the vorticity prior to $t^*=5$ ($t=500\ \mu\text{s}$) is largely concentrated in the front vortex ring. Thus the vorticity criterion cannot be deployed. Comparison of the other two criteria is made in Figure 6.8 (a). As evidenced, the jet trajectory defined by the phase-averaged streamline is more robust, thus suitable for this study.

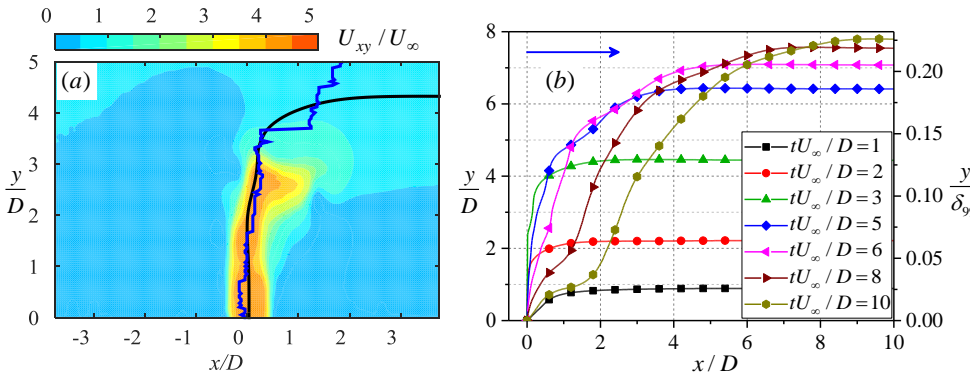


Figure 6.8: (a) Comparison of jet trajectories at $t^*=3$ ($t=300\ \mu\text{s}$) extracted from the positions of local velocity maxima (blue line) and the jet exit centre streamline (black line). (b) Temporal evolution of the phase-averaged streamlines originating from the jet exit centre.

The temporal evolution of the jet trajectories is shown in Figure 6.8(b). For each streamline, there exists an asymptotic plateau. The y -coordinate of this plateau reflects the phase-averaged jet penetration depth, which increases monotonically with non-dimensional time. In contrast to steady jets [128], the jet trajectories of the PSJ exhibit noticeable inflection points after $t^*=3$ ($t=300\ \mu\text{s}$). This phenomenon is attributed to the dynamic change of the jet exit velocity within an actuation cycle. Specifically, the ability of the jet body to resist the crossflow diminishes significantly with time, leading to an increased curvature of the jet trajectories and finally the formation of inflection points. Between $t^*=3$ and $t^*=10$, a considerable downstream drift of the jet body is evidenced by the streamwise offsets between the observed jet trajectories. After $t^*=10$, the actuator enters the refresh stage. In this stage, a stagnation point is formed just above the exit, separating the preceding ejection and the anticipating suction flow [8, 82]. Affected by this stagnation point, the streamline originating from the jet exit centre no longer rep-

resents the actual jet trajectory. An alternative method will be introduced at a later point to quantify the jet penetration during the refresh stage.

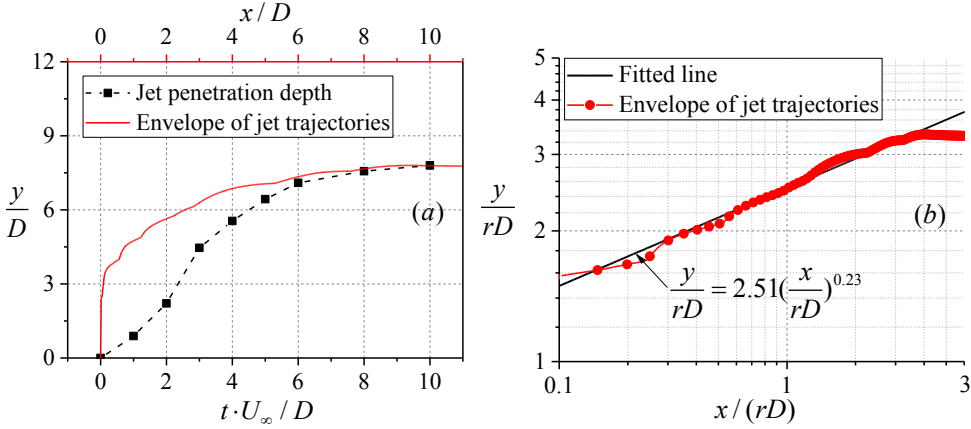


Figure 6.9: (a) Outer envelope of the jet trajectories and temporal variation of the jet penetration depth. (b) Jet trajectory envelope in double logarithmic coordinate. The formula of the fitted line is indicated.

The outer spatial envelope of the jet trajectories in Figure 6.8(b) is extracted and shown in Figure 6.9 (a). Below this envelope lies the region possibly swept by the jet. In addition, the variation of the jet penetration depth, defined as the y -coordinate of the plateau in Figure 6.8(b), is replotted as a function of the non-dimensional time (tU_∞/D) for reference. tU_∞/D can be interpreted as the maximum convective distance of the jet core in crossflow. As such, at any time of the jet stage ($t^* \leq 10$), the jet front should fall into the enclosed region defined in Figure 6.9 (a). The peak value of the jet penetration depth within the jet stage is estimated to be $7.8D$ ($0.45\delta_{99}$). The pronounced similarity between the jet trajectory envelope of the PSJ and the previously studied jet trajectory of steady jets allows a comparison of their penetration ability. Jet trajectories are most commonly scaled with rD [129], where r is the ratio of momentum flow velocity (U_m) to freestream velocity as follows,

$$\begin{cases} r = U_m/U_\infty \\ U_m = \sqrt{\frac{1}{T_{jet}} \int_0^{T_{jet}} U_{ey}(t)^2 \cdot dt} \end{cases} \quad (6.2)$$

For the investigated case, U_m and r are calculated to be 46.8 m/s and 2.34, respectively. In Figure 6.9 (b), the normalized jet trajectory envelope is plotted in a double logarithmic coordinate, and an approximate linear variation is exhibited in $x/rD < 2$. This suggests that the jet trajectory envelope of the PSJ can also be fitted by the following relation [130]:

$$\frac{y}{rD} = A\left(\frac{x}{rD}\right)^B \quad (6.3)$$

where A and B are coefficients to be fitted. For steady jets in the crossflow, Margason [130] summarized the possible ranges of $1.2 < A < 2.6$ and $0.28 < B < 0.34$. In the current case of PSJ in crossflow, the fitted value of B (0.23) is beyond that range, indicating that the penetration ability of the PSJ is not as strong as steady jets with the same momentum flow velocity. When rD is fixed, increasing the jet duration time (T_{jet}) is expected to enhance the penetration ability of PSJs.

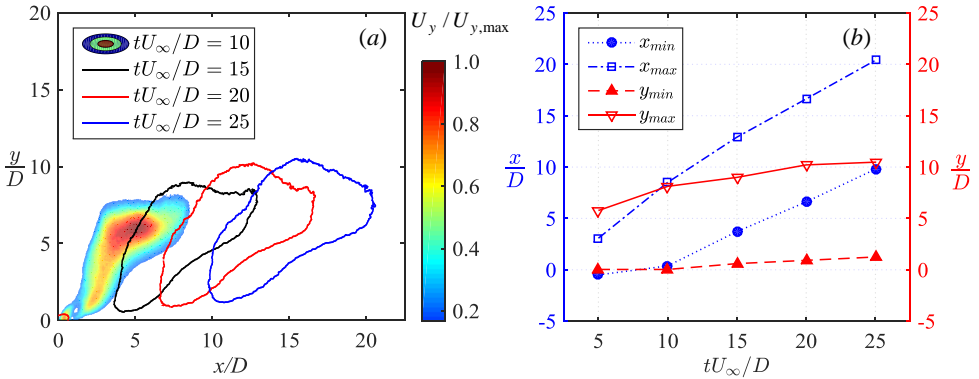


Figure 6.10: (a) Projection of the jet body outlines in the xy plane determined by the contour line of 20% of the maximum wall-normal velocity ($U_{y,max}$). (b) Streamwise and wall-normal bounds of the jet body outlines.

6

The above analysis is performed based on the jet trajectories during the jet stage. As mentioned previously, after $t^* = 10$ ($t=1000 \mu s$) an alternative method should be proposed to track the motion of the jet body. In the xy plane ($z=0$ mm), the jet body convects downstream and away from the wall after the jet issuing is terminated; thus, the region with large U_y can represent the projection of the jet body in the xy plane to some extent. In this study, a threshold value of 20% of the maximum wall-normal velocity (denoted as $U_{y,max}$) is exploited to extract a well-defined outline of the jet body in the xy plane [126], as shown in Figure 6.10 (a). While convecting downstream, the jet outline in the xy plane remains largely similar. The streamwise bounds (x_{min} , x_{max}) and wall-normal bounds (y_{min} , y_{max}) of the extracted outlines are plotted in Figure 6.10 (b) as a function of the convective time scale. The linear variation of x_{max} indicates an approximately unchanged convection velocity of the jet body (mean value: $0.85U_\infty$). $x_{max} - x_{min}$ defines the occupied streamwise extent of the jet body (L_{x0}). In principle, L_{x0} increases with non-dimensional time, due to the significant velocity gradient in the y -direction. At $t^* = 25$ ($t=2500 \mu s$), L_{x0} is about $10D$. y_{max} can be interpreted as the jet penetration depth of the PSJ. As expected, y_{max} experiences a monotonic increase and reaches a peak value of $10D$ ($0.58\delta_{99}$) at $t^* = 25$ ($t=2500 \mu s$). From this point of view, the PSJA used in this study still fits in the category of sub-boundary-layer vortex generators, although a peak velocity ratio of 4.6 is reported.

6.4.2. YZ-PLANE

Due to the convective nature of the emitted jet, several appropriate time delays are selected to perform the stereo-PIV measurement for each of the five yz planes listed in

Table 6.1. The captured flow fields exhibit two distinct topologies. For each topology, two representative samples are shown in Figure 6.11. In Figures 6.11 (a, c), a prominent counter-rotating vortex pair (CVP) is observed, similar to that perceived in steady jets in a crossflow [76]. Driven by the CVP, the low-momentum flow in the near-wall region is ejected upward while the high-momentum flow in the outer layer is swept downward, as indicated by the contour lines of U_x . The origin of the CVP remains to be a debated topic in JICF-related literature. Marzouk and Ghoniem [131] suggested that the stretch and deformation of the jet shear layer vortices initiate the CVP. However, Meyer, Pedersen, and Özcan [125] argued that the hanging vortices may be the origin of the CVP and contribute a significant part of the vorticity to the CVP. Since the available planar and stereo PIV measurements can only offer inconclusive conjectures on that issue, the origin of CVP in PSJICF will not be concluded concretely in this chapter.

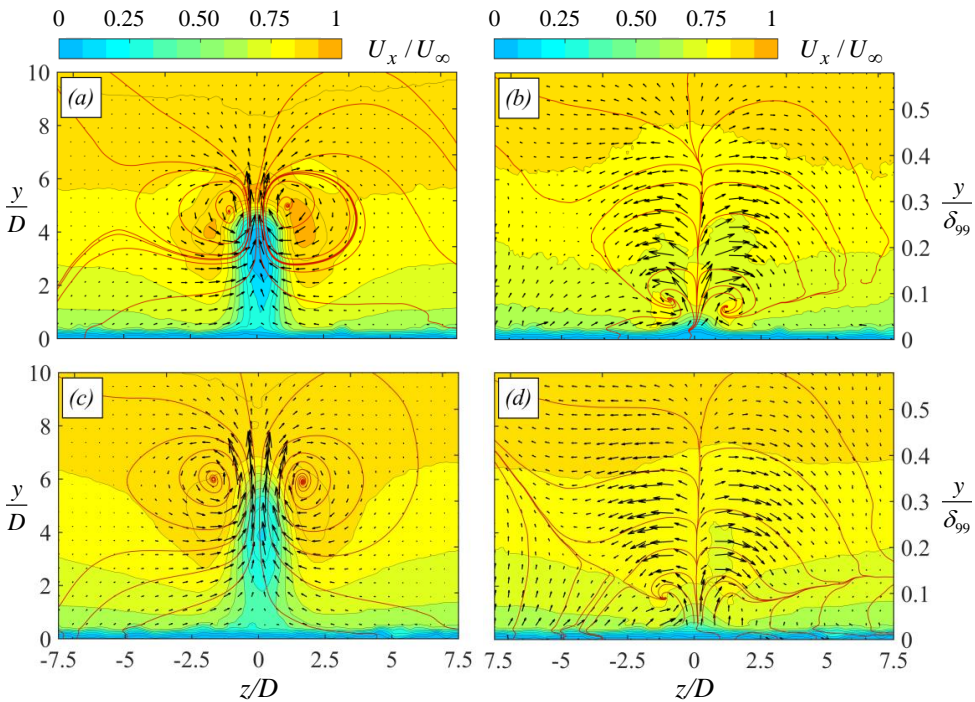


Figure 6.11: Representative velocity fields in the yz plane. (a) $t^* = 5$ ($t=500 \mu\text{s}$), $x/D = 2.5$; (b) $t^* = 10$ ($t=1000 \mu\text{s}$), $x/D = 2.5$; (c) $t^* = 10$ ($t=1000 \mu\text{s}$), $x/D = 5$; (d) $t^* = 15$ ($t=1500 \mu\text{s}$), $x/D = 5$. The out-of-plane velocity component (U_x) is plotted as contours, while the in-plane velocity components (U_y and U_z) are shown by black vectors and red streamlines.

Figures 6.11 (b, d) correspond to the second topological structure. In this topology, the CVP is not well defined, although the streamlines are severely curled at $z/D = -1$, $y/D = 1.5$. A positive bifurcation line is observed around $z/D = 0$, separating the velocity vectors with the opposite z -component. This flow scenario seems to be a plane projection of a second highly inclined counter-rotating vortex pair—possibly the so-called hanging vortex pair observed by [132]. The hanging vortex pair is a quasi-steady struc-

ture residing at the sides of the jet. In the near-wall region, its axis is highly inclined and interests with the wall. However, far away from the wall, it behaves unpredictably and possibly contributes vorticity to the CVP [132]. Its formation is closely related to the skewed mixing layer on the sides of the jet [133]. In the same streamwise location, the second flow topology appears $500 \mu\text{s}$ (5 convective time units) after the occurrence of the first topology.

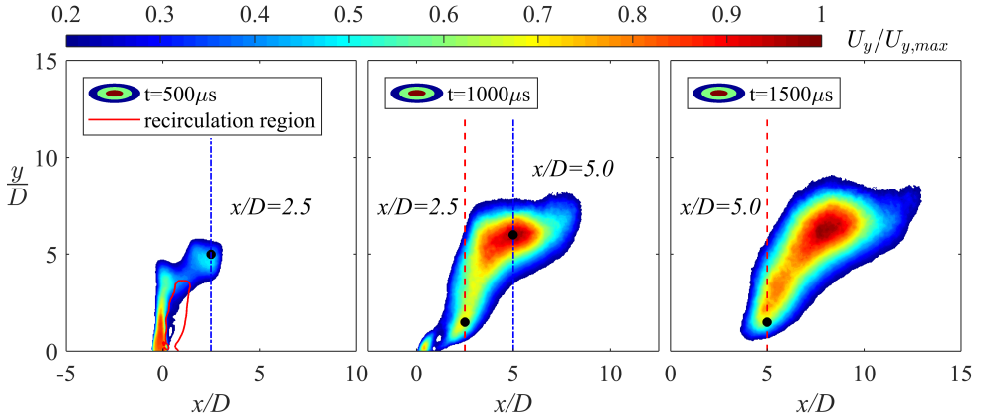


Figure 6.12: Relationship between the resolved flow topology and the streamwise measurement locations. The four vertical lines indicate the streamwise measurement locations of the four cases shown in Figure 6.11. The first and the second flow topologies are denoted by blue dashed-dotted lines and red dashed lines, respectively. The vortex center locations determined from the streamlines in Figure 6.11 are indicated by the solid points.

The measurement planes pertaining to the four cases in Figure 6.11 are further illustrated in Figure 6.12 in the xy plane. Due to the upwash effect, the CVP can be visualized by the region with high U_y (the case of $t^* = 5$ is not included, as the high value of U_y is directly associated with the high-speed jet, instead of the CVP). All the measurement planes presented in Figure 6.11 intersect the jet body. Judging from the spatial distribution of high U_y , the aforementioned hanging vortex pair seems to be connected with the CVP. Both of them bear a curved shape, following the jet outline. This conjecture is consistent with the perspective of Meyer, Pedersen, and Özcan [125] that the hanging vortices transport a significant part of the vorticity into the CVP. The two distinct flow topologies observed earlier can be ascribed to the different intersection angles between the CVP axis and the PIV measurement plane. At the jet front, the CVP bends largely to the crossflow, and thus can be well-depicted by the stereo-PIV results (Figures 6.11 *a, c*) in the yz plane. In contrast, with a measurement plane intersecting the “root” of jet body (Figures 6.11 *b, d*), only the induced wake flow of the hanging vortex pair is resolved.

In contrast to the steady jets in crossflow, the CVP produced by the PSJ in crossflow exhibits a strongly dynamic spatio-temporal behaviour. Due to the short jet duration time, the CVP occupies a rather limited streamwise extent which can be approximated by L_{x0} ($10D$). In addition, the CVP bares steady streamwise convection during the evolution. Thus, the residence time of the CVP (T_{CVP}) in a specific streamwise location is also finite and can be estimated by the jet duration time ($1000 \mu\text{s}$). From this point of

view, the actuation imposed by the PSJ is inherently intermittent due to the essential alternation between the jet stage (ejection) and the refresh stage (suction) [16].

The following analysis aims at quantifying the intensity of the CVP from two aspects: the total circulation ($\Gamma_{CVP}(x, t)$) and the variation of the TBL shape factor ($H(x, z, t)$). According to the results shown in the work of Zong and Kotsonis [85], the peak relative difference between the jet exit density and the ambient density is less than 8% for the current investigated cases. This observation, in conjunction with a peak jet velocity of less than Mach 0.3, fully justifies the assumption of an incompressible flow. The boundary layer shape factor in the incompressible flow is defined as follows [122]:

$$H(x, z, t) = \frac{\delta^*}{\theta} = \int_0^\infty \left(1 - \frac{U_x}{U_\infty}\right) dy \Big/ \int_0^\infty \frac{U_x}{U_\infty} \left(1 - \frac{U_x}{U_\infty}\right) dy \quad (6.4)$$

where δ^* and θ denote the displacement thickness and the momentum thickness, respectively. Based on the stereo-PIV results, the shape factor at different spanwise and streamwise locations is computed, as shown in Figure 6.13 (a). In addition, the boundary layer profiles corresponding to the streamwise locations and time delays of Figure 6.13 (a) are shown in Figure 6.13 (b) for several spanwise locations. The shape factor (1.3) and boundary layer velocity profiles pertaining to the baseline case (no plasma synthetic jet) are indicated as reference.

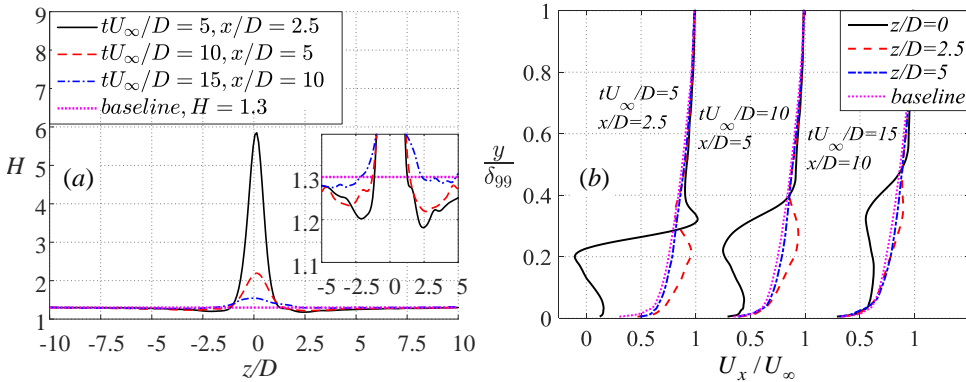


Figure 6.13: (a) Spanwise distribution of the boundary layer shape factor, H . A zoomed view of the variation is shown in the inset. (b) Boundary layer velocity profiles. The corresponding streamwise measurement stations and time delays are indicated by the annotations. Note that the x axis changes repeatedly from 0 to 1.

The spanwise distribution of H assumes the form of a Mexican hat function, where a large positive peak is observed in the middle ($z/D = 0$) surrounded by two negative peaks. For the case of $t^* = 5$ and $x/D = 2.5$, the positive peak of H is extremely high, reaching 5.85. This can be attributed to the recirculation region situated at the leeward side of the jet body, which creates a large velocity deficit in $y < 0.3\delta_{99}$ at $z/D = 0$ (Figure 6.5). The downwash effect of the CVP is most prominent at $z/D = -2.5$, where two negative peaks of H (approximately 1.2) are evident and the corresponding velocity profile becomes relatively fuller. Specifically, an accelerated region is formed below $y = 0.3\delta_{99}$, due to the continuous transport of the high-momentum flow from the outer layer to the

near-wall region. As a result, the TBL is energized and expected to have an enhanced ability to resist streamwise adverse pressure gradients [134].

As the CVP propagates downstream, both the deficit region and the accelerated region move away from the wall. Meanwhile, the actuated velocity profiles gradually recover to the baseline shape, suggesting a weakened intensity of the CVP. The velocity profiles at $z/D = \pm 5$ for all cases show little difference with the baseline cases. Therefore, the effective extent of the CVP in the spanwise direction is determined to be approximately $10D$. Compared to the results of conventional synthetic jets in the crossflow [135], the results reported here are considerably positive. Smith [135]) experimentally investigated the interaction between a piezoelectric synthetic jet array (three actuators, rectangle orifices, wallnormal jet) with a TBL. The ratio of the time-averaged jet velocity (11.3 m/s) to the freestream velocity (9.1 m/s) was 1.2. Considering a sinusoidal variation of the instantaneous jet velocity, the peak velocity ratio (not reported) is estimated to be around 3.8, comparable to the present case (4.6). The boundary layer shape factors were examined in a large streamwise and spanwise extent. As a result, no obvious decrease of the boundary layer shape factor was observed. However, a distinction should be made concerning the fact that the results from [135] are time-averaged, while in the present study are phase-averaged.

The following analysis concerns the characteristics of the CVP. A representative vorticity field in the yz plane ($x/D = 2.5$, $t^* = 5$) is shown in Figure 6.14(a). High vorticity mainly resides in the CVP cores and the near-wall region. To identify the CVP from the background, Q-criterion is used and the threshold value is chosen as 1% of the peak Q-value. The identified vortex regions are outlined by red lines in the vorticity contour. The total circulation (Γ) and the wall-normal location (y_c) of the CVP are defined as follows:

$$\left\{ \begin{array}{l} \Gamma = \iint_{\Omega} |\omega_x| dydz \\ y_c = \frac{1}{2\Gamma} \iint_{\Omega} y |\omega_x| dydz \end{array} \right. \quad (6.5)$$

where Ω denotes the identified vortex region. A preliminary sensitivity study shows that when the threshold reduces to 0.1% of the peak Q-value, a small portion of the near-wall shear-layer region will be included as the vortex region. Nevertheless, the relative variation in Γ and y_c is less than 7%.

The variations of Γ and y_c are shown in Figure 6.14(b) as a function of the non-dimensional time. Since the spanwise spacing and the peak vorticity of the CVP are expected to scale with D and rU_{∞}/D , respectively, the total circulation can be reasonably normalized by $rU_{\infty}D$. As a result, the non-dimensional total circulation $\Gamma/(rU_{\infty}D)$ is on the order of 0.1 and appears to be decreasing approximately linearly with the non-dimensional time. At $t^* = 25$ ($t=2500 \mu\text{s}$), the total circulation remains only 20% of that at $t^* = 5$ ($t=500 \mu\text{s}$). By extrapolation, the non-dimensional survival time of the CVP is estimated to be 32. As stated earlier, this non-dimensional time can be interpreted as the farthest propagation distance of the jet body. Thus, the maximum effecting extent of the CVP in the x -direction is also $32D$. Beyond this extent, the total circulation will drop to a negligible level. In addition, y_c increases monotonically with the non-dimensional time,

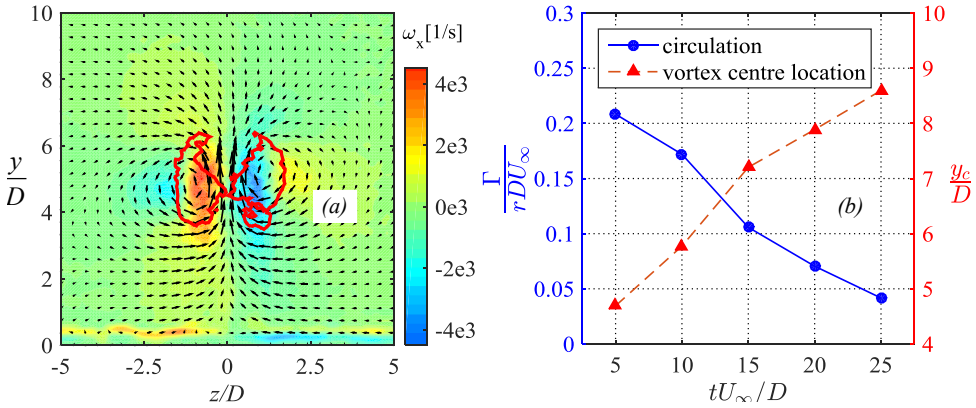


Figure 6.14: (a) Streamwise vorticity field superimposed with in-plane velocity vectors at $x/D = 2.5$, $tU_\infty D = 5$. The vortex regions identified by the Q-criterion are indicated by the red lines. (b) Temporal evolution of the total circulation and the wall-normal location. It should be noted that the five data points are acquired at different streamwise stations ($x/D = 2.5, 5, 10, 15, 20$).

indicating a lift motion of the CVP. This self-induced lift motion is a common behaviour of the vortex pair/vortex ring formed at orifice openings. In principle, the lifting velocity is positively proportional to the ratio of the total circulation to the vortex ring diameter [102]. As Γ drops, the rising rate of y_c declines. The peak value of y_c reached at $t^* = 25$ ($t = 2500 \mu\text{s}$) is just above $8.5D$.

Based on the previous analysis, the spatiotemporal characteristics of the CVP are summarized. The CVP bears a convective motion with the crossflow, meanwhile lifting slowly. The residence time at a specific streamwise location is estimated to be the jet duration time. The maximum effecting extents of the CVP in the three coordinate directions (x , y , and z) are approximately $32D$, $8.5D$, and $10D$, respectively.

6.5. TURBULENT KINETIC ENERGY

6.5.1. XY-PLANE

Since only two-component planar PIV measurements are performed in the xy plane ($z = 0 \text{ mm}$), the turbulent kinetic energy (TKE) is computed using the relation of $k_{xy} = (\overline{u_x^2} + \overline{u_y^2})/2$, where u_i ($i = x, y, z$) is the fluctuation velocity component and top bar represents statistical averaging. Contours of k_{xy}/u_τ^2 at different time delays are shown in Figure 6.15. The jet outlines extracted with the criterion of 20% of $U_{y,max}$ (see Figure 6.10) are plotted as red dashed-dotted lines for reference. Theoretically, the production rate of TKE can be expressed as $P_k = -\overline{u_i u_j} \cdot \partial U_i / \partial x_j$ [122]. Therefore, high TKE always resides in the region with a high velocity gradient, namely, the front vortex ring and the jet shear-layer. Additionally, the inevitable discharge timing uncertainty associated with pin-to-pin arc discharge can result in a fluctuation in the timing of the jet and finally the production of pseudo-TKE. The magnitude of this pseudo-TKE can be estimated by ζ^2/u_τ^2 , where ζ is the peak velocity fluctuation caused by discharge timing uncertainty (approximately 3 m/s, see the uncertainty analysis in Section 2.4.2). As a result,

the peak pseudo-TKE is about $14.4u_\tau^2$, significantly lower than the TKE value measured in the front vortex ring and jet shear-layer (Figure 6.15 *a – b*). Thus, the influence of discharge timing uncertainty can be neglected during the following analysis. Prior to $t^* = 5$ ($t=500 \mu\text{s}$), the TKE level in the jet shear-layer is lower than that in the front vortex ring. The peak value of k_{xy} at $t^* = 3$ ($t=300 \mu\text{s}$) is $1500u_\tau^2$, significantly larger than that for the baseline case (no jet, $4u_\tau^2$). From $t^* = 5$ to $t^* = 10$, the maxima of k_{xy} drop sharply from $750u_\tau^2$ to $75u_\tau^2$, which can be attributed to the breakdown of the front vortex ring.

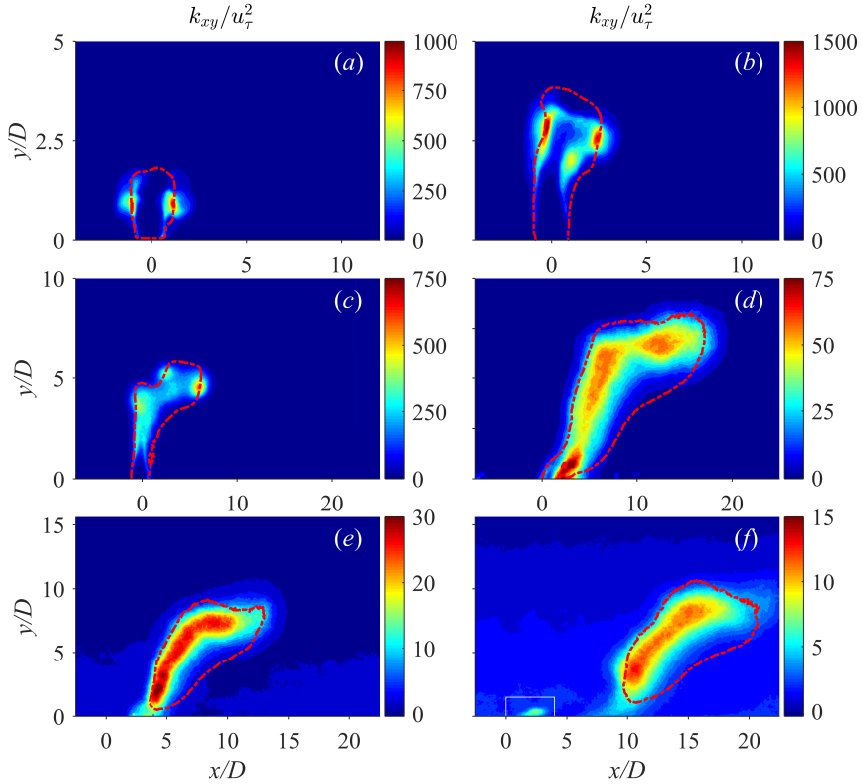


Figure 6.15: Contours of k_{xy}/u_τ^2 at different time delays. (a) $t^*=2$ ($t=200 \mu\text{s}$), (b) $t^*=3$ ($t=400 \mu\text{s}$), (c) $t^*=5$ ($t=500 \mu\text{s}$), (d) $t^*=10$ ($t=1000 \mu\text{s}$), (e) $t^*=15$ ($t=1500 \mu\text{s}$), and (f) $t^*=25$ ($t=2500 \mu\text{s}$). Using the same criterion described in Section 6.4.1 (20% of $U_{y,max}$), the jet outlines are extracted and plotted as red dashed-dotted lines. The solid white rectangle in (f) indicates an isolated high-TKE region caused by the second jet.

After $t^* = 10$ ($t=1000 \mu\text{s}$), the jet terminates and the high-TKE region is gradually transported downstream, following the general movement of the jet body (Figure 6.10). In Figure 6.15(f), a localised area in the vicinity of the orifice (highlighted by the white solid rectangle) is occupied by elevated TKE, which is attributed to the emission of a secondary jet. The existence of multiple jet stages in one working cycle was first predicated by the analytic model in the work of Zong et al. [16] and later validated by the PIV results in the work of Zong and Kotsonis [82]. The rather small area and short penetration depth suggest that the second jet has negligible influence on the crossflow.

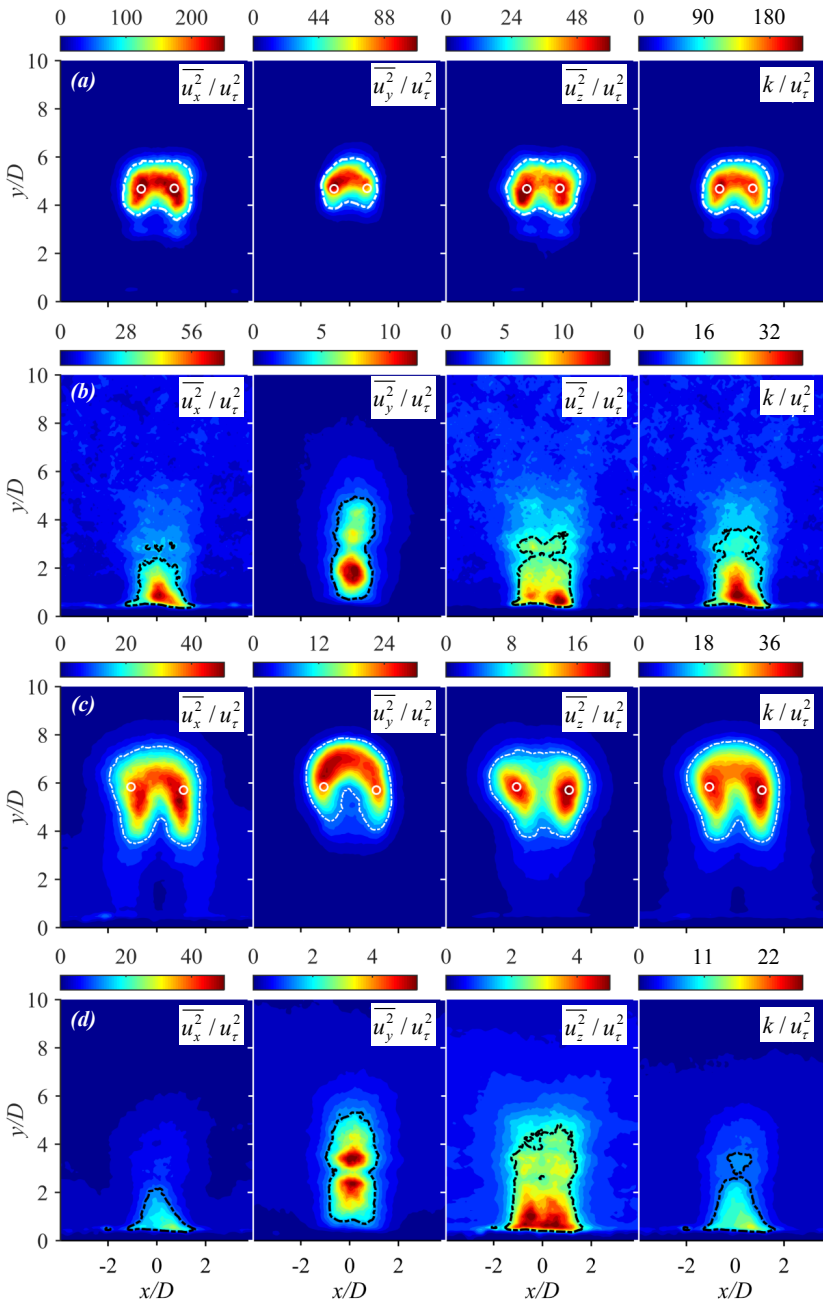


Figure 6.16: Contours of $\overline{u_i^2}$ and k at different yz measurement planes. (a) $t^* = 5$ ($t=500 \mu s$), $x/D = 2.5$; (b) $t^* = 10$ ($t=1000 \mu s$), $x/D = 2.5$; (c) $t^* = 10$ ($t=1000 \mu s$), $x/D = 5$; (d) $t^* = 15$ ($t=1500 \mu s$), $x/D = 5$. The four cases displayed here are consistent with the ones shown in Figure 6.11. The contour lines of 20% of the maxima are plotted as dashed-dotted lines for reference. The locations of the CVP determined in Section 6.4.2 are indicated in (a, c) by white circles.

6.5.2. YZ-PLANE

In the yz measurement planes, stereo-PIV measurements provide access to all three velocity components, thus fully defining TKE by the relation of $k = (\overline{u_x^2} + \overline{u_y^2})/2$. Contours of $\overline{u_i^2}$ and k are shown in Figure 6.16. The wall-normal locations of the CVP determined in Section 6.4.2 are superimposed as white circles for reference. The four cases used here are consistent with those used in Figure 6.11. In Figures 6.16 (a, c), the high-TKE region takes a shape of double lobe. The wall-normal location of this lobe pair agrees well with that of the corresponding CVP. For different Reynolds normal stresses, the spatial distributions are quite similar yet the absolute values differ largely. $\overline{u_x^2}$ contributes a significant part of the TKE, and $\overline{u_y^2}$ closely follows. Compared with Figure 6.16 (a), the high-TKE region in Figure 6.16 (c) expands moderately while the peak value of k drops sharply, which can be ascribed to the fast entrainment of the low-energy flow. Figures 6.16 (b, d) correspond to the second flow topology shown in Figures 6.11 (b, d), where the measurement planes intersect the root of the CVP. In this case, the majority of the TKE remains to be contributed by $\overline{u_x^2}$. However, the spatial distributions of different Reynolds normal stresses exhibit a distinct difference. High $\overline{u_x^2}$ is concentrated in the near-wall region, showing a triangle shape. High $\overline{u_y^2}$ is also situated in the near-wall region whereas spreads more widely in the y -direction than $\overline{u_x^2}$. The distribution of $\overline{u_z^2}$ takes a saddle shape, with two peaks observed at $y/D = 2.5$ and $y/D = 3.5$.

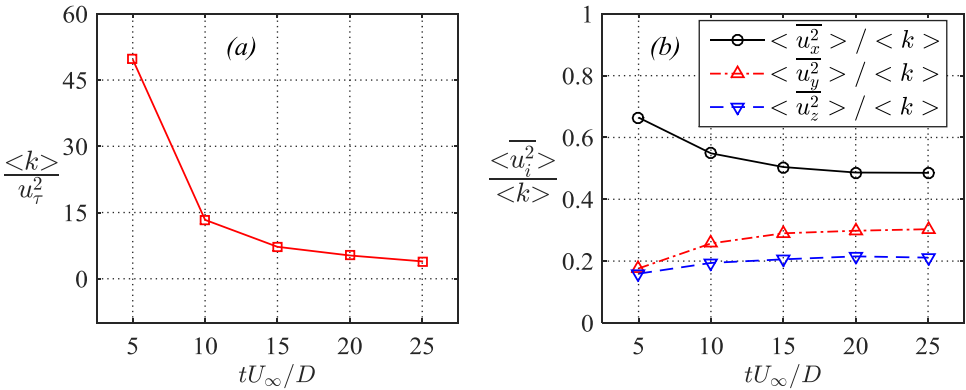


Figure 6.17: (a) Spatially averaged TKE in the jet effecting region (defined by $k > 10\overline{u_x^2}$) as a function of the non-dimensional convective time. (b) Contribution of different Reynolds normal stresses to the total TKE. It should be noted that the five data points at increasing time delays are collected at five different yz planes ($x/D = 2.5, 5, 10, 15, 20$), the same that in Figure 6.14 (b)

In order to further analyse the contribution of each Reynolds normal stress to the total TKE, the spatially averaged $\overline{u_i^2}$ (denoted as $\langle \overline{u_i^2} \rangle$) in the ‘jet effecting region’ is calculated and normalized by the spatially averaged TKE (denoted as $\langle k \rangle$). It should be noted that the jet effecting region here is defined by a criterion of $k > 10\overline{u_x^2}$, instead of the criterion used to extract the jet profiles in Section 6.4.1 (i.e. $U_y > 0.2U_{y,max}$). The evolution of $\langle k \rangle / \overline{u_x^2}$ and $\langle \overline{u_i^2} \rangle / \langle k \rangle$ ($i = x, y, z$) is shown in Figure 6.17 as a function of the

non-dimensional time. $\langle k \rangle$ decreases rapidly with time. The contribution of $\overline{\langle u_i^2 \rangle}$ to $\langle k \rangle$ is always dominant. At $tU_\infty/D = 5$ ($t = 500\mu\text{s}$), $\overline{\langle u_x^2 \rangle}/\langle k \rangle$ reaches the peak value of 66%. Afterwards, this ratio gradually decreases and finally remains constant at about 0.5. For the contribution of $\overline{\langle u_y^2 \rangle}$ and $\overline{\langle u_z^2 \rangle}$, their variation trends are opposite to that of $\overline{\langle u_x^2 \rangle}$. They grow slowly with time and reach the steady values (0.3 and 0.2, respectively) at about $tU_\infty/D = 20$ ($t = 2000\mu\text{s}$).

6.6. CONCLUSION

The interaction between a single PSJ pulse and a TBL (freestream velocity: 20 m/s, δ_{99} : 34.5 mm) under approximately zero pressure gradient is investigated with phase-locked PIV measurements. In crossflow condition, the exit velocity variation of the actuator in one cycle remains almost identical to that observed in the quiescent condition. However, the jet induced flow fields show abundant new features. In the xy plane ($z/D = 0$), the initially issued erect jet body gradually bends to the crossflow and a time-dependent jet trajectory is exhibited. The peak penetration depth is just above $10D$ ($0.58\delta_{99}$). Comparison of the non-dimensional jet trajectories suggests that the penetration ability of the PSJ is not as strong as the steady jets with the same momentum flow velocity. Prior to $t^* = 10$ ($t = 1000\mu\text{s}$), there exists a recirculation region in the leeward side of the jet body, experiencing an initial expansion and later contraction, with a peak area of three times of the exit orifice area. Additionally, a considerably high level of TKE is shown at the front vortex ring and jet shear-layer. The TKE level in the jet shear-layer is initially lower than and afterwards catches up with that in the front vortex ring.

In the yz plane, a signature vortical structure of JICE, CVP, is observed. The down-wash effect of the CVP transports the high-momentum fluids from the outer layer to the near-wall region, leading to a much fuller velocity profile and a decreased boundary layer shape factor between $-5D > z > 5D$. The non-dimensional total circulation of the CVP is on the order of 0.1 and decreases rapidly with the non-dimensional time. The maximum streamwise effecting extent of the CVP is determined to be $32D$, beyond which the total recirculation will drop to a negligible level. As the CVP drifts downstream, its wall-normal position increases as a result of the self-induction. The high-TKE regions in yz measurement planes are closely associated with the CVP, taking a shape of double lobe. The spatially averaged TKE in the double lobe decreases exponentially with time, peaking at approximately $50 u_T^2$. Of the total TKE, the streamwise component constitutes the majority proportion.

To summarize, the influence of a single PSJA on the TBL is significant in the sense of velocity profile change and TKE production, yet short-lived in the time domain and locally confined in the space domain. In future work, the interaction between a PSJA array working in a repetitive mode and a crossflow TBL should be investigated.

7

EFFECT OF VELOCITY RATIO

7.1. INTRODUCTION

INTERPRETATION of the control mechanism pertaining to PSJAs and optimisation of the control effect necessitate a clear understanding of the flow scenarios arising from the interaction of jets and crossflow. For pulsed jets in quiescent conditions, depending on how the stroke ratio (L^* , stroke length over orifice diameter) compares with the formation number (approximately 4), either isolated vortex rings ($L^* < 4$) or vortex rings with a trailing vorticity column have been observed ($L^* > 4$) [100, 136]. The presence of external crossflow complicates the above regime division by adding another dimension (i.e. velocity ratio, defined as the ratio of jet reference velocity to freestream velocity) to the parameter space. As a result, hairpin vortices are formed at a velocity ratio of less than 2, regardless of stroke ratio [137]. When the jet velocity ratio exceeds 2, downstream-tilting vortex rings ensued by a trailing jet column and isolated upstream-tilting vortex rings are produced respectively in the right side (larger) and left side (smaller) of the transition stroke ratio on the regime map. In contrast with pulsed jets without suction, conventional synthetic jets driven by piezoelectric membranes exhibit three different vortical structures (hairpin vortices, stretched vortex rings and tilted & distorted vortex rings) on the parameter map [138, 139]. For purposes of separation control where high wall shear stress is desired, the regime of stretched vortex rings is recommended [140].

Plasma synthetic jets morphologically lie in between pulsed jets (zero suction) and conventional synthetic jets (suction velocity equals injection velocity), in the sense that the peak suction velocity (no more than 20 m/s) over one period is typically much lower than the peak jet velocity. As such, much longer time is needed for refresh to satisfy mass conservation in the actuator cavity [39]. These features are expected to yield a peculiar regime map for PSJs in crossflow. Up to the present point, only Zong & Kotsonis [103] has investigated the interaction of PSJs with crossflow, based on a single case at a mean velocity ratio of 2.2 and a stroke length of approximately 18. As a result, a downstream-

Part of this chapter is submitted for review as **H. Zong** & M. Kotsonis, *Effect of velocity ratio on the interaction between plasma synthetic jets and turbulent crossflow*, Journal of Fluid Mechanics (2018).

titling vortex ring and a counter-rotating vortex pair evolved from the hanging vortex pair are generated. However, the influence of velocity ratio on the topological and quantitative characteristics of such interaction remains unclear. The elucidation of this dependency forms the goal of the present work.

In this chapter, the knowledge of plasma synthetic jets in crossflow (PSJICF) is improved from a single point in the 2D parameter space ($r = 2.2$, $L_s^* = 18$, [57]) to a line with constant Strouhal number ($St = 0.02$) and varying mean velocity ratio ($0.7 \leq r \leq 1.6$). High-speed phase-locked Particle Imaging Velocimetry (PIV) measurements are performed in both symmetry (i.e. streamwise) and spanwise planes to detect respectively the jet trajectory and emanating streamwise vortices. Setup and measurement schemes are described in Section 7.2. Baseline results of PSJs without crossflow and turbulent boundary layer without PSJs are introduced in Section 7.3. From Section 7.4 to Section 7.6, the time evolution of PSJs in crossflow at large and small velocity ratio is analysed in detail, and a conceptual model is proposed for the two identified flow regimes. Comparisons between pulsed jets in crossflow, conventional synthetic jets in crossflow and plasma synthetic jets in crossflow are executed throughout the analysis.

7.2. EXPERIMENTAL SETUP

7.2.1. WIND TUNNEL, ACTUATOR, AND POWER SUPPLY

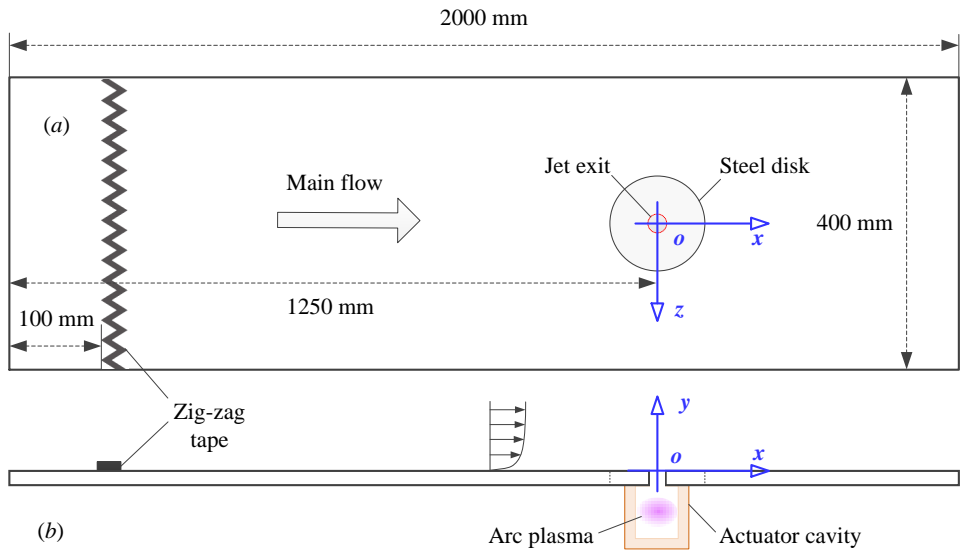


Figure 7.1: Bottom plate of the test section: (a) top view and (b) side view. The coordinate system used throughout this study is indicated in blue. Not to scale.

The present experiments are carried out in the W-tunnel of Delft University of Technology. A contraction part with $0.4 \times 0.4 \text{ m}^2$ exit area is used and further connected smoothly with a 2-meter long test section made of plexiglass. The freestream velocity

measured by a pitot tube installed in the test section is kept constant at $U_\infty = 20 \text{ m/s}$, and the corresponding freestream turbulence level is approximately 0.5%. As shown in Figure 7.1, the boundary layer originating from the settling chamber is developed naturally on the bottom plate of this test section and tripped by a zig-zag tape located 100 mm downstream of the leading edge. Due to the growth of boundary layer thickness, a slightly favourable pressure gradient is experienced in the test section and estimated to be less than $0.024\rho_0 U_\infty^2$ per meter, where ρ_0 is the ambient density determined by atmospheric pressure ($P_0 = 1.01 \times 10^5 \text{ Pa}$) and temperature ($T_0 = 293 \text{ K}$) [103]. A steel disk is flush-mounted in the bottom plate, and a circular orifice (diameter: $D = 2 \text{ mm}$) is drilled in the centre of this disk, serving as the exit of plasma synthetic jets. This steel disk accommodates the actuator cavity positioned underneath and provides the possibility of orifice shape investigation in future studies. The distance from the exit orifice centre to the leading edge of the bottom plate is 1250 mm. A coordinate system is established in the jet exit centre, with x , y and z being the streamwise direction, wall-normal direction and spanwise direction, respectively.

Plasma synthetic jets are issued from an enclosed ceramic cavity directly fitted underneath the steel disk via a circular step groove. The construction of the ceramic cavity (material: MACOR) has been shown in Figure 2.1 (a). No extra-trigger electrode is configured, and the inter-electrode gap is fixed to 2 mm. The sequential discharge power supply (i.e. a trigger discharge followed by a capacitive discharge) described in Figure 2.2 (b) is adopted to feed the actuator, and the capacitance of energy-storing capacitor C1 is fixed as $0.1 \mu\text{F}$.

7.2.2. MEASUREMENT TECHNIQUES AND TEST SCHEME

The primary focus of the present study is the effect of velocity ratio (denoted as r) on PSJICE. In order to enable variations in velocity ratio, the amplitude of the emitted jet is controlled by appropriate scaling of the discharge energy (E_d). This is consequently controlled by the initial capacitor voltage. Four cases with increasing initial capacitor voltage ($V_1 = 0.88 \text{ kV}$, 1.25 kV , 1.77 kV and 2.5 kV) are tested. The discharge frequency (f_d) is fixed at 200 Hz, as this value is slightly lower than the thermal cut-off frequency of a similar geometrical configuration (210 Hz) reported in Chapter 4. With discharge frequency below this thermal cut-off frequency, the mean cavity density is expected to remain close to the ambient density due to a sufficiently long refresh time.

Electrical measurements are necessary to quantify the discharge energy (E_d) and duration (T_d) in each case, which affect significantly the variation of the jet exit velocity [16]. The discharge voltage (u_d) and current (i_d) are measured by a high-voltage probe (Tektronix, P6015A) and a current monitor (Pearson, model 325) respectively, and the measurement stations are located respectively in the anode and between the cathode and ground. These waveforms are recorded by an oscilloscope (Tektronix, TDS 3054C) at a sampling rate of 1 GHz to compute the discharge energy. Similar to that in [54], the discharge energy is normalized by the internal energy of the cavity gas at initial state, resulting in a non-dimensional discharge energy as shown in Equation 7.1 where c_v is the

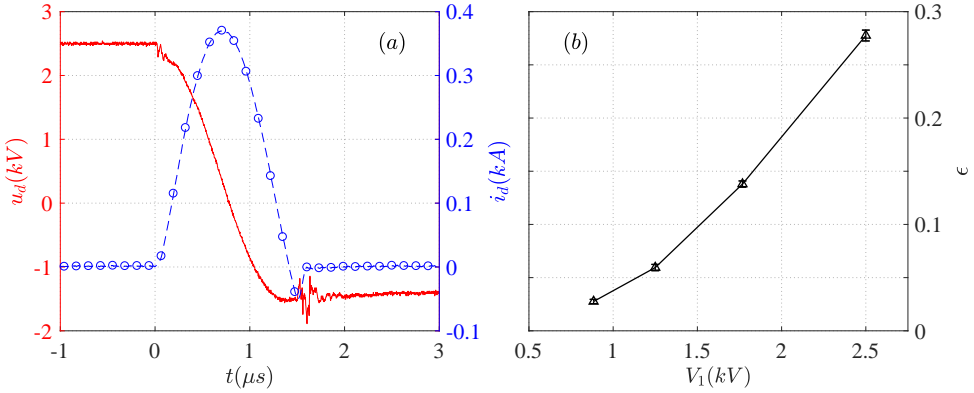


Figure 7.2: (a) Electrical waveforms measured at $V_1 = 2.5$ kV. —, capacitor voltage (red); -o-, discharge current (blue). (b) non-dimensional energy deposition at increasing initial capacitor voltage.

constant-volume specific heat capacity.

$$\epsilon_d = \frac{E_d}{E_g} = \frac{\int_0^{T_d} u_d \cdot i_d dt}{c_v \rho_0 V_{ca} T_0}. \quad (7.1)$$

Representative discharge waveforms at $V_1 = 2.5$ kV are shown in Figure 7.2 (a). Immediately after gas breakdown at $t = 0$ μ s, the capacitor voltage drops steadily, while the discharge current exhibits a half-sine wave. Periodical oscillations reported in [43] are not observed, which is ascribed to the addition of isolation diodes in the discharge circuit (Figure 2.1 (b)). The discharge duration is estimated to be 1.5 μ s, far less than the characteristic time of jet evolution (Helmholtz natural oscillation period, 607 μ s, see Equation 3.3). The non-dimensional discharge energy deposition (ϵ_d) in the four tested cases is shown in Figure 7.2 (b). ϵ_d ranges from 0.028 to 0.28. Simplified theoretical estimations [16, 54] with a typical electro-mechanical efficiency of 1% [85] have shown that this range will yield a peak velocity ratio ranging between 1 and 4, which is typically encountered in industrial applications as well as research studies [76].

Phase-averaged high-speed PIV measurements are carried out in three wall-normal planes. Of these planes, one is aligned in the streamwise direction (henceforth referenced as the symmetry plane, $z/D = 0$), while the remaining two are aligned in the spanwise direction ($x/D = 2$ and $x/D = 5$). As indicated in Figure 7.3, the symmetry-plane measurements aim at the elucidation of the jet trajectory while spanwise-plane measurements capture the streamwise vortices. The PIV system mainly consists of two high-speed cameras (Photron, Fastcam SA-1, 1024×1024 pixels), a high-speed laser (Quantronix, Darwin Duo 527-80-M) and a programmable timing unit (LaVision, HSC). Depending on the measurement type (planar for the symmetry plane, stereo for the spanwise planes), either one or two cameras are used. On each of the high-speed camera, a 200 mm objective (Nikon, Micro-Nikkor) fitted with a $2 \times$ teleconverter (Kenko) is mounted to image a field of view (FOV) of $7.5D \times 7.5D$ and $12D \times 12D$ in planar and stereo PIV, respectively. The view angle between the two cameras in stereo configuration is approximately 60° .

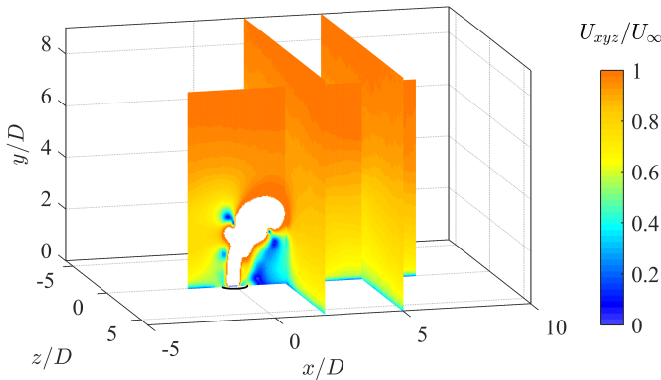


Figure 7.3: FOVs in 2C-planar and 3C-stereo PIV measurements. The magnitude of total velocity (U_{xyz}) at a time delay of $t = 300\mu s$ with regard to discharge ignition is displayed as contours. High-velocity regions ($U_{xyz}/U_{\infty} \geq 1$) are cropped to visualize the bending jet.

Scheimpflug adapters are mounted in between cameras and objectives to align the focus plane to the object plane. Laser beams are shaped into a thin sheet (thickness: 0.6 mm for planar configuration and 1 mm for stereo), using a combination of two spherical lenses and one cylindrical lens. This laser sheet is kept strictly normal to the bottom plate and transmitted in wall-parallel direction to minimize wall reflection. Liquid particles (mean diameter: 1 micron) are seeded in the setting chamber of the wind tunnel by a fog generator (SAFEX, Fog 2010+), using a working fluid of water-glycol mixture. The particle image size is kept as 2-3 pixels to avoid significant peak-locking errors [141].

Raw particle images are recorded in phase-locked mode, and the phase (t , namely the time delay between discharge ignition and image acquisition) can be adjusted by a digital delay generator (Stanford Research Systems, DG 535). Depending on the peak jet velocity observed in each phase, the time separation between two laser pulses varies between $2\mu s$ and $8\mu s$ to guarantee a peak particle displacement of approximately 10 pixels. For each of the four tested cases, 54 phases are selected in one cycle to retrieve the entire evolution of PSJICE, ranging from the emanation of incipient jets to the termination of the suction stage. For each of the 54 phases, 300 image pairs are recorded to arrive at statistically converged velocity fields. Both image acquisition and post-processing are implemented by Lavision Davis 8.3.1. In the final pass of cross-correlation operation, the interrogation window size and the overlapping ratio are 16×16 pixels² and 75% respectively, leading to a spatial resolution of 0.07 mm/vector and 0.1 mm/vector in planar and stereo PIV measurements. In addition to measurements under PSJICE conditions, the baseline unactuated boundary layer and the PSJs without crossflow boundary layer (quiescent flow) are also measured. In the case of baseline boundary layer test, 2000 samples are acquired at 2 kHz at each of the three measurement planes to get converged mean flow quantities as well as Reynolds stresses. The FOV in the symmetry plane ($z/D = 0$) is enlarged as $15D \times 15D$ to cover the entire boundary layer. For PSJs in qui-

escent flow, similar phase-averaged measurements as mentioned earlier are performed, whereas only 100 samples are acquired at each phase.

Peak locking error, finite sample size, finite laser sheet thickness and discharge timing uncertainty are identified as the four main sources of phase-averaged PIV measurement uncertainty. Following a similar procedure as described in Section 2.4.2, each of the four measurement uncertainties can be estimated a posteriori. The total measurement error is defined as the Euclidean sum (i.e. root-sum-square) of these four uncertainties [86]. As a result, the peak errors for U_x and U_y in planar PIV measurements are estimated to be 2.4% and 4.9% of the peak jet velocity. In stereo PIV measurements, camera view angle is taken into account during the estimation of peak locking error, and the peak uncertainties pertaining to the three velocity components (U_x , U_y , and U_z) are computed to be 6.0%, 3.0% and 3.5% of U_∞ , respectively.

7.3. BASELINE RESULTS

7.3.1. SYMBOL CONVENTION

Prior to introducing any results, symbol notation is defined. The instantaneous, phase-averaged and time-averaged velocity are denoted respectively by u , U and \bar{U} . τ_w and δ_{99} denote the wall shear stress and the boundary thickness determined by 99% U_∞ , respectively. δ^* and θ are the displacement thickness and the momentum thickness of the boundary layer defined by Equation 7.2 and Equation 7.3, where $U_{x, min}$ is the minimum velocity in the profile [142]. The ratio of the displacement thickness to momentum thickness defines the boundary layer shape factor, $H = \delta^*/\theta$. When no reverse flow occurs ($U_{x, min} = 0$ m/s), these definitions collapse to the orthodox definitions in [122]. However, in the case of strong reverse flow, these definitions can effectively suppress the rise of the shape factor. u_τ and δ_v denote the viscous velocity and length scale, respectively. y^+ and u^+ are defined as $y^+ = U_\tau y$ and $u^+ = u/\delta_v$, respectively.

$$\delta^* = \int_0^{\delta_{99}} \left(1 - \frac{U_x - U_{x, min}}{U_\infty - U_{x, min}}\right) dy \quad (7.2)$$

$$\theta = \int_0^{\delta_{99}} \frac{U_x - U_{x, min}}{U_\infty - U_{x, min}} \left(1 - \frac{U_x - U_{x, min}}{U_\infty - U_{x, min}}\right) dy \quad (7.3)$$

7.3.2. UNACTUATED TURBULENT BOUNDARY LAYER

The mean-velocity profile and the root-mean-square (RMS) of the turbulent velocity fluctuation (denoted as $u'_{i, rms}$) measured in the symmetry plane at $x/D = 2$ are shown in Figure 7.4. As a result, δ_{99} , δ^* and θ are computed to be 19.3 mm, 3.2 mm and 2.3 mm respectively. The boundary layer shape factor is 1.36 and changes marginally in the measurement domain, indicating a fully developed turbulent boundary layer. The Reynolds number based on the momentum thickness and freestream velocity (Re_θ) is approximately 2550. In the inertial range ($0.03 \leq y/\delta_{99} \leq 0.3$) of the turbulent boundary layer (TBL), the variation of mean velocity follows a logarithmic law [122], as shown in Equation 6.1 (Chapter 6).

Based on the log relation and the measured velocity profile, u_τ and δ_v are determined

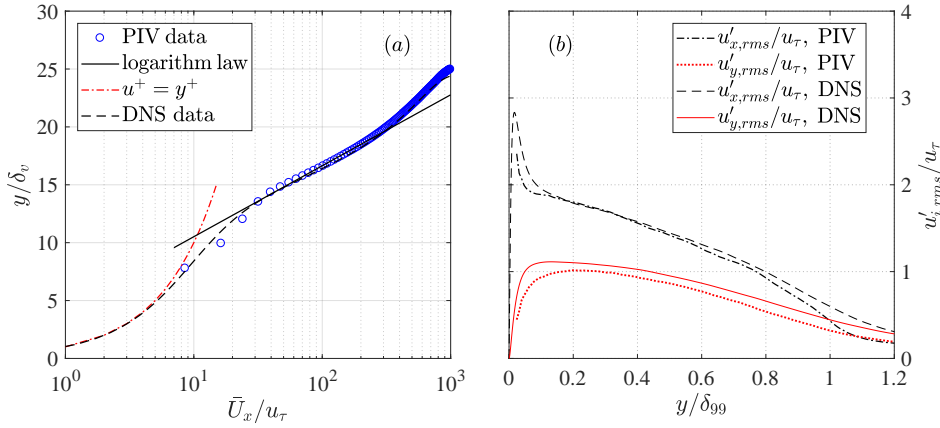


Figure 7.4: (a) Mean-velocity profiles and (b) Reynolds normal stresses measured at $x/D = 2$ and $z/D = 0$. DNS data from Wu et al. [143] at $Re_\theta = 2540$ are compared.

to be 0.80 m/s and $19.1 \mu\text{m}$ respectively. Direct numerical simulation (DNS) data from Wu et al. [102] at a similar momentum-thickness-based Reynolds number ($Re_\theta = 2540$) are plotted for comparison. As a result, the mean velocity profile collapses well even in the buffer layer ($8 \leq y^+ \leq 30$). The turbulent velocity fluctuations (Figure 7.4b) from DNS are slightly higher than PIV in the near-wall region ($y/\delta_{99} \leq 0.1$) and decay relatively slowly in the outer boundary layer ($y/\delta_{99} \geq 0.8$), further confirming the reliability and accuracy of the present PIV measurements.

7.3.3. PLASMA SYNTHETIC JETS IN QUIESCENT FLOW

The time evolution of the phase-averaged velocity fields in Case 1 ($\epsilon = 0.028$) and Case 4 ($\epsilon = 0.28$) is shown in Figure 7.5. Although no external flow is present, the freestream velocity pertaining to the flow cases (U_∞) and the exit orifice diameter (D) are used to normalize the physical time and facilitate comparison, resulting in a dimensionless convection time, $t^* = tU_\infty/D$. In both cases, a vortex ring is shed from the exit orifice as a result of an abrupt expansion of the cavity gas immediately after the pulsed arc discharge. This vortex ring propagates along the axisymmetry axis of the actuator throat and entrains the surrounding fluids into its core region, leading to growing size. This core region exhibits the highest velocity as a result of the self-induction effect of vortex rings. Suction flow, as visualized by the contour lines of $U_y/U_\infty = -0.1$, is initialized at the periphery of jet exit at $t^* = 4$. An inward growth of the suction region is experienced afterwards, and the entire orifice is occupied at $t = 5^*$. The general topology of the emanating jets agree well with results of past characterization studies [39, 144].

The leading vortex ring in Case 4 is initially connected with a trailing jet ($t^* = 2$) which severs from the jet front after $t^* = 5$. As a comparison, the vortex ring in Case 1 is always isolated during evolution. This morphological difference is attributed to the 'formation number' of vortex rings (L_s/D), which is reported to be 3.6-4.5 [100, 136]. Specifically, when the stroke ratio (L_s^*) defined by Equation 7.4 [8, 39] is below this for-

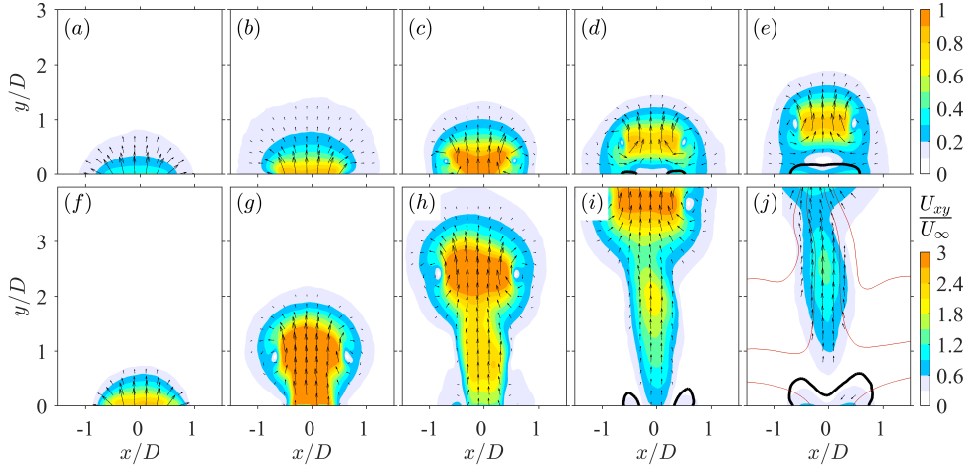


Figure 7.5: Phase-averaged velocity fields in Case 1 (top row, $\epsilon = 0.028$) and Case 4 (bottom row, $\epsilon = 0.28$). The dimensionless convective time is identical in each row and increases linearly from $t^* = 1$ to $t^* = 5$ in a step of 1 time unit (left to right). Direction and magnitude of the in-plane velocity (U_{xy}) are displayed as contours and vectors. The thick black lines near jet exit are contour lines of $U_y/U_\infty = -0.1$. The thin red lines in (j) are streamlines.

mation number, the vorticity shed from the jet exit will be absorbed completely by the vortex ring, and no trailing jet column will form.

$$L_s^* = \frac{L_s}{D} = \frac{1}{\rho_0 D} \int_0^{T_{jet}} \rho_e(t) U_{ey}(t) dt \quad (7.4)$$

Here, T_{jet} is the duration of the ejection stroke. ρ_e and U_{ey} are the spatially-averaged jet exit density and jet exit velocity, respectively. In the case of axisymmetric jets, the following relation can be derived straightforwardly.

$$U_{ey} = \frac{4}{D^2} \int_{-D/2}^{D/2} x \cdot U_y(x, t)|_{y=0} dx \quad (7.5)$$

The variation of U_{ey} with one actuation cycle is extracted from PIV results and shown in Figure 7.6. For all the cases, a prominent jet stage is perceived immediately after discharge ignition, where U_{ey} first rises and then decays. As energy deposition (ϵ) increases, the peak jet exit velocity (U_p) increases monotonically from $1.2U_\infty$ to $3.5U_\infty$, whereas the duration of primary jet stage (T_{jet}) changes marginally (400-450 μs). Periodical oscillations pivoting around $U_{ey}/U_\infty = -0.1$ with decaying amplitude are noticed in the later evolution of U_{ey} ($t^* > 5$), pertaining to the occurrence of weak suction flow. Based on the amount of velocity peaks within one period, the oscillation frequency is determined to be 1.6 kHz, which reconciles well with the estimated Helmholtz natural resonance frequency of the present PSJA cavity ($f_h = 1.65$ kHz) [39, 46]. The Helmholtz natural resonance frequency (f_h) is derived from the stiffness of the cavity gas and mainly affected by geometrical and atmospheric parameters as has been shown in Equation 3.2.

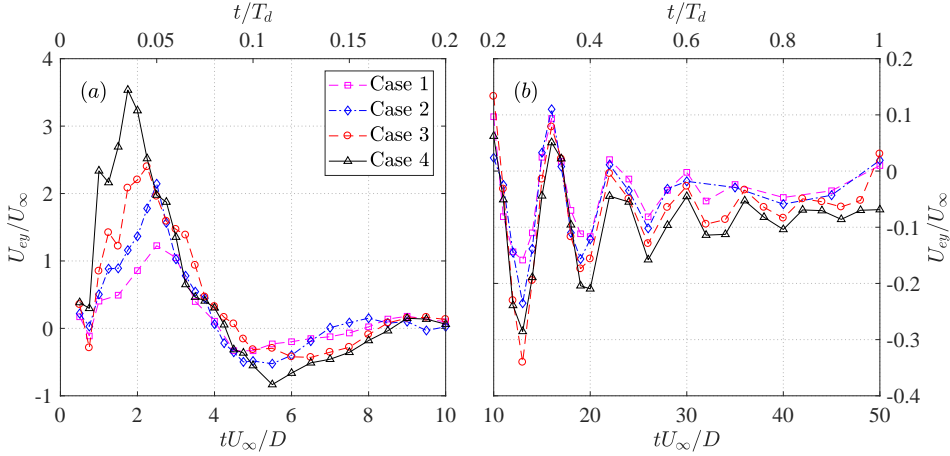


Figure 7.6: Evolution of the spatially-averaged exit velocity (U_{ej}) in one period for all the tested cases. Scales of y-axis are changed to adapt for the different velocity range.

For conventional SJAs driven by vibrating membranes, the frequency response of peak exit velocity exhibits a maximum at f_h [95, 145], i.e. operating at this frequency is beneficial. Nevertheless, for PSJAs f_h is generally interpreted as the theoretical limit working frequency above which significant misfires are expected due to a shortage of refresh time [15, 144]. In this study, the discharge frequency ($f_d=200$ Hz) is approximately $0.12f_h$, and no significant frequency effect (e.g. reduced jet density, increasing cavity temperature) is expected.

The manifestation of the Helmholtz natural frequency in Figure 7.6 can also be explained from a theoretical perspective. Specifically, the formation process of PSJs is essentially the time response of a fluid system (a cavity with an opening, i.e. Helmholtz resonator) to a localized heat disturbance. Since this heat disturbance (arc discharge) is imposed abruptly within $0.2\%T_h$, the solution collapses to the impulse response of this fluid system described by the second-order Navier-Stokes equation. This is somehow reasonable, as the curves in Figure 7.5 do resemble the impulse response of a second-order under-damped system. As such, the inherent resonance frequency of this fluid system will be excited and manifested in the time response.

Based on these exit velocity curves, the time-mean jet exit density in the ejection stroke ($\bar{\rho}_e$) can be estimated using the mass conservation law [39]. As a result, $\bar{\rho}_e/\rho_0$ varies from 0.9 to 0.8 with increasing energy deposition, and the total expelled gas mass in the jet stages is less than 2% of the initial cavity mass ($\rho_0V_c a$). Since the variation of jet intensity is small, the time-varying exit density in Equation 7.4 can be replaced by $\bar{\rho}_e$, and the stroke ratio for the four tested cases is computed to vary from 2.0 to 5.4 (see Table 7.1). This justifies the earlier interpretation of Figure 7.5 based on the formation number of vortex rings (3.6).

The time-mean velocity in the ejection stroke ($U_0 = L_s/T_{jet}$) is selected as the reference velocity to compute the jet Reynolds number ($Re_D = U_0 D/\nu$) and the velocity ratio

Table 7.1: Jet formation parameters for all the tested cases

No.	V_0 (kV)	f_d (Hz)	ϵ_d	U_p/U_∞	r	L_s/D	Re_D	St	δ_{99}/D	c_f
Case 1	0.88	200	0.028	1.2	0.7	2.0	1790	0.02	9.7	3.2×10^{-3}
Case 2	1.25	200	0.06	2.1	1.0	2.6	2620	0.02	9.7	3.2×10^{-3}
Case 3	1.77	200	0.14	2.4	1.2	3.7	3290	0.02	9.7	3.2×10^{-3}
Case 4	2.50	200	0.28	3.5	1.6	5.4	4300	0.02	9.7	3.2×10^{-3}

($r = U_0/U_\infty$) [10]. The Strouhal number is based on orifice diameter and freestream velocity, $St = f_d D/U_\infty$ [139]. These parameters (L_s^* , Re_D , r , St), plus the skin friction coefficient ($c_f = \tau_w/0.5\rho_0 U_\infty^2$), and the ratio of boundary layer thickness to orifice diameter ($h = \delta_{99}/D$), constitute the six dimensionless quantities that govern the pertinent physics of PSJICF, as listed in Table 7.1. The freestream Reynolds number based on boundary layer thickness is not included due to the following interdependency, $Re_\delta = Re_L \cdot h/(r \cdot L_s^*)$. In contrast with conventional synthetic jets driven by oscillating membranes [139], the Strouhal number is included in the parameter space of PSJs, since $St = 0.5r/L_s^*$ no longer holds. Of all these parameters, stroke length and velocity ratio play a dominant role in the flow field evolution [137, 140]. Since the jet duration time is fixed by the actuator geometry in this study, effects of r and L_s^* are effectively combined, i.e. high jet velocity always indicates large stroke length.

7

7.4. PLASMA SYNTHETIC JETS IN CROSSFLOW AT $r = 1.6$

This section focuses on Case 4 ($r=1.6$), which, based on the quiescent measurements, is characterised by the highest formation number ($L_s/D = 5.4$) among the tested cases. Phase-averaged velocity fields in the symmetry plane are first introduced, and effects of several pertinent flow features (shock waves, vortex rings, back flow, suction flow) on the boundary layer are analyzed in detail. Subsequently, streamwise vortices are identified in the spanwise measurement planes (yz -planes), and the interconnections between these streamwise vortices and the flow features in the symmetry plane are interpreted to establish a clear picture of PSJICF at high velocity ratio and large stroke length.

7.4.1. SYMMETRY PLANE

The time evolution of the phase-averaged velocity fields in the symmetry plane ($z=0$ mm) is shown in Figure 7.7. U_{xy} denotes the Euclidean norm of the in-plane velocity vectors, $U_{xy} = (U_x^2 + U_y^2)^{0.5}$. Since the peak jet velocity is much higher than the freestream velocity in this case ($U_p/U_\infty = 3.5$), the jet body can be roughly represented by the region with $U_{xy}/U_\infty > 1$. An incipient jet manifested in a bump shape is observed at $t^* = 1$. The vorticity residing in the periphery of this incipient jet rolls into a vortex ring ($t^* = 1.5$), and propagation of this vortex ring is ensued by a high-speed trailing jet column ($t^* = 2$), similar to the case of quiescent flow. This jet column is initially upright whereas bends to the crossflow during later evolution ($t^* = 3$), as a result of the streamwise pressure difference across the jet orifice [146]. Concurrently, the flow in the windward side is

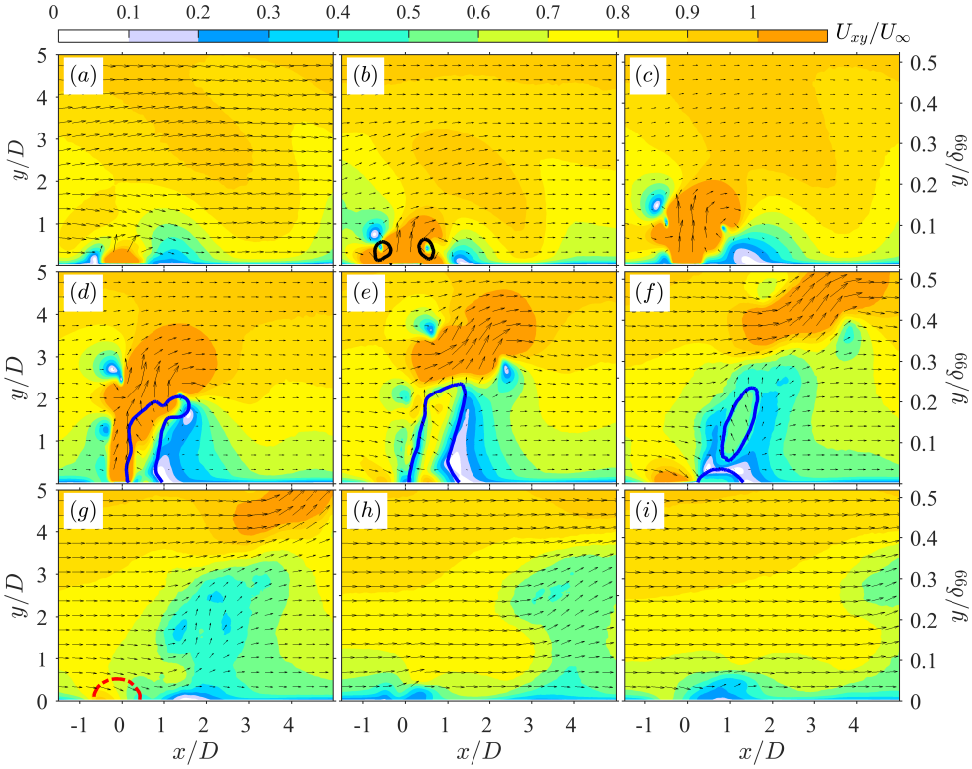


Figure 7.7: Phase-averaged velocity fields in Case 4 ($r=1.6$). (a) $t^* = 1$; (b) $t^* = 1.5$; (c) $t^* = 2.0$; (d) $t^* = 3$; (e) $t^* = 4$; (f) $t^* = 5.5$; (g) $t^* = 7$; (h) $t^* = 10$; (i) $t^* = 12$; Magnitude and direction of the in-plane velocity (U_{xy}) are displayed as contours and vectors. The black lines in Figure 7.7 (b) indicate the front vortex ring detected with a criterion of 10% of the peak Q -value. The blue lines in Figure 7.7 (d)-(f) are contour lines of $U_x/U_\infty = -0.1$. The red dash-dot lines in Figure 7.7 (g) are contour lines of $U_y/U_\infty = -0.2$.

stagnated, creating a high-pressure zone. Whereas, a back flow region associated with a hanging vortex pair (HVP) is generated in the leeward side of jet column [128], analogous to the recirculation region in cylinder flow and produces a low-pressure core. The back flow diminishes in area after the jet terminates ($t^* \geq 4$) and leaves a significant momentum deficit in the symmetry plane. Additionally, a weak suction region and a low-speed ejection can be perceived near the exit orifice during later evolution ($7 \leq t^* \leq 12$).

At $t^* = 1$, the velocity contour lines in the outer boundary layer ($y/\delta_{99} > 0.3$) manifest a noticeable undulation, which seems peculiar as the incipient jet is still embedded within $y/\delta_{99} < 0.1$. To further gauge this effect, contours of U_y , the boundary layer velocity profiles as well as the shape factor are shown in Figure 7.8. As evidenced, multiple compression/expansion waves at a wall-normal spacing of approximately $2D$ are issued from the exit orifice. These waves are generated from the nonuniform heating of the pulsed arc discharge, and their locations are synchronized by the discharge igni-

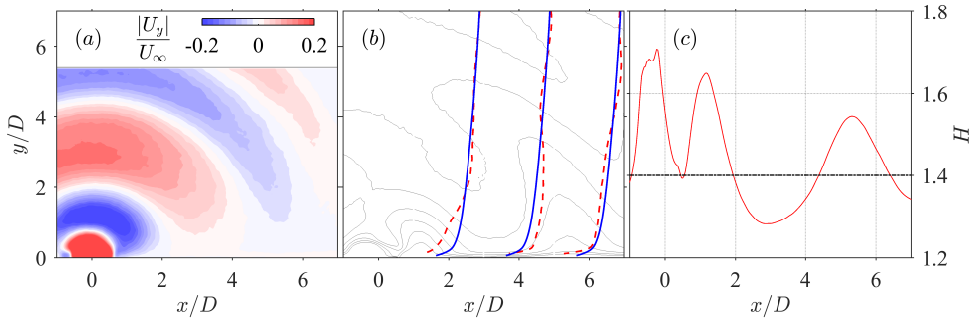


Figure 7.8: (a) Contour of wall-normal velocity (U_y) at $t^* = 1$ for Case 4. (b) Boundary layer velocity profiles at $t^* = 1$ and $x/D = 1, 3, 5$ (red dash lines); The velocity profiles of unactuated boundary layer are indicated by solid blue lines. The thin dark lines superimposed in the background are contour lines of streamwise velocity ranging from $U_x/U_\infty = 1.0$ (top) to $U_x/U_\infty = 0.4$ (bottom) in a step of -0.1 . (c) Streamwise variation of the boundary layer shape factor (H) at $t^* = 1$. The baseline value (1.4) is indicated as a thick black line for comparison.

tion within an uncertainty of approximately $1 \mu\text{s}$ [91]. Periodical alternations of outward and inward disturbance velocity on the order of several m/s are induced by these propagating waves [82]. This disturbance velocity is superimposed on the existing boundary layer velocity profile, leading to a valley-shape velocity contour line and a corresponding undulation of the boundary layer shape factor. Specifically, at the time instant of $t^* = 1$, the superimposition of compression wavefronts on the boundary layer leads to a fuller velocity profile between $2 < x/D < 4$, whereas the regions influenced by expansion wavefronts are decelerated.

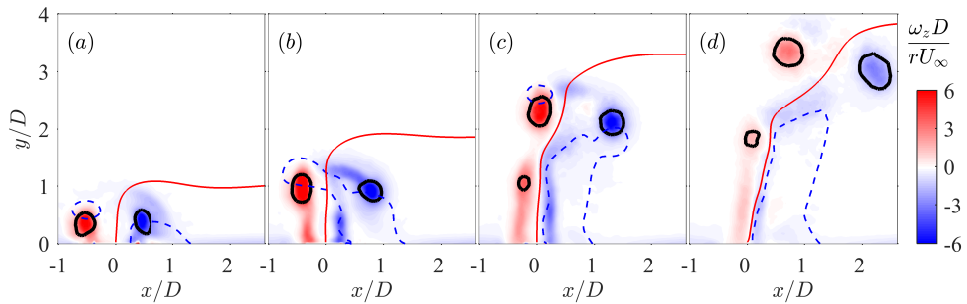


Figure 7.9: Time evolution of vorticity contour in Case 4. (a) $t^* = 1.5$; (b) $t^* = 2.0$; (c) $t^* = 3$; (d) $t^* = 4$; Vortices indicated by the black lines are detected with a criterion of 10% of the peak Q-value. The blue dash lines are contour lines of $U_x/U_\infty = -0.1$. The red solid lines are the streamlines originating from exit orifice centre.

The time evolution of the vorticity field between $t^* = 1.5$ and $t^* = 4$ is shown in Figure 7.9. Vortices are identified with the Q-criterion using a threshold of 10% of the peak Q-value to filter trivial vortex filaments [147]. Spanwise vorticity (ω_z) is normalized by rU_∞/D . High-vorticity resides in the front vortex ring (FVR) and jet shear layer. The di-

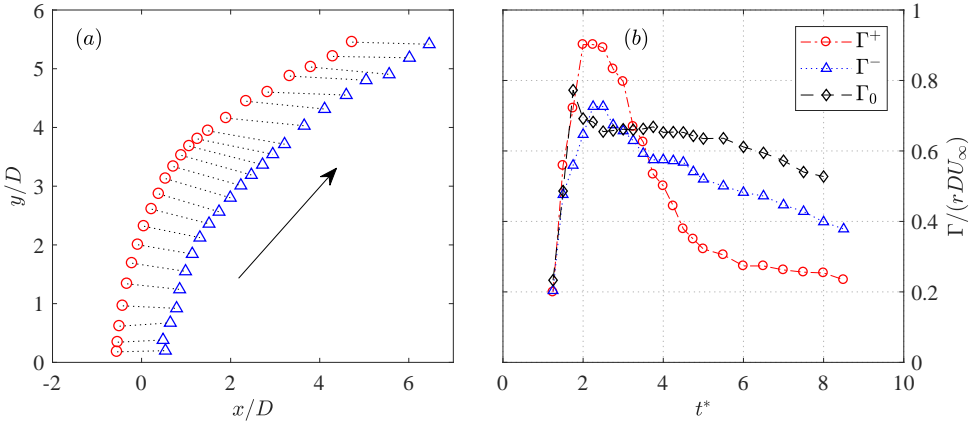


Figure 7.10: (a) Propagation of the front vortex ring in crossflow. \circ , windward vortex center (x_v^+, y_v^+) ; \triangle , leeward vortex center (x_v^-, y_v^-) . (b) Variation of the dimensionless vortex circulation (Γ) against time. Γ^+ , upstream side circulation in crossflow condition; Γ^- , downstream side circulation in crossflow condition; Γ_0 , vortex circulation in quiescent condition.

ameter of the front vortex ring expands as a result of entrainment, and the axis of the vortex ring tilts downstream after $t^* \geq 3$. This downstream tilting is an unstable process, related to the uneven momentum injection received by the two sides of the FVR [82]. Specifically, as the FVR penetrates higher in the TBL, it experiences a higher convection velocity than the base of the trailing jet, which causes a misalignment of the FVR axis with respect to the trailing jet column ($t^* = 2$). This misalignment brings more momentum from the high-speed trailing jet to the upstream side of the ring, whereas partially cuts off the momentum injection to the downstream side. As a result, the two sides exhibit a different propagation velocity, and the FVR tilts downstream. This developing downstream tilting pinches off the connection of the FVR with the trailing jet column and creates a kink point in the middle streamline. In the windward side of this kink-point, shear layer vortices are identified. In the leeward side of jet body, the negative vorticity diminishes after $t^* = 4$ due to the upstream growth of backflow. These observations are consistent with the DNS results of pulsed jets in laminar crossflow [137].

Circulation (Γ) and centre location (x_v, y_v) of the two sides of the FVR can be computed with Equations 7.6-7.8, where the integral is limited to the identified vortex region in Figure 7.9.

$$\Gamma^+ = \iint \omega_z^+ dx dy \quad (7.6)$$

$$x_v^+ = \frac{1}{\Gamma^+} \iint x \cdot \omega_z^+ dx dy \quad (7.7)$$

$$y_v^+ = \frac{1}{\Gamma^+} \iint y \cdot \omega_z^+ dx dy \quad (7.8)$$

Superscripts (+ or -) are added to distinguish the upstream side from the downstream side. Figure 7.10 shows the trajectory of the FVR. It is evident that the downstream tilting

of the ring reaches a maximum between $3 < y/D < 4$, and a gradual recovery to wall-normal orientation is exhibited afterwards. This recovery is caused by Kutta–Joukowski lift, which dominates the motion of isolated vortex rings in crossflow. In this situation, the upstream side experiences a downward lift force, whereas the downstream side undergoes an upward force [137]. This natural tendency to tilt upstream is initially inhibited by the presence of the trailing jet column and finally manifested after the pinch-off. In Figure 7.10 (b), the dimensionless vortex ring circulation (Γ/rDU_∞) in both crossflow and quiescent condition is plotted against time (t^*). A non-monotonic variation is exhibited by these curves, and the peak circulations are close to each other (0.7–0.9). In the later evolution ($t^* > 3$), a faster dissipation rate of circulation is exhibited in crossflow, which can be ascribed to the higher entrainment rate of vortex rings in crossflow [137]. Additionally, Γ^+ is always higher than Γ^- at $t^* > 3$, indicating the possible connection of the FVR with other vortices, as will be further discussed in Section 7.4.2.

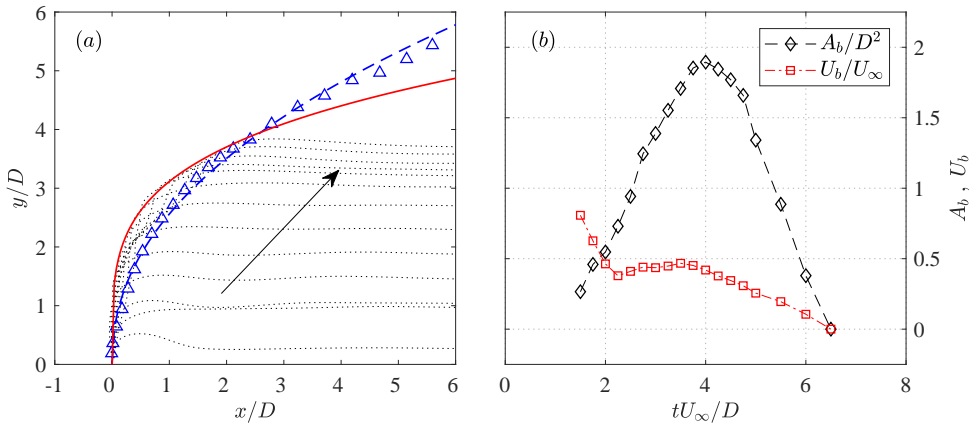


Figure 7.11: (a) \cdots , middle streamlines at increasing time delay; Δ , vortex ring center trace (x_v, y_v); — , jet trajectory fitted from the envelop of middle streamlines; -- , jet trajectory fitted from the vortex ring center trace. (b) Time variation of the normalized backflow area (A_b/D^2) and the mean backflow velocity (U_b/U_∞).

For steady jets, jet trajectories are commonly defined as the time-averaged streamline originated from the exit centre, positions of local velocity maxima, scalar maxima or vorticity maxima [76]. However, for plasma synthetic jets, the definition of jet trajectories is not straightforward. In Chapter 6, the envelop of the middle streamlines at different ejection phases were extracted to fit the jet trajectory describe by Equation 6.3.

As shown in Figure 7.11 (a), this streamline definition yields a jet trajectory ($A = 2.2$, $B = 0.25$) that is lower than the trace of vortex ring centre in far field ($A = 2.0$, $B = 0.45$). For steady jets, typical ranges for the two coefficients in Equation 6.3 are $1.2 < A < 2.6$ and $0.28 < B < 0.34$ [130]. Thus, it is evident that the high penetration ability of pulsed jets in crossflow is actually contributed by the vortex rings. This observation has been utilized by M'closkey et al. [148] to maximize the jet penetration by optimizing the time-varying exit velocity. The time variation of the backflow area (A_b) in the leeward side of the jet body as well as the mean velocity in this region (U_b) is shown in Figure

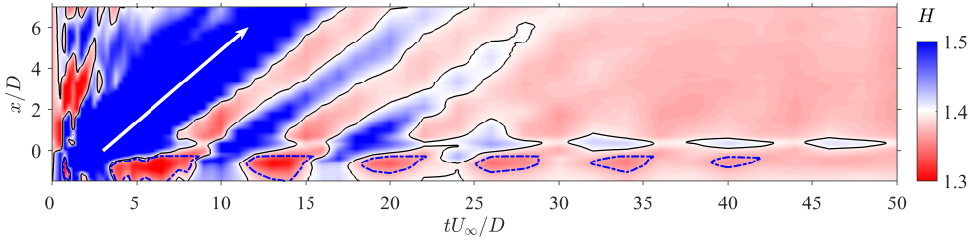


Figure 7.12: Spatial-temporal map of the boundary layer shape factor in xy -plane. The black thin lines and blue dash lines are contour lines of $H = 1.4$ (baseline value) and $H = 1.37$, respectively. The white arrow indicates a propagation velocity of $0.7U_\infty$.

7.11 (b). As a result, A_b/D^2 increases linearly during the primary jet stage ($t^* \leq 4$) and decreases after the jet diminishes. Peak value of A_b/D^2 is approximately 2. This variation trend is attributed to the wax and wane of the virtual blockage effect created by the erect high-speed jet body. By contrast, the mean backflow velocity experiences a monotonic decreasing trend, and a plateau of $0.5U_\infty$ is observed at $2 \leq t^* \leq 4$.

Phase-averaged effects of PSJ on TBL in the symmetry plane can be illustrated from the spatial-temporal map of the boundary layer shape factor, as shown in Figure 7.12. Note that the shape factor under the baseline condition is 1.40. Blue and red colors indicate degradation (i.e. deceleration) and energisation (i.e. acceleration) of the boundary layer respectively. The upright high-speed jet and the leeward backflow region incur significant momentum deficits to the near-exit boundary layer at $t^* < 7$. This momentum-deficit area travels downstream at approximately $0.7U_\infty$ and creates a parallelogram of high boundary layer shape factor. Similar narrow streaks are formed when the secondary weak jets are issued. Upstream of the jet exit, several spots of low shape factor occur periodically along the time axis, which is associated with the fluctuating suction velocity as shown in Figure 7.6 (b). The period of these spots corresponds to the Helmholtz natural oscillation period (approximately $600 \mu\text{s}$). Additionally, as weak suction dominates the later evolution of plasma synthetic jets (see Figure 7.6), the right-half of the map is dominated by boundary layer energisation.

Figure 7.13 (a) shows the time-averaged velocity field reconstructed with Equation 2.16. Upstream of the jet orifice, velocity contours are shifted to the near wall region by suction flow, while a time-averaged reduction of the boundary layer shape factor is perceived, as shown in Figure 7.13 (b). For velocity contour lines of $0.5 \leq U_x/U_\infty \leq 0.7$, a distortion is manifested right underneath the jet trajectory fitted from the vortex ring centre trace. This region corresponds to the time-averaged momentum deficit caused by the backflow area and the lifting jets, leading to high shape factor ($H > 1.4$, retarded flow) between $0.5 < x/D < 2$. After $x/D > 2$, the shape factor remains unchanged at baseline value. Additionally, the variation of wall shear stress can be estimated from the velocity vector closest to wall at approximately $y^+ = 10$, as shown in Equation 7.9.

$$k_\tau = \frac{U_x|_{y^+=10}}{U_{x0}|_{y^+=10}} \quad (7.9)$$

U_x and U_{x0} denote the streamwise velocity in Case 4 and under baseline condition, respectively. k_τ can be interpreted as the normalized wall shear stress, provided that

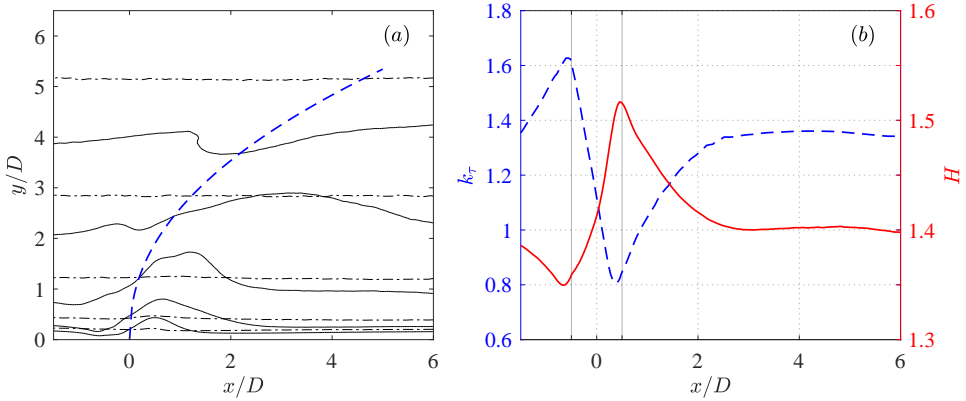


Figure 7.13: (a) Contours lines of time-averaged streamwise velocity; - -, baseline condition; —, Case 4. From top to down, U_x/U_∞ varies from 0.9 to 0.5 in a step of -0.1 . - -, jet trajectory fitted from the trace of vortex ring center. (b) Streamwise variation of normalized wall shear stress and boundary layer shape factor (baseline value: 1.4) in time-averaged flow field; - -, k_r ; —, H . Boundaries of the jet exit are indicated by two thin lines.

the near-wall velocity gradient does not change considerably until $y^+ = 10$. Particular attention should be drawn to the relative uncertainty in wall shear estimation, which can reach 15% due to an ambiguous wall position (1 pixel). As a result, the wall shear stress is inversely proportional to the shape factor as expected, and an increase of up to 60% is attained just upstream of the exit orifice. Downstream of the exit, k_r recovers from 0.8 to approximately 1.35 and remains unchanged afterwards. This elevated wall shear stress in the symmetry plane is also observed in the interaction between conventional synthetic jets and laminar boundary layer [140].

7.4.2. SPANWISE PLANES

Phase-averaged velocity fields at $x = 2D$ for increasing time delays ($t^* = 3, 4$ and 5.5) are shown in the middle column of Figure 7.14. The corresponding velocity fields in symmetry plane are displayed in the left column for comparison. In the right column, wall-normal variations of $U_y/U_{y,max}$ at $x = 2D, z = 0$ and normalized Q-value variation along a wall-normal line that passes through the nearest vortex centres (white lines in Figure 7.14(a, d, g)) are plotted together. $U_{y,max}$ and Q_{max} denote the peak values of U_y and Q-value, respectively. At $t^* = 3$, the front vortex ring is located upstream of $x = 2D$, and the downwash effect of the downstream side of the FVR can be visualized clearly in Figure 7.14 (b). The position of peak downwash velocity corresponds well to the centre of the downstream vortex (Q-value peak) as expected. The head of the high-speed jet is intersected by the spanwise measurement plane in a circular shape as indicated by the contour line of $U_{xyz}/U_\infty = 1$. Significant momentum deficit is observed underneath the jet head. At $t^* = 4$, the measurement plane of $x = 2D$ cuts through the vortex ring. As a result, a counter-rotating vortex pair (CVP) is perceived in Figure 7.14 (e), corresponding to the two longitudinal edges of the ring. The position of the peak upwash velocity is slightly higher than that of the downstream vortex centre, which can be ascribed to the downstream tilting of the FVR as described in Section 7.4.1. The high-momentum flow

entrained in the ring is spread outwards and upwards, leading to a mushroom-shape cross-section of the high-speed jet.

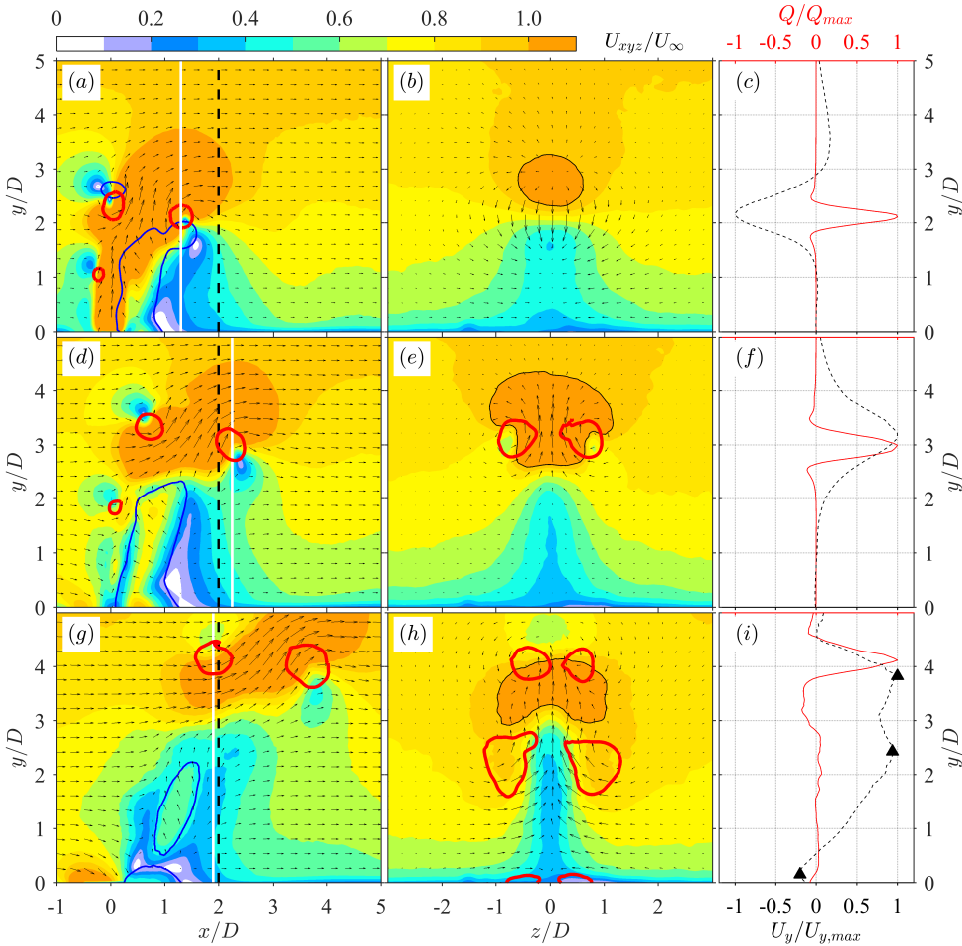


Figure 7.14: Time evolution of the phase-averaged velocity fields at $x = 2D$ (middle column). The corresponding velocity field in symmetry plane is shown in the left column. Top row, $t^* = 3$; middle row, $t^* = 4$; bottom row, $t^* = 5.5$. The thick red lines superimposed on contours indicate vortices detected with 10% of the maximum Q -value. Thin blue lines in the left row and thin dark lines in the middle row are contour lines of $U_x/U_\infty = -0.1$ and $U_{xyz}/U_\infty = 1$, respectively. Black dash lines and red solid lines in the right column plot respectively the wall-normal variations of the upwash velocity at $x = 2D$, $z = 0$ and the Q -value variation along the white lines placed at vortex centre in the left row.

At $t^* = 5.5$, the measurement plane of $x = 2D$ intersects with the upstream portion of the ring, and three counter-rotating vortex pairs are detected in Figure 7.14 (h). The top one is the cross-section of the ring, featuring a double-lobe jet body underneath. The middle one appears to be connected with the reverse flow area, and is inferred as a cross-section of the inclined hanging vortex pair. Specifically, this hanging vortex pair is

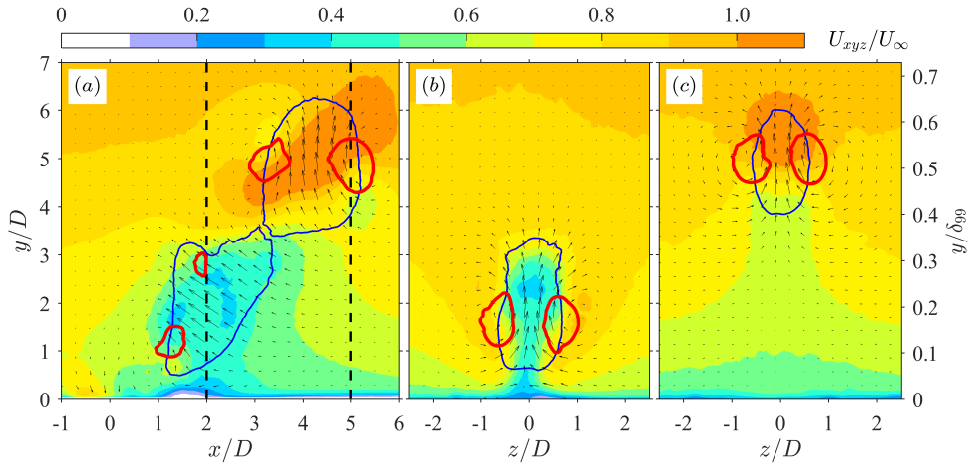


Figure 7.15: Phase-averaged velocity fields at $t^* = 7$. (a) symmetry plane; (b) $x = 2D$; (c) $x = 5D$. Thick red lines indicate vorticities detected with a criterion of 10% of the maximum Q-value. Thin blue lines are contour lines of $U_y/U_\infty = 0.2$. In Figure 7.15 (a), arrows indicate the directions of in-plane periodical fluctuation velocity components, namely $(\tilde{u}_x, \tilde{u}_y)$. As a comparison, arrows in Figure 7.15 (b)-(c) indicate the directions of in-plane phase-averaged velocity components (U_x, U_y) .

generated by the shear between the main flow and the reverse flow. It resides in the leeward side of the jet body and initially orients in wall-normal direction ($t^* = 3$) [125, 128]. While the jet body bends to the crossflow, the hanging vortex pair tilts accordingly (Figure 7.7 (g)) and evolves into a quasi-streamwise counter-rotating vortex pair underneath the FVR. This vortex pair rotates in the same direction as the two longitudinal edges of the ring, and induces a downwash velocity at its two sides ($z/D > 1$ and $z/D < -1$). This downwash effect sweeps the high-momentum flow in the outer boundary layer to the near-wall region and curves locally the streamwise velocity contour lines. Additionally, as this primary counter-rotating vortex pair (*p*-CVP) resides in close proximity to the wall (approx. $y = 2.4D$), a secondary counter rotating vortex pair (*s*-CVP) located at $y = 0.16D$ is induced. This *s*-CVP rotates contrary to the primary CVP and induces a weak downwash velocity in the middle. This flow scenario is consistent with that of conventional synthetic jets in a laminar boundary layer at large velocity and stroke ratio [140, 149].

Phase-averaged velocity fields at $t^* = 7$ in both symmetry and spanwise planes ($x = 2D, 5D$) are shown in Figure 7.15. Note that the vector arrows in Figure 7.15 (a) correspond to the direction of in-plane periodical fluctuation velocity components, $(\tilde{u}_x, \tilde{u}_y)$. Namely, the time-averaged motion has been subtracted, and only the relative change brought by PSJs at this specific phase remains. As a result, two regions with significant lifting motion ($U_y/U_\infty > 0.2$) are perceived. One is located in the middle of the FVR, and the other is induced by the primary counter-rotating vortex pair. These two vortical structures are detected respectively in the measurement plane of $x = 2D$ and $x = 4D$. Based on the mean vector direction in the bottom upwash region in Figure 7.15 (a), the inclination angle of the *p*-CVP at this phase is estimated to be 45 degrees. Additionally, the two upwash regions in the symmetry plane seem to be jointed together, indicating

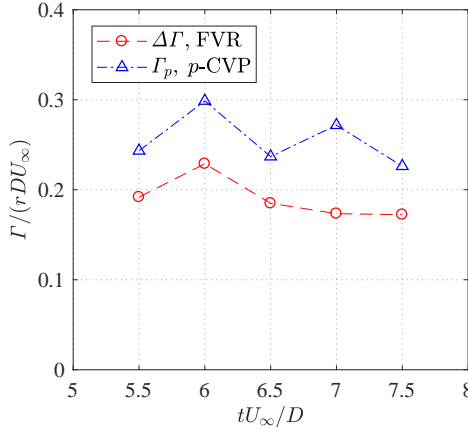


Figure 7.16: Time evolution of the circulation of primary counter-rotating vortex pair (p -CVP) and the circulation difference between upstream and downstream sides of the front vortex ring (FVR).

the possible connection between the two vortical structures (FVR and p -CVP).

Simulation results in [149] demonstrated that, for conventional synthetic jets in laminar incoming boundary layer ($r=1.04$, $L^*=2.7$; under equivalent definition), this primary counter rotating vortex pair is branched from the middle of the FVR, and extends downwards to the wall. As circulation is conserved within a vortex tube [102], the branch of the p -CVP from the FVR will lead to a different circulation between the upstream and downstream sides of the ring. This difference in circulation ($\Delta\Gamma = \Gamma^- - \Gamma^+$, see Figure 7.10 (b)) should be compensated by the circulation of the p -CVP (denoted by Γ_p). To validate this conjecture, the time-evolution of Γ_p and $\Delta\Gamma$ are plotted together in Figure 7.16. As a result, the dimensionless circulation of p -CVP pivots around 0.25 between $t^* = 5.5$ and $t^* = 7.5$, which is in close proximity to the mean value of $\Delta\Gamma/rDU_\infty$ (0.19). This confirms the inter-connection between the FVR and the p -CVP. The residual between these two circulation values can be attributed to the different thresholds of vortex detection as well as the inclined orientation of the p -CVP.

Assembling the stereo-PIV results measured at the same location ($x = 2D$) but increasing time delays, a three-dimensional dataset spreading along t , y and z directions can be constructed. Contour surfaces of streamwise vorticity and downwash velocity in this space are plotted in Figure 7.17 to visualize the pseudo-3D vortical structures (FVR, p -CVP and s -CVP). Different views are provided, and organizations of these vortical structures agree with the earlier analysis. Based on Taylor's frozen turbulence hypothesis [150], these pseudo-3D structures can represent the physical flow topology only if negligible deformation is exhibited during downstream convection. Namely the material derivatives approximate zero, $dU_i/dx \approx 0$. In this study, this prerequisite is violated by the noticeable lifting-motion of the FVR and the bending of the p -CVP between $2 < t^* < 15$, which should be corrected while projecting these pseudo vortical structures back to physical 3D-space (x, y, z). Specifically, the downstream-tilting of FVR is exaggerated in the side view, and should be less than 13° based on Figure 7.10. The spatial orientation of p -CVP is also far from level and should be highly inclined (45° at $t^* = 7$).

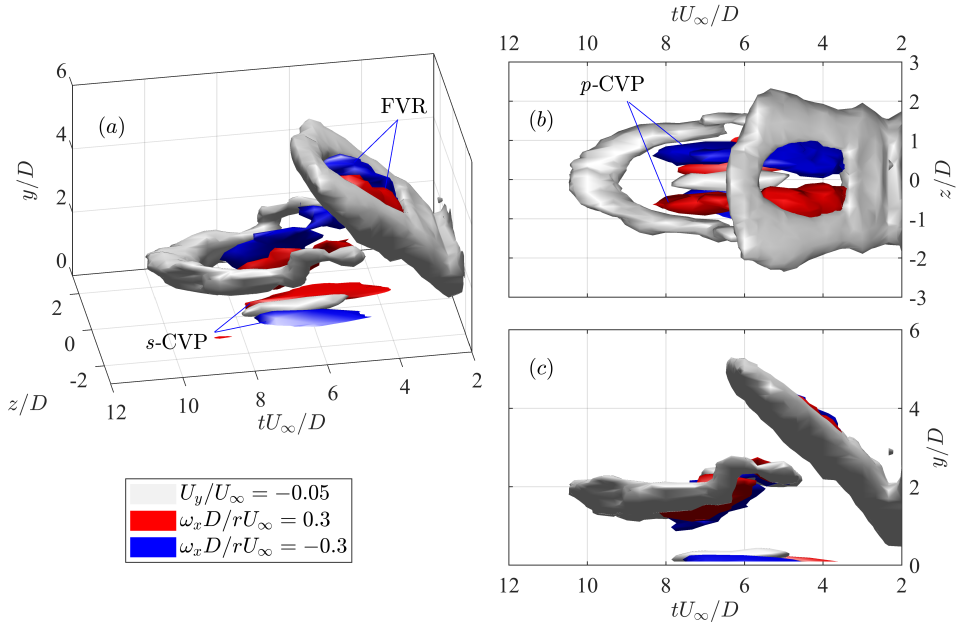


Figure 7.17: Pseudo-3D vortical structures generated by plasma synthetic jets in crossflow at $r = 1.6$. (a) Axonometric view; (b) top view; (c) side view

Notwithstanding these considerations, pseudo-3D visualizations serve as valuable topological interpretations of the pertinent flow behaviour.

It is striking to note that in Figure 7.17 (b), the two downwash streaks induced by the p -CVP are connected at the tail at approximately $tU_\infty/D = 10$. This connection indicates that the two ends of the p -CVP are joined by spanwise vortices, namely shear layer vortices (SVs). SVs are generated in the windward side of the jet body [133] and have already been identified by Q-criterion in Figure 7.14 (a) and (d), as well as in Figure 7.15 (a). These shear layer vortices are inferred to be in an arch shape and seated on the p -CVP (hanging vortex pair), as will be detailed later on in Section 7.6.

The spatial-temporal map of the boundary layer shape factor measured at $x/D = 2$ is shown in Figure 7.18 (a). Contour lines of $H = 1.4$ and $H = 1.37$ are extracted to assist the interpretation. A triangular region with high shape factor ($H > 1.4$) is observed at $t^* < 10$, which corresponds to the significant momentum deficit incurred by the diminishing reverse flow. In the two sides of this triangular region ($5 < t^* < 10$), low shape factor ($H < 1.4$) is manifested, as a result of the downwash effect of the p -CVP. This downwash effect is most significant in the spanwise extent of $1 < |z/D| < 3$ and diminishes completely at $|z/D| > 5$, which agrees with the large eddy simulation (LES) results in [151]. In Figure 7.18 (b) and (c), variations of the boundary layer shape factor at several representative locations/time instants are plotted as curves. During the interval of $t^* \geq 12$, the boundary layer shape factor at $z/D = 0$ rises with increasing time delay, whereas that at $z/D = 2$ drops slightly. These variations can be associated with the weak secondary jet (see Figure 7.7 (i)). Specifically, this secondary jet also induces a weak

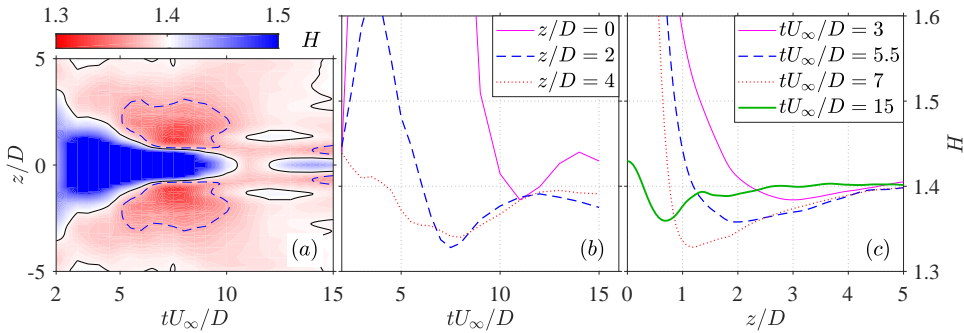


Figure 7.18: (a) Spatial-temporal map of the boundary layer shape factor at $x/D = 2$. The black thin lines and blue dash lines are contour lines of $H = 1.4$ (baseline value) and $H = 1.37$, respectively. (b) Time evolution and (b) spanwise variation of the boundary layer shape factor at selected locations/time instants.

streamwise counter-rotating vortex pair in the near-wall region (not shown). Between and beside the two legs of this CVP, weak upwash and downwash effects are experienced respectively by the boundary layer, resulting in the aforementioned variations of H .

7.5. EFFECT OF VELOCITY RATIO

In this section, the effect of velocity ratio on vortex ring evolution, jet penetration, and boundary layer shape factor is analysed in detail. Case 1 ($r=0.7$) is taken as an example to illustrate the distinct flow topology that occurs at low velocity ratio.

7.5.1. VORTEX RING EVOLUTION

The time evolution of the spanwise vorticity contours in Case 1 ($r=0.7$) is shown in Figure 7.19. At $t^* \leq 2$, incipient jets protrude from the exit orifice, displacing the boundary layer vorticity upwards. In the vicinity of the exit orifice edges, positive and negative vorticity rolls into a vortex ring. This vortex ring breaks the constraints of the boundary layer vorticity at $t^* = 3$ and tilts upstream afterwards. This contrasts with the initial downstream tilting motion exhibited by Case 4 and can be ascribed to the different stroke ratio. Specifically, the stroke ratio in Case 1 (2.0) is smaller than the formation number (3.6) [152], and no trailing vorticity column is formed behind vortex rings as shown in Figure 7.19 (d). Consequently, vortex rings are isolated in the crossflow, and upstream tilting driven by Kutta-Joukowski lift is exhibited.

The spatial evolution of the front vortex ring in crossflow is shown in Figure 7.20 (a). The dimensionless circulations of the two sides of the ring in both quiescent and cross-flow conditions are plotted in Figure 7.20 (b). In contrast to the high-velocity ratio case (Case 4), the vortex ring stays in the vicinity of the jet exit ($x/D < 3$) and undergoes a significant upstream tilting with a peak pitching angle (α) of approximately 40 degrees. The circulation of upstream vortex (Γ^+) is always lower than that of the downstream vortex (Γ^-), and their difference can be interpreted from the boundary layer vorticity. As shown in Figure 7.19 (c), part of the boundary layer vorticity is entrained in the downstream side of the developing ring, leading to an increased positive circulation. Whereas for the upstream side of the ring, part of the vorticity is cancelled out due to the reverse sign,

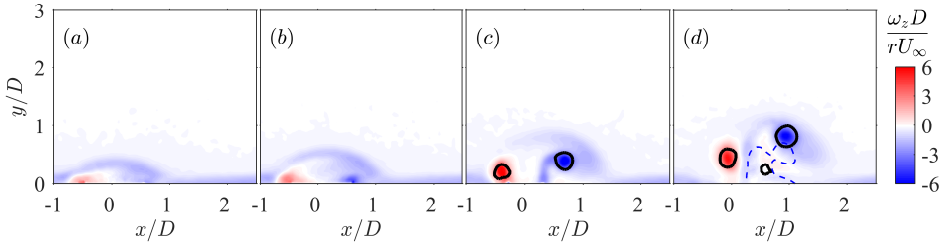


Figure 7.19: Time evolution of vorticity contour at $r=0.7$. (a) $t^* = 1.5$; (b) $t^* = 2.0$; (c) $t^* = 3$; (d) $t^* = 4$; Plotting methods are inherited from Figure 7.9.

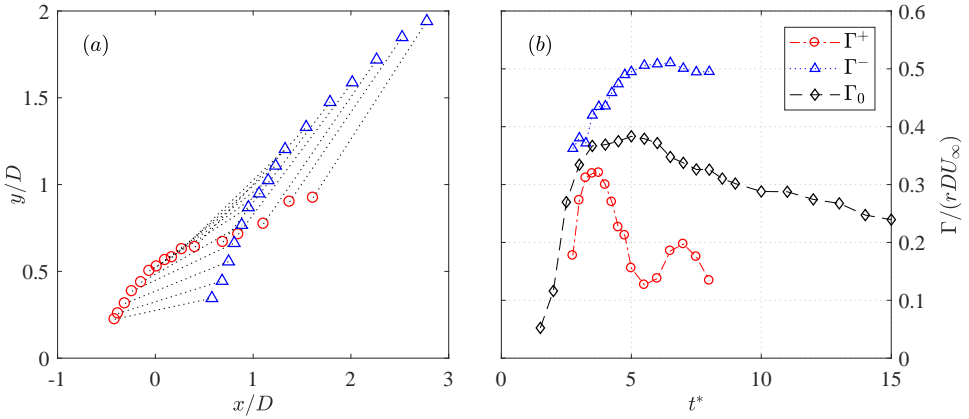


Figure 7.20: (a) Propagation of the front vortex ring in crossflow at $r=0.7$. \circ , windward vortex center (x_v^+, y_v^+); Δ , leeward vortex center (x_v^-, y_v^-). (b) Variation of the dimensionless vortex circulation (Γ) in both quiescent air and crossflow.

resulting in a reduced negative circulation. The mean values of Γ^+ and Γ^- roughly follow the trend of Γ_0 , indicating a comparable dissipation/mixing rate between quiescent and crossflow condition. This contrasts with Case 4, where the dissipation rate of vortex ring circulation is evidently higher in crossflow than that in quiescent condition. The distinct dissipation rate is associated with the different volume entrainment rate of vortex rings. In [137], the difference in volume entrainment rate between crossflow and quiescent conditions is demonstrated to increase with stroke ratio. For low stroke length ($L^* < 2$, Case 1), marginal difference ($< 20\%$) is expected, whereas for high stroke length ($L^* > 4$, Case 4), this difference can reach up to 70%. As a result, Case 1 exhibits a comparable dissipation rate of circulation in crossflow and quiescent conditions.

It must be noted that during later evolution, the upstream vortex is never ceased completely and can always be detected with decreasing threshold Q-value. This observation contrasts with the results in [137, 149], where hairpin vortices are reported. Further comparisons will be provided in Section 7.6.

A collective representation of vortex ring trajectories for all tested cases is shown in Figure 7.21 (a). As a result, the penetration ability of the vortex rings improves with ve-

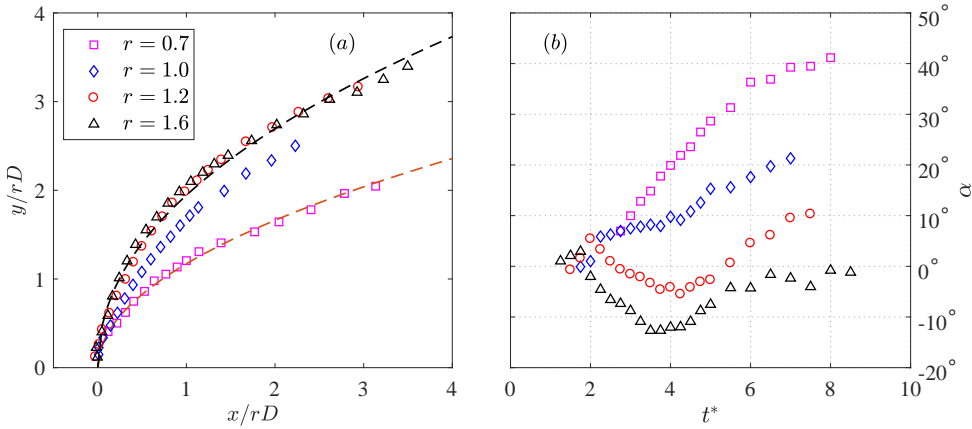


Figure 7.21: (a) Normalized traces of the front vortex ring at different velocity ratios. (b) Time variation of the pitching angle (α) of front vortex ring.

velocity ratio at $r \leq 1.2$ and remains unchanged afterwards. Using Equation 6.3 to fit the vortex ring trace at $r = 0.7$, the two coefficients are estimated to be $A = 1.2$ and $B = 0.50$, which yields a trajectory lower than steady jets in the near-field ($rD < 10$, reference value: $A = 1.9$, $B = 0.31$) [130]. This weak penetration ability in low velocity ratio can be traced back to the orientation of the emitted vortex rings. As shown in Figure 7.21 (b), the pitching angle of vortex rings (α , positive value for upstream tilting) exhibits a similar variation trend at $r = 1.2$ and $r = 1.6$, namely decreasing at $t^* < 4$ and increasing afterwards. This variation trend is ascribed to the presence of the trailing vorticity column behind the vortex rings at large stroke ratio ($L^* > 3.6$) (see Section 7.4.1). As the pitching angle pivots around 0° in these two cases, the induced velocity of the vortex rings always has a large component in wall-normal direction, which favours fast penetration. As a comparison, the pitching angle at $r = 0.7$ and $r = 1.0$ increases monotonically to 20° and 40° , respectively. With increasing pitching angle, the wall-normal component of the induced velocity of the vortex rings decreases, which leads to weak penetration ability. For pulsed jets in laminar cross flow with fixed velocity ratio ($r > 2$), the optimal stroke ratio for maximum jet penetration collapses on a line that lies to the left side (smaller side) of the ‘transition stroke ratio’ [153].

7.5.2. PSEUDO-3D VORTEX STRUCTURE, BOUNDARY LAYER SHAPE FACTOR AND WALL SHEAR STRESS

In Case 1 ($r = 0.7$), the pseudo-3D vortical structures constructed from the stereo-PIV results measured at $x = 2D$ are shown in Figure 7.22. Different from Case 4, only a front vortex ring and a near-wall secondary CVP are perceived. The primary CVP evolved from the hanging vortex pair disappears. This is somehow expected and can be interpreted as follows. At large velocity ratio, reverse flow is formed in the leeward side of the jet due to the virtual blockage created by the erect high-speed jet body (see Figure 7.9). The skewed mixing layer between reverse and main flow evolves into a hanging vortex pair residing in the leeward side of the jet [125, 132]. At low velocity ratio, only the FVR is

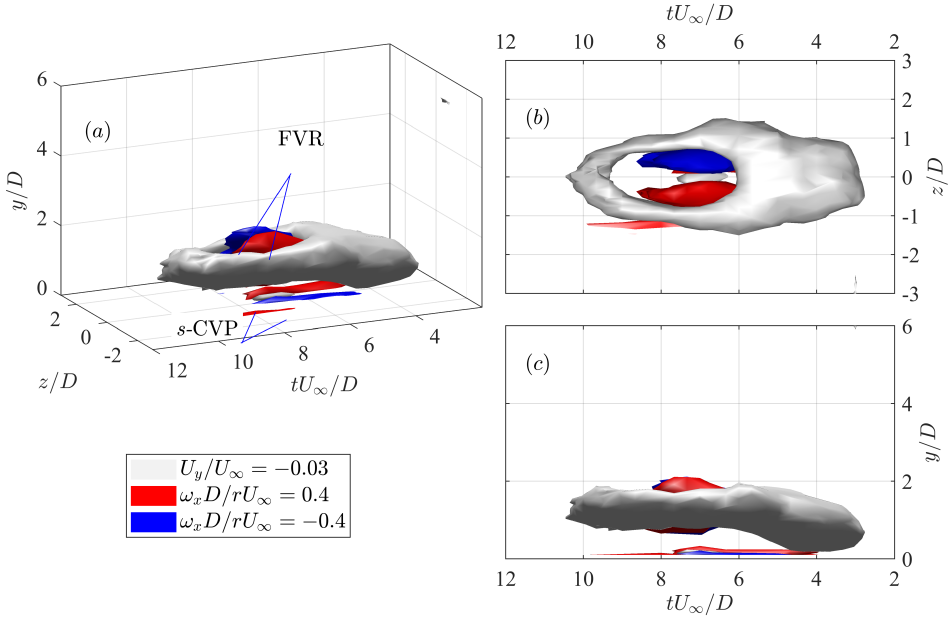


Figure 7.22: Pseudo-3D vortical structures generated by plasma synthetic jets in crossflow at $r = 0.7$. (a) Axonometric view; (b) top view; (c) side view

issued (Figure 7.9), and the small reverse flow located underneath the downstream side of the ring diminishes rapidly after formation ($t^* > 4$). As such, no hanging vortex pair is generated in the case of low velocity ratio. The s -CVP residing in the near-wall region at $r = 0.7$ is directly induced by the two longitudinal edges of the ring. In cases of $r = 1.0$ and $r = 1.2$, the 3D vortex organization is similar to that at $r = 1.6$, thus will not be detailed.

For Cases 1-3, spatial-temporal variations of the boundary layer shape factor measured at $x = 2D$ are shown in Figure 7.23. The contours pertaining to different cases show morphological similarity. A region with high shape factor is observed in between $|x/D| < 1$ and $2 < t^* < 10$, corresponding to the momentum deficit created by the erect jet. Beside this region, there exist two cores of low shape factor, which can be ascribed to the downwash effect of either the FVR (Case 4) or the p -CVP (Cases 1-3). These two cores are centred around $z = \pm 1D$ and $t^* = 7.5$, and expand with velocity ratio. In later phases ($t^* > 12$), a secondary jet manifests with another a narrow band of low shape factor.

At different velocity ratios, streamwise variations of the time-averaged boundary layer shape factor and normalized wall-shear stress in the symmetry plane are shown in Figure 7.24. Similar trends are shared by all the tested cases. Upstream of the exit orifice, lower shape factor is perceived, due to the removal of low-momentum flow at the inner boundary layer by suction. Downstream of the exit orifice, the shape factor rapidly increases, and a gradual recovery of H to baseline value is exhibited after $x/D > 3$. The normalized wall shear stress follows an opposite trend of the boundary layer shape fac-

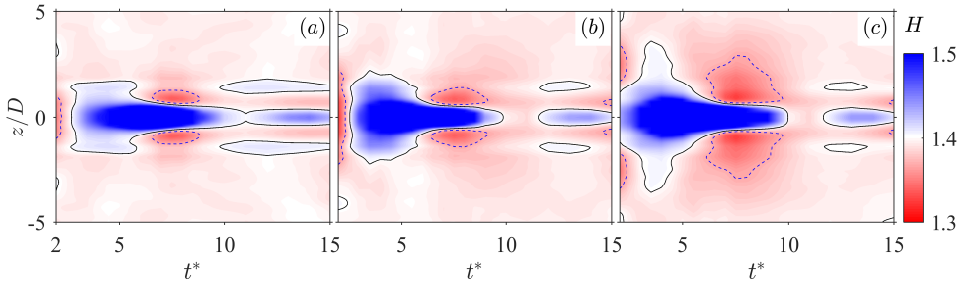


Figure 7.23: Spatial-temporal variations of the boundary layer shape factor measured at $x = 2D$ for increasing velocity ratio. (a) $r=0.7$; (b) $r=1.0$; (c) $r=1.2$. Solid and dash lines correspond to contour lines of $H = 1.4$ and $H = 1.37$, respectively.

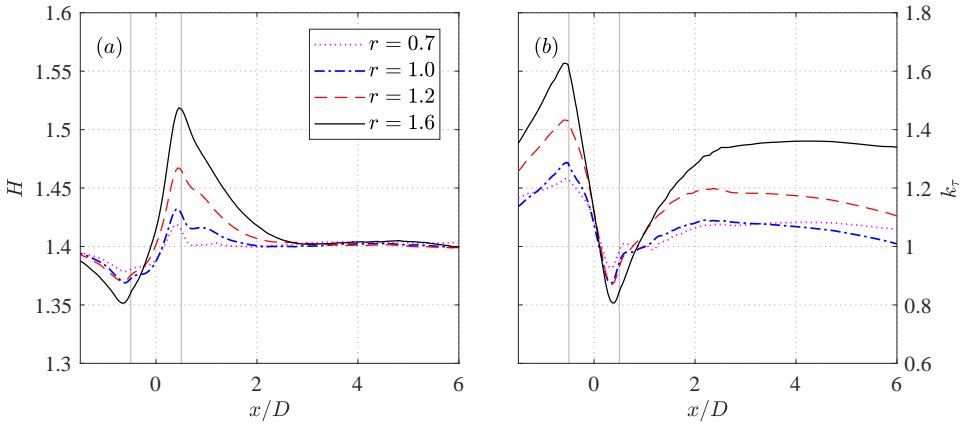


Figure 7.24: Streamwise variations of (a) time-averaged boundary layer shape factor and (b) dimensionless wall shear stress in symmetry plane for increasing velocity ratio. Two grey lines ($x = \pm 0.5D$) are added to indicate the location of exit orifice.

tor as expected. While velocity ratio decreases, peak value of k_τ drops. Nevertheless, a noticeable increase of approximately 10% of k_τ is still perceived downstream of the exit orifice at $r = 0.7$ (Case 1).

7.6. CONCEPTUAL MODEL

A conceptual model of the two regimes of PSJICF (representative cases: Cases 2-4 for regime A and Case 1 for regime B) is shown in Figure 7.25. For each regime, vortical structures in the near- and far-field with respect to the exit orifice are sketched. In regime A ($r > 1$, $L^* > 2.6$), a starting vortex ring is issued and followed by a trailing jet column. Due to the asymmetric momentum addition, this starting vortex ring initially tilts downstream. Shear-layer vortices (SVs) and an erect hanging vortex pair (HVP) are formed in the windward and leeward side of this jet column, respectively. After the jet dimin-

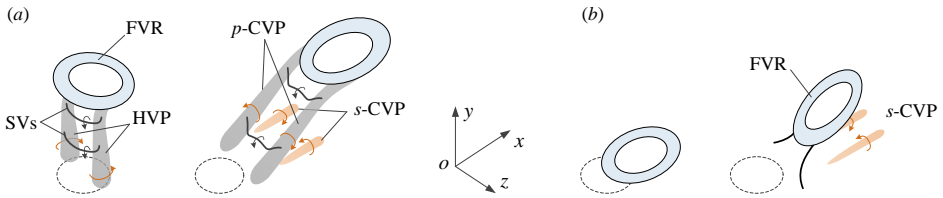


Figure 7.25: Conceptual models of plasma synthetic jets in crossflow. (a) Regime A, high velocity and stroke ratio. (b) Regime B, low velocity and stroke ratio.

ishes, the hanging vortex pair bends to the crossflow and evolves into a quasi-streamwise counter-rotating vortex pair (p -CVP) that branches from the middle of FVR and extends to the near-wall region. The two legs of the p -CVP are bridged by weak shear-layer vortices. Underneath the two legs of the p -CVP, a secondary counter-rotating vortex pair (s -CVP) is induced. Additionally, the downstream tilting of the FVR transforms to upstream tilting after the pinch-off of the trailing vorticity column. The timing of this transformation advances with decreasing velocity ratio. Particularly, the initial downstream tilting in Case 2 is marginal. With regards to regime B, FVR exhibits a consistent upstream tilting since formation. Both trailing jet column and p -CVP are absent. The s -CVP in near-wall region is directly induced by the two longitudinal edges of the ring. The tail of FVR is conjectured to be connected with boundary layer vorticity, as the circulation in upstream side of the ring is significantly lower than the downstream side.

Sau & Mahesh [137] proposed a parameter map that classifies the possible flow regimes of pulsed jets in crossflow. For comparison, the four cases tested here are also indicated in that regime map, as shown in Figure 7.26 (a). A relatively good match is obtained, when the peak jet velocity is taken as reference velocity. The near-exit flow scenarios in Cases 3-4, namely a downstream tilting vortex ring followed by a trailing jet column, are predicated reasonably in Figure 7.26 (a). In [137], the transition stroke ratio is defined as the non-dimensional stroke length where no significant upstream or downstream tilting of vortex rings is exhibited. Namely, the time-mean pitching angle of vortex rings approximate zero. For the PSJs in the present study, this transition stroke ratio occurs between $L^* = 3.7$ and $L^* = 5.4$ ($3.7 < L^* < 5.4$), which is higher than that of pulsed jets (red solid line in Figure 7.26 (a), $L^* = 3.6 - 5.6 \cdot \exp(-0.5r)$) [137]. Additionally, for pulsed jets in crossflow at low velocity ratio ($r < 2$), a train of hairpin vortices is expected, which deviates from the observation of upstream-tilting vortex ring in Case 1. These differences can be attributed to the different Reynolds number. Specifically, both the boundary layer and PSJs are in turbulent state in this experiment, with $Re_\theta = 2540$ and Re_D ranging from 1790 to 4300. For the simulation performed by Sau & Mahesh [137], Re_D is kept at 600, and a laminar boundary layer is prescribed as the inflow. The different boundary layer thickness between turbulent and laminar status affects the extent to which the positive vorticity of FVR is cancelled and finally the formation of vortical structures.

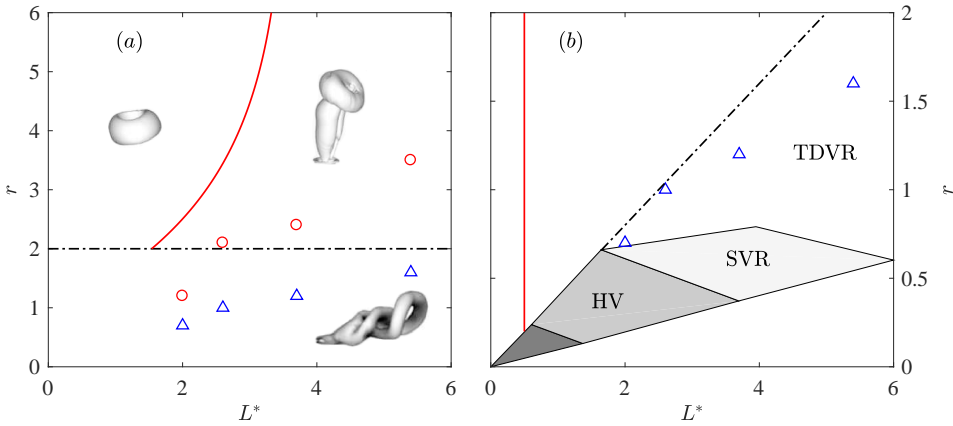


Figure 7.26: Possible flow regimes pertaining to (a) pulsed jets in crossflow [137] and (b) conventional synthetic jets in crossflow [139]. Markers pertain to the present study. Δ , peak velocity ratio (U_p/U_∞) against stroke ratio; \circ , mean velocity ratio (U_0/U_∞) against stroke ratio.

For conventional synthetic jets in crossflow, three flow regimes including hairpin vortices (HV), stretched vortex rings (SVR) and titled & distorted vortex rings (TDVR) are demonstrated at different stroke length and velocity ratios [139], as shown in Figure 7.26 (b). Note that the reference velocity ratio in the original regime map has been doubled to match the definition in this study. As a result, Cases 2-4 fall into the regime of TDVR, while Case 1 is subject to the category of SVR. A conceptual model of TDVR is provided in [140] (Figure 13 in their study), which is similar to the far-field flow scenario of PSJCF sketched in Figure 7.25 (a), except for the absence of shear-layer vortices. The flow scenario of SVR is featured by an upsteam-tilting vortex ring highly elongated in the stream-wise direction [139], which is also consistent with the conceptual model in Figure 7.25 (b), to some extent.

Jabbal & Zhong [140] visualized the wall-shear stress of conventional synthetic jets in laminar crossflow, using liquid crystals. In the regime of TDVR, a single wide steak of high wall-shear stress is observed in the symmetry plane, contrasting with the two narrow streaks perceived in other regimes. The formation of this single high wall-shear-stress streak was ascribed to the downwash effect of *s*-CVP by Jabbal & Zhong [140]. However, based on our observations in Figure 7.14 (c), 7.18 (a) and 7.23, the weak downwash effect of this *s*-CVP prevailed between $4 \leq t^* \leq 8$ is not able to counteract the negative effects brought by reverse flow, largely because the fluids swept to near-wall region is degraded flow with low momentum. In the authors' perspective, the presence of this high wall-shear-stress streak in the symmetry plane is associated with the enhanced suction at high velocity ratio. Specifically, in the regimes of HV and SVR, the velocity ratio is relatively low and the amount of low-energy flow ingested by PSJAs is negligible. The two narrow high wall-shear-stress streaks are a direct consequence of the downwash effect of the two legs of FVR or HV. As velocity ratio increases, this suction effect prevails, and the wall-shear stress upstream and downstream of the exit orifice is increased significantly

(see Figure 7.24), as a result of the removal of low-energy fluids in inner boundary layer. Consequently, the gap between the two narrow streaks observed in regimes of FVR or HV is filled, resulting in a wide streak of high wall-shear stress, as observed in [139, 140].

7.7. CONCLUSIONS

The present study examines the effect of velocity ratio (r) on plasma synthetic jets (PSJs) issuing normally towards a turbulent boundary layer ($\delta_{99}/D = 9.7$, $Re_\theta = 2540$) in a range of $0.7 < r < 1.6$. Different from the sinusoidal exit velocity generated by conventional synthetic jets, the exit velocity of PSJs exhibits noticeable oscillations at Helmholtz natural frequency (1.65 kHz in this study), leading to a multiple alternation between ejection and suction phases in one cycle. Two regimes are identified in the four tested cases, with distinct emitted vortex ring dynamics and flow topology.

Vortex ring dynamics directly determines the jet penetration. At high velocity and stroke ratio ($r = 1.6$, $L^* = 5.4$), vortex rings are ensued by a high-speed trailing jet column and tilt downstream initially. The downstream tilting is attributed to an uneven momentum injection received by the upstream and downstream sides of vortex rings. After the pinch-off of the jet column from the ring, the downstream tilting is transformed into an upstream tilting driven by Kutta-Joukowski lift. As a comparison, in the case of low velocity and stroke ratio ($r = 0.7$, $L^* = 2.0$), vortex rings always tilt to upstream and the pitching angle increases monotonically. A maximum penetration is demonstrated, when the mean pitching angle approximates zero (Cases 3-4). The transition stroke ratio for PSJs (3.7–5.4) is higher than that for pulsed jets.

The near-wall flow topology affects the boundary layer shape factor and wall shear stress. At high velocity and stroke ratio ($r \geq 2.1$, $L^* \geq 2.6$), several shear-layer vortices and a reverse flow region are observed in the windward and leeward side of the jet body, respectively. The reverse flow region accommodates a hanging vortex pair which evolves into a quasi-streamwise counter-rotating vortex pair (p -CVP) after the jet terminates. On the sides of the two legs of this p -CVP, a downwash velocity is induced, which creates a region with low shape factor. Low-momentum flow originating from the reverse flow is trapped in the middle of the p -CVP and FVR, leading to a high boundary layer shape factor in the symmetry plane. At low velocity ratio, no p -CVP is formed. Nevertheless, similar downwash effect is experienced beside the two longitudinal edges of the vortex rings. Consequently, similar spatial distributions of boundary layer shape factor are exhibited. In the symmetry plane, the time-averaged wall shear stress is always higher than baseline value and can be attributed to the removal of low-energy fluids during suction phases. As velocity ratio increases, the time-averaged wall shear stress also increases.

IV

FLOW CONTROL APPLICATIONS

8

AIRFOIL LEADING EDGE SEPARATION CONTROL

8.1. INTRODUCTION

FLOW separation can be found extensively in engineering applications including rotor blades (pitching airfoil), landing gears (cylinder flow), trucks (blunt body flow), inlets of supersonic aircrafts (shock wave/boundary layer interaction, SWBLI) and so on [154]. In most occasions, separation is undesired, as extra drag which lowers the vehicle efficiency and unsteady loads that advance structural fatigue are induced. In an attempt to eliminate airfoil flow separation, both passive (vortex generators, turbulators etc.) and active approaches are developed [155]. Compared to passive approaches, active flow control, utilizing plasma-based actuators are more attractive as no moving components are present and no parasitic drag is created during off-operation condition [4, 156].

The current work deals with the application of PSJA in airfoil flow separation control. Compared to other plasma actuators, PSJAs have the potential to control several types of flow separation by leveraging both momentum and instability mechanisms. Specifically, for turbulent trailing-edge separation, PSJAs can act as vortex generators, creating streamwise vortices to enhance the mixing and suppress the separation [62]. Alternatively in the case of leading-edge separation where hydrodynamic instabilities are present, the thermal/momentum perturbations generated by PSJAs are expected to be analogous to the mechanism employed by nanosecond SDBDAs. In [62], the feasibility of PSJAs in trailing edge separation control was demonstrated experimentally. 20 PSJAs were embedded $0.32c$ (c is the chord length) downstream of the leading edge to eliminate the limited trailing edge separation over a NACA-0015 airfoil. At a freestream velocity of 20 m/s ($Re_c = 6.7 \times 10^5$), a drag reduction of up to 13% was reported by examining the wake velocity profile.

Part of this chapter is submitted as **H. Zong**, T. van Pelt, & M. Kotsonis, *Airfoil Flow Separation Control with Plasma Synthetic Jets at Moderate Reynolds Number*, Experiments in fluids (2018).

In contrast, results on leading-edge control with PSJAs haven't been reported yet. The present work fills this gap and validates the control authority of PSJAs in leading edge separation at moderate Reynolds number ($Re_c = 1.7 \times 10^5$). This Reynolds number is lower from what is typically encountered in commercial aircrafts/ transportation trucks ($O(10^6 - 10^7)$), yet still relevant to small-scale unmanned vehicles and low-speed vertical axis wind-tunnels [157]. 26 PSJAs are embedded in a NACA-0015 airfoil and fed by a novel sequential discharge power supply. The overall change of the lift and drag coefficients are measured by a balance system, while the control mechanisms at various actuation frequencies are exploited with a high-speed Particle Imaging Velocimetry (PIV) system. Details on the experimental setup are introduced in Section 8.2. Force measurement results and PIV results are presented in Section 8.3 and Section 8.4.

8.2. EXPERIMENTAL SETUP

8.2.1. WIND TUNNEL, AIRFOIL MODEL AND ACTUATORS

A NACA-0015 airfoil was 3D-printed in polyamide and used in this study, as shown in Figure 8.1 (*a - b*). The chord length and the span are 250 mm and 400 mm, respectively. Near the leading edge, a rectangular groove extending the whole span (height: 10 mm, depth: 13 mm) is milled to accommodate the actuators. Amitay et al. [158] demonstrated that the optimal actuation position for synthetic jets-based separation control should be just upstream of the separation point. In this study, the separation point at stall angle of attack (15.5°) is located at approximately $0.12c$ downstream of the leading edge. To avoid the high wall shear stress created by synthetic jets in cross flow, damped out during downstream convection, the distance between separation point and jet exit should be limited to 5 – 7 times of the exit orifice diameter (i.e. 3%-5% chord length) [103, 151]. As such, the chordwise distance between the actuator exit orifice centre and the leading edge is designed to be 20 mm ($0.08c$). A spacious chamber (width: 58 mm, height: 16 mm) is created inside the airfoil model to accommodate the capacitors and resistors necessary for the realisation of multi-channel arc discharge (see Section 8.2.2). As a result, only two thin soft wires are connected to power the actuators, largely mitigating the interference of stiff cable connections on force balance measurements.

This model is tested in the W-tunnel of Delft University of Technology. A wooden contraction segment with a square $400 \times 400 \text{ mm}^2$ exit is used in this study, and the freestream turbulence level is typically less than 0.5% at the maximum achievable velocity of 35 m/s. As shown in Figure 8.1 (*a*), the contraction part is further followed by a rectangular plexiglass test section (length: 600 mm) which enables optical measurements. The airfoil model is mounted between the two side walls of the plexiglass test section, and the pivot point is located at $0.25c$ away from the leading edge.

Multiple plasma synthetic jet actuators are arranged in one row to cover the entire span of the airfoil. As shown in Figure 8.1 (*b*), the actuator array is mainly constructed out of a ceramic bar (material: MACOR, cross section: $10 \text{ mm} \times 10 \text{ mm}$) where multiple cylindrical cavities are machined, and a ceramic cap (thickness: 3 mm) with uniformly distributed orifices in the spanwise direction (z -direction). The inner diameter and height of the cylindrical cavities are 6 mm and 8 mm respectively, resulting in a cavity volume of 226 mm^3 . For each cavity, two electrodes are inserted from opposite

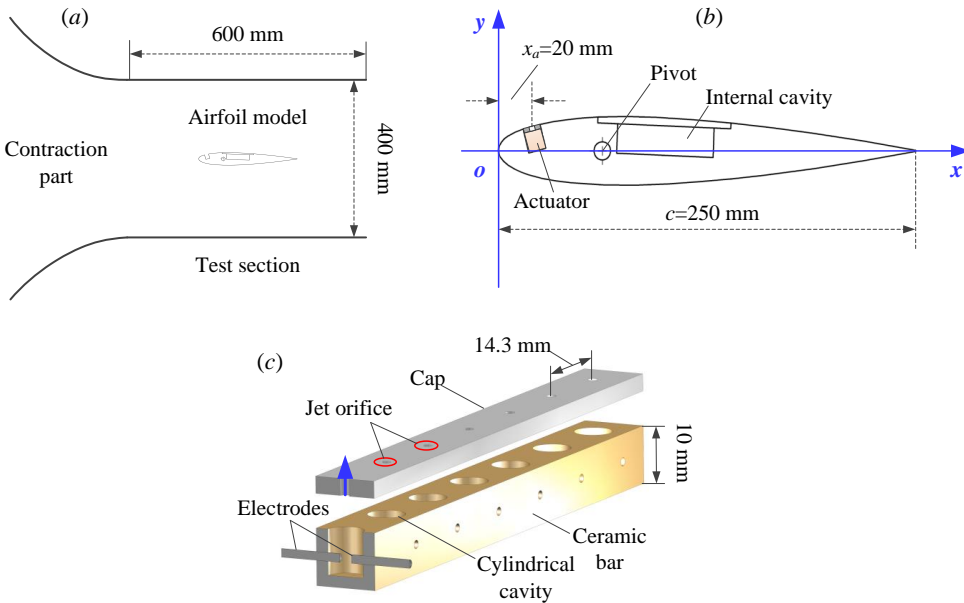


Figure 8.1: Sketches of (a) model placement in test section (to scale), (b) airfoil model and (c) actuator array.

directions, acting as anode and cathode respectively. The inter-electrode gaps are set uniformly as 2 mm for all the actuators except for the first two for trigger purposes as will be explained later on. The axes of the cavities and the circular orifices in the cap are aligned to create pulsed jets that are normal to the local airfoil surface (i.e. ‘vertical’ jets), as Postl et al. [159] have shown that the pulsed ‘vertical’ injection outperforms the pulsed angled injection in separation control. Limited by the trigger discharge stability of the used power supply as well as necessary high-voltage insulation between connection cables, 26 actuators with a spanwise spacing of 14.3 mm are accommodated in the specially arranged groove in the airfoil model. In [103], the spanwise affected extent of PSJs is demonstrated to be approximately 10 times the orifice diameter. Based on this consideration, the jet orifice diameter in this study is designed as 1.5 mm (one tenth of the spanwise spacing) in order to enable sufficient spanwise influence of adjacent PSJs.

8.2.2. DISCHARGE SCHEME AND POWER SUPPLY SYSTEM

The discharge circuits proposed by [52] and [160] are combined to power the actuator array in this study. Figure 8.2 shows the power supply system. A high-voltage amplifier (Trek model, 20-20HS), a current-limiting resistor R_0 (resistance: 500 k Ω , power: 200 W) and an energy-storing capacitor C_0 (capacitance: 4 nF, withstanding voltage >20 kV) constitute the charge circuit. All the gaps are connected in series with the energy-storing capacitor. One virtual relay is added between every two actuators and the ground to enable the sequential breakdown of these gaps [52]. The virtual relay, namely a parallel connection of a small capacitor (capacitance: 0.1 nF) and a large resistor (resistance: 2 M Ω , power: 6 W), is designed to match the dynamic impedance of the pulsed arcs.

Depending on whether all the gaps have been ignited, the working process of this power supply system can be split into two phases, pre-trigger discharge phase and capacitive discharge phase.

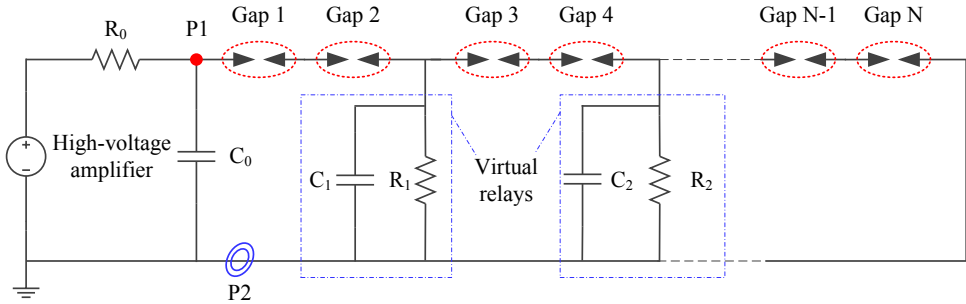


Figure 8.2: Power supply system. The actuators are modeled as the gaps. P1 and P2 indicate the measurement stations of the discharge voltage and the current respectively.

In the pre-trigger discharge phase, high-voltage pulses (voltage: 20 kV, pulse width: 3 ms) are delivered by the amplifier to the charge capacitor C_0 . As all the capacitors (C_1, C_2, \dots) are vacant (zero initial voltage) prior to discharge ignition, the virtual relays can be treated as short-circuits at this stage. Thus, the increasing voltage across C_0 is carried solely by Gap 1 and Gap 2. For two gaps with 2 mm spacing, the breakdown voltage (denoted as U_b) is approximately 9 kV [160]. After the ignition of Gap 1 and Gap 2, the capacitor in the first virtual relay (C_1) is charged by C_0 in less than $1 \mu\text{s}$, and the high-voltage across C_1 is further transferred to Gap 3 and Gap 4. Consequently, Gap 3 and Gap 4 are ignited. This sequence repeats until the complete junction of all the gaps. Note that there is no virtual relay between the last actuator and the ground. During this pre-trigger process, the arc is relatively weak in intensity (energy level: $C_1 U_b^2/2$) and mainly sustained by the leakage current running through the resistors (R_1, R_2, \dots). After the complete junction of the gaps, the energy stored in all the capacitors is released simultaneously through the multi-arc channel, creating an intense capacitive discharge (energy level: $C_0 U_b^2/2$) that is responsible for heating and pressurising the cavity gas. The working frequency of this actuator array can be tuned directly by the discharge frequency. Limited by the output power of the high-voltage amplifier, the maximum reliable discharge frequency is approximately 100 Hz.

The discharge current (i_d) and the discharge voltage (u_d) are measured by a high-voltage probe (Tektronix, P6015a) and a current monitor (Pearson, Model 325) respectively, at the stations indicated in Figure 8.2. The measured signals are recorded by a digital oscilloscope (Tektronix, TDS3054C) at a sampling rate of 1 GHz. Representative voltage and current waveforms are shown in Figure 8.3. Note that the first two electrode gaps are enlarged to 3 mm in order to create an overshoot breakdown voltage (14 kV) for the subsequent gaps (spacing: 2 mm) so that the energy dissipated in the pre-trigger discharge phase can be compensated [161]. The pre-trigger discharge sustains approximately $0.8 \mu\text{s}$ and is characterised by a staggered declination of the discharge voltage and a relatively low discharge current ($O(10 \text{ A})$). In the capacitive discharge phase, both the

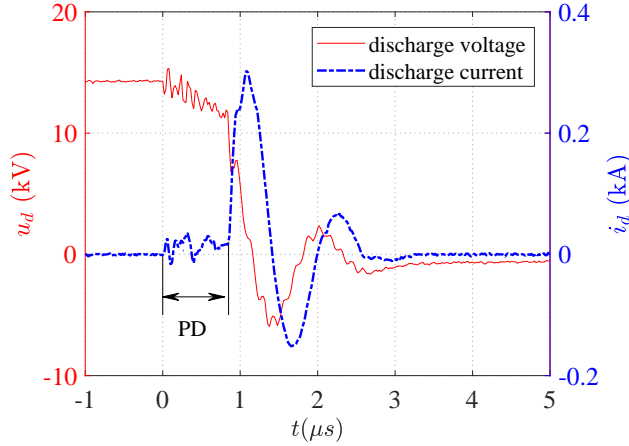


Figure 8.3: Representative voltage and current waveforms. PD indicates the pre-trigger discharge.

discharge voltage and the discharge current oscillate periodically with damping amplitudes. This is largely expected, as the capacitors, arc channels and the parasitic wire inductance constitute a typical RLC oscillation circuit [43]. The peak current at this phase reaches about 300 A and the duration is approximately $2 \mu\text{s}$. The total discharge energy integrated from the voltage and the current waveforms is approximately 0.42 J, and a vast majority is deposited in the capacitive discharge phase.

8.2.3. BASELINE ACTUATOR CHARACTERISTICS

Extensive characterization studies of plasma synthetic jets operating in quiescent air have been performed by [40, 85], using phase-locked PIV measurements. As a result, the peak jet velocity (U_p) and mean jet momentum (M_e) are mainly determined by the non-dimensional energy deposition (ϵ , defined as the ratio of arc discharge energy to the initial internal energy of the cavity gas) [39], and the gas heating efficiency (η_h) which can be influenced significantly by the electrode configuration and atmospheric parameters [57, 162]. Based on the measured discharge energy (E_d) and the geometrical parameters of actuator cavity in this study (cavity volume, electrode distance etc.), ϵ and η_h are estimated to be 0.28 and 10%, respectively. Using these parameters as the input, the peak jet velocity can be estimated with the analytical relations 8.1 [16, 42, 54],

$$\left\{ \begin{array}{l} T_{ca}/T_0 = 1 + \eta_h \epsilon \\ P_{ca} = \rho_0 R T_{ca} \\ P_{ca}/P_0 = \left(1 + \frac{\gamma-1}{2} M a_p^2\right)^{\gamma/(\gamma-1)} \\ T_{jet}/T_{ca} = (P_0/P_{ca})^{(\gamma-1)/\gamma} \\ U_p = M_p \cdot \sqrt{\gamma R T_{jet}} \end{array} \right. \quad (8.1)$$

where R and γ are the gas constant and the specific heat ratio of air, respectively; P_0 and ρ_0 denote the ambient temperature and density; T_{ca} and P_{ca} represent the peak temperature and pressure of the actuator cavity reached after energy deposition; Ma_p and U_p are the peak exit Mach number and the peak exit velocity in jet stage.

These relations are derived under the assumptions that energy deposition stage and jet stage can be treated respectively as a constant volume heating process and an isentropic expansion process [16]. As a result, U_p is computed to be 68 m/s ($M_p = 0.2$), resulting in a peak jet-to-crossflow ratio of 6.8. Additionally, Zong et al. [39, 144] have demonstrated that the duration of primary jet stage (T_{jet} , jet duration time) is close to the natural Helmholtz oscillation period of the actuator cavity, which is computed to be $362 \mu\text{s}$ based on the throat length, cavity volume and exit orifice diameter [39, 46].

In [54], the non-dimensional impulse pertaining to single jet pulse (I_p^*) is derived as a function of the dimensionless energy deposition (Equation (36) in their study). With this relation, the jet-to-crossflow momentum ratio (C_μ , i.e. blowing momentum coefficient) can be estimated as follows [5],

$$C_\mu = \frac{f_d \cdot I_p^* \sqrt{\rho_0 V_{ca} E_d \eta_h}}{\rho_0 U_\infty^2 \cdot c s_a} \quad (8.2)$$

where s_a is the actuator spacing in spanwise direction (14.3 mm, see Figure 8.1). As evidenced, the blowing momentum coefficient increases linearly with the discharge frequency. For the peak value of $f_d = 80$ Hz used in this investigation, C_μ is computed to be 4.5×10^{-5} , which falls into the typical range of oscillatory jets and conventional synthetic jets, i.e. $O(0.001-0.1 \%)$ [5, 158].

8.2.4. MEASUREMENT SCHEME

A six-component load-cell balance system developed by NLR (National Aerospace Laboratory, the Netherlands) is used to measure the overall aerodynamic forces and moments imposed on the airfoil model. At each angle of attack, the balance signals are acquired for 3 seconds at a sampling rate of 2 kHz. Low-pass filtering and ensemble averaging are applied on the recorded signals later on to reduce the measurement uncertainty. The errors for lift and drag measurement are estimated to be less than 5 mN (0.1% of peak lift) and 10 mN (0.3% of peak drag) respectively. Wind tunnel blockage corrections are applied on the computed lift and drag coefficient using the methods proposed in [163].

The mid-span velocity field above the suction side of the airfoil is measured by a high-speed planar PIV system which consists of a high-speed camera (Photron Fastcam SA-1, resolution: 1024×1024 pixels), a high-speed laser (Quantronix, Darwin Duo 527-80-M) and a programmable timing unit (LaVison, high-speed PTU). The laser beams emitted from the laser head are shaped into a laser sheet (thickness: 1 mm) by a combination of two spherical lenses and one cylindrical lens. This laser sheet passing through the mid-span plane is kept strictly normal to the airfoil surface. Liquid particles are produced by a SAFEX fog generator in the settling chamber of the wind tunnel using water-glycol mixture as the working fluid. The mean particle diameter is approximately $1 \mu\text{m}$, and the particle image size is kept to approximately 2 pixels. The camera is mounted with an objective of 105 mm (Nikon, Micro Nikkor) to image a field of view (FOV) of $270 \text{ mm} \times 270 \text{ mm}$, leading to a magnification ratio of 0.075. LaVision Davis 8.3.1 is used for

recording and processing the raw particle images pairs. The interrogation window size and the overlapping ratio in the final pass are set as 32×32 pixels² and 75% respectively, resulting in a final spatial resolution of 2.1 mm/vector.

In this study, the nominal free stream velocity (U_∞) is kept constant at 10 m/s, corresponding to a chord-based Reynolds number (Re_c) of 1.7×10^5 (ambient temperature: 293 K, ambient pressure: 1.01 bar). The dimensionless actuation frequency (namely Strouhal number) is defined as $F^* = f_d c / U_\infty$, where f_d denotes the discharge frequency. Similarly, time is normalised by c / U_∞ , resulting in a dimensionless convection time, $T^* = t U_\infty / c$. A wide range of $0.1 \leq F^* \leq 2$ is tested with plasma actuation. PIV measurements are performed at several representative angles of attack where flow separation is expected. For each of the tested cases, a long sequence containing 2400 image pairs is acquired at a sampling rate of 800 Hz, which is 40 times higher than the vortex shedding frequency reported in [164] (reference value: $0.5 U_\infty / c$) and sufficient to get relevant frequency spectrums. Both balance and PIV measurements are synchronised with the discharge ignition to facilitate the computation of phase-averaged results.

Peak detection error and finite ensemble size are identified as the two main sources of velocity measurement uncertainty in this study. The maximum particle displacement is kept as 10 pixels. Considering a typical peak detection error of 0.2 pixels in cross-correlation maps, a relative uncertainty of 2% is expected on the instantaneous velocity field. For ensemble-averaged velocity fields, the uncertainty caused by finite sample size can be computed from the the root mean square of velocity fluctuations [86]. As a result, the total uncertainty in time-averaged and phase-averaged velocity fields is estimated to be less than 1% and 5% of U_∞ , respectively.

8.3. BALANCE MEASUREMENT RESULTS

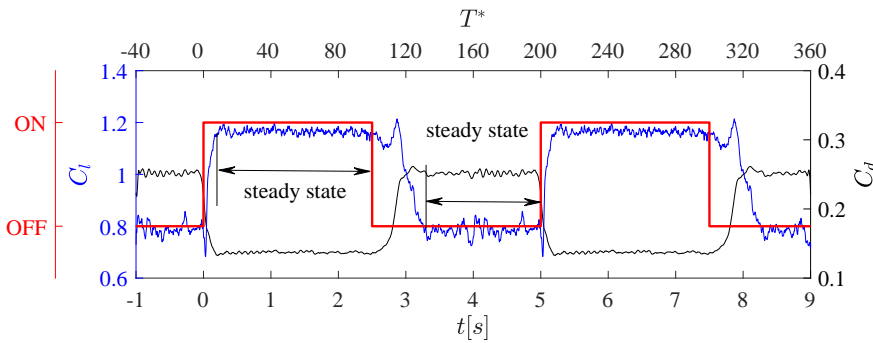


Figure 8.4: Phase-averaged variations of the lift and drag coefficients (C_l , C_d) at $\alpha = 15.5^\circ$ during a square wave test. 'ON' and 'OFF' indicate the status of the plasma actuation. The dimensionless discharge frequency at 'ON' status is $F^* = 1$.

Square-wave tests are first preformed to determine the timescales needed by the flow to respond to plasma actuation. During these tests, PSJAs are switched on and off alternately (cycle period: 5 seconds, duty cycle: 50%), and the instantaneous lift and

drag traces obtained from multiple repetitive measurements are phase-averaged. Figure 8.4 shows the phase-averaged traces of the lift and drag coefficients (denoted as C_l and C_d) measured at $F^* = 1$ and $\alpha = 15.5^\circ$ (stall angle). After plasma actuation is switched on, it takes approximately 2-3 dimensionless time units for the forces to reach a steady state. Comparing the steady-state values to the baseline ones, a considerable augmentation/reduction in lift/drag is observed. Once the actuation is seized, these forces start to resume, experiencing a considerably longer transient process (30 time units). During this process, the high-lift low-drag status is sustained for roughly 15 dimensionless time units before a mild recovery to the original status begins. The distinct timescales for separation and reattachment to occur were carefully interpreted by Benard & Moreau [165]. For the forced attachment case, the spanwise vortices created by plasma actuation propagate rapidly downstream at a velocity of $0.43U_\infty$, leading to a rapid transition of the separation point from leading edge to trailing edge. As a comparison, during the natural separation process, the growth of localised trailing-edge separation to massive leading-edge separation is much slower, ostensibly due to the low backflow velocity (typically less than $0.2U_\infty$). This hysteresis effect is further utilised by Benard & Moreau [165] to create a real-time feedback control system which operates DBD actuators in low duty cycle to minimise the power consumption.

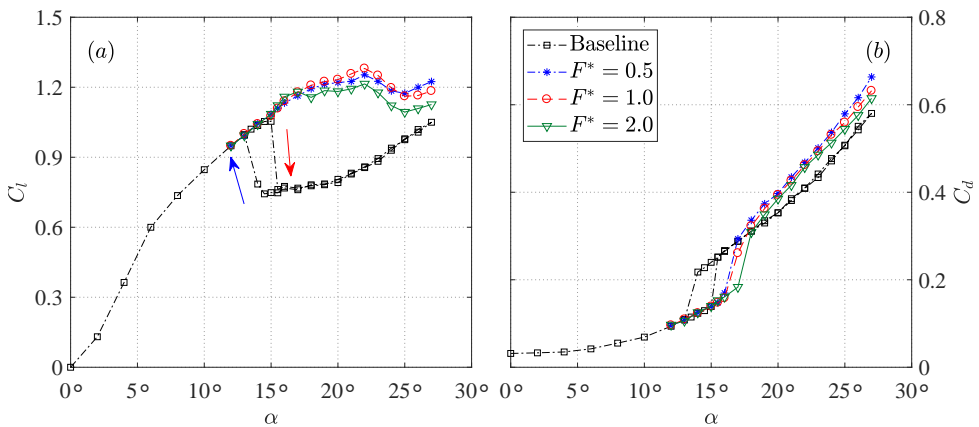


Figure 8.5: (a) lift and (b) drag coefficients for both baseline and actuated cases. The hysteresis loop is indicated by a red arrow for increasing α and a blue arrow for decreasing α .

The lift and drag coefficients at increasing angles of attack for both baseline and actuated cases are shown in Figure 8.5. Without PSJ actuation, the airfoil stalls at $\alpha = 15.5^\circ$, signified by an abrupt change of the lift and drag coefficients. A hysteresis loop is exhibited between $\alpha = 13^\circ$ and $\alpha = 15^\circ$, which is expected for this type of airfoil at a chord-based Reynolds number of $O(10^5)$ [157]. When PSJ actuation is applied, the stall angle is postponed to approximately 22° , and the hysteresis loop observed in the baseline case is completely eliminated, which is consistent with the observations of [166] where the same airfoil (NACA-0015) is tested with SDBDAs at $Re_c = 1.6 \times 10^5$. These results indi-

cate that PSJAs can be potentially applied to increase the blade loads of vertical-axis wind turbines [157], or to mitigate the unsteady force of pitching airfoils, where the structure fatigue is tightly associated with the hysteresis loops [167]. It should be noticed that the boundary layer status at the separation point is left undetermined in this investigation, thus the above-mentioned flow phenomenon could be altered when the chord-based Reynolds number changes. In terms of peak lift augmentation ($\alpha = 22^\circ$), $F^* = 1$ outperforms the other two cases and the peak lift coefficient is increased by 21%. For the drag coefficient shown in Figure 8.5 (b), each curve consists of two segments. The first segment ($\alpha < 13^\circ$) roughly follows a quadric relation corresponding to the induced and parasitic drags of attached flow, while the second segment ($\alpha > 13^\circ$) is resulting from the high pressure drag under stall conditions. In the range of $0.5 \leq F^* \leq 2.0$, higher actuation frequency can prolong the first segment of the drag curves to higher angle of attack (16.5° at $F^* = 2.0$), while slightly increasing the drag in the second segment.

A metric quantifying the effectiveness of actuators (power saving ratio, η_p) can be defined as shown in Equation 8.3. ΔD represents the variation in drag force. η_p is essentially the ratio of the power saved from drag reduction to the power needed to feed the actuators. At $\alpha = 15.5^\circ$ and $F^* = 0.5$, the power saving ratio is estimated to be 0.74, thus further efforts should be made to elevate the efficiency of PSJA array for industrial applications. In [59], the denominator of Equation 8.3 is replaced by the fluidic power generated by plasma, and the power saving ratio of SDBDAs in cylinder flow control is estimated to be 1500. This ostensibly astonishing distinction (almost 2000 times) can be well explained by the electro-mechanical efficiency of plasma actuators, which is defined as the ratio of the fluidic power outputted to the electrical power ingested. [168] has reported that the electro-mechanical efficiency of SDBDAs is $O(0.1\%)$. Taking this into account, the power saving ratios of PSJAs and DBDAs fall in the same order, $\eta_p \sim O(1)$.

$$\eta_p = \frac{\Delta D \cdot U_\infty}{f_d \cdot \int_0^{T_d} U_d(t) I_d(t) \cdot dt} \quad (8.3)$$

8.4. PIV RESULTS AND ANALYSIS

This part is organised as follows. An overview of the baseline flow scenarios is provided in Section 8.4.1, according to which two cases ($\alpha = 15.5^\circ$, and 22°) are picked out to perform detailed PIV measurements. Subsequently, the control effects as well as the control mechanisms in these two cases are presented in Section 8.4.2 and Section 8.4.3.

8.4.1. TIME-AVERAGED VELOCITY FIELDS FOR BASELINE CASE

The time-averaged velocity fields at increasing angle of attack are shown in Figure 8.6 for the baseline case (i.e. no actuation). At $\alpha = 13^\circ$, a small region of separated flow is observed near the trailing edge, as bounded by the dividing stream line. It must be noted here that the dividing streamline is defined as the flow streamline originating at the separation point, and not to be confused with the zero-velocity line. The near-wall flow in this separation region is directed upstream by the adverse pressure gradient, producing a prominent backflow region underneath the zero-velocity line ($U_x = 0$ m/s). This zero-velocity line, serving as the interface between forward and backward flow, defines

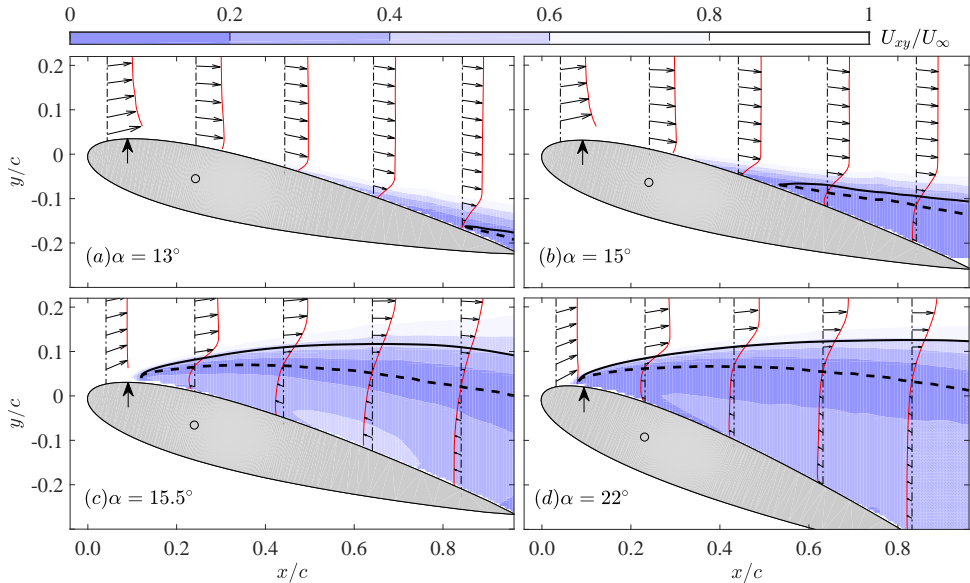


Figure 8.6: Time-averaged velocity fields without plasma actuation (baseline case); The Euclidean sums of the in-plane velocity (denoted as U_{xy}) are shown as contours. The velocity profiles at selected chordwise locations are indicated by thin black arrows and red lines. The black solid lines are dividing streamlines, while the dashed black lines are contour lines of $U_x = 0$ m/s (termed as zero-velocity lines hereinafter). The jet orifice location is pinpointed by a thick black arrow.

the time-averaged location of the separated shear layer. With increasing angle of attack from $\alpha = 13^\circ$ to $\alpha = 15^\circ$, the separation region extends upstream. The airfoil stalls at 15.5° , indicated by a jump of the separation point from mid-chord to the vicinity of the leading edge. This causes a sudden drop of the lift and a considerable increase of the drag as shown in Figure 8.5. Based on the observed changes and regimes in separation location and separation type [163], two angles of attack ($\alpha = 15.5^\circ$ and 22°) are selected to execute detailed PIV measurements, where the separation point lies respectively $4\%c$ downstream and $1\%c$ upstream of the jet orifices. These two angles represent the stall angles at baseline and actuation conditions. In both cases, a wide range of $0.1 \leq F^* \leq 2$ is tested to elucidate the pertinent frequency effects.

8.4.2. LEADING EDGE SEPARATION CONTROL AT $\alpha = 15.5^\circ$

The first examined case pertains to the stall angle (15.5°). Figure 8.7 shows the time-averaged velocity fields at $\alpha = 15.5^\circ$ with PSJ actuation. In the range of $0.25 \leq F^* \leq 2.0$, all the cases exhibit noticeable reduction of the backflow area (A_b , defined as the area enclosed by the dividing streamline, airfoil model and a vertical line passing through the trailing edge). At $F^* = 0.25$, the separation point remains near the leading edge, whereas the dividing streamline bends towards the suction surface compared to the baseline in Figure 8.6 (c), reducing the separation region into a narrow band. For cases of $F^* \geq 0.5$ (Figure 8.7 (b)-(d)), a much fuller velocity profile is observed near the leading edge, and

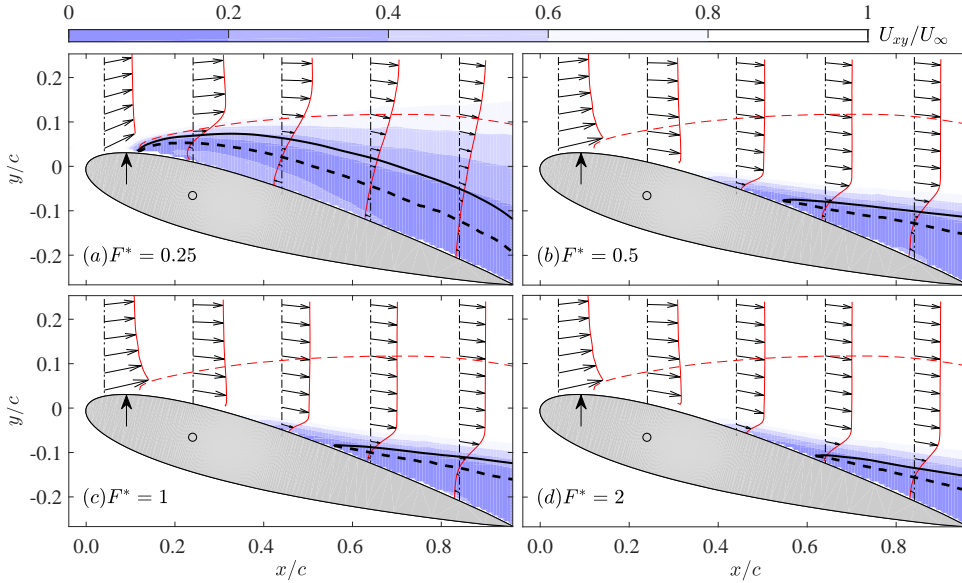


Figure 8.7: Time-averaged velocity fields at $\alpha = 15.5^\circ$ with PSJ actuation. The plotting methods are identical to the ones used in Figure 8.6. The thin red dashed line indicates the zero-velocity line corresponding to the baseline condition.

the flow remains attached during the first half chord. Large-scale leading edge separation is converted into localised trailing edge separation, similar to the base flow scenario exhibited at $\alpha = 15^\circ$. To quantify the frequency effect, the dimensionless backflow area (A_b^*) and separation length (L_{sep}^*) are defined,

$$\begin{cases} A_b^* = \frac{A_b}{0.5c^2 \cdot \sin(\alpha)\cos(\alpha)} \\ L_{sep}^* = 1 - \frac{x_s}{c \cdot \cos(\alpha)} \end{cases} \quad (8.4)$$

where x_s denotes the x -coordinate of the separation point; the triangular area formed by chord and its projections in two axes, namely $0.5c^2 \cdot \sin(\alpha)\cos(\alpha)$, is used to normalize the backflow area A_b .

Variation of the dimensionless backflow area, separation length and lift coefficient with actuation frequency at $\alpha = 15.5^\circ$ is shown in Figure 8.8 (a). Under baseline condition, A_b^* is close to 1. With increasing frequency, the dimensionless backflow area decreases monotonically and reaches approximately 0.14 at $F^* = 2$. Note that a kink point exists at $F^* = 0.5$ after which the decrease of A_b is marginal. The separation length remains approximately unchanged ($0.88c$) before this kink point, drops sharply between $F^* = 0.25$ and $F^* = 0.5$, and changes mildly afterwards. Additionally, the lift coefficient increases with decreasing backflow area as expected. These observations lead to a reduced-frequency range of $F^* \geq 0.5$ for favourable leading-edge separation control, which agrees with the review in [5].

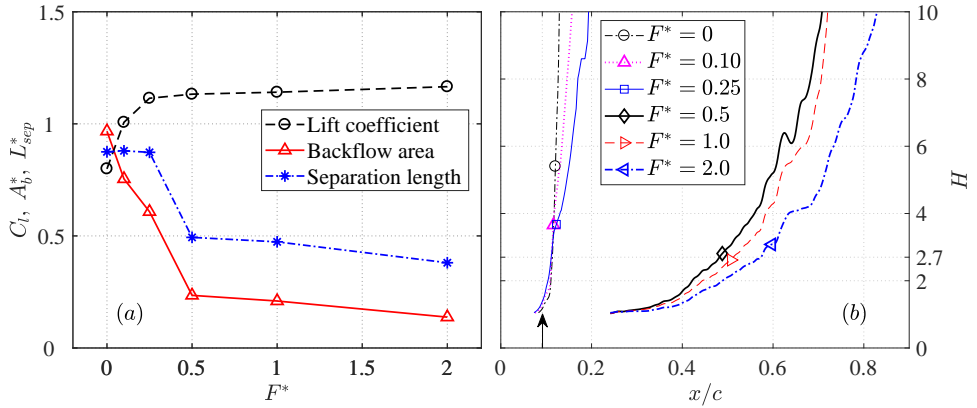


Figure 8.8: (a) Variation of dimensionless backflow area, separation length and lift coefficient with actuation frequency at $\alpha = 15.5^\circ$; (b) Chordwise variation of the boundary layer shape factor (H) for increasing actuation frequency; The actuation position is indicated by a black arrow. The separation points determined by zero-velocity line are superimposed as markers.

Flow separation is closely related to the velocity profiles in the boundary layer. A widely-used metric to quantify the fullness of velocity profiles is the shape factor, which is defined as the ratio of momentum thickness to displacement thickness ($H = \delta^*/\theta$) as shown in Equation 8.5 [122]. U_t denotes the wall-parallel velocity component in the boundary layer. These integrals are computed along the wall-normal direction, starting from the suction surface (y_w) and ending at the position where the peak value of wall-parallel velocity ($U_{t,max}$) is attained (y_{ref}).

$$\begin{cases} \delta^* = \int_{y_w}^{y_{ref}} \left(1 - \frac{U_t}{U_{t,max}}\right) dy \\ \theta = \int_{y_w}^{y_{ref}} \frac{U_t}{U_{t,max}} \left(1 - \frac{U_t}{U_{t,max}}\right) dy \end{cases} \quad (8.5)$$

Chordwise variations of boundary layer shape factor for increasing frequency are shown in Figure 8.8 (b). Note that boundary layer transition near the leading edge is not determined from the current PIV measurements due to a large vector pitch (2.1 mm). For all cases, the shape factor grows monotonically in the chordwise direction. Under low-frequency actuation of $F^* \leq 0.25$, the growth rate of H is slightly postponed by plasma actuation, whereas at high-frequency actuation of $F^* \leq 0.5$, the boundary layer shape factors are suppressed below 2 until $x = 0.2c$. In [154], a criterion of $H = 2.7$ is suggested for turbulent flow detachment. The separation point determined by this criterion (not shown) is consistent with that obtained from the zero-velocity line in Figure 8.8 (a). According to the boundary layer equations [122], evolution of the boundary layer velocity profile is affected by both the Reynolds stresses and the streamwise pressure gradient. The low boundary layer shape factor in the actuated cases suggests a fuller velocity profile and thus higher mixing rate in boundary layers, which can be attributed to the earlier transition or the counter-rotating vortex pairs generated by PSJs in cross flow [103]. Fur-

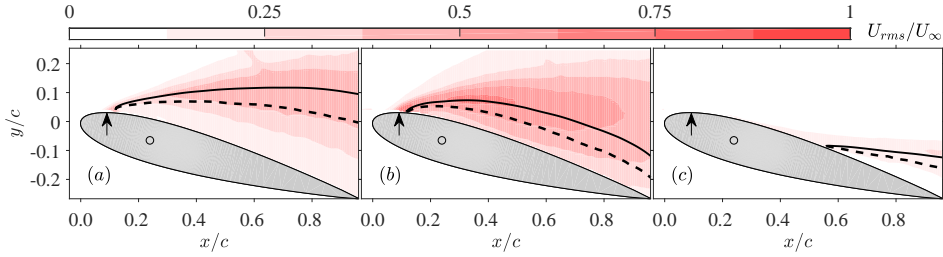


Figure 8.9: Root mean square (RMS) of velocity fluctuations at $\alpha = 15.5^\circ$. (a) $F^* = 0$; (b) $F^* = 0.25$; (c) $F^* = 1.0$.

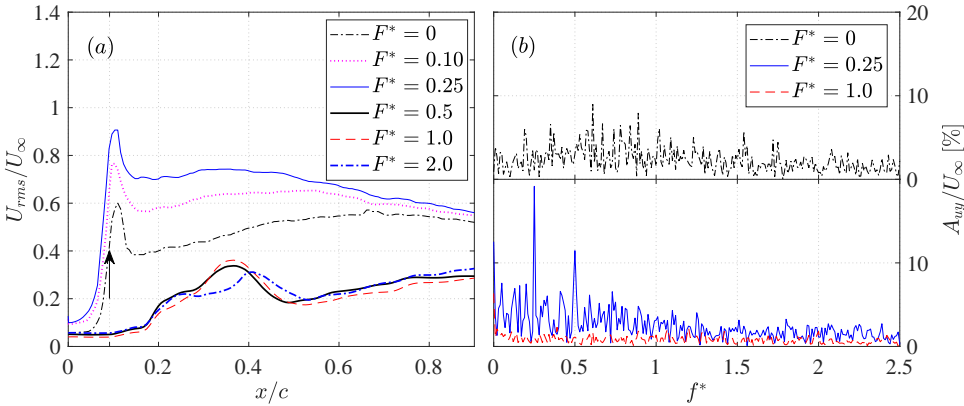


Figure 8.10: (a) Chordwise variation of the peak RMS velocity at $\alpha = 15.5^\circ$ for increasing actuation frequency; (b) Frequency spectrum of velocity fluctuations probed on the dividing streamline at $x/c = 0.4$. The actuation position is indicated by a black arrow.

ther studies are necessary to identify which mechanism plays a dominant role.

Figure 8.9 displays the velocity fluctuations (U_{rms}) in three representative cases. U_{rms} is computed as the Euclidean sum of the root mean square (RMS) of in-plane velocity components. High RMS values are always observed in the separation region, which can be associated with the unsteady motion of shear layers. For all cases, the locus of peak RMS in each profile seems to collapse well on the dividing streamline. This is consistent with the development of coherent flow motions due to shear layer instabilities, in a fashion similar to Laminar Separation Bubbles [169]. Compared to the baseline case, significant increase of velocity fluctuations is observed just downstream of the plasma actuation at $F^* = 0.25$. For the case of $F^* = 1$, the velocity fluctuation is suppressed considerably as a result of the limited separation region. Chordwise variations of the peak RMS in each velocity profile are further shown in Figure 8.10 (a). At $F^* \leq 0.25$, the changing trends of RMS show qualitative similarities. Maximum velocity fluctuations are unexceptionally attained near the separation point (approximately $x = -0.12c$) and increase monotonically with actuation frequency. For the cases of $F^* \geq 0.5$, actuation

frequency has negligible effect on the chordwise variation of RMS, and maximum velocity fluctuations are reached always upstream of the actuation position (approximately $x = 0.1c$). These two distinct regimes in velocity fluctuations suggest the existence of two respectively distinct mechanisms of PSJ-based flow control. Further analysis on these two mechanisms is provided in the following sections.

The effect of actuation frequency on velocity fluctuations can also be illustrated in the frequency domain using fast fourier transformation (sample size: 2700, frequency resolution: 0.6 Hz). Three representative cases are analysed, where probes are placed on the dividing streamline at $x = 0.5c$ to sense the fluttering motion of the separated shear-layers. The instantaneous velocity in y -direction (u_y) is monitored and the corresponding amplitude spectrum is denoted as A_{u_y} . As shown in Figure 8.10 (b), the baseline shear layer exhibits several noticeable peaks in the range of $0.5 \leq f^* \leq 1$ with an amplitude of 5% – 10% of U_∞ . When PSJ actuation is applied at $F^* = 0.25$, two prominent peaks are created ($f^* = 0.25$ and $f^* = 0.5$), suggesting that the fluttering motion of the separated shear layer has been modulated accordingly. The mechanisms of this periodical modulation will be introduced later on. For the case of $F^* = 1.0$, the separated shear layer shifts downstream and the unsteady motion is largely suppressed. No dominant frequency components can be picked at $f^* \leq 2.5$, possibly due to the long convection distance between actuation and separation.

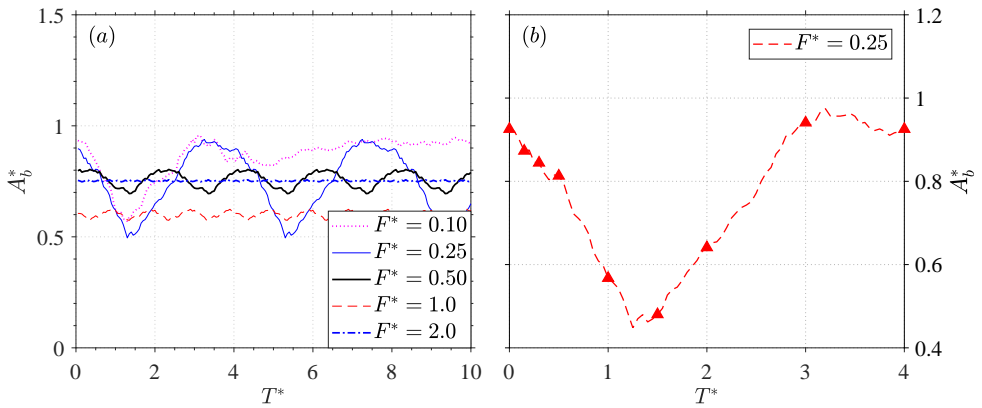


Figure 8.11: (a) Phase-averaged variation of the backflow area with increasing frequency at $\alpha = 15.5^\circ$. (b) Zoomed-in view of the backflow area within one actuation period at $\alpha = 15.5^\circ$ and $F^* = 0.25$. The instants shown in Figure 8.12 are indicated by triangles.

Based on the signals registered from the discharge and PIV systems, phase-averaged velocity fields at different actuation frequencies can be computed. Figure 8.11 (a) shows the phase-averaged variation of backflow area. For cases of $F^* \geq 0.5$ (namely limited trailing edge separation cases), the backflow area remains almost unchanged in one cycle. In contrast, considerable variations of A_b^* are experienced in cases of $F^* \leq 0.25$, which is consistent with the frequency spectrum analysis. For these cases, the backflow area keeps unchanged during the first half time unit after actuation, experiences a sharp drop subsequently and resumes gradually to the undisturbed value. The min-

imum backflow area is reached at about $tU_\infty/c = 2$. In the case of $F^* = 0.1$, a plateau is observed at $T^* \geq 5$, indicating that the disturbance created by a single pulsed jet has been propagated away from the airfoil after 5 time units. This time scale will be termed as separation reset time (T_r) hereinafter.

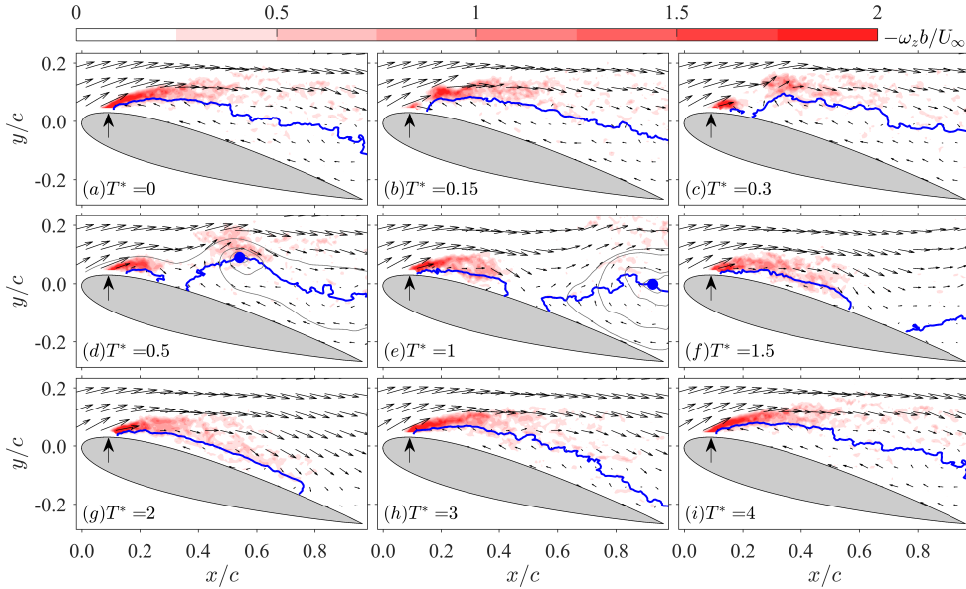


Figure 8.12: Representative phase-averaged flow fields at $F^* = 0.25$. The in-plane velocity is presented as thin arrows. The dimensionless spanwise vorticity is superimposed as contours. The thin grey lines and thick blue lines represent respectively streamlines and contour lines of $U_x = 0$. Jet positions are indicated by thick black arrows. Vortex centres identified from streamlines are marked by blue dots.

To reveal the mechanisms of periodic modulations of the separated shear layer at low actuation frequency, several representative phase-averaged flow fields at $F^* = 0.25$ are shown in Figure 8.12. The vorticity (ω_z) is normalised by U_∞ and half of the maximum airfoil thickness (denoted as b). b is used for normalization as the thickness of vorticity layer is close to the airfoil thickness. Additionally, to link the flow field evolution with the variation of integral parameters, a zoomed-in view of the phase-averaged backflow area at $F^* = 0.25$ in one actuation cycle is plotted in Figure 8.11 (b) as a reference. In the undisturbed flow field ($T^* = 0$), vorticity is shed continuously from the leading edge, convecting downstream along the zero-velocity line. After the jet pulse is released, the vorticity shedding is temporarily interrupted ($T^* = 0.15$) and the original vortex sheet is cut into two ($T^* = 0.3$). The downstream vortex sheet gradually rolls into a concentrated vortex ($T^* = 0.3$ and $T^* = 0.5$) and pushes the original zero-velocity line to the trailing edge during its downstream convection, leading to a decreasing backflow area ($0.5 \leq T^* \leq 1.5$). At the same time, the upstream vortex sheet gradually convects downstream and remains close to the airfoil surface. Underneath this vortex sheet, a closed separation bubble is formed between $T^* = 0.5$ and $T^* = 2$. As this separation

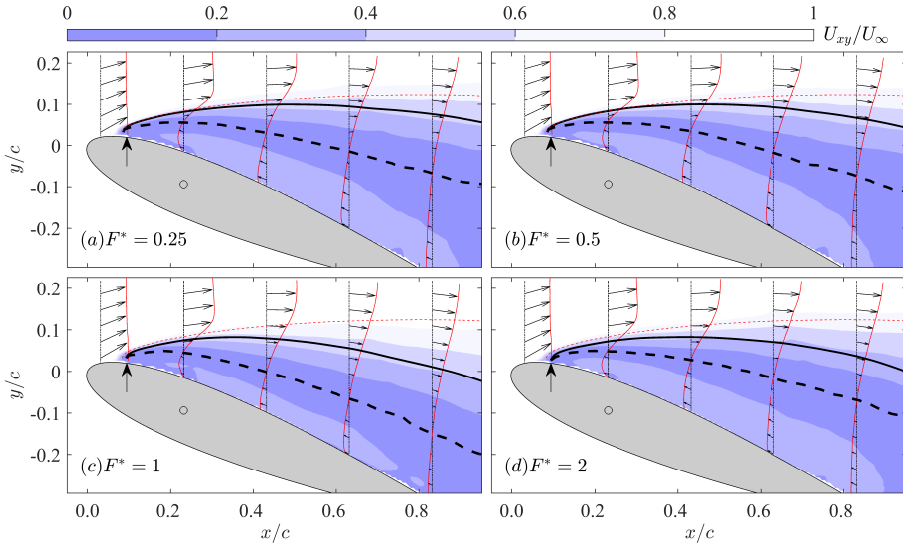


Figure 8.13: Time-averaged velocity fields at $\alpha = 22^\circ$ with PSJ actuation. (a) $F^* = 0.25$, (b) $F^* = 0.5$, (c) $F^* = 1$, (d) $F^* = 2$. Identical notation as Figure 8.6.

bubble grows, the backflow area increases ($2 \leq T^* \leq 4$), and the vortex sheet is lifted away from the suction surface, resuming towards the undisturbed status. The presence of the closed recirculation region will superimpose a virtual hump on the shape of the original airfoil, thus increasing the effective airfoil camber and the phase-averaged lift. This effect is expected to persist until the bubble bursts at $T^* = 2.7$ (namely leading-edge separation occurs).

8

8.4.3. LEADING EDGE SEPARATION CONTROL AT $\alpha = 22^\circ$

The time-averaged velocity fields at $\alpha = 22^\circ$ for increasing actuation frequency are shown in Figure 8.13. As a result, the separation region can not be reduced effectively by PSJ actuation. This differs significantly from the case shown in Figure 8.7 (b)-(d), where large-scale leading-edge separation is converted into localized trailing edge separation. The distinct control effects between $\alpha = 15.5^\circ$ and $\alpha = 22^\circ$ can be ascribed to either the relative shift of actuation location (upstream) or the elevated adverse pressure gradient, or both effects simultaneously. The relative importance of these factors cannot be distinguished in the current investigation due to the fixed actuation location. Figure 8.14 (a) plots the variation of the normalized backflow area, separation length and lift coefficient with actuation frequency. A non-monotonic change of the backflow area is observed, and the minimum value of A_b^* (0.65) is reached at $F^* = 1$. L_{sep}^* changes marginally from 0.94 to 0.93 and the separation point remains always upstream of the actuation. Although leading-edge separation is not completely eliminated at $\alpha = 22^\circ$, the lift coefficient increase remarkably at $F^* \leq 1$, corresponding to the trends pertaining to upstream actuation shown in Figure 8.8 (a). At high actuation frequency ($F^* = 2$), C_l begins to decrease, leading to an optimal actuation frequency of $F^* = 1$.

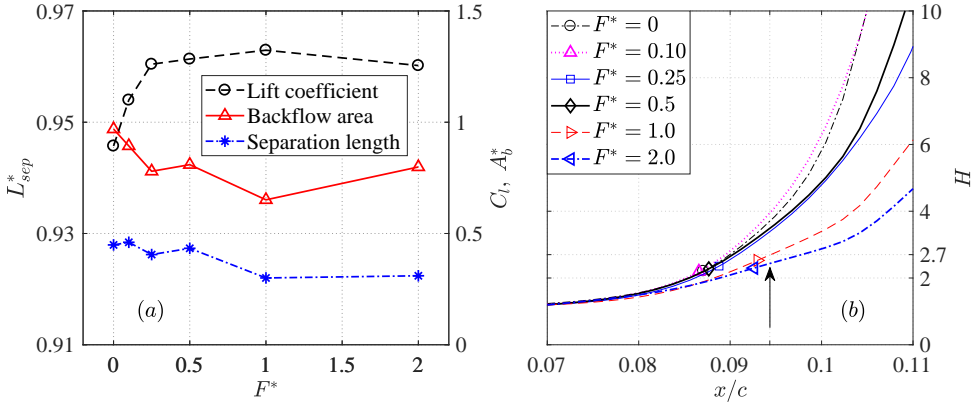


Figure 8.14: (a) Variation of dimensionless backflow area, separation length and lift coefficient with actuation frequency at $\alpha = 22^\circ$; (b) Chordwise variation of the boundary layer shape factor at $\alpha = 22^\circ$; The actuation position is indicated by a black arrow. The separation points are superimposed as markers.

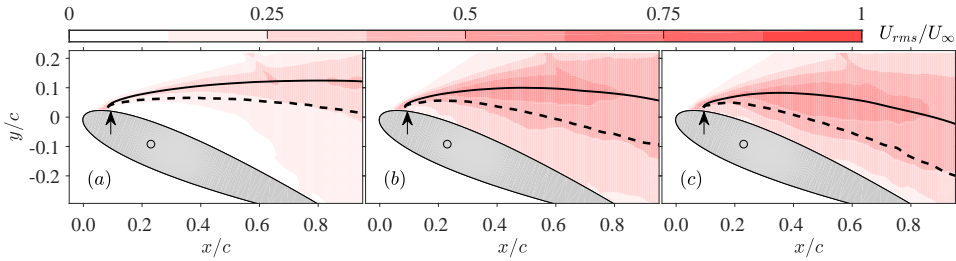


Figure 8.15: Root mean square (RMS) of velocity fluctuations at $\alpha = 22^\circ$. (a) $F^* = 0$; (b) $F^* = 0.25$; (c) $F^* = 1.0$.

Chordwise variations of the boundary layer shape factor for increasing frequency are shown in Figure 8.14 (b). For all the tested cases, the shape factor sharply increases at $x \leq -0.14c$, and the growth rate is affected marginally by plasma actuation. These observations suggest that the incoming boundary layer is not energised sufficiently to withstand the elevated adverse pressure gradient at $\alpha = 22^\circ$. Figure 8.15 displays the RMS of velocity fluctuations in three representative cases. Similar to the flow scenario in Figure 8.10, intense velocity fluctuations are generated in the vicinity of the dividing streamlines. Actuated cases exhibit notably higher RMS level than the baseline case, indicating an enhanced unsteady motion within the separated shear layers due to actuation.

Chordwise evolutions of the peak RMS in wall-normal direction at $\alpha = 22^\circ$ are shown in Figure 8.16 (a). The baseline case ($F^* = 0$) exhibits similar variation as that at $\alpha = 15.5^\circ$. Specifically, maxima of RMS are attained near the separation point (approximately $x = -0.15c$) and a slow increasing trend is experienced downstream of $x \geq -0.1c$. With plasma actuation, the RMS located upstream of the jet orifices including the maximum value remains unchanged, whereas the downstream RMS initially increases with actuation frequency and saturates afterwards. This differs noticeably from the upstream ac-

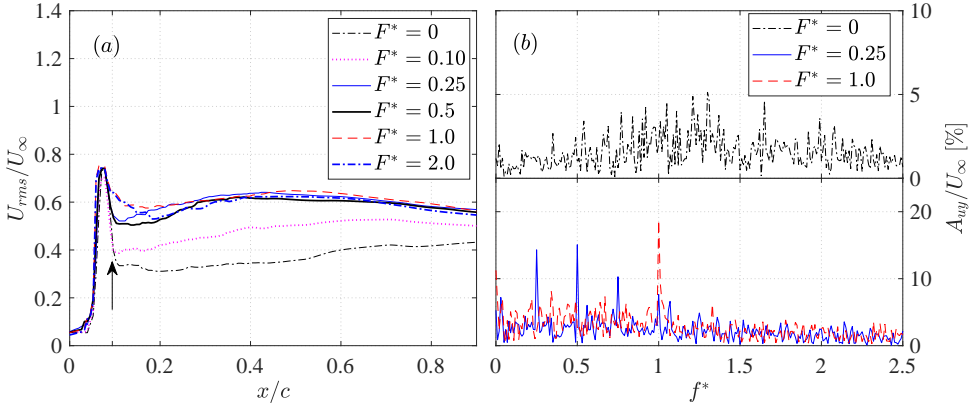


Figure 8.16: (a) Chordwise variation of the peak RMS at $\alpha = 22^\circ$ for increasing frequency; (b) Frequency spectrums probed in the dividing streamline at $x/c = 0.4$; The actuation position is indicated by a black arrow.

tuation case shown in Figure 8.10 ($F^* \leq 0.25$) where the entire RMS curve is lifted with increasing frequency. This distinction suggests that PSJ actuation at a location downstream of the separation point is suboptimal in introducing shear layer instabilities and thus enhancing the mixing in the incoming boundary layer. At $\alpha = 22^\circ$, PSJs are expelled $1\%c$ downstream of the separation point, interacting with the reverse flow. As the reverse flow is usually of low velocity, the issued pulsed jets will penetrate through the separated region and leave the upstream boundary layer largely unaffected. This together with an elevated adverse pressure gradient results in a leading-edge detached flow in all the tested cases, and correspondingly low PSJA control authority.

The frequency spectrums probed in the dividing streamlines at $x = 0.5c$ are displayed in Figure 8.16 (b). Under baseline condition, the separated shear layer exhibits abundant frequency components in the range of $0.5 \leq f^* \leq 1.7$. Nevertheless, no dominant peaks are perceived, suggesting a rather broadband receptivity process for the shear layer, near separation. As the baseline spectrum is the result of this broadband amplification of natural disturbances, the range of $0.5 \leq f^* \leq 1.7$ can be treated as the receptive frequency range of the separated shear layer. This range is wider than the baseline case of $\alpha = 15.5^\circ$ ($0.5 \leq f^* \leq 1.0$). When plasma actuation is applied within this receptive range ($F^* = 1.0$), only one pronounced peak at the base actuation frequency is created. By contrast, at $F^* = 0.25$, several high-order harmonics residing inside the receptive range also appear.

The phase-averaged evolution of the backflow area within one actuation cycle is shown in Figure 8.17 (a). Periodic variations of A_b^* are observed for cases of $F^* \leq 1.0$, pertaining to the dynamic modulation of the separated shear layers by plasma actuation. At $F^* = 0.1$, the time response of A_b^* to a single PSJ pulse is similar to that depicted in Figure 8.11, where A_b^* undergoes a steady decrease shortly after plasma actuation. The minimum value of A_b^* is attained at about 1.2 time units, slightly earlier than the case shown in Figure 8.8 (1.5 time units). Additionally, the time needed for the separated flow to resume after plasma actuation (T_r) is approximately 3 time units, which is also shorter than the case of $\alpha = 15.5^\circ$ (5 time units). The advance of these moments can be attributed to the increasing local velocity associated with wind tunnel blockage,

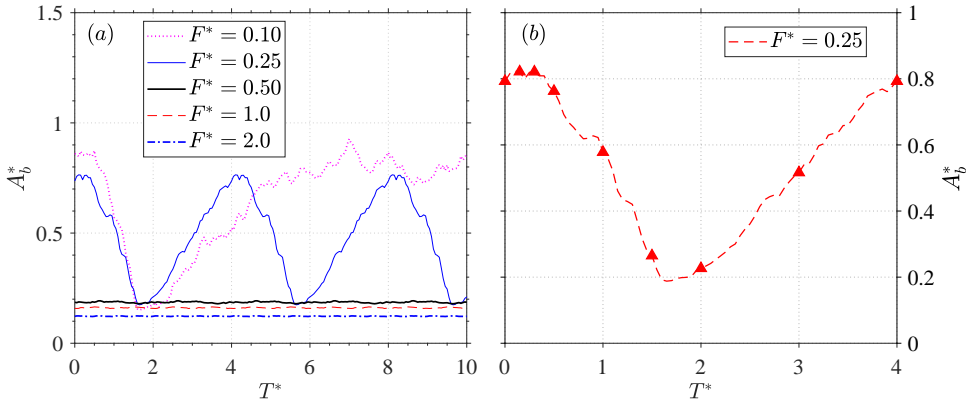


Figure 8.17: (a) Phase-averaged variation of the backflow area with increasing frequency at $\alpha = 22^\circ$. (b) Zoomed-in view of the phase-averaged backflow area in one actuation period at $F^* = 0.25$, $\alpha = 22^\circ$. The instants shown in Figure 8.18 are indicated by triangles.

due to the higher angle of attack. The variation of the backflow area at $F^* = 0.25$ almost duplicates that at $F^* = 0.1$, since the corresponding cycle period (4 time units) is long enough to reset the separated flow and the adjacent two jet pulses are essentially independent. Therefore, in the frequency regime of $F^* \leq 1/T_r$, increasing the actuation frequency will raise the duty cycle of separation suppression. Consequently, a linear relationship between A_b^* (as well as C_l) and the reduced frequency is expected at $F^* \leq 0.33$, which is valid in Figure 8.14 (a). When F^* exceeds $1/T_r$, the adjacent two jet pulses will inevitably interact with each other and the modulation of the separated flow becomes less effective. Consequently, the variation in amplitude of the backflow area decreases with actuation frequency as evidenced by Figure 8.17 (a).

The time evolution of the phase-averaged flow fields at $F^* = 0.25$ within one actuation cycle is shown in Figure 8.18. A zoomed-in view of the corresponding backflow area is plotted in Figure 8.17 (b). Overall, the dynamic response of the separated flow to PSJ actuation at $\alpha = 22^\circ$ is similar to that at $\alpha = 15.5^\circ$. The vortex shedding is also temporally intercepted by the pulsed jet at $T^* = 0.15$, and the new-born vortex sheet evolves into a concentrated spanwise vortex which can be well visualized by the streamlines at $T^* = 1.5$ and $T^* = 2.0$. However, unlike the case shown in Figure 8.12, the backflow region underneath this spanwise vortex is always connected to the original backflow region after $T^* = 0.3$, and no closed separation bubble is formed. This phenomenon illustrates that the high-momentum fluids transported from the free-stream to the near-wall region are not enough to withstand the severe adverse pressure gradient, ostensibly because the center of this vortex is located too far away from the airfoil surface due to the large angle of attack. Nevertheless, the downwash effect of the spanwise vortex is able to sweep the zero-velocity line towards the suction surface during downstream propagation, leading to a reduced backflow area between $T^* = 0.5$ and $T^* = 1.5$. After $T^* = 1.5$, the vortex sheet as well as the suppressed zero-velocity line starts to recover, resulting in an increasing backflow area.

Based on Figures 8.12 and 8.18, the post-stall flow scenario excited by PSJs seems

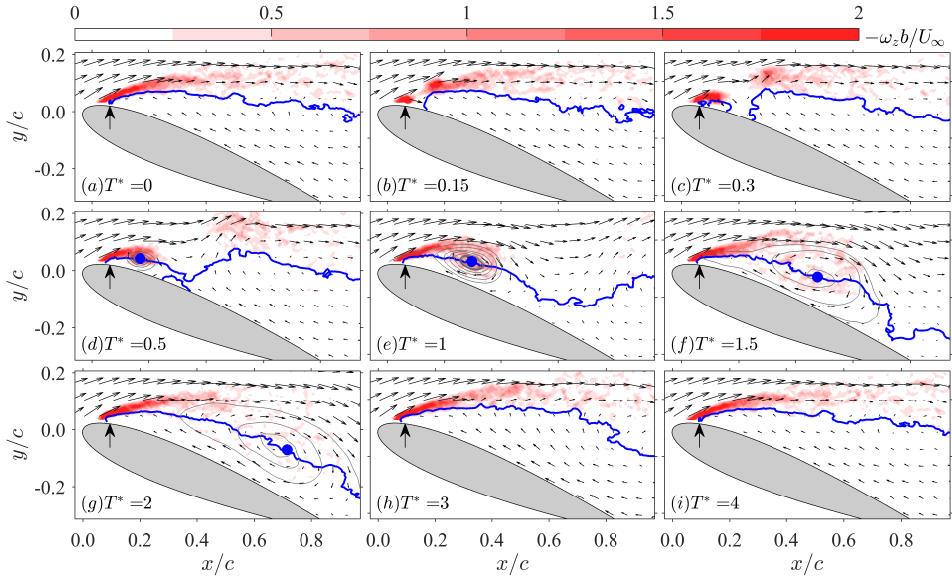


Figure 8.18: Representative phase-averaged flow fields at $F^* = 0.25$ and $\alpha = 22^\circ$; (a) $T^* = 0$, (b) $T^* = 0.15$, (c) $T^* = 0.3$, (d) $T^* = 0.5$, (e) $T^* = 1$, (f) $T^* = 1.5$, (g) $T^* = 2$, (h) $T^* = 3$, (i) $T^* = 4$. Identical notations are inherited from Figure 8.12.

to be dominated by the large-scale vortices shed from the separated shear layer. These vortices convect periodically over the suction surface, increasing the time-averaged lift coefficient at post-stall regime in a similar fashion as that observed in the dynamic stall of pitching airfoils [167]. Specifically, once the pitching angle exceeds the static stall angle, a stall vortex is shed from the leading edge and creates a convective low-pressure core over the suction side, resulting in a lift that is much higher than the static peak lift. This separation control mechanism is consistent with that of SDBDAs driven by high-voltage nanosecond pulses [170].

The phase-averaged flow fields at $F^* = 1$ and $F^* = 2$ are further presented in Figure 8.19 and Figure 8.20 to interpret the formation mechanism of the optimal actuation frequency in Figure 8.14 (a). At $F^* = 1$, two vortices, approximately half a chord apart, can be clearly identified from the streamline patterns throughout the time. As explained earlier, these vortices are created by periodically intercepting the leading-edge vorticity shedding with pulsed jets. The modulation extent of the zero-velocity lines increases with the intensity and size of these spanwise vortices. For the presented case of $F^* = 1$, the interaction between adjacent vortices is insignificant due to the sufficient convection distance in one period ($0.5c$). As such, each vortex can grow to considerable size and modulate the backflow area effectively. In the case of $F^* = 2$, the vortices are generated every half a time unit and the chordwise spacing is reduced to approximately $0.3c$. On the one hand, the total vorticity entrained into each vortex (namely circulation) is largely decreased, as a result of the limited growth time. On the other hand, the mutual interaction between adjacent vortices aggravates at short spacing. Specifically, the generated vortices are rotating in the clockwise direction. The downwash effect of a newborn vor-

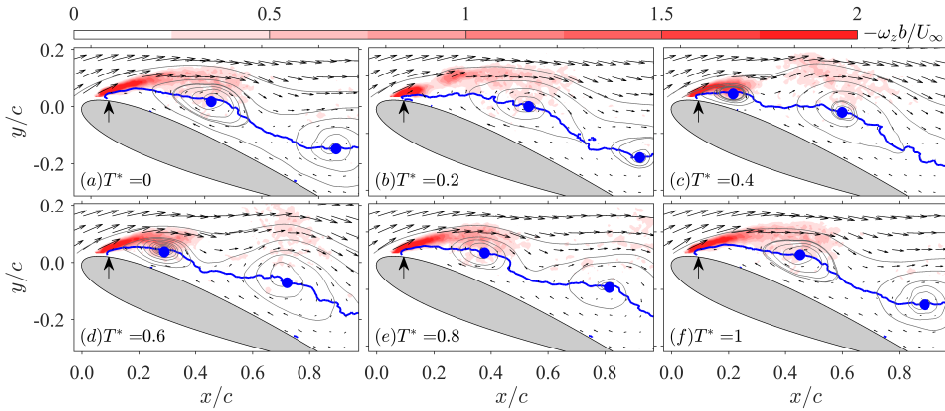


Figure 8.19: Representative phase-averaged flow fields at $F^* = 1$ and $\alpha = 22^\circ$; (a) $T^* = 0$, (b) $T^* = 0.2$, (c) $T^* = 0.4$, (d) $T^* = 0.6$, (e) $T^* = 0.8$, (f) $T^* = 1$. Identical notation as Figure 8.12.

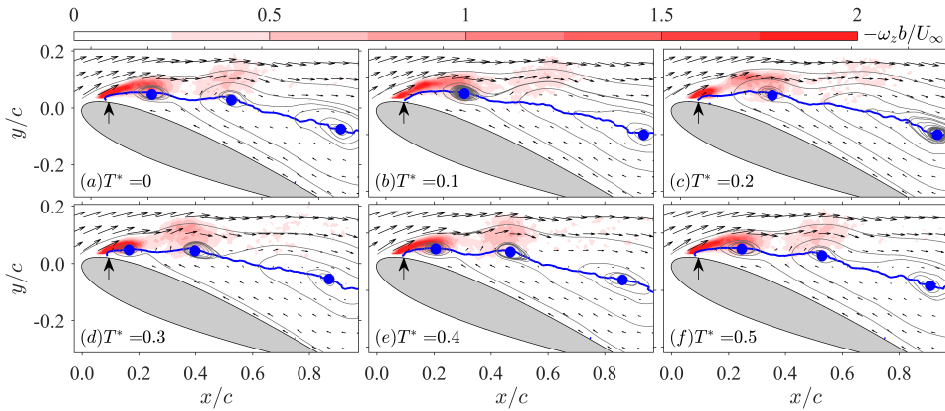


Figure 8.20: Representative phase-averaged flow fields at $F^* = 2$ and $\alpha = 22^\circ$; (a) $T^* = 0$, (b) $T^* = 0.1$, (c) $T^* = 0.2$, (d) $T^* = 0.3$, (e) $T^* = 0.4$, (f) $T^* = 0.5$. Identical notation as Figure 8.12.

tex can be partially counteracted by the upwash effect of the antecedent vortex while propagating downstream, which leads to an ineffective modulation of the backflow area and a decreasing trend of the lift coefficient after $F^* \geq 1$ (Figure 8.14 a).

8.5. CONCLUDING REMARKS

In this chapter, a PSJA array consisting of 26 individual actuators is embedded at 8% chord away from the leading edge of a NACA0015 airfoil model to control the flow separation at moderate Reynolds number ($Re_c = 1.7 \times 10^5$, $U_\infty = 10 \text{ m/s}$). Balance measurements are performed to evaluate the overall airfoil performance, while high-speed PIV measurements are conducted to reveal the control mechanisms at two critical angles of attack ($\alpha = 15.5^\circ$ and 22°), corresponding respectively to the incipient and deep stall. In the range of $0.5 \leq F^* \leq 2$, the stall angle is postponed from 15.5° to approximately 22° ,

accompanied by 21% increase in the peak lift coefficient and 40% decrease in the drag coefficient at $\alpha = 15.5^\circ$. Hysteresis loops are completely eliminated by PSJ actuation in all cases, while the power saving ratio of PSJAs at $F^* = 0.5$ and $\alpha = 15.5^\circ$ is comparable to that of SDBDAs in cylinder flow control by same definition.

At $\alpha = 15.5^\circ$, the flow detaches approximately $4\%c$ downstream of the jet orifice. When PSJ actuation is applied at $F^* \geq 0.5$, the large-scale leading-edge separation under baseline condition is converted into localised trailing-edge separation, similar to the flow scenario observed at $\alpha = 15^\circ$. Energising the boundary layer resulting from mixing enhancement is responsible for the separation suppression in this frequency range, and the backflow area decreases consistently with increasing frequency. With low-frequency actuation imposed at $F^* \leq 0.25$, the separation point still resides near the leading edge, nevertheless the backflow area decreases and the lift coefficient increases linearly with actuation frequency. In these cases, coherent spanwise vortices are generated during the interaction between the array of pulsed jets and the separated shear layer. These vortices transport the high-momentum flow from free stream to the near-wall region and sweep the zero-velocity line periodically towards the suction surface, leading to a reduction of time-averaged separation area. Additionally, these spanwise vortices will create low-pressure cores on the suction surface which resume the lift.

When α increases to 22° , the separation point displaces upstream of the jet orifice ($1\%c$ apart). For PSJ actuation applied between $F^* = 0.25$ and $F^* = 2$, the separation zone retreats downstream marginally as the incoming boundary layer is insufficiently energised. A non-monotonic variation of the lift coefficient and backflow area is observed with increasing frequency, with the optimal actuation frequency located at $F^* = 1$. The time evolution of the separated flow at $F^* \leq 1$ remains similar to the cases of $F^* \leq 0.25$ and $\alpha = 15.5^\circ$, where spanwise vortices are generated consecutively and modulate the separated flow independently. However, at higher actuation frequency ($F^* = 2$), the adjacent spanwise vortices start to interact with each other inevitably due to short streamwise spacing, leading to an ineffective modulation of the separation flow. As a result, the backflow area increases and the lift coefficient declines with increasing frequency after $F^* = 2$.

9

SWBLI CONTROL AT MACH NUMBER 2: PRELIMINARY RESULTS

9.1. INTRODUCTION

OBLIQUE shock waves serve as an efficient form of compression for supersonic intakes. However, when they interact with the intake walls, the induced adverse pressure gradient can trigger large-scale separation. This unsteady separation not only causes significant total pressure loss and flow distortion in supersonic intakes, but also imposes large structural loads that accelerate material fatigue [77]. To prevent shock-induced separation, several methods have been deployed to control shock wave/ boundary layer interaction. Bleeding is a conventional form of active flow control, which removes low-momentum fluid through a porous intake surface. Although widely used, this method reduces the engine mass flow rate and increases system complexity. Micro vanes and micro ramps can create streamwise vortices that promote the mixing in supersonic boundary layers and increase their ability to resist adverse pressure gradient [171]. However, an inevitable drag penalty is introduced when the flow inside intakes is fully attached.

As an active device that can be deployed on demand, PSJA has demonstrated sufficient control authority towards supersonic flow. Narayanaswamy, Raja, and Clemens [63, 65, 69] showed that the PSJs were capable of penetrating 1.5 boundary layer thickness in Mach 3 cross flow, meanwhile reducing the pressure fluctuations associated with the large-scale separated flow in SWBLI by 30%. Greene et al. [70] utilized a similar experimental setup and examined the effect of skew and pitch angles of the pulses jets on mean flow separation. The 20° pitch-angle and 0° skew-angle jets outperformed the other tested cases, and the distance between separation line and compression ramp corner was reduced by up to 40%. Although promising, the results mentioned above are mostly based on Schlieren imaging and dynamic pressure measurements, instead of quantitative PIV methods. The flow scenario pertaining to the interaction between PSJ and SWBLI is still unclear and the underlying control mechanism needs to be revealed.

This chapter takes the first step toward the quantification of SWBLI under PSJA. A row of five PSJAs is issued upstream of the incident shock wave/boundary layer interaction region to eliminate or mitigate the reversal of flow. The unit-length Reynolds number based on the freestream velocity and density reaches $Re_L = 4.4 \times 10^7$ [1/m]. Dynamic response of the shock system to plasma actuation and the variation of mean and fluctuation velocity in the interaction region are diagnosed with high-speed schlieren imaging and PIV system, respectively.

9.2. EXPERIMENTAL SETUP

9.2.1. TEST SECTION, ACTUATOR AND DISCHARGE CIRCUITRY

The experiments were performed in the ST-15 wind tunnel of TU Delft. The ST-15 wind tunnel is a supersonic blow-down wind tunnel equipped with inflexible wall nozzles. Interchangeable sets of Laval nozzles are used to obtain Mach numbers of either 1.5, 2, or 3 in a 150 mm (width) \times 160 mm (height) test section. High-pressure air is stored in a 300 m³ pressure vessel, leading to a total running time of about 18 minutes before recharging is required. For the purposes of this investigation, a Mach number 2 nozzle set is configured, and a thin liner (peak thickness: 10 mm, material: aluminum) is laid on top of the bottom wall of test section *a posteriori*, to create space necessary for accommodating the actuator cavities without permanently milling the original nozzle sets (Figure 9.1 *a*). The leading edge of the liner is sharpened and attached smoothly to the diverging part of the nozzle to minimize weak shock waves generated by nozzle profile discontinuity. This modification leads to a slightly asymmetric nozzle and a reduced area of the test section. As a result of the decreasing throat-to-exit area ratio, the actual Mach number in the modified test section ($M_\infty \approx 1.86$, computed from PIV results) is lower than the nominal Mach number 2.

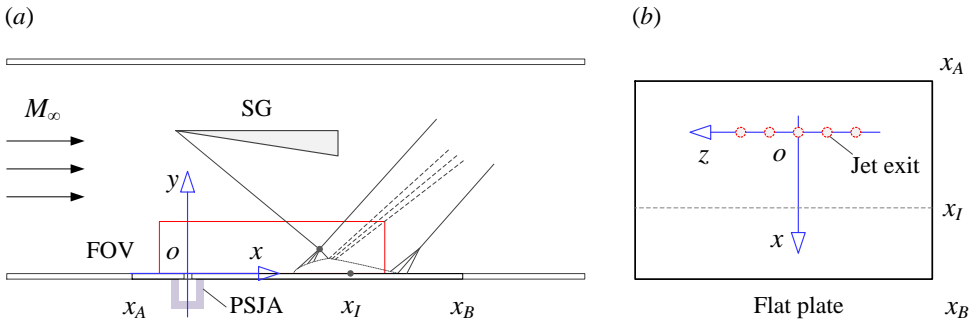


Figure 9.1: (a) Test section configuration (not in scale). SG—shock generator; FOV—field of view in PIV measurements; x_A and x_B denote respectively the streamwise locations of the leading and trailing edge of the flat plate; x_I is the inviscid shock impinging position on the wall. (b) Flat plate with five circular orifices.

Figure 9.1 (a) shows the test section configuration (not to scale). The oblique shock wave is generated by a 120 mm width wedge with 8.8 degrees downward compression angle, interacting with the turbulent boundary layer (TBL) developing on the bottom wall. The undisturbed boundary layer thickness determined from 99% of the freestream

velocity ($U_\infty = 486$ m/s) is $\delta_{99} \approx 6.3$ mm. Using the freestream velocity as the reference length and velocity scales, the unit-length Reynolds number is computed as $Re_L = 4.4 \times 10^7$ [1/m]. The plasma synthetic jet actuator array is designed in a similar fashion as that in airfoil separation control (Figure 8.1), consisting of multiple cylindrical cavities and a flat-plate cap made of machinable ceramic glass (MACOR). These components can be fitted tightly on the remaining segments of the liner, thus to form an integral flat surface on top. The inner diameter and height of the actuator cavity are 6 mm and 4 mm, respectively, resulting in a cavity volume of 113 mm³. Compared to the values in previous chapters (~ 1000 mm³), the reduced cavity volume in this investigation is aimed to get a high non-dimensional energy deposition, thus a peak jet velocity comparable to freestream velocity. Two tungsten needles are inserted oppositely inside the actuator cavity, acting as anode and cathode respectively. As shown in Figure 9.1 (b), the flat plate has a dimension of $150 \times 100 \times 3$ mm³, in spanwise, streamwise and wall-normal direction, respectively. A row of five circular orifices are drilled normal to the wall, at a streamwise location of 42.4 mm ($6.7\delta_{99}$) upstream of the inviscid shock impinging position on the wall (x_I). The exit orifice diameter and the spanwise spacing of these plasma synthetic jets are $D = 2$ mm and $s_a = 15$ mm, respectively. A coordinate system is arranged in the center of the middle exit orifice, with x -, y -, and z -axis along the streamwise, wall-normal and spanwise direction, respectively.

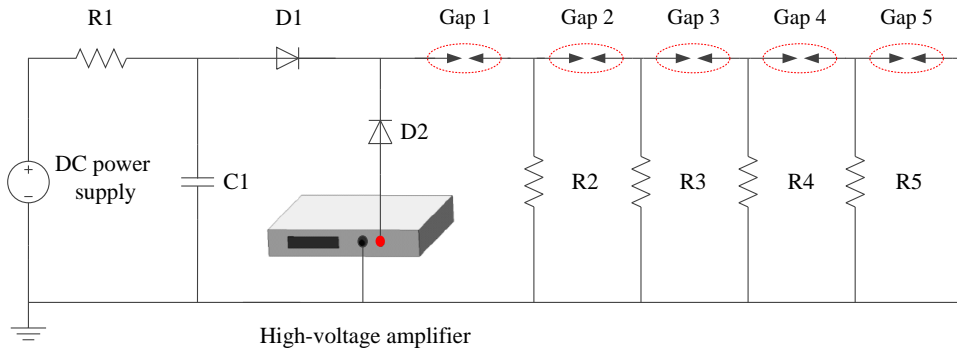


Figure 9.2: Discharge circuitry used to create multiple plused arcs.

As the characteristic frequency ($O(1$ kHz)) and velocity ($O(100$ m/s)) of SWBLI are much higher than that of the separated flow investigated in Chapter 8 ($Re_c = 1.7 \times 10^5$), the discharge circuitry shown in Figure 8.2 can not be inherited straightforwardly, and a new circuitry was devised as shown in Figure 9.2. Similar to these in Figure 2.2, the high-voltage amplifier and the DC power supply are responsible for discharge ignition and arc energy addition. During discharge ignition, to guarantee the successful transfer of high-voltage trigger pulses from one gap to another, a high-voltage resistor (R2-R5; resistance: 5 M Ω ; withstand voltage >20 kV) is added between each of the adjacent electrode gaps, matching the rapid impedance variation in the trigger process. Specifically, prior to gas breakdown, the electrode gaps can be modeled as a resistor with infinite resistance (i.e. open circuit), and the high-voltage trigger pulse is burdened solely by Gap 1. After Gap 1 is ignited, the resistance of the discharge channel drops sharply to $O(10$ Ω) and becomes

negligible compared to R2-R5. As such, the majority of the high-voltage trigger pulse is carried by Gap 2, and similar breakdown processes repeat until a complete discharge channel through Gaps 1-5 is established. In this study, all the gaps are fixed as 2 mm, and the capacitance and initial voltage of C1 are set as $C_1 = 0.1 \mu\text{F}$ and $V_1 = 2.5 \text{ kV}$, respectively. Based on Equation 3.1, the non-dimensional energy deposition is determined to be $\epsilon = 7.7$.

9.2.2. SCHLIEREN AND PIV SYSTEM

Schlieren imaging is deployed to qualitatively diagnose the dynamics response of SWBLI to plasma actuation. Basics of the Z-type schlieren system have been detailed in Section 2.3.1, thus will not be repeated here. The knife-edge filter is oriented in the wall-normal direction, to visualize the streamwise density gradient. The schlieren images (resolution: $512 \times 256 \text{ pixels}^2$) are acquired by a high-speed camera (Photron, FastCam SA-1) at 40 kHz, in phase-locked mode. For each phase, 80 samples are realized at a discharge frequency of 10 Hz for statistical averaging operation.

High-speed PIV measurements are performed in the middle of spanwise plane (yoz plane). The PIV system consists of two high-speed cameras (Photron, FastCam SA-1), a high-speed laser (Quantronix, Darwin Duo 527-80-M) and a programmable timing unit (LaVision, high-speed controller). Di-Ethyl-Hexyl-Sebacat (DEHS) particles are produced by an aerosol generator (PivPart 45, PIVTEC) and further introduced in the settling chamber of the wind tunnel by a seeding rake. The laser beam emitted from the laser head is delivered to the test section by an in-house periscope. Within the periscope, a set of cylindrical and spherical lenses are configured to shape the circular laser beam into a thin laser sheet (thickness: 1 mm), which passes strictly through the center of the middle exit orifice (see Figure 9.1 *b*). For each of the two cameras, an objective of 200 mm focal length (Nikon, Micro Nikkor) is mounted to image a field of view (FOV) of $3\delta_{99} \times 6\delta_{99}$ on the cropped sensor (resolution: $1024 \times 512 \text{ pixels}^2$). The two views are stitched in the streamwise direction with an overlap of approximately 10 mm. DaVis 8.3.1 is used to record and process the images, and the interrogation window size and overlapping ratio in the final pass are set as $48 \times 48 \text{ pixels}^2$ and 75% respectively, resulting in a spatial resolution of 0.47 mm/vector. The weighting function of the interrogation window is selected as elliptical to maximize the spatial resolution in wall-normal direction.

The PIV system is working in double frame mode, with a laser separation time of $2 \mu\text{s}$ and a peak particle displacement of 26 pixels. Four cases with constant energy deposition and increasing discharge frequencies ($f_d = 0 \text{ Hz}$, 100 Hz, 500 Hz, 1000 Hz) are tested. In each case, a long sequence of 5400 image pairs are acquired at a peak sampling rate of 5100 Hz, which is sufficient to get statistically-converged mean and fluctuation velocity components. It should be noted that although the dataset is acquired at high frequency, no frequency-domain analysis (e.g. flourier transformation) can be performed as a significant amount of the velocity vectors (up to 30%) are missing in the time series due to an intermittency of seeding streams.

9.3. PHASE-AVERAGED SCHLIEREN RESULTS

Two representative phase-averaged schlieren images are shown in Figure 9.3 (*a*) and (*b*). In baseline condition, the incident shock wave imposes a strong adverse pressure gradi-

ent to the incoming boundary layer, resulting in flow separation and a significant shift of the incident shock foot away from the wall. Upstream of the separation bubble, several weak compression waves coalesce into a reflected shock and intersects with the incident shock. This scenario is largely expected from the free-interaction theory [77], as the pressure rise for incipient flow separation (1.79, Equation 9.1) is much lower than that created by the incident-reflected shock wave system (2.44). Here, the reference friction coefficient, $c_f = 1.9 \times 10^{-3}$, is taken from the measurements of a comparable TBL [172].

$$\frac{P_1}{P_0} = 1 + 6 \frac{\gamma}{2} M_0^2 \sqrt{\frac{2C_{f0}}{(M_0^2 - 1)^{1/2}}} \quad (9.1)$$

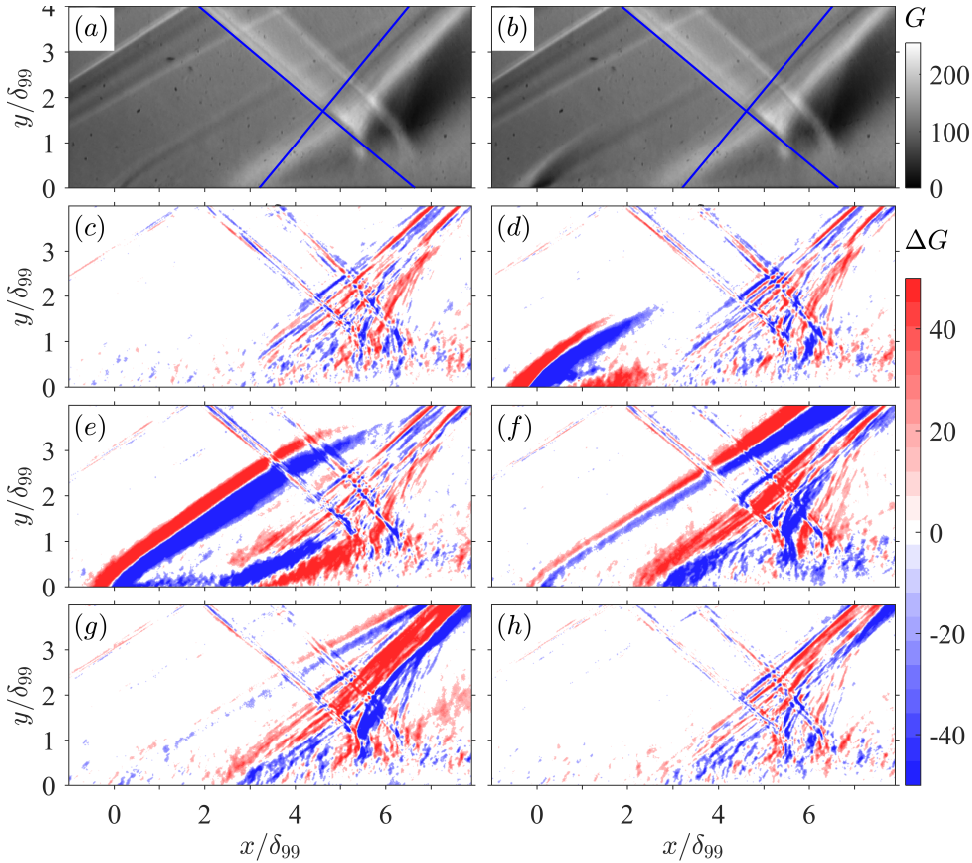


Figure 9.3: (a – b) Representative phase-averaged schlieren images at the baseline condition (left) and a time delay of $50\mu\text{s}$ w.r.t discharge ignition (right). G denotes the image grayscale. The incident and reflected shocks extracted from Figure 9.6 (b) are indicated by the blue solid lines and further extrapolated to the wall. (c – h) Contours of the grayscale difference (ΔG) between phase-averaged jet affected images and the baseline image. From left to right and top to bottom, the time delays are respectively (c) $t = 0\mu\text{s}$, (d) $t = 50\mu\text{s}$, (e) $t = 100\mu\text{s}$, (f) $t = 200\mu\text{s}$, (g) $t = 300\mu\text{s}$ and (h) $t = 400\mu\text{s}$.

At a time delay of $t = 50 \mu\text{s}$ w.r.t discharge ignition, high-velocity jet is issued out of the exit orifice and creates an attached bow-shape shock wave in the upstream, which is consistent with the observation from [50, 73, 75]. The bow-shape shock wave is resulting from an elevated pressure in the windward side of the jet due to flow stagnation [76], and its angle decreases while extending downstream. The lower limit of the shock wave angle is approximately 32 degrees, which agrees well with the theoretical angle of Mach waves. In later phases, to accentuate the relative variation of the interaction region caused by plasma actuation, the baseline SWBLI image (i.e. Figure 9.3 *a*) is first subtracted from the jet-actuated images (e.g. Figure 9.3 *b*), and the grayscale difference (ΔG) is plotted as contours in Figure 9.3 (*c* – *h*). Between $t = 50\mu\text{s}$ and $t = 100\mu\text{s}$, the fluids expelled from exit orifice seem to be confined in the turbulent boundary layer, convecting downstream towards the interaction region. At a streamwise location of $x/\delta_{99} \approx 3$, the disturbances reach the separation region, and interacts with the detached shear layer. Based on the grayscale variation pattern of the shear layer, it is conjectured that the separation region executes an initial downstream movement at $t = 100\mu\text{s}$ (i.e. blue preceding red), followed by an upstream recovering motion between $t = 200\mu\text{s}$ and $t = 300\mu\text{s}$ (i.e. red preceding blue). Additionally, when the jet induced shock wave extends through the incident shock wave (see Figures 9.3 *f* – *g*), an upstream motion of the reflected shock is observed, which agrees well with the observation in [15] and can be ascribed to the slight decrease of the local Mach number upstream of the reflected shock wave. After $t = 500\mu\text{s}$, the grayscale variation becomes negligible, and the effect of PSJs ceases.

9.4. PIV RESULTS AND DISCUSSIONS

Phase-averaged PIV results at increasing discharge frequency are shown in Figure 9.4. U_{xy} denotes the euclidean sum of in-plane velocity components, $U_{xy} = (U_x^2 + U_y^2)^{1/2}$. The incident and reflected shock waves identified from the contour of wall-normal velocity fluctuation (see Figure 9.6 *b*) are extrapolated towards the wall, and the distance between the two intersection points (x_F and x_I) is defined as the interaction length, L_I . Using the undisturbed value of interaction length ($L_I = 22.7 \text{ mm}$) and the freestream velocity (U_∞ , 486 m/s) as the reference length and velocity scales, a non-dimensional discharge frequency (Strouhal number) can be derived, i.e. $F^* = f_d U_\infty / L_I$. For all the tested cases, no reversal flow is observed in time-averaged velocity fields. The effects of plasma actuation, although not as prominent as that of micro-ramps [172], can still be substantiated by the comparison of sonic line as well as the velocity contour in interaction region. Compared to baseline condition ($F^* = 0$), the upstream most position of the sonic line retreats approximately $0.5\delta_{99}$ downstream at $F^* = 0.02$, meanwhile the minimum streamwise velocity (U_x) increases from $0.21U_\infty$ to $0.28U_\infty$. For the other two actuated cases, the sonic line is shifted slightly downstream by $0.2\delta_{99}$, and the minimum streamwise velocity pivots around $0.24U_\infty$. These observations conclude an optimal actuation frequency of $F^* = 0.02$, which is close to the optimal frequency reported in [70] ($F^* = 0.018$) as well as the non-dimensional excursion frequency of the shock foot [173].

Based on the mean velocity field, the incompressible boundary layer shape factor (H) is computed with Equation 6.4, and the integrals are preformed from the vector row most close to the wall ($y = 0.08\delta_{99}$) to the upper limit of the FOV ($y = 2.9$). Figure 9.5 (*a*) shows the streamwise variations of the boundary layer shape factor with increasing

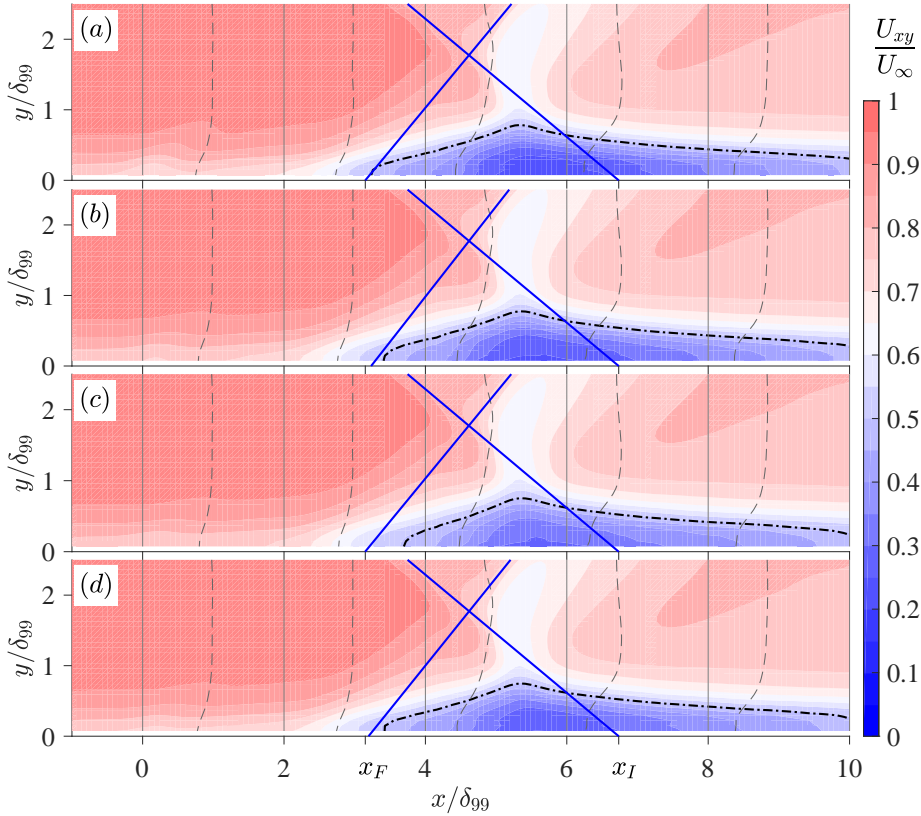


Figure 9.4: Time-averaged flow organization at (a) $F^* = 0$ ($f_d = 0$ Hz), (b) $F^* = 0.004$ ($f_d = 100$ Hz), (c) $F^* = 0.02$ ($f_d = 500$ Hz), and (d) $F^* = 0.04$ ($f_d = 1000$ Hz). The incident and reflected shock in each cases are represented by the blue solid lines and further extrapolated to the wall. In all the plots, the extrapolated intersection points of these two shocks in baseline case are indicated as x_I and x_F .

discharge frequency. As the bottom part of the TBL velocity profile is absent due to low spatial resolution of PIV measurements, the values of H are slightly underestimated. In baseline condition, the shape factor changes marginally at $x/\delta_{99} < 2$, whereas exhibiting a sharp increase and a subsequent decrease in the interaction region. A bump is observed near the origin, corresponding to the weak shock wave induced by jet exit orifice (see Figure 9.3 a). The height of the bump is reduced noticeably for all actuated cases (i.e. energized boundary layer in time-averaging perspective), indicating a favorable effect of PSJs on the near exit flow, which can be ascribed to the weak suction flow and agrees well with the observations in Figure 7.13. Additionally, in interaction region, the shape factor ($3 < x/\delta_{99} < 10$) is reduced unexceptionally by plasma actuation. The boundary layer velocity profiles at $x = x_F$ (approximately interaction onset) and $x = 5.7\delta_{99}$ (location of maximum shape factor) are further plotted in Figure 9.5 (b). As evidenced, the bottom part of the TBL has already been energized prior to interaction, and the energisation is most effective at $F^* = 0.02$.

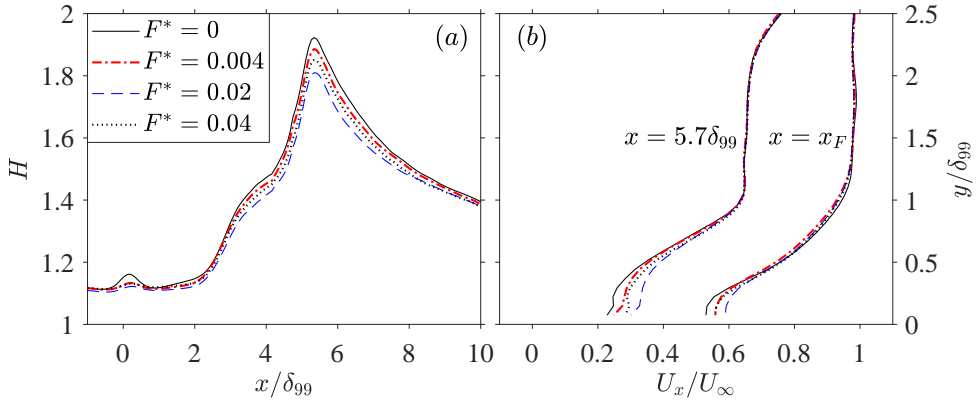


Figure 9.5: (a) Streamwise variation of the boundary layer shape factor with increasing actuation frequency. (b) Boundary layer velocity profiles measured at $x = 5.7\delta_{99}$ and $x = x_F$.

The source of boundary layer energisation can be traced back to mixing enhancement. Figure 9.6 (a, b) shows the contour of in-plane velocity fluctuations (u_x , u_y) at baseline condition. The friction velocity ($u_\tau = 20.8$ m/s) taken from a similar TBL measurement in [172] is used for normalization, as the bottom part of the TBL ($y/\delta_{99} < 0.1$) is not resolved in this study. High magnitude of streamwise velocity fluctuations ($u_x/u_\tau > 4$) mainly reside in the interaction region, particularly within the sonic line. In contrast, the wall-normal velocity component fluctuates significantly not only in the interaction region but also near the incident and reflected shock waves. These fluctuation levels are much higher than that in the incoming turbulent boundary layer and can be related to the low-frequency unsteadiness of the separation bubble, whose size and streamwise location vary from shot to shot [173]. Additionally, the peak value of u_x/u_τ is approximately three times higher than the peak value of u_y/u_τ , which is consistent with the observations in [174].

To elucidate the effects of plasma actuation on velocity fluctuations, the in-plane turbulent kinetic energy (TKE) is computed as $k_{xy} = 0.5 \cdot (u_x^2 + u_y^2)$, and the peak value of k_{xy} in each streamwise location is plotted in Figure 9.6. For all the tested cases, a non-monotonic variation of k_{xy}/u_τ^2 is exhibited, resembling the trend of boundary layer shape factor shown in Figure 9.5. When plasma actuation is applied, the rising slope of the TKE curve is shifted downstream, corresponding to a shrinkage of upstream interaction length. The postponed interaction together with an elevated peak TKE in the interaction region, indicates that the mixing in upstream interaction region ($3 < x/\delta_{99} < 5$) is enhanced significantly by plasma actuation, which is consistent with the observation in Figure 9.3 (e). The disturbances responsible for promoting the mixing are essentially the plasma synthetic jets issued upstream of the interaction region. On the one hand, these disturbances yield a fuller turbulent boundary layer which can maintain attached further downstream. On the other hand, these periodical disturbances are selectively amplified by the separated shear layer in upstream interaction region, resulting in higher peak TKE levels favouring flow reattachment. From Figure 9.6, the receptive frequency band of the separated shear layer is inferred to be $0.004 < F^* < 0.02$.

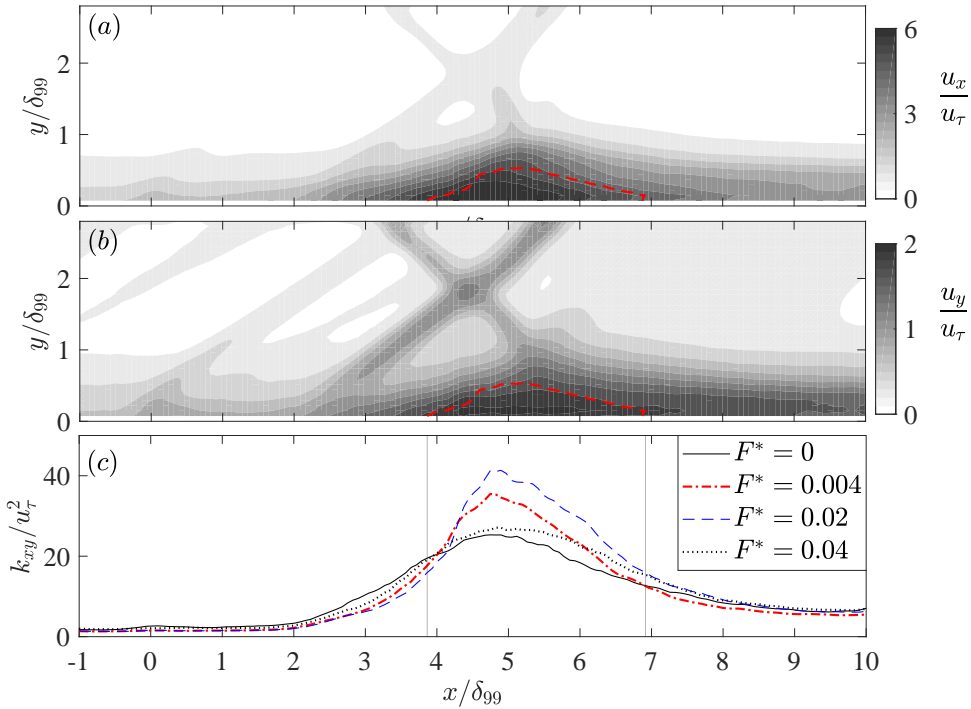


Figure 9.6: (a – b) Root-mean-square of the fluctuations of in-plane velocity components (u_x/u_τ , u_y/u_τ) at $F^* = 0$. The red dash lines superimposed on the contours are contour lines of $p_s = 0.05$. (c) Streamwise variations of the peak turbulent kinetic energy (k_{xy}/u_τ^2) with increasing frequency. The streamwise extent of the sonic line in baseline condition is indicated by two grey lines.

Notwithstanding the absence of separation region in the time-averaged velocity field (Figure 9.4), flow reversal occurs frequently in instantaneous snapshots. For all the tested cases, contours of the flow reversal probability ($p_s(x, y)$), defined as the percentage of negative streamwise velocity in one time series, are shown in Figure 9.7. In baseline condition, the peak value of p_s is 0.22, and the streamwise extent of the flow reversal region (reference contour line, $p_s = 0.03$) is roughly limited by the two extrapolated intersection points of incident and reflected shock waves, i.e. $(x_I, x_F) \approx (3.1\delta_{99}, 6.7\delta_{99})$. With plasma actuation at $F^* = 0.004$ and $F^* = 0.02$, a noticeable shrinkage of the separation region in streamwise direction is exhibited compared to baseline case, and the peak separation probability reduces to 19% and 16% respectively. In the case of $F^* = 0.04$, the peak separation probability is also decreased, whereas the streamwise and wall-normal extents of the separation region remains approximately the same as that in baseline case.

Integrating the separation probability within the entire domain, the total separation area can be computed, i.e. $A_s = \iint p_s(x, y) dx dy$ [172]. Variation of the dimensionless separation area (A_s/δ_{99}^2) with actuation frequency is shown in Figure 9.7 (b). A_s/δ_{99}^2 is on the order of 0.1. With increasing frequency, an initial decrease of the separation area is exhibited, followed by a slow increase. $F^* = 0.02$ proves to be the optimal actuation frequency, at which 14% reduction of the separation area is obtained. In Giepman et al.

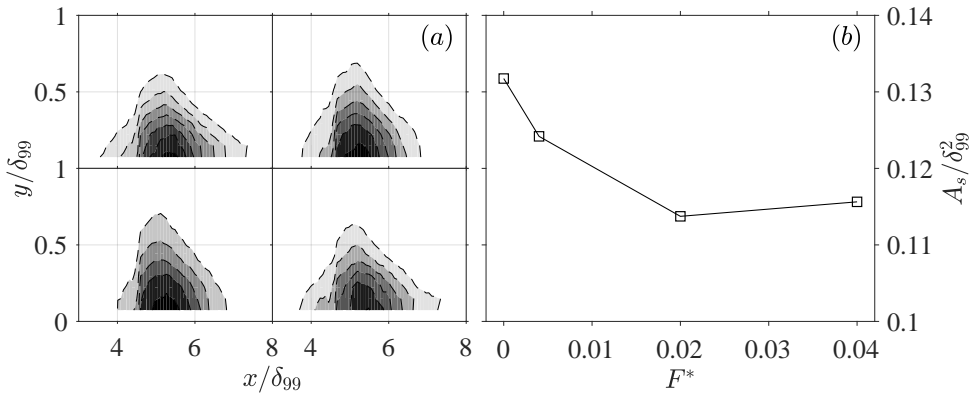


Figure 9.7: (a) Flow reversal probability (p_s). Contour line values of p_s increase inwards with a step of 0.03. From left to right and top to bottom: $F^* = 0$, $F^* = 0.004$, $F^* = 0.02$ and $F^* = 0.04$. (b) Variation of dimensionless separation area A_s/δ_{99}^2 with increasing frequency.

[172], micro-ramp vortex generators are used to control the SWBLI, and the reduction of separation area depends strongly on the actuation location and ramp size (i.e. vortex size). In the optimal case, the time-averaged separation area is reduced by 87%. To some extent, plasma synthetic jets can also be treated as vortex generators, nevertheless the life time of these vortices is rather short (jet duration time, approximately $200\mu\text{s}$ in this study, see Figure 9.3). In future steps, parametric studies including jet velocity, location, as well as duration should be performed to maximize the control authority of PSJAs.

9.5. CONCLUSIONS

In this chapter, an array of five plasma synthetic jets are used to control the flow separation induced by SWBLI at a nominal Mach number 2. Four cases with increasing discharge frequency ($F^* = 0, 0.004, 0.02, 0.04$) and constant discharge energy ($\epsilon = 7.7$) are tested, and the optimal discharge frequency for separation suppression is demonstrated to be $F^* = 0.02$. A transient bow shock is induced by the issuing jet, due to the flow stagnation upstream of the exit orifice. As the jets convect downstream to the interaction region, the shock foot executes an initial downstream movement followed by an upstream recovery. Compared to non-actuated case, the sonic line in time-averaged velocity field is shifted downstream by approximately $0.5\delta_{99}$ at $F^* = 0.02$, meanwhile the separation area derived from flow reversal probability is reduced by 14%. The control mechanisms of PSJs are supposed to be twofold. On the one hand, PSJs serve as virtual vortex generators, promoting the mixing within the turbulent boundary layer and yielding a fuller velocity profile that can withstand a higher adverse pressure gradient. On the other hand, the periodical disturbances created by PSJs are convected downstream to the interaction region and selectively amplified by the separated shear layer, resulting in higher TKE levels favouring earlier reattachment.

V

EPILOGUE

10

CONCLUSIONS AND OUTLOOK

10.1. PLASMA SYNTHETIC JETS IN QUIESCENT FLOW

THE effects of three crucial factors including non-dimensional energy deposition (ϵ), dimensionless discharge frequency (f^*) and orifice shape (slot versus circular) on the formation and evolution characteristics of plasma synthetic jets (PSJs) in quiescent air are examined in Part II, based on experimental observations and theoretical analysis. A high-speed jet, localized weak suction and a front vortex ring (FVR) are the three prominent features in the phase-averaged flow fields of the PSJ. With increasing ϵ , the peak jet velocity (U_p) increases monotonically, whereas the jet duration time extends moderately. A theoretical model developed in this thesis reveals that the expelled gas mass (M_e), impulse (I_p) and jet mechanical energy (E_m) are proportional to the jet duration time, cavity density and increasing powers of the peak jet velocity. When the total efficiency, jet duration time and cavity density remain approximately unchanged, U_p scales linearly with $\epsilon^{1/3}$. The velocity of the FVR initially shows a sharp increase and subsequently a moderate decay. The peak propagation velocity ($\approx 0.43U_p$) is reached at two diameters away from the exit orifice, regardless of discharge frequency and energy. The diameter of the FVR increases monotonically in one cycle and collapses well when plotted against the dimensionless propagation distance. The peak circulation of the ring remains $0.62U_p/D$ for different energy deposition levels.

As the discharge frequency increases, the jet duration time reduces, whilst the peak suction velocity goes up. The mean suction rate in one cycle becomes comparable to the mean ejection rate at $f^* \geq 0.739$. The three integral parameters (M_e , I_p , and E_m) also exhibit a decreasing trend with increasing frequency, nevertheless mainly related to the decreasing cavity density instead of the variation in jet duration time. Based on the energy equilibrium analysis of the cavity gas in one cycle, the mean cavity density is demonstrated to decline monotonically with the square root of discharge frequency. The declining rate is related to the convective heat transfer coefficient between the actuator shell and cavity gas, as well as the internal surface area of the actuator cavity. In the time-averaged flow field, the jet centreline velocity changes non-monotonically

with the axial coordinate (x -coordinate). The peak centreline velocity normalized by the product of discharge frequency and ejection length remains at around 1.5 for $f^* < 0.148$ (low-frequency) and drops slowly to 1.0 afterwards. Peak values of the centreline velocity are reached between $1 < x/D < 4$, and the post-peak decay rate increases with discharge frequency. The spreading rates of the PSJ, ranging from 0.09-0.14, are much higher than comparable steady jets nevertheless lower than conventional synthetic jets.

The shape of exit orifice directly determines the shape of issued vortex ring, as the vorticity is originated from the jet shear layer. In the case of slot orifice, the elongated vortex ring gradually opens up, and its two ends become severely warped during the propagation. The quasi-2D slot jet creates a thin shear layer in the flow field, which allows the periodical disturbance on the jet exit angle being amplified as a wavy jet. In the case of circular orifice ($D = 3$ mm), a distinct asymmetric flow field is presented, where the front vortex ring and the high speed jet lean in opposite directions during their propagation. Development of the asymmetric flow field is essentially an unstable process with positive feedback. Initial misalignment between the vortex ring and the jet, caused by the asymmetric electrode configuration, triggers the amplification of asymmetry. In pseudo time-averaged velocity fields, the entrainment rate of the surrounding low-energy fluids pertaining to slot jet is almost twice as that for the circular jet, thus resulting in a faster decay of penetration rate. With the deposited energy and exit area kept constant, orifice shapes have little influence on the variation of jet exit velocity.

10.2. PLASMA SYNTHETIC JETS IN CROSS FLOW

Compared to that in quiescent condition, the exit velocity variation of the actuator in crossflow remains approximately unchanged, whereas the jet induced flow fields show abundant new features. In the symmetry plane, the initially-issued erect jet body gradually bends to the crossflow and a time-dependent jet trajectory is exhibited. Comparison of the non-dimensional jet trajectories suggests that the penetration ability of PSJs is not as strong as steady jets. For the cases of different jet-to-crossflow velocity ratio, the vortex ring dynamics directly determine the jet penetration. At high velocity ratio, vortex rings are ensued by a high-speed trailing jet column and tilt downstream initially. After the pinch-off of jet column from the ring, the initial downstream titling is transformed into an upstream tilting driven by Kutta-Joukowski lift. In contrast, for low velocity ratio, vortex rings always tilt to upstream and the pitching angle increases monotonically during downstream convection. A maximum penetration is demonstrated when the mean pitching angle approximates zero.

Variations of the boundary layer shape factor and wall shear stresses can be traced back to the near-wall flow topologies. At high velocity ratio, shear-layer vortices and reverse flow are perceived in the windward and leeward side of the jet, respectively. The flow reversal region accommodates a hanging vortex pair which gradually evolves into a quasi-streamwise counter-rotating vortex pair (p -CVP) after jet terminates. Beside the two legs of the p -CVP, a downwash velocity is induced, resulting in a region with low shape factor. Conversely, high shape factor is observed in the symmetry plane, as the flow trapped between the p -CVP is of low-momentum fluids originated from the reverse flow. In cases of low velocity ratio, a similar spatial distribution of the boundary layer shape factor is observed. Nevertheless, the downwash effects are imposed by the two

longitudinal edges of the vortex rings, instead of the p -CVP. The time-averaged wall shear stress in the symmetry plane is always higher than the baseline undisturbed value and can be attributed to the removal of low-energy fluids during suction phases. As velocity ratio increases, the time-averaged wall shear stress also increases.

10.3. FLOW CONTROL

Two types of flows, namely the leading-edge flow separation over a NACA-0015 airfoil at 10 m/s ($Re_c = 1.7 \times 10^5$) and the incident shock wave/ boundary layer interaction at Mach number 2 ($Re_L = 4.4 \times 10^7$ [1/m]), are selected to validate the control authority of plasma synthetic jets. Both cases exhibited promising results.

In the former case, an array of 26 actuators are embedded at 8% chord away from the leading edge of the airfoil model. In the range of $0.5 \leq F^* \leq 2$, the stall angle is postponed from 15.5° to approximately 22° by plasma actuation, meanwhile the peak lift coefficient is increased by 21%. Hysteresis loops are completely eliminated in all the actuated cases, and the power saving ratio of PSJAs is comparable to that of SDBDAs in cylinder flow control by same definition. PSJAs exhibit distinctive separation control mechanisms depending on the relative location between actuation and separation, as well as the reduced frequency of actuation (F^*). At an angle of attack of $\alpha = 15.5^\circ$, the non-actuated flow separates approximately 4% chord length downstream of the jet orifices. Plasma synthetic jets (PSJs) applied at $F^* \geq 0.5$ can displace the separation point downstream to mid-chord position, as a result of energizing the incoming boundary layer through mixing enhancement. By contrast, with actuation frequency of $F^* \leq 0.25$, the separation point at $\alpha = 15.5^\circ$ remains near the leading edge and the zero-velocity line is periodically swept towards the suction surface by the convecting spanwise vortices generated from plasma actuation, leading to a reduction of time-averaged backflow area. For the case of separation control at $\alpha = 22^\circ$, the peak lift coefficient is attained at $F^* = 1$, and the decreasing lift at higher actuation frequency is ascribed to the severe interaction between adjacent spanwise vortices at short spacing (approximately $0.3c$).

In the latter case, five plasma synthetic jets are arranged in a row to control the downstream flow separation induced by SWBLI. Four cases with increasing discharge frequency ($F^* = 0, 0.004, 0.02, 0.04$) and constant discharge energy ($\epsilon = 7.7$) are tested, and the optimal discharge frequency for separation suppression is determined to be $F^* = 0.02$. A transient bow shock is induced by the issuing jet, due to the flow stagnation upstream of the exit orifice. As the jet convects downstream to the interaction region, the shock foot executes an initial downstream movement followed by an upstream recovery. Compared to baseline condition, the sonic line in time-averaged velocity field is shifted downstream by approximately $0.5\delta_{99}$ at $F^* = 0.02$, meanwhile the separation area derived from flow reversal probability is reduced by 14%. The control mechanisms of PSJs are supposed to be twofold. On the one hand, PSJs serve as virtual vortex generators, promoting the mixing within the turbulent boundary layer and yielding a fuller velocity profile that can withstand a higher adverse pressure gradient. On the other hand, the periodical disturbances created by PSJs are convected downstream to the interaction region and selectively amplified by the separated shear layer, resulting in higher TKE levels favouring earlier reattachment.

10.4. OUTLOOK

Since the proposal of the ‘sparkjet’ concept by Grossman et al. in 2003 [14], considerable efforts have been made to characterize the performance of PSJAs in quiescent condition. So far, the majority of the parameters that potentially affect the actuator performance have been identified and classified into three categories, i.e. electrical, geometrical and atmospheric. These parameters were combined as non-dimensional metrics (e.g. non-dimensional energy deposition, frequency, and heating volume) to generalize/collapse the trends observed at different operation conditions. Based on these generalized trends, it is already possible to ‘optimally’ (efficiency-oriented) design an actuator that meets certain performance criteria including frequency response, peak velocity, momentum flux et al., with minimum trial and error. These performance metrics are generally derived from the characteristics scales of the target flow, using Strouhal number, velocity ratio, momentum coefficient and so on. Notwithstanding how charming this design process could be, the unknown total efficiency ranging from 0.01% to 1% imposes considerable uncertainties while we are trying to project the jet intensity metrics back to the input electric parameters. As such, future parametric studies on the formation process of PSJs are recommended to give indications of the energy loss mechanisms inside the actuator cavities (e.g. gas ionization, heat conduction, radiation), in order to improve the prediction accuracy of total and sub- efficiencies. Particularly, a better understanding of the plasma heating mechanism for various gas discharges is necessitated, and an empirical model of the arc heating efficiency that can be applied to a wide range of operating conditions (i.e. discharge energy, discharge type, electrode size), is highly demanded.

Investigation of PSJs in crossflow provides insights and prerequisite knowledges for optimally selecting the actuation parameters in flow control practices (e.g. frequency, jet velocity, location, spacing). Based on the results in this thesis, the actuators are recommended to be placed within 2-5 exit diameters upstream of the separation point to avoid the high-wall shear stress damped out during downstream convection. The spanwise spacing of the actuator should be less than 10 exit orifice diameters to ‘seamlessly’ stitch the spanwise effect of adjacent jets. In future steps, a wide range of velocity and stroke ratios should be tested to establish a clear regime map of plasma synthetic jets in crossflow, analogous to those of pulsed jets and conventional synthetic jets reported in [137, 139]. In the regime map, distinct flow topologies as well as their relevance to flow control should be clearly marked, to instruct the determination of jet velocity and duration in different types of flow control. Additionally, the ratio of boundary layer thickness to orifice diameter should be included to appropriately scale up the actuators to cases with thick boundary layer.

Compared to the characterization studies of PSJAs, the application studies progress relatively slowly and only a few groups have been involved. Apart from the inherent difficulties of performing numerical simulations/measurements in high-Reynolds-number high-speed flow, the slow progress of application studies is also attributed to the complexity of designing a reliable discharge circuit that can feed multiple actuators at high repetition rate [52, 160, 161, 175], as well as the overwhelming EMI incurred by rapid arc discharges which frequently disrupts proper operation of the measurement equipments (PIV, hotwire, dynamic pressure transducers etc.) [15, 41, 94]. From the author’s experience, the EMI is mainly associated with the high-voltage trigger discharge and can be

suppressed effectively by limiting the peak trigger current to $O(\text{mA})$ and slowing down the rising/dropping edge to $O(10 \mu\text{s})$. In the future studies, these technical issues should be noticed, and detailed parametric studies shall be carried out to get the optimal actuation parameters and the control mechanisms at different target flows including SWBLI, shock buffet control, high-Reynolds number airfoil separation control and so on. Most importantly, it has to be evaluated whether the benefits returned by the modification of the target flow can sufficiently cover the penalties incurred by implementing the active flow control system. For drag reduction cases, a preferred evaluation parameter is the power saving ratio, which considers the relative weight between the power saved by drag reduction and the electrical power consumed to feed the actuators. Additionally, as the issued jet diminishes rapidly in one cycle, the flow control effect should always be checked from the time-averaged perspective when the actuators work repetitively.

REFERENCES

- [1] L. Prandtl, *Über flüssigkeitsbewegung bei sehr kleiner reibung*, Verhandl. III, Internat. Math.-Kong., Heidelberg, Teubner, Leipzig, 1904 , 484 (1904).
- [2] M. Gad-el Hak, *Flow control: The future*, Journal of Aircraft **38**, 402 (2001).
- [3] M. Gad-el Hak, *Flow control: passive, active, and reactive flow management* (Cambridge University Press, 2000).
- [4] L. N. Cattafesta III and M. Sheplak, *Actuators for active flow control*, Annual Review of Fluid Mechanics **43**, 247 (2011).
- [5] A. Seifert, D. Greenblatt, and I. J. Wygnanski, *Active separation control: an overview of reynolds and mach numbers effects*, Aerospace Science and Technology **8**, 569 (2004).
- [6] E. A. Whalen, A. Shmilovich, M. Spoor, J. Tran, P. Vijgen, J. C. Lin, and M. Andino, *Flight test of an afc enhanced vertical tail*, in *Proceedings of the 8th AIAA Flow Control Conference* (2016).
- [7] J. C. Lin, M. Y. Andino, M. G. Alexander, E. A. Whalen, M. A. Spoor, J. T. Tran, and I. J. Wygnanski, *An overview of active flow control enhanced vertical tail technology development*, in *54th AIAA Aerospace Sciences Meeting* (2016) p. 0056.
- [8] A. Glezer and M. Amitay, *Synthetic jets*, Annual Review of Fluid Mechanics **34**, 503 (2002).
- [9] L. Wang, Z. Luo, Z. Xia, B. Liu, and X. Deng, *Review of actuators for high speed active flow control*, Science China Technological Sciences **55**, 2225 (2012).
- [10] B. L. Smith and A. Glezer, *The formation and evolution of synthetic jets*, Physics of Fluids **10**, 2281 (1998).
- [11] T. M. Crittenden and A. Glezer, *A high-speed, compressible synthetic jet*, Physics of Fluids **18**, 017107 (2006).
- [12] T. Van Buren, C. M. Leong, E. Whalen, and M. Amitay, *Impact of orifice orientation on a finite-span synthetic jet interaction with a crossflow*, Physics of Fluids **28**, 037106 (2016).
- [13] T. Crittenden, A. Glezer, R. Funk, and D. Parekh, *Combustion-driven jet actuators for flow control*, in *15th AIAA Computational Fluid Dynamics Conference* (2001) p. 2768.

- [14] K. Grossman, C. Bohdan, and D. VanWie, *Sparkjet actuators for flow control*, in *41st Aerospace Sciences Meeting and Exhibit* (2003) p. 57.
- [15] V. Narayanaswamy, L. L. Raja, and N. T. Clemens, *Characterization of a high-frequency pulsed-plasma jet actuator for supersonic flow control*, *AIAA Journal* **48**, 297 (2010).
- [16] H. Zong, Y. Wu, Y. Li, H. Song, Z. Zhang, and M. Jia, *Analytic model and frequency characteristics of plasma synthetic jet actuator*, *Physics of Fluids* **27**, 027105 (2015).
- [17] B. Cybyk, K. Grossman, and D. Van Wie, *Computational assessment of the sparkjet flow control actuator*, in *33rd AIAA fluid dynamics conference and exhibit* (2003) p. 3711.
- [18] S. Haack, T. Taylor, B. Cybyk, C. Foster, and F. Alvi, *Experimental estimation of sparkjet efficiency*, in *42nd AIAA Plasmadynamics and Lasers Conference in Conjunction with the 18th International Conference on MHD Energy Conversion (ICMHD)* (2011) p. 3997.
- [19] S. H. Popkin, T. M. Taylor, and B. Z. Cybyk, *Development and application of the sparkjet actuator for high-speed flow control*, *Johns Hopkins APL technical digest* **32**, 404 (2013).
- [20] T. M. Reedy, N. V. Kale, J. C. Dutton, and G. S. Elliott, *Experimental characterization of a pulsed plasma jet*, *AIAA Journal* **51**, 2027 (2013).
- [21] P. Hardy, P. Barricau, D. Caruana, C. Gleyzes, A. Belinger, and J. P. Cambronne, *Plasma synthetic jet for flow control*, in *40th Fluid Dynamics Conference and Exhibit* (2010) p. 5103.
- [22] L. Wang, Z.-x. Xia, Z.-b. Luo, and J. Chen, *Three-electrode plasma synthetic jet actuator for high-speed flow control*, *AIAA Journal* **52**, 879 (2013).
- [23] H. Zong, Y. Wu, M. Jia, H. Song, H. Liang, Y. Li, and Z. Zhang, *Influence of geometrical parameters on performance of plasma synthetic jet actuator*, *Journal of Physics D: Applied Physics* **49**, 025504 (2015).
- [24] L. Wang, Z. Xia, Z. Luo, and Y. Zhang, *Effect of pressure on the performance of plasma synthetic jet actuator*, *Science China Physics, Mechanics & Astronomy* **57**, 2309 (2014).
- [25] A. Belinger, P. Hardy, P. Barricau, J. Cambronne, and D. Caruana, *Influence of the energy dissipation rate in the discharge of a plasma synthetic jet actuator*, *Journal of Physics D: Applied Physics* **44**, 365201 (2011).
- [26] A. Schutze, J. Y. Jeong, S. E. Babayan, J. Park, G. S. Selwyn, and R. F. Hicks, *The atmospheric-pressure plasma jet: a review and comparison to other plasma sources*, *IEEE Transactions on Plasma Science* **26**, 1685 (1998).

- [27] J.-J. Wang, K.-S. Choi, L.-H. Feng, T. N. Jukes, and R. D. Whalley, *Recent developments in dbd plasma flow control*, Progress in Aerospace Sciences **62**, 52 (2013).
- [28] A. Santhanakrishnan and J. D. Jacob, *Flow control with plasma synthetic jet actuators*, Journal of Physics D: Applied Physics **40**, 637 (2007).
- [29] B. Cybyk, K. Grossman, and J. Wilkerson, *Performance characteristics of the spark-jet flow control actuator*, in *2nd AIAA Flow Control Conference* (2004) p. 2131.
- [30] T. Emerick, M. Ali, C. Foster, F. Alvi, S. Haack Popkin, and B. Cybyk, *Sparkjet actuator characterization in supersonic crossflow*, in *6th AIAA Flow Control Conference* (2012) p. 2814.
- [31] D. Jin, Y. Li, M. Jia, H. Song, W. Cui, Q. Sun, and F. Li, *Experimental characterization of the plasma synthetic jet actuator*, Plasma Science and Technology **15**, 1034 (2013).
- [32] H. Zong, W. Cui, Y. Wu, Z. Zhang, H. Liang, M. Jia, and Y. Li, *Influence of capacitor energy on performance of a three-electrode plasma synthetic jet actuator*, Sensors and Actuators A: Physical **222**, 114 (2015).
- [33] M. Golbabaei-Asl, D. Knight, and S. Wilkinson, *Novel technique to determine sparkjet efficiency*, AIAA Journal **53**, 501 (2014).
- [34] H. Zong, Y. Wu, H. Song, and M. Jia, *Efficiency characteristic of plasma synthetic jet actuator driven by pulsed direct-current discharge*, AIAA Journal, 3409 (2016).
- [35] Y. Zhu, Y. Wu, M. Jia, H. Liang, J. Li, and Y. Li, *Influence of positive slopes on ultrafast heating in an atmospheric nanosecond-pulsed plasma synthetic jet*, Plasma Sources Science and Technology **24**, 015007 (2014).
- [36] V. Narayanaswamy, J. Shin, N. Clemens, and L. Raja, *Investigation of plasma-generated jets for supersonic flow control*, in *46th AIAA Aerospace Sciences Meeting and Exhibit* (2008) p. 285.
- [37] L. Wang, Z.-B. Luo, Z.-X. Xia, and B. Liu, *Energy efficiency and performance characteristics of plasma synthetic jet*, Acta Physica Sinica **62**, 125207 (2013).
- [38] J. Shin, *Characteristics of high speed electro-thermal jet activated by pulsed dc discharge*, Chinese Journal of Aeronautics **23**, 518 (2010).
- [39] H. Zong and M. Kotsonis, *Formation, evolution and scaling of plasma synthetic jets*, Journal of Fluid Mechanics **837**, 147 (2018).
- [40] H. Zong, Y. Wu, H. Song, M. Jia, H. Liang, Y. Li, and Z.-b. Zhang, *Investigation of the performance characteristics of a plasma synthetic jet actuator based on a quantitative schlieren method*, Measurement Science and Technology **27**, 055301 (2016).
- [41] B. Cybyk, H. Land, D. Simon, J. Chen, and J. Katz, *Experimental characterization of a supersonic flow control actuator*, in *44th AIAA Aerospace Sciences Meeting and Exhibit* (2006) p. 478.

- [42] S. Haack, T. Taylor, J. Emhoff, and B. Cybyk, *Development of an analytical sparkjet model*, in *5th Flow Control Conference* (2010) p. 4979.
- [43] A. Belinger, N. Naudé, J. Cambronne, and D. Caruana, *Plasma synthetic jet actuator: electrical and optical analysis of the discharge*, *Journal of Physics D: Applied Physics* **47**, 345202 (2014).
- [44] M. Tang, Y. Wu, H. Wang, D. Jin, S. Guo, and T. Gan, *Effects of capacitance on a plasma synthetic jet actuator with a conical cavity*, *Sensors and Actuators A: Physical* (2018).
- [45] D. Jin, W. Cui, Y. Li, F. Li, M. Jia, Q. Sun, and B. Zhang, *Characteristics of pulsed plasma synthetic jet and its control effect on supersonic flow*, *Chinese Journal of Aeronautics* **28**, 66 (2015).
- [46] M. Chiatto and L. de Luca, *Numerical and experimental frequency response of plasma synthetic jet actuators*, in *55th AIAA Aerospace Sciences Meeting* (2017) p. 1884.
- [47] K. Grossman, B. Cybyk, D. VanWie, and M. Rigling, *Characterization of sparkjet actuators for flow control*, in *42nd AIAA Aerospace Sciences Meeting and Exhibit* (2004) p. 89.
- [48] L. Wang, Z. Xia, Z. Luo, Y. Zhou, and Y. Zhang, *Experimental study on the characteristics of a two-electrode plasma synthetic jet actuator*, *Acta Physica Sinica* **63**, 194702 (2014).
- [49] S. H. Popkin, B. Z. Cybyk, C. H. Foster, and F. S. Alvi, *Experimental estimation of sparkjet efficiency*, *AIAA Journal*, 1831 (2016).
- [50] T. Emerick, M. Ali, C. Foster, F. Alvi, and S. Popkin, *Sparkjet characterizations in quiescent and supersonic flowfields*, *Experiments in Fluids* **55**, 1858 (2014).
- [51] Z. Zhang, Y. Wu, M. Jia, H. Zong, W. Cui, H. Liang, and Y. Li, *Influence of the discharge location on the performance of a three-electrode plasma synthetic jet actuator*, *Sensors and Actuators A: Physical* **235**, 71 (2015).
- [52] Z. Zhang, Y. Wu, M. Jia, H. Song, Z. Sun, H. Zong, and Y. Li, *The multichannel discharge plasma synthetic jet actuator*, *Sensors and Actuators A: Physical* **253**, 112 (2017).
- [53] Y. Li, M. Jia, Y. Wu, Y.-h. Li, H.-h. Zong, H.-m. Song, and H. Liang, *Influence of air pressure on the performance of plasma synthetic jet actuator*, *Chinese Physics B* **25**, 095205 (2016).
- [54] K. V. Anderson and D. D. Knight, *Plasma jet for flight control*, *AIAA Journal* **50**, 1855 (2012).
- [55] G. Sary, G. Dufour, F. Rogier, and K. Kourtzanidis, *Modeling and parametric study of a plasma synthetic jet for flow control*, *AIAA journal* **52**, 1591 (2014).

- [56] M. Chiatto, A. Palumbo, and L. de Luca, *A calibrated lumped element model for the prediction of psj actuator efficiency performance*, in *Actuators*, Vol. 7 (Multidisciplinary Digital Publishing Institute, 2018) p. 10.
- [57] H. Zong, *Influence of nondimensional heating volume on efficiency of plasma synthetic jet actuators*, *AIAA Journal*, 1 (2017).
- [58] G. Dufour, P. Hardy, G. Quint, and F. Rogier, *Physics and models for plasma synthetic jets*, *International Journal of Aerodynamics* **3**, 47 (2013).
- [59] T. N. Jukes and K.-S. Choi, *Long lasting modifications to vortex shedding using a short plasma excitation*, *Physical Review Letters* **102**, 254501 (2009).
- [60] Z. Zhang, Y. Wu, M. Jia, H. Song, Z. Sun, and Y. Li, *Mhd-rlc discharge model and the efficiency characteristics of plasma synthetic jet actuator*, *Sensors and Actuators A: Physical* **261**, 75 (2017).
- [61] H. Ko, S. Haack, H. Land, B. Cybyk, J. Katz, and H. Kim, *Analysis of flow distribution from high-speed flow actuator using particle image velocimetry and digital speckle tomography*, *Flow Measurement and Instrumentation* **21**, 443 (2010).
- [62] D. Caruana, F. Rogier, G. Dufour, and C. Gleyzes, *The plasma synthetic jet actuator, physics, modeling and flow control application on separation*, *AerospaceLab*, p (2013).
- [63] V. Narayanaswamy, L. L. Raja, and N. T. Clemens, *Control of a shock/boundary-layer interaction by using a pulsed-plasma jet actuator*, *AIAA Journal* **50**, 246 (2012).
- [64] O. Léon, D. Caruana, and T. Castelain, *Increase and decrease of the noise radiated by high-reynolds-number subsonic jets through plasma synthetic jet actuation*, in *Acoustic Climate Inside and Outside Buildings* (2014).
- [65] V. Narayanaswamy, L. L. Raja, and N. T. Clemens, *Control of unsteadiness of a shock wave/turbulent boundary layer interaction by using a pulsed-plasma-jet actuator*, *Physics of Fluids* **24**, 076101 (2012).
- [66] R. Liu, Z. Niu, M. Wang, M. Hao, and Q. Lin, *Aerodynamic control of naca 0021 airfoil model with spark discharge plasma synthetic jets*, *Science China Technological Sciences* **58**, 1949 (2015).
- [67] M. Arena, M. Chiatto, F. Amoroso, R. Pecora, and L. de Luca, *Feasibility studies for the installation of plasma synthetic jet actuators on the skin of a morphing wing flap*, in *Active and Passive Smart Structures and Integrated Systems XII*, Vol. 10595 (International Society for Optics and Photonics, 2018) p. 105950M.
- [68] F. Chedeveigne, O. Léon, V. Bodoc, and D. Caruana, *Experimental and numerical response of a high-reynolds-number $m=0.6$ jet to a plasma synthetic jet actuator*, *International Journal of Heat and Fluid Flow* **56**, 1 (2015).

- [69] V. Narayanaswamy, *Investigation of a pulsed-plasma jet for separation shock/boundary layer interaction control*, Ph.D. thesis (2010).
- [70] B. Greene, N. Clemens, P. Magari, and D. Micka, *Control of mean separation in shock boundary layer interaction using pulsed plasma jets*, *Shock Waves* **25**, 495 (2015).
- [71] D. Jin, M. Jia, H. Song, Y. Wu, and F. Li, *Control effect of arc-driven plasma synthetic jet on supersonic shockwave*, in *21st AIAA International Space Planes and Hypersonics Technologies Conference* (2017) p. 2228.
- [72] H. Wang, J. Li, D. Jin, H. Dai, T. Gan, and Y. Wu, *Effect of a transverse plasma jet on a shock wave induced by a ramp*, *Chinese Journal of Aeronautics* **30**, 1854 (2017).
- [73] H. Wang, J. Li, D. Jin, Z. Zhang, M. Tang, and Y. Wu, *Manipulation of ramp-induced shock wave/boundary layer interaction using a transverse plasma jet array*, *International Journal of Heat and Fluid Flow* **67**, 133 (2017).
- [74] H. Wang, J. Li, D. Jin, M. Tang, Y. Wu, and L. Xiao, *High-frequency counter-flow plasma synthetic jet actuator and its application in suppression of supersonic flow separation*, *Acta Astronautica* **142**, 45 (2018).
- [75] Y. Zhou, Z. Xia, Z. Luo, and L. Wang, *Effect of three-electrode plasma synthetic jet actuator on shock wave control*, *Science China Technological Sciences* **60**, 146 (2017).
- [76] K. Mahesh, *The interaction of jets with crossflow*, *Annual Review of Fluid Mechanics* **45**, 379 (2013).
- [77] H. Babinsky and J. K. Harvey, *Shock wave-boundary-layer interactions*, Vol. 32 (Cambridge University Press, 2011).
- [78] G. Yang, Y. Yao, J. Fang, T. Gan, and L. Lu, *Large-eddy simulation of shock-induced flow separation control using sparkjet concept*, in *54th AIAA Aerospace Sciences Meeting* (2016) p. 0045.
- [79] G. S. Settles, *Schlieren and shadowgraph techniques: visualizing phenomena in transparent media* (Springer Science & Business Media, 2012).
- [80] C. G. Lomas, *Fundamentals of hot wire anemometry* (Cambridge University Press, 2011).
- [81] M. Raffel, C. E. Willert, F. Scarano, C. J. Kähler, S. T. Wereley, and J. Kompenhans, *Particle image velocimetry: a practical guide* (Springer, 2018).
- [82] H. Zong and M. Kotsonis, *Characterisation of plasma synthetic jet actuators in quiescent flow*, *Journal of Physics D: Applied Physics* **49**, 335202 (2016).
- [83] R. J. Adrian and C.-S. Yao, *Pulsed laser technique application to liquid and gaseous flows and the scattering power of seed materials*, *Applied optics* **24**, 44 (1985).

- [84] F. Scarano, S. Ghaemi, G. C. A. Caridi, J. Bosbach, U. Dierksheide, and A. Sciacchitano, *On the use of helium-filled soap bubbles for large-scale tomographic piv in wind tunnel experiments*, *Experiments in Fluids* **56**, 42 (2015).
- [85] H. Zong and M. Kotsonis, *Electro-mechanical efficiency of plasma synthetic jet actuator driven by capacitive discharge*, *Journal of Physics D: Applied Physics* **49**, 455201 (2016).
- [86] A. Sciacchitano and B. Wieneke, *Piv uncertainty propagation*, *Measurement Science and Technology* **27**, 084006 (2016).
- [87] H. Huang, D. Dabiri, and M. Gharib, *On errors of digital particle image velocimetry*, *Measurement Science and Technology* **8**, 1427 (1997).
- [88] J. Chen and J. Katz, *Elimination of peak-locking error in piv analysis using the correlation mapping method*, *Measurement Science and Technology* **16**, 1605 (2005).
- [89] F. Scarano, *Theory of non-isotropic spatial resolution in piv*, *Experiments in Fluids* **35**, 268 (2003).
- [90] F. Scarano, *Iterative image deformation methods in piv*, *Measurement Science and Technology* **13**, R1 (2001).
- [91] F. Laurendeau, O. Léon, F. Chedevergne, J.-M. Senoner, and G. Casalis, *Particle image velocimetry experiment analysis using large-eddy simulation: application to plasma actuators*, *AIAA Journal* **55**, 3767 (2017).
- [92] D. Ragni, F. Schrijer, B. Van Oudheusden, and F. Scarano, *Particle tracer response across shocks measured by piv*, *Experiments in Fluids* **50**, 53 (2011).
- [93] W. Reynolds and A. Hussain, *The mechanics of an organized wave in turbulent shear flow. part 3. theoretical models and comparisons with experiments*, *Journal of Fluid Mechanics* **54**, 263 (1972).
- [94] V. Narayanaswamy, N. T. Clemens, and L. L. Raja, *Method for acquiring pressure measurements in presence of plasma-induced interference for supersonic flow control applications*, *Measurement Science and Technology* **22**, 125107 (2011).
- [95] L. de Luca, M. Girfoglio, and G. Coppola, *Modeling and experimental validation of the frequency response of synthetic jet actuators*, *AIAA Journal* **52**, 1733 (2014).
- [96] R. Holman, Y. Utturkar, R. Mittal, B. L. Smith, and L. Cattafesta, *Formation criterion for synthetic jets*, *AIAA journal* **43**, 2110 (2005).
- [97] J. M. Shuster and D. R. Smith, *Experimental study of the formation and scaling of a round synthetic jet*, *Physics of Fluids* **19**, 045109 (2007).
- [98] B. J. Cantwell, *Viscous starting jets*, *Journal of Fluid Mechanics* **173**, 159 (1986).
- [99] F. Laurendeau, F. Chedevergne, and G. Casalis, *Transient ejection phase modeling of a plasma synthetic jet actuator*, *Physics of Fluids* **26**, 125101 (2014).

- [100] M. Gharib, E. Rambod, and K. Shariff, *A universal time scale for vortex ring formation*, *Journal of Fluid Mechanics* **360**, 121 (1998).
- [101] H. Zong and M. Kotsonis, *Effect of slotted exit orifice on performance of plasma synthetic jet actuator*, *Experiments in Fluids* **58**, 17 (2017).
- [102] J.-Z. Wu, H.-Y. Ma, and M.-D. Zhou, *Vorticity and vortex dynamics* (Springer Science & Business Media, 2007).
- [103] H. Zong and M. Kotsonis, *Interaction between plasma synthetic jet and subsonic turbulent boundary layer*, *Physics of Fluids* **29**, 045104 (2017).
- [104] Y. K. Chang and A. Vakili, *Dynamics of vortex rings in crossflow*, *Physics of Fluids* **7**, 1583 (1995).
- [105] H. J. Hussein, S. P. Capp, and W. K. George, *Velocity measurements in a high-reynolds-number, momentum-conserving, axisymmetric, turbulent jet*, *Journal of Fluid Mechanics* **258**, 31 (1994).
- [106] J. E. Cater and J. Soria, *The evolution of round zero-net-mass-flux jets*, *Journal of Fluid Mechanics* **472**, 167 (2002).
- [107] M. Rekalić and V. Vukanović, *Temperature distribution in a dc free burning arc in nitrogen with and without addition of li 2 co 3*, *Applied Spectroscopy* **28**, 244 (1974).
- [108] N. S. J. Braithwaite, *Introduction to gas discharges*, *Plasma Sources Science and Technology* **9**, 517 (2000).
- [109] S. Pope, *Turbulent flows*, (2000).
- [110] B. Morton, G. I. Taylor, and J. S. Turner, *Turbulent gravitational convection from maintained and instantaneous sources*, *Proc. R. Soc. Lond. A* **234**, 1 (1956).
- [111] H. Johari and R. Paduano, *Dilution and mixing in an unsteady jet*, *Experiments in Fluids* **23**, 272 (1997).
- [112] W. E. Eagle, M. P. Musculus, L.-M. Malbec, and G. Bruneaux, *Measuring transient entrainment rates of a confined vaporizing diesel jet.*, Tech. Rep. (Sandia National Laboratories (SNL-CA), Livermore, CA (United States), 2014).
- [113] M. Q. Brewster, *Thermal radiative transfer and properties* (John Wiley & Sons, 1992).
- [114] A. Hashiehbaf and G. Romano, *Particle image velocimetry investigation on mixing enhancement of non-circular sharp edge nozzles*, *International Journal of Heat and Fluid Flow* **44**, 208 (2013).
- [115] E. Gutmark and F. Grinstein, *Flow control with noncircular jets*, *Annual Review of Fluid Mechanics* **31**, 239 (1999).

- [116] M. Dhanak and B. D. Bernardinis, *The evolution of an elliptic vortex ring*, Journal of Fluid Mechanics **109**, 189 (1981).
- [117] M. Golbabaei-Asl, D. Knight, K. Anderson, and S. Wilkinson, *Sparkjet efficiency*, in *51st AIAA aerospace sciences meeting including the new horizons forum and aerospace exposition* (2013) p. 928.
- [118] A. Krothapalli, D. Baganoff, and K. Karamcheti, *On the mixing of a rectangular jet*, Journal of Fluid Mechanics **107**, 201 (1981).
- [119] F. F. Grinstein, *Self-induced vortex ring dynamics in subsonic rectangular jets*, Physics of Fluids **7**, 2519 (1995).
- [120] B. Lee, *Some measurements of spatial instability waves in a round jet*, AIAA Journal **14**, 348 (1976).
- [121] T. Van Buren, M. Beyar, C. M. Leong, and M. Amitay, *Three-dimensional interaction of a finite-span synthetic jet in a crossflow*, Physics of Fluids **28**, 037105 (2016).
- [122] H. Schlichting and K. Gersten, *Boundary-layer theory* (Springer, 2016).
- [123] M. Bernardini, S. Pirozzoli, and P. Orlandi, *Velocity statistics in turbulent channel flow up to $re_\tau = 4000$* , Journal of Fluid Mechanics **742**, 171 (2014).
- [124] S. Krajnovic and L. Davidson, *Large-eddy simulation of the flow around a bluff body*, AIAA Journal **40**, 927 (2002).
- [125] K. E. Meyer, J. M. Pedersen, and O. Özcan, *A turbulent jet in crossflow analysed with proper orthogonal decomposition*, Journal of Fluid Mechanics **583**, 199 (2007).
- [126] E. J. Gutmark, I. M. Ibrahim, and S. Murugappan, *Dynamics of single and twin circular jets in cross flow*, Experiments in Fluids **50**, 653 (2011).
- [127] X. Wen and H. Tang, *On hairpin vortices induced by circular synthetic jets in laminar and turbulent boundary layers*, Computers & Fluids **95**, 1 (2014).
- [128] L. L. Yuan and R. L. Street, *Trajectory and entrainment of a round jet in crossflow*, Physics of Fluids **10**, 2323 (1998).
- [129] S. Smith and M. Mungal, *Mixing, structure and scaling of the jet in crossflow*, Journal of Fluid Mechanics **357**, 83 (1998).
- [130] R. J. Margason, *Fifty years of jet in cross flow research*, in *In AGARD, Computational and Experimental Assessment of Jets in Cross Flow 41 p (SEE N94-28003 07-34)* (1993).
- [131] Y. M. Marzouk and A. F. Ghoniem, *Vorticity structure and evolution in a transverse jet*, Journal of Fluid Mechanics **575**, 267 (2007).
- [132] L. L. Yuan, R. L. Street, and J. H. Ferziger, *Large-eddy simulations of a round jet in crossflow*, Journal of Fluid Mechanics **379**, 71 (1999).

- [133] R. M. Kelso, T. Lim, and A. Perry, *An experimental study of round jets in cross-flow*, Journal of Fluid Mechanics **306**, 111 (1996).
- [134] J. P. Johnston and M. Nishi, *Vortex generator jets-means for flow separation control*, AIAA Journal **28**, 989 (1990).
- [135] D. R. Smith, *Interaction of a synthetic jet with a crossflow boundary layer*, AIAA Journal **40**, 2277 (2002).
- [136] R. Sau and K. Mahesh, *Passive scalar mixing in vortex rings*, Journal of Fluid Mechanics **582**, 449 (2007).
- [137] R. Sau and K. Mahesh, *Dynamics and mixing of vortex rings in crossflow*, Journal of Fluid Mechanics **604**, 389 (2008).
- [138] M. Jabbal and S. Zhong, *Flow measurement of synthetic jets in a boundary layer*, in *37th AIAA Fluid Dynamics Conference and Exhibit* (2007) p. 3852.
- [139] M. Jabbal and S. Zhong, *The near wall effect of synthetic jets in a boundary layer*, International Journal of Heat and Fluid Flow **29**, 119 (2008).
- [140] M. Jabbal and S. Zhong, *Particle image velocimetry measurements of the interaction of synthetic jets with a zero-pressure gradient laminar boundary layer*, Physics of Fluids **22**, 063603 (2010).
- [141] K. Christensen, *The influence of peak-locking errors on turbulence statistics computed from piv ensembles*, Experiments in Fluids **36**, 484 (2004).
- [142] J. Dandois, E. Garnier, and P. Sagaut, *Numerical simulation of active separation control by a synthetic jet*, Journal of Fluid Mechanics **574**, 25 (2007).
- [143] X. Wu, P. Moin, J. M. Wallace, J. Skarda, A. Lozano-Durán, and J.-P. Hickey, *Transitional-turbulent spots and turbulent-turbulent spots in boundary layers*, Proceedings of the National Academy of Sciences, 201704671 (2017).
- [144] H. Zong and M. Kotsonis, *Experimental investigation on frequency characteristics of plasma synthetic jets*, Physics of Fluids **29**, 115107 (2017).
- [145] Q. Gallas, R. Holman, T. Nishida, B. Carroll, M. Sheplak, and L. Cattafesta, *Lumped element modeling of piezoelectric-driven synthetic jet actuators*, AIAA Journal **41**, 240 (2003).
- [146] S. Muppidi and K. Mahesh, *Study of trajectories of jets in crossflow using direct numerical simulations*, Journal of Fluid Mechanics **530**, 81 (2005).
- [147] P. Chakraborty, S. Balachandar, and R. J. Adrian, *On the relationships between local vortex identification schemes*, Journal of Fluid Mechanics **535**, 189 (2005).
- [148] R. M'closkey, J. King, L. Cortelezzi, and A. Karagozian, *The actively controlled jet in crossflow*, Journal of Fluid Mechanics **452**, 325 (2002).

- [149] J. Zhou and S. Zhong, *Numerical simulation of the interaction of a circular synthetic jet with a boundary layer*, *Computers & Fluids* **38**, 393 (2009).
- [150] *The spectrum of turbulence* (JSTOR, 1938).
- [151] S. Lardeau and M. Leschziner, *The interaction of round synthetic jets with a turbulent boundary layer separating from a rounded ramp*, *Journal of Fluid Mechanics* **683**, 172 (2011).
- [152] M. Samimy, J.-H. Kim, J. Kastner, I. Adamovich, and Y. Utkin, *Active control of high-speed and high-reynolds-number jets using plasma actuators*, *Journal of Fluid Mechanics* **578**, 305 (2007).
- [153] R. Sau and K. Mahesh, *Optimization of pulsed jets in crossflow*, *Journal of Fluid Mechanics* **653**, 365 (2010).
- [154] R. L. Simpson, *Turbulent boundary-layer separation*, *Annual Review of Fluid Mechanics* **21**, 205 (1989).
- [155] M. Gad-el Hak, A. Pollard, and J.-P. Bonnet, *Flow control: fundamentals and practices*, Vol. 53 (Springer Science & Business Media, 2003).
- [156] H. Choi, W.-P. Jeon, and J. Kim, *Control of flow over a bluff body*, *Annual Review of Fluid Mechanics* **40**, 113 (2008).
- [157] W. Timmer, *Two-dimensional low-reynolds number wind tunnel results for airfoil naca 0018*, *Wind Engineering* **32**, 525 (2008).
- [158] M. Amitay, D. R. Smith, V. Kibens, D. E. Parekh, and A. Glezer, *Aerodynamic flow control over an unconventional airfoil using synthetic jet actuators*, *AIAA Journal* **39**, 361 (2001).
- [159] D. Postl, W. Balzer, and H. Fasel, *Control of laminar separation using pulsed vortex generator jets: direct numerical simulations*, *Journal of Fluid Mechanics* **676**, 81 (2011).
- [160] H. Zong and M. Kotsonis, *Realisation of plasma synthetic jet array with a novel sequential discharge*, *Sensors and Actuators A: Physical* **266**, 314 (2017).
- [161] Z. Zhang, Y. Wu, M. Jia, H. Song, Z. Sun, and Y. Li, *Modeling and optimization of the multichannel spark discharge*, *Chinese Physics B* **26**, 065204 (2017).
- [162] P. Smy, R. Clements, J. Dale, D. Simeoni, and D. Topham, *Efficiency and erosion characteristics of plasma jet igniters*, *Journal of Physics D: Applied Physics* **16**, 783 (1983).
- [163] E. Maskell, *A theory of the blockage effects on bluff bodies and stalled wings in a closed wind tunnel*, Tech. Rep. (Aeronautical Research Council London (United Kingdom), 1963).

- [164] S. Yarusevych, P. E. Sullivan, and J. G. Kawall, *On vortex shedding from an airfoil in low-reynolds-number flows*, *Journal of Fluid Mechanics* **632**, 245 (2009).
- [165] N. Benard and E. Moreau, *Electrical and mechanical characteristics of surface ac dielectric barrier discharge plasma actuators applied to airflow control*, *Experiments in Fluids* **55**, 1846 (2014).
- [166] M. L. Post and T. C. Corke, *Separation control on high angle of attack airfoil using plasma actuators*, *AIAA Journal* **42** (2004).
- [167] T. C. Corke and F. O. Thomas, *Dynamic stall in pitching airfoils: aerodynamic damping and compressibility effects*, *Annual Review of Fluid Mechanics* **47**, 479 (2015).
- [168] R. Giepmans and M. Kotsonis, *On the mechanical efficiency of dielectric barrier discharge plasma actuators*, *Applied Physics Letters* **98**, 221504 (2011).
- [169] T. Michelis, S. Yarusevych, and M. Kotsonis, *Response of a laminar separation bubble to impulsive forcing*, *Journal of Fluid Mechanics* **820**, 633 (2017).
- [170] J. Little, K. Takashima, M. Nishihara, I. Adamovich, and M. Samimy, *Separation control with nanosecond-pulse-driven dielectric barrier discharge plasma actuators*, *AIAA Journal* **50**, 350 (2012).
- [171] H. Babinsky, Y. Li, and C. Pitt Ford, *Microramp control of supersonic oblique shock-wave/boundary-layer interactions*, *AIAA Journal* **47**, 668 (2009).
- [172] R. Giepmans, F. Schrijer, and B. van Oudheusden, *Flow control of an oblique shock wave reflection with micro-ramp vortex generators: effects of location and size*, *Physics of Fluids* **26**, 066101 (2014).
- [173] N. T. Clemens and V. Narayanaswamy, *Low-frequency unsteadiness of shock wave/turbulent boundary layer interactions*, *Annual Review of Fluid Mechanics* **46**, 469 (2014).
- [174] B. Van Oudheusden, A. Jöbbsis, F. Scarano, and L. Souverein, *Investigation of the unsteadiness of a shock-reflection interaction with time-resolved particle image velocimetry*, *Shock Waves* **21**, 397 (2011).
- [175] C. Zhang, L. Han, J. Qiu, T. Shao, Z. Luo, and L. Wang, *A pulsed generator for synchronous discharges of high-energy plasma synthetic jet actuators*, *IEEE Transactions on Dielectrics and Electrical Insulation* **24**, 2076 (2017).
- [176] B. Cybyk, K. Grossman, J. Wilkerson, J. Chen, and J. Katz, *Single-pulse performance of the sparkjet flow control actuator*, in *43rd AIAA Aerospace Sciences Meeting and Exhibit* (2005) p. 401.
- [177] B. Cybyk, J. Wilkerson, and D. Simon, *Enabling high-fidelity modeling of a high-speed flow control actuator array*, in *14th AIAA/AHI Space Planes and Hypersonic Systems and Technologies Conference* (2006) p. 8034.

- [178] S. Haack Popkin, B. Cybyk, B. Land, C. Foster, T. Emerick, and F. Alvi, *Recent performance-based advances in sparkjet actuator design for supersonic flow applications*, in *51st AIAA Aerospace Sciences Meeting including the New Horizons Forum and Aerospace Exposition* (2013) p. 322.
- [179] T. Taylor and B. Cybyk, *High-fidelity modeling of micro-scale flow-control devices with applications to the macro-scale environment*, in *15th AIAA International Space Planes and Hypersonic Systems and Technologies Conference* (2008) p. 2608.
- [180] S. H. Popkin, *One-dimensional analytical model development of a plasma-based actuator*, Ph.D. thesis, University of Maryland, College Park (2014).
- [181] Y. Zhou, Z. Xia, Z. Luo, L. Wang, and X. Deng, *A novel ram-air plasma synthetic jet actuator for near space high-speed flow control*, *Acta Astronautica* **133**, 95 (2017).
- [182] D. Caruana, P. Barricau, and P. Hardy, *The "plasma synthetic jet" actuator: aerothermodynamic characterization and first flow control applications*. in *47th AIAA aerospace sciences meeting including the new horizons forum and aerospace exposition* (2009) p. 1307.
- [183] D. Caruana, *Plasmas for aerodynamic control*, *Plasma Physics and Controlled Fusion* **52**, 124045 (2010).
- [184] L. Yuanwei, S. Yong, Z. Jingzhou, and T. Xiaoming, *A numerical investigation of the sparkjet actuator in multiple-shot mode*, *Procedia Engineering* **99**, 1514 (2015).
- [185] J. Qiu, C. Zhang, L. Han, C. Ren, and T. Shao, *Characteristics of repetitive discharges of plasma synthetic jet actuators*, in *Power Modulator and High Voltage Conference (IPMHVC), 2016 IEEE International* (IEEE, 2016) pp. 576–579.
- [186] M. Seyhan, Y. E. Akansu, F. Karakaya, C. Yesildag, and H. Akbıyık, *Effect of the duty cycle on the spark-plug plasma synthetic jet actuator*, in *EPJ Web of Conferences*, Vol. 114 (EDP Sciences, 2016) p. 02104.
- [187] J. F. Kolb, A.-A. H. Mohamed, R. O. Price, R. J. Swanson, A. Bowman, R. Chiavarini, M. Stacey, and K. Schoenbach, *Cold atmospheric pressure air plasma jet for medical applications*, *Applied Physics Letters* **92**, 241501 (2008).
- [188] T. Abe, Y. Takizawa, S. Sato, and N. Kimura, *Experimental study for momentum transfer in a dielectric barrier discharge plasma actuator*, *AIAA Journal* **46**, 2248 (2008).
- [189] T. C. Corke, C. L. Enloe, and S. P. Wilkinson, *Dielectric barrier discharge plasma actuators for flow control*, *Annual Review of Fluid Mechanics* **42**, 505 (2010).
- [190] M. Forte, J. Jolibois, J. Pons, E. Moreau, G. Touchard, and M. Cazalens, *Optimization of a dielectric barrier discharge actuator by stationary and non-stationary measurements of the induced flow velocity: application to airflow control*, *Experiments in Fluids* **43**, 917 (2007).

- [191] S. Grundmann and C. Tropea, *Experimental transition delay using glow-discharge plasma actuators*, Experiments in Fluids **42**, 653 (2007).
- [192] F. O. Thomas, A. Kozlov, and T. C. Corke, *Plasma actuators for cylinder flow control and noise reduction*, AIAA Journal **46**, 1921 (2008).
- [193] J. Wang, Y. Li, and F. Xing, *Investigation on oblique shock wave control by arc discharge plasma in supersonic airflow*, Journal of Applied Physics **106**, 073307 (2009).
- [194] D. Xu, M. Shneider, D. Lacoste, and C. Laux, *Thermal and hydrodynamic effects of nanosecond discharges in atmospheric pressure air*, Journal of Physics D: Applied Physics **47**, 235202 (2014).
- [195] B. L. Smith and A. Glezer, *Jet vectoring using synthetic jets*, Journal of Fluid Mechanics **458**, 1 (2002).
- [196] R. Mittal and P. Rampungoon, *On the virtual aeroshaping effect of synthetic jets*, Physics of Fluids **14**, 1533 (2002).

SCIENTIFIC CONTRIBUTIONS

IN THIS THESIS

JOURNAL ARTICLES

11. **H. Zong**, M. Chiatto, M. Kotsonis & L. de Luca, *Plasma synthetic jet actuators for active flow control (invited review paper)*, Actuators, submitted, (2018).
10. **H. Zong** & M. Kotsonic, *Effect of velocity ratio on plasma synthetic jets in turbulent crossflow*, Journal of Fluid Mechanics, submitted, (2018).
9. **H. Zong**, *Airfoil flow separation control with plasma synthetic jets at moderate Reynolds number*, Experiments in Fluids, accepted, (2018).
8. **H. Zong**, *Influence of nondimensional heating volume on efficiency of plasma synthetic jet actuators*, AIAA Journal, **56**, 2075 (2018).
7. **H. Zong** & M. Kotsonis, *Experimental investigation on frequency characteristics of plasma synthetic jets*, Physics of Fluids, **29**, 115107 (2018).
6. **H. Zong** & M. Kotsonis, *Formation, evolution and scaling of plasma synthetic jets*, Journal of Fluid Mechanics, **837**, 147-181 (2018).
5. **H. Zong** & M. Kotsonis, *Realisation of plasma synthetic jet array with a novel sequential discharge*, Sensors and Actuators A: Physical, **266**, 314-317 (2017).
4. **H. Zong** & M. Kotsonis, *Interaction between plasma synthetic jet and subsonic turbulent boundary layer*, Physics of Fluids, **29**, 045104 (2017).
3. **H. Zong** & M. Kotsonis, *Effect of slotted exit orifice on performance of plasma synthetic jet actuator*, Experiments in Fluids, **58**, 17 (2017).
2. **H. Zong** & M. Kotsonis, *Electro-mechanical efficiency of plasma synthetic jet actuator driven by capacitive discharge*, Journal of Physics D: Applied Physics, **49**, 455201 (2016).
1. **H. Zong** & M. Kotsonis, *Characterisation of plasma synthetic jet actuators in quiescent flow*, Journal of Physics D: Applied Physics, **49**, 335202 (2016).

CONFERENCE ABSTRACTS

2. **H. Zong** & M. Kotsonis, *Influence of nondimensional heating volume on performance characteristics of plasma synthetic jet actuator*, 14th International Conference on Fluid Control, Measurements and Visualization–FLUCOME, October 9-12, 2017, Notre Dame, USA.
1. **H. Zong** & M. Kotsonis, *Influence of working frequency on performance characteristics of plasma synthetic jet actuator*, European Drag Reduction and Flow Control Meeting–EDRFCM, April 3–6, 2017, Rome, Italy.

NOT IN THIS THESIS

JOURNAL ARTICLES

5. **H. Zong** et al., *Investigation of the performance characteristics of a plasma synthetic jet actuator based on a quantitative Schlieren method*, Measurement Science and Technology, **27**, 055301 (2016).
4. **H. Zong** et al., *Efficiency characteristic of plasma synthetic jet actuator driven by pulsed direct-current discharge*, AIAA Journal, **54**, 3409 (2016).
3. **H. Zong** et al., *Influence of geometrical parameters on performance of plasma synthetic jet actuator*, Journal of Physics D: Applied Physics, **49**, 025504 (2016).
2. **H. Zong** et al., *Analytic model and frequency characteristics of plasma synthetic jet actuator*, Physics of Fluids, **27**, 027105 (2015).
1. **H. Zong** et al., *Influence of capacitor energy on performance of a three-electrode plasma synthetic jet actuator*, Sensors and Actuators A: Physical, **222**, 141-121 (2015).

ACKNOWLEDGEMENTS

Sitting quietly and routinely in the almost empty PhD room at 10 O'clock in a summer morning, waiting peacefully for the afternoon session of FMT oral exam, breathing the chilly and refreshing air underneath a cloudy and dark sky that is called Dutch style, I hereby declare voicelessly that my doctorate journey is adjourned... Looking back to the time, I did not regret any choices I have made in the past three years, exactly as an amateur Cypriot philosopher (Marios Kotsonis) had said in one of his student's graduation party, 'go ahead, at least you tried...'. Although this sentence has unexpectedly de-motivated one of the best PhD candidates in the aerodynamic Lab (Guiseppe Caridi), 'try' does interpret well my trajectory, from the right beginning until the very end.

I still clearly remember the day in 2015 when Fulvio and Marios interviewed me in skype, asking me fundamental aerodynamic concepts such as Strouhal number, frequency analysis and leading/trailing edge stall. Undoubtedly, I was anxious and stressful, trying the best to show off knowledge in an accented and staggered English, yet still in a level that I wouldn't accept my future student be. Luckily, they opened the door and decided to do an experiment—give me a 'try'. For this 'try', I would like to extend my paramount gratitude to the Promoter, Fulvio Scarano and the daily supervisor, Marios Kotsonis. Without your risky decision, I shall never have the chance to discover my full potentials in Delft and expose my capabilities to a wide international stage.

After the journey was kicked off, it was my turn to 'show'. I was born in the Chinese calendar year of Monkey, predestined to be 'smart' (than idiots), 'ambitious' and 'hasty'. For the ambition of becoming an eligible PhD researcher in TU Delft, I worked 12/7 (hours/days) before go/no go meeting, getting experiments running as quickly as possible and writing papers as much as it should not be. During that period, I found out how lucky I was to have a multifaceted daily supervisor by side. In the experiments, he was an experienced and energetic technician who enthusiastically helped me to set up the beams, adjust the laser optics and troubleshoot DaVis issues. While revising my manuscripts, he became a rigorous, knowledgeable scholar who was patient enough to go through iteratively the crap figures and meaningless texts. Finally, during the rebuttal, he transformed into an undefeatable legendary knight who shielded our papers from the nasty and tricky comments of reviewers. For these countless time, energy and guidance, I would like to devote once again my sincerest gratefulness and highest respect to the daily supervisor—MARIOS KOTSONIS!

Due to the 'hasty' character in work, I was easily indulged into the endless experimental data analysis and paper writing, frequently forgetting to raise my head and aim the 'stars'. As the promoter, Fulvio can always precisely perceive these moments, timely catch me in the coffee corner, FMT exam or his office, and inject my brain with vivid and insightful stories ranging from 'a good narrator' to 'a best football player'. For these occasional

mind sparks as well as the full research freedom you granted me at the very beginning, I would express my heartfelt acknowledgement to the promoter–FULVIO SCARANO!

Now, the journey in TU Delft has come to an end. Quickly flashing my mind, I could not forget the lovely smiling face of our dearest secretary–Colette Russo, and the generous favors offered by the technicians (Nico, Peter, Frits, Denis, Stefan, and Henk-Jan). Without Colette, I would be failed in the PhD registration due to a lack of Master degree, possibly residing in a dark corner of nowhere and begging for food right now. Without the technicians, I could have killed myself while conducting experiments, just because of the DaVis license issues, wind tunnel malfunctions, actuator model burnout, and unexpected laser shooting. Thank you all for creating a clean, safe, and trouble-free working environment where PhD candidates can focus 100 percent on the research topics!

I also want to acknowledge the PhD candidates who once fought with me in this room, ‘one floor to heaven’. They are André, Qinging, Rakesh, Shaafi, Varun, Tiago, Beppe, Theo, Jacobo, Martin, Wouter, Zeno, Alberto, Koen, Jan, Henry, Paul, Sagar, Alexander, Alessandro, Constantin, Luis. Without the one-hour lunch talk every day, my office life would be as plain as the Dutch landscape, and my oral English would remain the same level as I first came here. Thank you all for the memorable time together. Additionally, I am credited to my first and also the last Master student–Timo van Pelt, who has endured my torture for almost one year, contributed significantly to Chapter 8 of this thesis and translated the summary and propositions precisely in Dutch.

Special thanks to my countable friends here. They are Weibo Hu, Jianbing Jin, Juan Tang, Jintao Yu, Chenteng Sun, Yu Zhang, Yi Zhang, Jun Nie and Xiaodong Li. Without your faithful accompany and unconditional support, this sweet, fruitful, and exciting over-sea trip to the Kingdom of Flower would end up into a nightmare filled with loneliness and bitterness. Cheers once again to the not-so-yummy dinners we cooked, not-so-bad beers we drank, could-be-better blonds we screamed at, so-far-the-best landscapes we viewed, and many more things we shared together...

Last, to my family and those who I love! Without you, I will never be today's me!

July 13th, 2018

BIOGRAPHY



Haohua Zong was born at 08/10/1992, in a small village affiliated to Ruzhou, Henan Province in China. Both of his parents are authentic farmers, who have devoted majority of their lives to field works such as growing and harvesting wheats, corns and peanuts. While Haohua was still in the primary and middle school, he proved to be the naughtiest boy in the campus and often tricked his classmates and teachers with wild ugly animals caught in the nearby forests and rivers. As you may noticed, these inappropriate naughty behaviors have left permanent scars on his fore and back head. Haohua's early interests in mechanical and electrical engineering were ignited by the

gift toys he received in festivals. These toys, mostly movable and controllable, were frequently detached into tiny pieces and reassembled together to satisfy Haohua's curiosity.

In September 2009, Haohua was admitted as a Bachelor student by Air Force Engineering University in Xi'an, China, major in Flight Vehicle Propulsion Engineering. During the four-years persistent study, he gained basic knowledge in aircraft structure, control, and propulsion, which to some extent paved his way as a researcher. Between September 2013 and December 2015, he worked in the National Key Laboratory on Plasma Dynamics as a Master student, luckily enough to be supervised by many of the excellent professors there. These professors led him to the field of plasma flow control and imparted him all the essential elements for doing research. In December 2015, he moved to Delft University of Technology to further pursue the doctoral education.